Self-assembly and multiscale characterization of structures and interfaces

Nicholas Turetta

UNIVERSITÉ DE STRASBOURG

ÉCOLE DOCTORALE DES SCIENCES CHIMIQUES

UMR 7006 - Institut de Science et d'Ingénierie Supramoléculaires

THÈSE

présentée par :

Nicholas TURETTA

soutenue le : **14 Décembre 2022**

pour obtenir le grade de : **Docteur de l'université de Strasbourg**

Discipline/ Spécialité : Chimie

Auto-assemblage et caractérisation multi-échelle des structures et des interfaces

THÈSE dirigée par :

M. SAMORI' Paolo	Professeur, Université de Strasbourg, France

RAPPORTEURS :

M. CAVALLINI Massimiliano	Directeur de Recherche, CNR, Italie
Mme. MAS-TORRENT Marta	Professeur, ICMAB-CSIC, Espagne

AUTRES MEMBRES DU JURY :

Mme. RUIZ CARRETERO Amparo	Chargé de recherches HDR, Université de Strasbourg, France

Résumé

La compréhension et le contrôle du transport de charge et des mécanismes de transport sont une condition indispensable du développement de dispositifs optoélectroniques fonctionnels basés sur des semi-conducteurs organiques. L'auto-assemblage des molécules organiques est contrôlé par le rôle des interactions intramoléculaires, intermoléculaires et interfaciales. Plus précisément, les matériaux organiques sont constitués de molécules individuelles qui sont maintenues ensemble par de faibles interactions intermoléculaires non covalentes, ce qui leur confère une complexité sans précédent par rapport à leurs homologues inorganiques. La détermination de la relation entre la structure chimique et l'état solide des semi-conducteurs organiques et les propriétés électriques observées dans les matériaux nécessite une approche détaillée multi-échelle et multi-technique. En raison des nombreux degrés de liberté structurelle et conformationnelle résultant des interactions non covalentes entre les molécules dans les matériaux organiques, la complexité de la microcristallinité et de la morphologie observée dans les films organiques se reflète sur les propriétés de transport de charge. La disposition spatiale des molécules dans les domaines cristallins détermine comment les porteurs de charge sont transférés d'une molécule à l'autre, d'un domaine à l'autre, à travers les joints de grains. Des petites molécules aux polymères, la fraction relative des phases amorphes et ordonnées dépend fortement du traitement de l'échantillon, ce qui constitue un défi majeur dans le domaine des semi-conducteurs organiques. En plus, une même espèce chimique peut présenter des phases interfaciales, des phases induites par le substrat et d'autres types de phases polymorphes compliquant encore plus la caractérisation de ces systèmes. Bien qu'une approche possible pour atténuer cette complexité repose sur le dépôt de films monocristallins pour exclure les effets indésirables provenant des joints de grains, la fabrication de tels films ordonnés est très difficile et reste limitée à quelques systèmes de référence optimisés. En outre, la plupart des semi-conducteurs organiques s'auto-assemblent dans des films polycristallins, et il est donc particulièrement intéressant d'étudier l'influence effective des défauts structurels sur les performances des matériaux et sur les mécanismes de transport de charge. L'objectif final est, naturellement, d'obtenir le meilleur ordre structurel et une orientation des domaines alignée dans la direction du transport des charges, ce qui ne correspond pas nécessairement à la réalisation d'un monocristal unique. En effet, il est plus probable d'obtenir un film constitué de multiples domaines cristallins, orientés parallèlement les uns aux autres, et s'interfaçant entre eux avec des joints de grains

latéraux. Le contrôle de la morphologie du film est essentiel pour la réalisation de dispositifs optimaux car, en raison de leur structure moléculaire particulière, les semi-conducteurs organiques présentent des propriétés structurelles et électriques fortement anisotropes. L'empilement à l'état solide implique généralement l'empilement latéral des molécules conjuguées, ce qui produit une conductivité 2D presque isotrope dans le plan et une conductivité hors plan plus faible, influencée par la présence éventuelle de chaînes latérales. Les aspects liés à la relation structure-propriété, cruciaux pour le développement de dispositifs fonctionnels organiques, sont examinés à plusieurs reprises dans cette thèse et représentent l'un des pivots principaux.

L'objectif de cette thèse est d'étudier et de développer des dispositifs (opto)électroniques basés sur des semi-conducteurs organiques à base de petites molécules ou de polymères. La thèse commence par une brève introduction sur les semi-conducteurs organiques en se focalisant sur les aspects structurels qui sont essentiels pour comprendre le transport de charge dans le domaine de l'électronique organique. Liée à ce premier chapitre, une introduction pratique concernant les différentes techniques expérimentales qui ont été utilisées tout au cours de mon travail de doctorant est présentée de manière comparative. Les trois chapitres suivants se réfèrent chacun à un dispositif fonctionnel particulier, en commençant par les détails de fabrication et de fonctionnement et en terminant par la détermination des paramètres caractéristiques de chaque type de dispositif. Pour résumer, le sujet de chaque chapitre est le suivant :

1. Capteurs d'humidité basés sur une petite molécule organique hydrophile.
2. Transistors électrochimiques organiques optiquement commutables basés sur un mélange de polymères avec une molécule photochromique.
3. Etude du transport de charge hors plan dans des transistors organiques à effet de champ basés sur de petites molécules organiques.

L'étude des capteurs d'humidité basés sur les matériaux organiques est non seulement nécessaire pour le développement du capteur en tant que tel, mais fournit également des informations fondamentales relatives aux effets de l'humidité sur le fonctionnement des transistors organiques aux conditions ambiantes. L'environnement autour du dispositif fonctionnel peut, en effet, influencer sévèrement ses performances et des précautions supplémentaires doivent être prises pour s'assurer que les matériaux actifs sont suffisamment stables en conditions expérimentales. D’un côté, l'environnement

peut compromettre l'intégrité de la couche mince, mais, de l'autre côté, on peut exploiter les changements réversibles des propriétés de la couche pour des applications de capteurs par exemple. Les événements de reconnaissance règlent l'interaction de la matière organique (opportunément fonctionnalisée) avec les composants de l'environnement, en permettant l'identification de l'analyte. Comme pour les interactions intermoléculaires qui maintiennent la matière organique en place, l'interaction de la matière active avec les constituants de l'environnement se produit au niveau non covalent. Lorsqu'il est prouvé qu'un matériau est sensible à un analyte, son intégration dans le dispositif est réalisée en optimisant la déposition de la couche mince et en trouvant la meilleure configuration du dispositif (par exemple, top ou bottom contacts) et la meilleure géométrie (par exemple, profondeur, largeur et longueur du canal). Lors du développement d'un capteur, cette dernière étape nécessite l'évaluation de la contribution des autres parties du dispositif (telles que les électrodes, le substrat et les différentes interfaces) au fonctionnement. Un autre point central de ce projet consiste en une méthode expérimentale visant à clarifier le rôle joué par chaque partie du dispositif. Une performance supérieure est finalement obtenue en optimisant la contribution synergique de tous les éléments fonctionnels.

Notre collaborateur, le Prof. Yves Geerts de l'Université Libre de Bruxelles, a synthétisé un nouveau dérivé du [1]benzothiéno[3,2-b][1]benzothiophène (BTBT) conçu pour être sensible à l'humidité en fonctionnalisant le BTBT par des chaînes latérales hydrophiles d'oligoéthylène glycol (OEG). Cette petite molécule, dénommée OEG-BTBT, est capable de s'auto-assembler en couches minces cristallines et (semi)conductrices afin de réaliser des dispositifs à deux électrodes qui transduisent électriquement les variations de l'humidité ambiante avec des rapports de courant élevés ($>10^4$) à de basses tensions (2 V). Grâce à une approche multi-échelle et multitechnique combinant la diffractométrie des rayons X et les méthodes optiques non linéaires avec des mesures électriques en courant alternatif et continu, les mécanismes de transport de charge gouvernant la conduction mixte électronique/protonique (H+) observée dans les capteurs ont été dévoilés. La sensibilité de ces capteurs peut être améliorée par la fonctionnalisation chimique du substrat avec des alkylsilanes ou par un traitement d'oxydation UV/ozone afin de modifier la mouillabilité de la surface.

Le second projet concerne le mélange d'un polymère, connu pour être un excellent conducteur mixte, avec un dérivé photochromique du spiropyranne. Ces deux matériaux ont été mélangés pour fabriquer des transistors électrochimiques organiques (OECT) à

commutation optique. L'application d'une tension variable à une électrode en solution est capable de modifier l'environnement local à la surface d'un matériau électrochimiquement actif situé dans la même solution. Des changements de l'environnement de fonctionnement d'un dispositif peuvent ainsi être déclenchés par des stimuli électrochimiques. Ces stimuli sont appliqués à travers un électrolyte pour induire un dopage électrochimique dans certains matériaux organiques qui doivent présenter une conductivité mixte ionique/électronique pour assurer le fonctionnement de l'OECT, le dispositif prototype d'une nouvelle discipline émergente appelée iontronique. Cette discipline est une branche importante de la bioélectronique qui vise à contrôler le caractère conductif des matériaux pour interfacer les dispositifs fonctionnels avec les tissus biologiques et les systèmes vivants. Les matériaux de pointe pour les interfaçages en bioélectronique sont en effet organiques, notamment les polymères conjugués et les polyélectrolytes à base organique. L'intérêt croissant de la communauté scientifique vers le couplage entre l'électronique et la biologie est motivé par les récentes découvertes et par les potentialités de progrès qui pourraient être concrétisées grâce à cette technologie. Les enjeux auxquels la bioélectronique essaie déjà de faire face sont la communication avec les cellules vivantes pour capter les paramètres cellulaires vitaux ou pour activer des fonctions in-vitro, la réalisation de systèmes d'administration de médicaments dans les organismes vivants grâce à la signalisation électrochimique, la régulation des mécanismes sous-jacents à l'expression de macro(bio)molécules ou le développement de nouvelles stratégies thérapeutiques par le suivi des états pathologiques. Dans ce contexte, le développement de systèmes capables de répondre à des signaux multiples tels que des stimuli électroniques, des gradients ioniques et de la lumière est une condition préalable à l'intégration complète des dispositifs bioélectroniques dans le corps humain.

Le mélange optiquement commutable est formé de deux éléments : (i) un semi-conducteur mixte utilisable pour les OECT et (ii) un additif moléculaire photochromique. Un polymère conjugué possédant des chaînes latérales OEG, le poly(2-(4,4’-bis(2-méthoxyéthoxy)-5’-méthyl-[2,2’-bithiophène]-5-yl)-5-méthylthiéno[3,2-b]thiophène, ou pgBTTT, a été synthétisé et fourni par le groupe du Prof. Iain McCulloch. Un dérivé de spiropyranne fonctionnalisé par une chaîne latérale OEG (pour favoriser le mixage et l'interdigitation des chaînes latérales dans le mélange) a été synthétisé par un de mes collègues, Dr. Wojciech Danowski, à l'Université de Strasbourg. Les OECT optiquement commutables basés sur ce mélange opèrent dans des solutions aqueuses

0.5 M NaCl, en tant qu'électrolyte, avec une réduction d'environ un facteur 10 de la performance du dispositif par rapport à l'OECT à base de pgBTTT pur, alors que la commutation réversible entre deux états (séparés par ~ 20% du courant de fonctionnement) est induite par l'illumination de l'OECT avec une lumière UV (365 nm) ou visible (530 nm). Le comportement photosensible du OECT basé sur le mélange est remarquablement différent de celui de l'échantillon de contrôle (pgBTTT pur) qui ne présente pas deux états distincts mais répond uniquement par une augmentation du courant ON sous photostimulation UV et visible. Grâce à une caractérisation photophysique, structurelle, électronique et compositionnelle du mélange, il a été possible de comprendre les mécanismes qui sont à la base du fonctionnement de ces dispositifs et d'identifier les processus de photofatigue qui doivent être considérés pour améliorer les performances.

Le troisième projet concerne la détermination de la conductivité hors plan des transistors organiques à effet de champ (OFET) basés sur de petites molécules. Les dispositifs OFET ont été largement étudiés au cours des dernières 45 années en raison de leur grand potentiel pour la fabrication à moindre coût sur de grandes surfaces avec des substrats flexibles. La plupart des activités de recherche de la dernière décade ont été dédiées à l'amélioration de la mobilité des porteurs de charge, même si la fréquence de transit de ces dispositifs OFET n'était pas suffisamment élevée pour permettre le fonctionnement des circuits électroniques à commutation rapide (conventionnellement fixés à des fréquences supérieures à 1 GHz). Afin que l'OFET puisse connaître une percée technologique mondiale, les chercheurs doivent encore surmonter certains défis, tels que la nanofabrication uniforme de dispositifs sur de grandes surfaces avec une longueur de canal réduite (inférieure à 100 nm). Ces strictes spécifications représentent un progrès considérable dans l'optimisation des protocoles de fabrication des dispositifs, mais une investigation plus approfondie sur les possibilités de réduction de la résistance de contact, qui est le paramètre du dispositif qui limite actuellement le fonctionnement des OFET à haute fréquence, est également requise. Le développement futur des dispositifs OFET dans l'électronique commerciale dépendde la découverte de stratégies efficaces pour contrôler et minimiser la résistance de contact. Le transport de charge hors plan n'a pas été aussi étudié que le transport latéral, ce qui a entraîné un manque de compréhension des processus de transfert de charge qui se produisent, par exemple, depuis l'injection du porteur à l'interface métal/semiconducteur jusqu'au canal conducteur de l'OFET. Une méthode permettant de résoudre efficacement certains des

problèmes liés à la résistance de contact devrait inclure une caractérisation multi-échelle des propriétés électriques et électroniques des interfaces métal/organique semi-conducteur.

À cette fin, le chapitre se concentre sur la quantification des paramètres cruciaux qui affectent la résistance de contact avec une combinaison de techniques microscopiques et macroscopiques, plutôt que sur la fabrication et la caractérisation de l'OFET avec le seul but d'analyser ses caractéristiques électriques. La mesure des niveaux électroniques des semi-conducteurs organiques et des électrodes en métal (Au simple ou Au modifié par une monocouche auto-assemblée (SAM)), soit le niveau de Fermi, l'énergie d'ionisation et la bande interdite optique, pour les semi-conducteurs, et le travail de sortie, pour les métaux, est le point de départ pour construire le diagramme des niveaux d'énergie d'un OFET. Ces paramètres sont ici quantifiés pour une large liste de semi-conducteurs organiques à petites molécules (et pour certaines surfaces Au modifiées par SAM) et les propriétés électroniques sont comparées sur la base d'arguments structurels au niveau moléculaire et à l'état solide. Le décalage entre les niveaux d'énergie électronique de l'électrode et du semi-conducteur est à l'origine de la barrière d'énergie d'injection au niveau d'une hétérojonction métal/semiconducteur, c'est-à-dire la barrière Schottky, qui est l'un des facteurs déterminant la résistance de contact. La microscopie à force atomique à pointe conductrice (C-AFM) est utilisée pour déterminer la conductivité hors plan dans des couches minces d'une petite molécule, le dinaphto[2,3-b:2',3'-f]thiéno[3,2-b]thiophène (DNTT), et son dérivé fonctionnalisé avec des chaînes latérales octyliques, appelé C8-DNTT. Tout d'abord, les paramètres qui régulent l'injection de charges aux électrodes dans les OFET sont décrits et quantifiés pour l'ensemble du système étudié. Ensuite, les données C-AFM des films de DNTT sur Au sont traitées comme un système modèle pour le régime de courant limité par la charge d'espace (SCLC). Enfin, le comportement électrique des films minces de C8-DNTT fabriqués par dépôt d'une solution à l'aide d'une lame et par sublimation thermique est comparé, en mettant en évidence les avantages et les désavantages des deux méthodes de déposition. On constate que la planéité et la rugosité des couches minces de matériaux organiques influencent considérablement le comportement de l'échantillon lorsqu'il est nécessaire d'obtenir une image locale et fidèle des propriétés électroniques et structurelles. La présence de chaînes latérales favorise un meilleur ordre cristallin mais réduit l'efficacité du transport de charges hors plan. L'intérêt de cette étude repose également sur le développement d'un protocole expérimental

permettant la détermination de la conductivité hors plan via C-AFM qui peut être facilement adapté à la topographie de la surface.

En conclusion, cette thèse tente d'aborder certains des aspects cruciaux dans le développement de dispositifs fonctionnels basés sur des semi-conducteurs organiques.

Les résultats obtenus ouvrent une nouvelle perspective sur la conception des matériaux organiques en éclairant certains des aspects qui caractérisent profondément les prestations des dispositifs, tels que les capteurs d'humidité, les OECT et les OFET. Grâce à la corrélation entre la structure chimique et les propriétés à l'état solide des semi-conducteurs organiques auto-assemblés réalisée avec l'aide d'une méthodologie multitechnique, les points clés du développement des dispositifs sont facilement identifiés et exploités pour, par exemple, améliorer les performances d'un capteur, intégrer plusieurs fonctionnalités dans un seul dispositif, ou simplement concevoir des méthodes alternatives pour l'étude des systèmes semi-conducteurs.

Summary

Understanding and controlling charge transport and transport mechanisms is a prerequisite for the development of functional optoelectronic devices based on organic semiconductors. Self-assembly of organic molecules is controlled by the interplay of intramolecular, intermolecular and interfacial interactions. More specifically, organic materials consist of individual molecules that are held together by non-covalent weak intermolecular interactions, hence providing unprecedented complexity compared to their inorganic counterpart. Discerning how the chemical and solid-state structure of organic semiconductors relates to the observed electrical properties in the material requires a detailed multi-scale and multi-technique approach. As a consequence of the many degrees of structural and conformational freedom resulting from the non-covalent interactions between molecules, the complexity of the observed microcrystallinity and morphology in organic films is reflected in the charge transport properties. The spatial arrangement of molecules within the crystal domains determines how charge carriers are transferred from one molecule to another, from one domain to another, through the domain boundaries. From small molecules to polymers, the relative fraction of amorphous and ordered phases strongly depends on the sample processing, the latter being a major challenge in the field of organic semiconductors. In addition, one single chemical species can exhibit interfacial, substrate-induced and other types of polymorphic phases, thus further complicating the characterization of these systems. While one possibility to mitigate this complexity relies on the deposition of single-crystal films to exclude undesired effects arising from grain boundaries, the fabrication of such ordered films is very challenging and still limited to a few optimized reference systems. Instead, most organic semiconductors self-assemble in polycrystalline films, hence it is of broader interest to study the effective influence of structural defects on the performance of materials and on charge transport mechanisms. The final aim is, of course, to achieve the best structural order and a domain orientation aligned to the charge transport direction, which does not necessarily correspond to having a unique single crystal. Indeed, it is more probable to obtain a film consisting of multiple crystalline domains, oriented in parallel to each other, and interfacing one another with grain boundaries on the side. The control of the film morphology is critical for the realization of optimal devices because, as a result of their peculiar molecular structure, organic semiconductors possess highly anisotropic structural and electrical properties. The solid-state packing generally involves the lateral stacking of the conjugated

molecules giving rise to almost isotropic 2D in-plane conductivity with a lower the out-of-plane conductivity that is influenced by the eventual presence of side chains. The aspects related to the structure and property relationship, crucial for the development of organic functional devices, are addressed in multiple instances within this thesis and represent one of the main pivotal points.

The aim of this thesis is to study and develop (opto)electronic devices based on small-molecule or polymer organic semiconductors. The thesis begins with a brief introduction on organic semiconductors focusing on the structural aspects that are key to understanding charge transport in organic electronics. Tied to this first chapter, a practical introduction concerning the different experimental techniques that have been employed throughout my work as a Ph.D. student is presented in a comparative way. The three following chapters each refer to a particular functional device, starting from the fabrication and operation aspects and concluding with the determination of characteristic parameters for each type of device. To summarize, the topic of each chapter is:

1. Humidity sensors based on a hydrophilic small organic molecule
2. Optically switchable organic electrochemical transistors based on a polymer blend with a photochromic molecule
3. Study of the out-of-plane charge transport in organic field effect transistors based on small organic molecules

The study of humidity sensors based on organic materials is not only relevant for the development of the sensor itself, but it also provides fundamental information about the effects of humidity for the operation of organic transistors at ambient conditions. The environment surrounding the functional device can, in fact, severely affect its performance and additional care must be taken to ensure that the active materials are sufficiently stable under the experimental working conditions. On the one hand, the environment may be detrimental to the thin-film integrity, but, on the other hand, reversible changes in the film properties can be exploited for e.g., sensing applications. Recognition events rule the interaction of the suitably functionalized organic material with the components of the environment, enabling the analyte identification. Similar to the intermolecular interactions holding organic materials in place, the interaction of the active material with environmental components occurs at the non-covalent level. Once a material is proven to be sensitive to some analyte, its integration in the device is

performed by optimizing the thin-film deposition and finding the best device configuration (e.g., top or bottom contacts) and geometry (e.g., channel depth, width and length). In the development of a sensing device, this latter part requires the evaluation of the contribution of the other device components (such as the electrodes, the substrate and the various interfaces) to the observed device behavior. Another pivotal point of this work is represented by an experimental approach targeting the disentanglement of the role played by each component of the responsive system. High performance is finally achieved by optimizing the synergistic contribution of all functional elements.

Our collaborator, Prof. Yves Geerts from Université Libre de Bruxelles, synthesized a novel [1]benzothieno[3,2-b][1]benzothiophene (BTBT) derivative designed to be humidity-responsive by functionalizing the BTBT core with hydrophilic oligoethylene glycol (OEG) side chains. This small molecule, named OEG-BTBT, is capable of self-assembling into (semi)conducting crystalline thin films to give humidity responsive two-terminal devices that electrically transduce the changes in environmental humidity with high current ratios ($>10^4$) at low voltages (2 V). Thanks to a multiscale and multitechnique characterization combining X-ray diffractometry and non-linear optical methods with AC and DC electrical measurements, the mechanisms of charge transport governing the mixed electronic/protonic (H^+) conduction observed in the chemiresistors have been revealed. The responsivity of these sensors can be further tuned upon chemical functionalization of the substrate with alkylsilanes or via a UV/ozone oxidating treatment to change the surface wettability.

The second project regards the blending of a polymer, known to be a very good mixed conductor, with a photochromic spiropyran derivative. These two materials were mixed together to fabricate optically switchable organic electrochemical transistors (OECTs). The application of a variable voltage to an electrode in solution is capable of altering the local environment at the surface of an electrochemically active material present in the same solution. Changes in the environment of operation of a device can be thus driven by electrochemical stimuli. These stimuli can be applied through the electrolyte to induce an electrochemical doping in some organic materials which must show a mixed ionic/electronic conductivity to enable the operation of the OECT, the prototypical device of a new emerging discipline called iontronics. Iontronics is an important branch of bioelectronics which aims to control the conductive character of materials for the interfacing of functional devices with biological tissues and living systems. State-of-the-

art materials for electrical interfacing in bioelectronics are indeed organic, such as conjugated polymers and organic-based polyelectrolytes. The rising interest of the scientific community towards the coupling electronics and biology is justified by its recent discoveries and by the potential advances that could be made true thanks to this technology. A few examples of the challenges that bioelectronics is already trying to face are the communication with living cells to sense the cell vital parameters or to actuate functions in-vitro, the realization of drug delivery systems in living mediated by electrochemical signaling, regulating the mechanisms underlying the expression and release of macro(bio)molecules or developing new therapeutical approaches by the local monitoring of disease states. Within this context, the development of systems that can operate with or respond to multiple inputs such as electronic stimuli, ionic gradients and light pulses is a prerequisite for the full integration of bioelectronic devices with the human body.

The optically switchable polymer blend consists of two components: (i) a mixed semiconductor suitable for OECTs and (ii) a photochromic molecular additive. A conjugated polymer with OEG side chains, poly(2-(4,4’-bis(2-methoxyethoxy)-5’-methyl-[2,2’-bithiophen]-5-yl)-5-methylthieno[3,2-b]thiophene, or pgBTTT, was synthesized in the group of Prof. Iain McCulloch from King Abdullah University of Science and Technology. A spiropyran derivative functionalized with an OEG side chain (to promote the mixing and interdigitation of the side chains in the blend) was synthesized by one of my colleagues, Dr. Wojciech Danowski, at the University of Strasbourg. The optically switchable OECT based on this blend operate with 0.5 M NaCl solutions in water as electrolyte with about a factor 10 loss in the device performance compared to the neat pgBTTT OECT while introducing a reversible switching between two states (separated by ~ 20% of the device ON current) induced by the OECT illumination with either UV (365 nm) or visible (530 nm) light. The photoresponsive behavior of the OECT device based on the polymer blend is strikingly different from the control neat pgBTTT sample that does not exhibit two distinct states but only responds with an increase in ON current for both UV and visible photostimulation. Thanks to a photophysical, structural, electronic and compositional characterization of the polymer blend it was possible to understand the phenomena underlying the functioning of these optically switchable OECTs and to identify the processes of photofatigue that must be addressed to further improve the device performance.

The third project regards the experimental determination of the out-of-plane conductivity of in organic field effect transistors (OFETs) based on small molecules. OFET devices have been intensively studied during the last 45 years due to their great potential for low-cost fabrication over large areas on flexible substrates. Most of the research efforts in the past decade have been devoted to the improvement of the charge carrier mobility, even though the transit frequency of these OFET devices was not high enough to enable the operation of fast switching electronics (conventionally set at frequencies above 1 GHz). For OFETs to experience a breakthrough in worldwide technology, there are still some challenges to be faced by researchers, such as a uniform large area nanofabrication of devices with a reduced channel length (down to 100 nm). These strict requirements not only represent a huge step forward in the optimization of the device fabrication protocols, but also highlight the need for a deeper investigation on the possible methodologies towards the reduction of the contact resistance, that is the device parameter that is currently limiting the fast operation of OFETs. The future scale up of OFETs into commercial electronics depends on the finding of successful strategies to control and minimize the contact resistance. The charge transport in the vertical direction has not been studied as intensively as the lateral one, with a consequent lack of understanding of the charge transfer processes occurring e.g., from the carrier injection at the metal/semiconductor interface to the carrier reaching the OFET conductive channel. A method that can effectively address some of the challenges associated to the contact resistance must include a multiscale characterization of the electrical and electronic properties of metal/organic semiconductor interfaces.

Towards this end, this chapter focuses on the quantification of crucial parameters affecting the contact resistance with a combination of microscopic and macroscopic techniques, rather than on fabricating and characterizing OFET devices with the only aim of analyzing the resulting electrical characteristics. The determination of the electronic levels of organic semiconductors and metal electrodes (bare Au or self-assembled monolayer (SAM) modified Au), i.e., the Fermi level, the ionization energy and the optical bandgap, for semiconductors, and the work function, for metals, is the starting point for constructing the energy level diagram of an OFET. These parameters are hereby quantified for a broad list of small-molecule organic semiconductors (and for some SAM-modified Au) and the electronic properties are compared based on structural arguments at the molecular and solid-state levels. The mismatch between the electronic energy levels of the electrode and the semiconductor is at the origin of the energy

barrier experienced by electrons at a metal/semiconductor heterojunction, i.e., the Schottky barrier, which is one of the factors determining the contact resistance. Conductive atomic force microscopy (C-AFM) is employed to investigate the correlation between morphology and the out-of-plane conductivity in thin films of a small molecule, dinaphtho[2,3-b:2',3'-f]thieno[3,2-b]thiophene (DNTT), and its derivative functionalized with octyl side chains, named C8-DNTT. Firstly, the parameters that regulate the charge injection at the electrodes in OFETs, including the energy level alignment, the Schottky barrier and the contact resistance, are described for the whole system under study. Secondly, C-AFM data of DNTT films on Au is treated as a model system for the space charge limited current (SCLC) regime. Finally, the electrical behavior of C8-DNTT thin films fabricated via blade coating and via thermal evaporation is compared, highlighting advantages and disadvantages of the two depositions methods. Remarkably, the flatness and roughness of thin films of organic materials is found to dramatically influence the suitability of the sample for an accurate local imaging of electronic and structural properties. The presence of side chains promotes a much better crystalline order but it reduces the effectiveness of the out-of-plane charge transport. The relevance of this study also resides on the development of an experimental protocol for the determination the out-of-plane conductivity, via C-AFM, that can be easily adapted to the topography of the surface.

In conclusion, this thesis attempts to tackle some of the open challenges in the development of functional devices based on organic semiconductors. The reported findings bring a new perspective on the design of organic materials by highlighting some of the aspects that deeply characterize the performance of devices, such as humidity sensors, OECTs and OFETs. By correlating the chemical structure with the solid-state properties of self-assembled organic semiconductors with the help of a multitechnique approach, the key points in the development of devices can be easily identified and harnessed for e.g., improving a sensor performance, integrating multiple functionalities into a single device, or simply devising alternative methods for the investigation of semiconductive systems.

Table of Contents

Symbols and abbreviations

Symbols:

- **C**: capacitance
- **d**: channel depth
- **D**: diameter
- **e**: elementary charge
- **ε**: electric permittivity
- $\mathbf{E_F}$: Fermi level
- $\mathbf{E_G}$: band gap
- $\mathbf{E_{OPT}}$: optical gap
- **f**: frequency
- **Φ**: work function
- **g**: transconductance
- **I**: current
- **k**: elastic constant
- **L**: channel length
- **μ**: mobility
- **n**: charge carrier density
- **R**: resistance
- $\mathbf{R_{RMS}}$: root-mean-square roughness
- **σ**: conductivity
- **t**: time
- **T**: Temperature
- **τ**: time constant
- **θ**: angle, phase
- **V**: voltage
- **W**: channel width
- **[X]**: concentration
- **Z**: impedance

Abbreviations:

- **AC**: Alternate Current
- **AFM**: Atomic Force Microscopy
- **AuNPs**: gold (Au) NanoParticles
- **BC**: Bottom Contact
- **BTBT**: [1]BenzoThieno[3,2-b][1]-BenzoThiophene
- **C-AFM**: Conductive Atomic Force Microscopy
- **CA**: Contact Angle
- **CB**: Conduction Band
- **CELIV**: Charge Extraction by Linearly Increasing Voltage
- **CPD**: Contact Potential Difference
- **CV**: Cyclic Voltammetry
- **C16SH**: Hexadecanethiol
- **DC**: Direct Current
- **DBTTT**: DiBenzoThiophenoThieno[3,2-b]Thiophene
- **DL**: Detection Limit
- **DN4T**: naphtho[2,3-b]thieno-[2‴,3‴:4″,5″]thieno[2″,3″:4′,5′]thieno[3′,2′-b]naphtho[2,3-b]thiophene
- **DNTT**: DiNaphtho[2,3-b:2′,3′-f]Thieno[3,2-b]Thiophene
- **EA**: Electron Affinity
- **EC**: ElectroChemical
- **EDX**: Energy-Dispersive X-ray spectroscopy
- **EIS**: Electrochemical Impedance Spectroscopy

- **FBT**: 4-FluoroBenzeneThiol
- **FV**: Force Volume
- **GIWAXS**: Grazing-Incidence Wide-Angle X-ray Scattering
- **GO**: Graphene Oxide
- **HBT**: 4-HydroxyBenzeneThiol
- **HOMO**: Highest Occupied Molecular Orbital
- **HOPG**: Highly Oriented Pyrolytic Graphite
- **HR-TEM**: High Resolution Transmission Electron Microscopy
- **IDEs**: InterDigitated Electrodes
- **IE**: Ionization Energy
- **ITO**: Indium-Tin Oxide
- **KP**: Kelvin Probe
- **KPFM**: Kelvin Probe Force Microscopy
- **LUMO**: Lowest Unoccupied Molecular Orbital
- **MBA**: 4-MercaptoBenzoic Acid
- **MC**: MeroCyanine
- **NBT**: 4-NitroBenzeneThiol
- **NDI**: Naphthalenediimide
- **ODTS**: OctaDecylTrichloroSilane
- **OECT**: Organic ElectroChemical Transistor
- **OEG**: OligoEthylene Glycol
- **OFET**: Organic Field-Effect Transistor
- **OLED**: Organic Light-Emitting Diode
- **OPV**: Organic PhotoVoltaics
- **OSC**: Organic SemiConductor
- **OT**: OligoThiophene
- **OTFT**: Organic Thin-Film Transistor
- **P-XRD**: Powder X-Ray Diffraction
- **P3AT**: Poly(3-AlkylThiophene-2,5-diyl)
- **pBTTT**: Poly[2,5-Bis(3-alkylThiophen-2-yl)Thieno[3,2-b]Thiophene]
- **PEDOT**: Poly(3,4-EthyleneDiOxyThiophene)
- **PFBT**: PentaFluoroBenzeneThiol
- **PFDT**: PerFluoroDecaneThiol
- **PSS**: PolyStyrene Sulfonate
- **PY**: Photoelectron Yield
- **PYSA**: Photoelectron Yield Spectroscopy in Air
- **rGO**: reduced Graphene Oxide
- **RH**: Relative Humidity
- **SAM**: Self-Assembled Monolayer
- **SC-XRD**: Single-Crystal X-Ray Diffraction
- **SCLC**: Space-Charge-Limited Current
- **SEM**: Scanning Electron Microscopy
- **SFG**: Sum Frequency Generation
- **SNOM**: Scanning Optical Near-Field Microscopy
- **SP**: SpiroPyran
- **STM**: Scanning Tunneling Microscopy
- **STXM**: Scanning Transmission X-ray Microscopy
- **tBu**: tert-Butyl
- **TC**: Top Contact
- **TLM**: Transmission Line Method
- **TMDC**: Transition Metal DiChalcogenides
- **ToF**: Time of Flight
- **TPA**: n-TetradecylPhosphonic Acid
- **TSM**: Transverse Shear Microscopy
- **TUNA**: Tunneling Atomic Force Microscopy
- **UPS**: Ultraviolet Photoelectron Spectroscopy

- **UV-Vis**: UltraViolet-Visible
- **VASE**: Variable Angle Spectroscopic Ellipsometer
- **VB**: Valence Band
- **VOFET**: Vertical Organic Field-Effect Transistor
- **WF**: Work Function
- **XPS**: X-ray Photoelectron Spectroscopy
- **XRD**: X-Ray Diffraction
- **XRR**: X-Ray Reflectivity

1 Introduction to the Thesis

This Ph.D. thesis aims at addressing some of the open challenges in the field of organic electronics, seen from a more chemistry, thus materials, viewpoint. Due to the technological relevance of the research in such field, the endeavor necessarily bridges aspects of importance in fundamental science with technological applications. The choice of the organic molecule represents the first key step one should consider in view of its intrinsic chemical structure which determines the way it assembles into supramolecular systems. In organic electronics, the various properties of such assemblies are determined by the order at the supramolecular level. Hence controlling intermolecular and interfacial interactions is of paramount importance and it offers a broad perspective beyond the physics required to model the functioning of devices. Processes occurring in organic electronic devices, including charge transport, gas sensing and material doping can be fully understood only upon performing a multiscale characterization of materials' properties. Hence, the identification of the mechanisms underlying molecular interactions based on supramolecular chemistry requires experimental techniques that are not only limited to determining the bare device performance but are also aimed to pointing out structural, energetical, interfacial and optoelectronic aspects of materials. In complex systems where both covalent and non-covalent interaction are involved, such as organic materials, the number of techniques that have been developed can each provide a little piece of information that serves as a small hint in capturing the whole picture.

The development of new active materials for technological applications can be accomplished by chemical design which sees organic synthesis as the most flexible and versatile tool for tailoring material properties towards (multi)functionality. This thesis work focuses on the latter stage of materials development: it bypasses the synthesis of new materials that have been provided by our scientific collaborators and it anticipates the steps of final device optimization and engineering stages prior to commercial implementation by characterizing some of the most relevant thin-film properties of organic materials for (opto)electronics. It starts from sample preparation and functional device fabrication (in particular humidity sensors, field-effect and electrochemical transistors), it continues with the exploration of the fundamental surface and bulk properties of materials considering how all the different interfaces and components were influencing the device performance. It therefore demonstrates how one can control chemical functionality by design in order to gain in-depth understanding on fundamental

properties ruling device operations with the ultimate goal of developing multifunctional and multiresponsive devices for applications in opto-electronics and sensing.

1.1 Motivations and aim of the Thesis

Organic electronics is a multidisciplinary field of materials science where (soft) materials based on organic polymers and small molecules are used as key components in functional devices. Many scientists from chemistry, physics, engineering and, more recently, biology and medicine, are synergically investigating the design, synthesis, processing and characterization of these materials towards the development of new device components and technologies. Compared to the conventional inorganic counterpart, which is often indicated as a high-performance, but very expensive technology and with mostly rigid mechanical components, organic electronics has the potential to enable the fabrication of cheaper and flexible devices for a wide range of applications. Technologies based on organic molecules involve, in most cases, solution-processed and additive methods that make use of low-temperature fabrication protocols suitable for low-cost and flexible plastic substrates. Despite these many advantages, the field of organic electronics has been facing different challenges for the effective implementation of these new materials due to their inferior thermal and, in some cases, environmental stability. Other issues regard solution processing and the reproducibility of fabrication protocols, all of which are current topics of interest of the related industry and scientific community.

The first studies demonstrating the possibility to have a modulation of the electrical conductivity in organic polymers date back to the late seventies, when Hideki Shirakawa, Alan MacDiarmid and Alan Heeger (who later were awarded the Nobel prize for chemistry in 2000) showed that the conductivity of polyacetylene, a conjugated polymer, could be enhanced by oxidation or, in other words, by doping the material.[1] Today, organic electronics has achieved many technological goals with the successful development of electronic devices such as organic light-emitting diodes (OLEDs),[2] organic thin-film transistors (OTFTs),[3] organic photovoltaics (OPVs),[4] organic sensors,[5] organic memories,[6] and radio frequency identification (RF-ID) tags.[7] Some of these applications, such as OLEDs in displays,[8] have already had a strong impact in our lives with a wide commercial availability of the associated electronic consumables and many other items, like organic solar cells, are going to be more and more diffuse in the global market.

This Ph.D. work has been focused on OTFTs and organic sensors. More specifically, the main chapters of this thesis discuss: (i) humidity sensors based on small molecules, (ii) organic electrochemical transistors (OECTs) based on polymers and (iii) the electronic properties of small molecules for OFETs. My interests spanned from more fundamental aspects of charge transport, such as the mechanisms underlying the transport of carriers, to a more applicative perspective of the materials (i.e., the realization of sensing and transistor devices). From the perspective of a materials' scientist, in all the above-cited applications, fast device responses and long-term stability of the performance are critical aspects that must be addressed when studying a material for device applications. Transistors, in particular, and sensors require an active material with high charge carrier mobility (or conductivity) and exhibiting a controllable modulation of conductivity via e.g., change of the environment composition, field effect or reversible electrochemical doping. Regardless of the modulation mechanism, the transport of charge carriers (electrons or holes, ions or protons) has to occur within the bulk or within some interface of the active material. An efficient conductive pathway is made possible by a strategic molecular design.

Based on our current understanding of materials for organic electronics, the most important property that molecules must possess for electron/hole transport is conjugation.[9] The presence of an extended orbital delocalization along the backbone of a polymer, an oligomer or a small molecule is necessary for effective charge transport within the molecular structure. At larger scales, the charge carriers must be transferred from one molecule to the other, hence the long-range order mediated by inter- and intramolecular weak interactions plays a crucial role. The self-assembly in the solid state then governs the supramolecular structure and crystallinity of the materials, whose electrical properties are strongly dependent on the efficient transport of charge through the (semi)conductive channel.

Some promising organic materials are also able to transport ions and, henceforth, the field of iontronics (merging "ionics" and "electronics") is rapidly developing thanks to its huge potential of integration with biological systems (giving birth to a novel discipline called "bioelectronics"). Iontronics is the discipline studying the electronic properties and functions of (non-necessarily organic) materials controlled by ionic motion and arrangement.[10] Iontronics differs from ionics because the emphasis is mainly given on the electronic function, rather than on the ionic one. More and more frequently the worlds of ionics and electronics are finding common ground in the current research as

the development of new devices, such as OECTs, requires expertise and knowledge from both fields. The synergy between these two fields brings reciprocal benefits, such as networking opportunities and scientific exchanges, an improved and more holistic understanding of organic systems and also holds the promise to further develop the technology based on organic materials. An unexplored variety of chemical structures exhibiting a mixed electron/ion conductivity is set to be discovered thanks to this this dual effort.

To the best of our understanding, the current strategy to obtain a mixed conductor is via chemical functionalization of the electron-conductive conjugated backbone or core with lateral chains to introduce some form of ion transport. This modification, however, can strongly affect the electronic transport, so that a compromise must be reached in order to obtain a good mixed ionic-electronic conductor. The design of these kind of systems not only poses a synthetic challenge to the chemist but also involves a slow, stepwise structural modification of the state-of-the-art OSCs. It also requires the re-optimization of experimental procedures to yield a long-range order in the processed material as the previously achieved order or crystallinity might not be realized in the novel material. Therefore, the scientific crosstalk between organic ionics and electronics specialists is key for a successful future of the field.

In describing these two intersecting worlds, this introductive chapter will cover the fundamentals of organic electronics and also offering an interlacing comparison with organic iontronics. With principal reference to organic electronics, the reader will go through the description of the key aspects underlying the research in organic functional devices. Aiming to offer a broader and more comprehensive view of these future developments, organic iontronics fundamentals will be also described.

A first section will describe the type of structures that represent the state of the art of organic materials for transistors and sensors, focusing on the molecular characteristics that enable the transport of carriers. A second section will deal with the structural aspects of these materials and how the order in thin films affects the charge transport. A third section will then outline the electronic properties of metal, organic semiconductors and the interfaces formed by the joining of these two components.

1.2 Organic Semiconductors

Organic semiconductors (OSCs) are strongly π-conjugated systems whose conjugation contributes to the observed solid-state properties. The conjugation can be: (i) confined to the core of a small molecule, which then assembles via non-covalent interactions with other similar components, or (ii) many building blocks are bound together via covalent bonding to obtain oligomers or polymers having an electron delocalization that extends over the entire molecular structure. Despite being formed of a short sequence of monomeric units, oligomers are usually included in the small-molecule category, as their structural, packing and electronic properties resemble more those of small molecules rather than polymers. The extended π-conjugation provides the pathway for charge carriers to move throughout the bulk of all these OSC materials. This is a necessary property to consider when designing new chemical structures.[11] The intramolecular π-conjugation can not only extend in one direction, as in the case of 1D polymers, but also an in-plane conjugation can be achieved by designing new synthetic structures inspired by graphene, called 2D polymers.[12]

In this thesis, the compounds of interest can be grouped (with a few exceptions) to a class of thiophene derivatives. The past development of thiophene-based derivatives has been done via an intensive trial and error process that involved the synthesis of thiophenes with small structural variations. Then, thin films based on these materials were integrated into devices for further electrical and structural characterization. The most common modification is the attachment of alkyl side chains to increase the solubility and thus the processability of the OSC. Another approach involves the polymerization or condensation of multiple thiophene and/or benzene cores to increase the conjugation in the semiconducting core, with a consequent loss in solubility. Here, there are few examples of the most studied OSC structures based on a thiophene core that have been subsequently chemically modified and/or polymerized to change their charge transport properties (Figure 1.1).

Within the context of this Ph.D. work, the small-molecule OSC materials that were object of investigation are analogues of dialkyl-[1]benzothieno[3,2-b][1]-benzothiophene (BTBT), dinaphtho[2,3-b:2′,3′-f]thieno[3,2-b]thiophene (DNTT) and naphtho[2,3-b]thieno-[2‴,3‴:4″,5″]thieno[2″,3″:4′,5′]thieno[3′,2′-b]naphtho[2,3-b]thiophene (DN4T). For OECTs, the analogue of poly[2,5-bis(3-tetradecyllthiophen-2-yl)thieno[3,2-b]thiophene] (pBTTT) has been used in which the tetradecyl side chains have been replaced by oligoethyleneglycol (OEG) chains (pgBTTT).

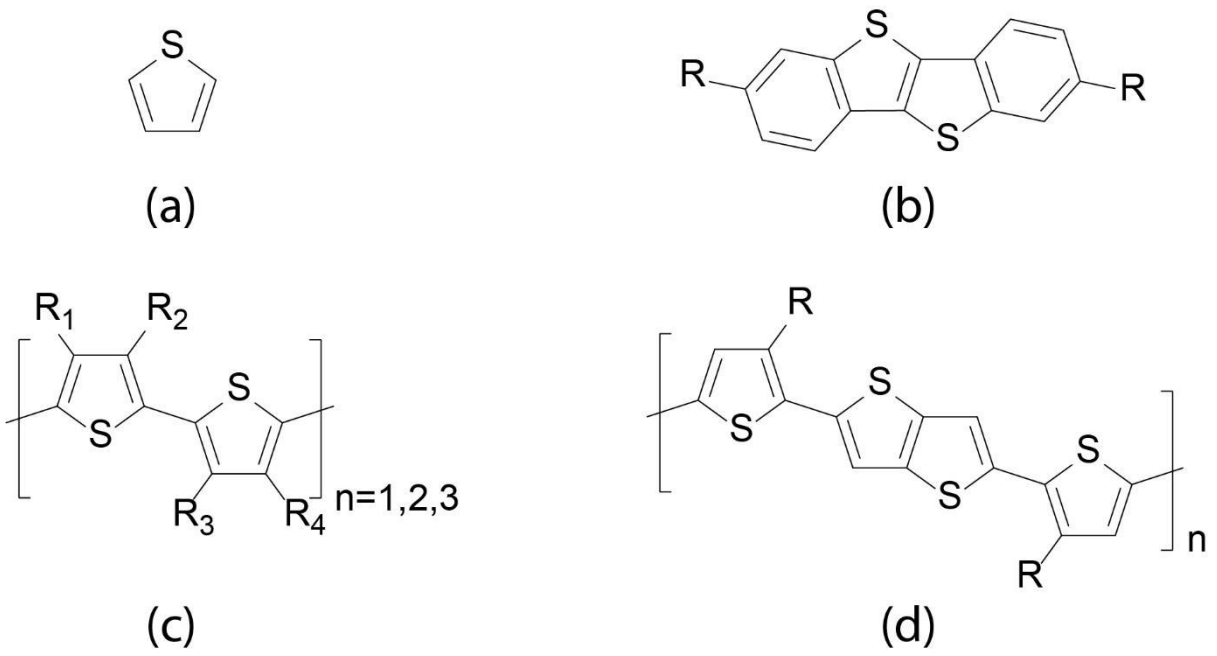

Figure 1.1: Examples of OSC based on thiophene derivatives. (a) The thiophene building block. (b) A small molecule OSC: dialkyl-[1]benzothieno[3,2-b][1]-benzothiophene (BTBT). (c) An oligomer OSC: oligothiophene (OT). (d) A polymer OSC: Poly[2,5-bis(3-alkylthiophen-2-yl)thieno[3,2-b]thiophene] (pBTTT).

By consecutive structural adjustments, new OSC materials are designed to achieve sufficiently high electrical performance to compete with other classes of materials in some microelectronics applications.[13] However, the development of OSCs for high-speed electronics is far from being a close objective. The last decades of research gave OSCs a very promising twist. A new branch called bioelectronics,[14] where the mixed electronic and ionic conductivity are essential features of the active materials, aims to integrate man-made electronics with living systems. A subbranch named organic iontronics aims to specifically develop OSC and organic materials that are inspired by chemical and mechanical similarities to the soft tissues of living beings. Within this context, the change of perspective in the design of OSCs regards conferring the ionic conductivity to the state-of-the-art electrical conductors.

Restricting OSCs to purely electrical conductors is nowadays obsolete. Depending on the electronic structure, the OSC material can transport both electrons and ions (examples in Figure 1.2). As a material can be (electro)chemically oxidized or reduced by the removal or addition of electrons to achieve a charge carrier doping, an analogue process can be carried out with ions. Whether this process is mediated by the environment or by a purposeful modification of the material's composition, OSCs (semi)conductivity can also be modulated by ions. Hence, the field of organic iontronics started its development from chemical structures that were previously known in organic

electronics to introduce an ionic transport by chemical modification. In some cases, like PEDOT:PSS (Figure 1.2b), the material was initially designed to be a simply conductive polymer.[15] It was lately shown to be an excellent material for OECTs and quickly become the reference benchmark compound[16] with already numerous bioelectronics applications today (e.g., in tissue implants in living animals, for neural interfacing, for metabolite sensing).[14] Compounds like those in Figure 1.2a, c and d combine semiconducting cores and hydrophilic side chains based on ethylene glycol oligomers, which is the most diffuse strategy to achieve ionic conductivity in OSCs. While polymers benefit from higher stability of operation in water environments, the structural stability of small-molecule OSC in water might be limited by the water uptake. The side chain engineering must thus carefully balance ionic and electronic conduction without compromising the non-covalent interactions that hold the film intact.[17] Still, the field is at its very beginning and many molecular design strategies will be explored in the future to adapt the material properties and functionalities to the desired application.

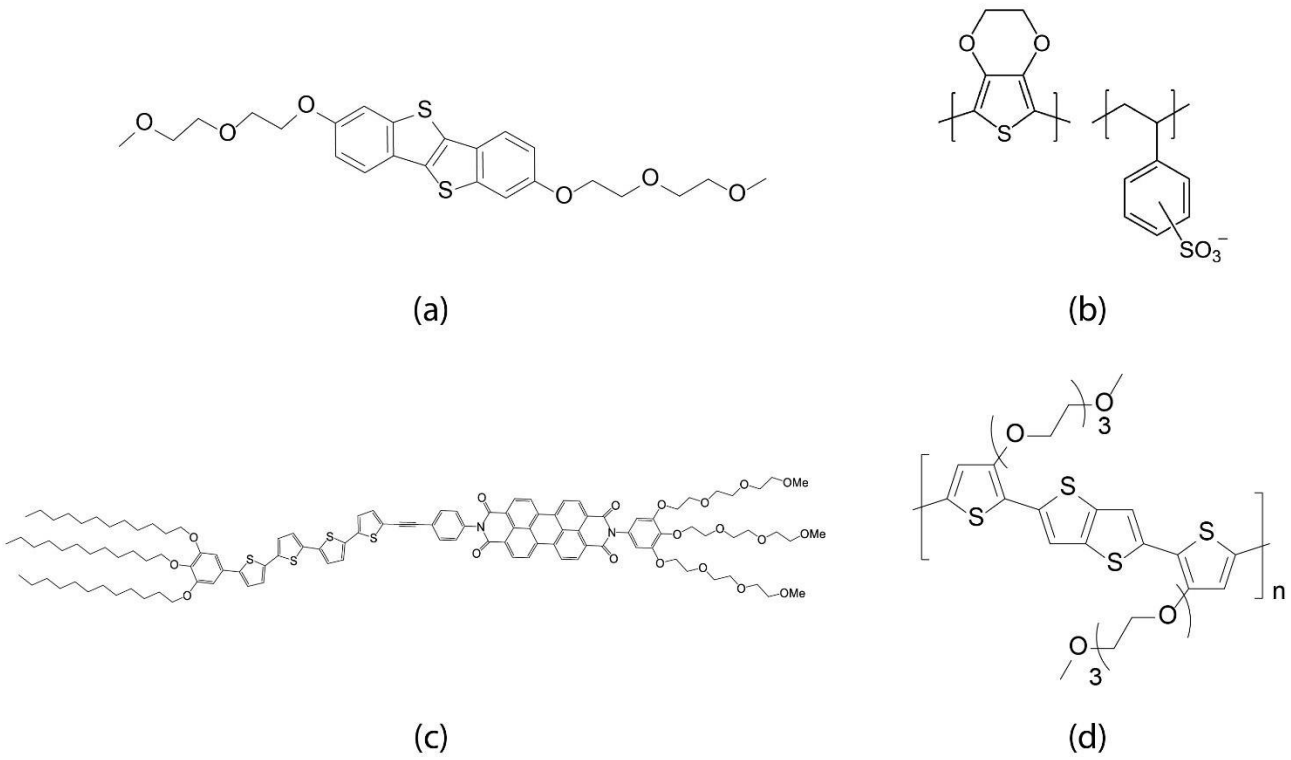

Figure 1.2: Examples of mixed OSC based on thiophene derivatives. (a) Oligoethyleneglycol-BTBT (OEG-BTBT) (b) Poly(3,4-ethylenedioxythiophene) polystyrene sulfonate (PEDOT:PSS) (c) a tetrathiophene and perylenediimide dyad connected by a conformationally rigid ethynylene bridge (d) Poly(2-(4,4'-bis(2-methoxyethoxy)-5'-methyl-[2,2'-bithiophen]-5-yl)-5-methylthieno[3,2-b]thiophene) (pgBTTT).

1.2.1 Polarity of OSCs

The electronic structure determines whether the OSC can be a good p-type (hole), n-type (electron) or ambipolar conductor. The OSC polarity also depends on the material (typically a metal) chosen as injection and/or collection electrode. Each OSC is characterized by both a hole and an electron charge carrier density, whose values can be modulated through the intrinsic (or induced) doping of the material. Depending on the electronic structure (i.e., the existence and availability of electronic states) and the relative occupation of the energy levels, an OSC can exhibit a p- on a n-type conductivity. When device (e.g., a transistor) is characterized, the polarity of the prevalent charge carriers is experimentally determined. Further characterization can lead to the quantification of the charge carrier density, which is an important physical quantity controlling the mobility (μ) of the OSC. Mobility is often considered first benchmark parameter to be considered (among many) when comparing transistor performances.

Regardless the material being an electron or hole carrier, only electrons are the particles that are actually moving; however, the hole description better (and more easily) captures the physics of p-type semiconductors. In the first place, the frontier orbitals/bands of an OSC are usually more relevant for charge transport. The molecular (chemist's) picture identifies the frontier orbitals, i.e., the highest occupied molecular orbital (HOMO) and the lowest unoccupied molecular orbital (LUMO), as the energy levels determining whether the OSC is p- or n-type based on the energy matching with the electrode work function (WF). Useful combinations of OSC/electrode material are usually obtained for electrode WF values similar (≈0.3 eV difference) to E_{HOMO} ≈ -5.0 eV and E_{LUMO} ≈ -4.0 eV. It is generally referred to as p-type or n-type semiconductors for the OSC falling in the two respective categories. A more formally correct (and experimentally accessible) way of defining the electrical properties of OSCs is expressed in the form of ionization energy (IE) and electron affinity (EA). These definitions overcome the reductive view of the electrical properties of the molecule in a vacuum to replace them with experimentally determined quantities that prescind from the modeling of the OSC charge transport as a (localized) hopping or a (delocalized) band dominated regime. On the other hand, the material (physicist's) picture of the electronic structure identifies a valence band (VB) and a conduction band (CB). Despite this picture better represents the solid-state electronic properties of the material, compared to the frontier orbital description, it lacks a proper description of the charge transport via

hopping. Hopping occurs when the electron is well delocalized along the structure of a single molecule but needs to "jump" from one molecule to the other to go across the conductive channel.

To sum up, one has to keep in mind that there are two limit descriptions of the charge transport process and that the classification of p- and n- type OSCs actually relies on the experimental determination of the charge carrier mobility.

1.2.2 Chemical Design of OSC materials

When it comes to the synthesis of a novel OSC material for device applications, the role played by the chemical design is the first aspect to consider.[13] If polymers and small molecules are compared, the former have very good film-forming properties (e.g.; are easy to process via spin coating when soluble enough) and the films show very high flexibility. The latter are monodispersed, easier to synthesize and purify, they do not suffer from broad molecular-weight distributions and the contribution from end groups and, finally, their processing can be done both via solution and vacuum deposition.[18] Structural modifications in molecular OSCs are also much easier to confer, as the stringent requirement of having reactive groups for monomer propagation is not a requisite in small molecules. The introduction of solubilizing side chains is thereby facilitated in small-molecule OSCs, despite anticipating the self-assembly of the material at the solid state driven by non-covalent interaction is still an open challenge.[19]

This subsection concerns the different chemical design strategies that have been developed to address some issues related to material properties. During the past decades, modifying the π-conjugated core to promote a closer π-stacking and a better intermolecular orbital overlap in heteroaromatic compounds has been the first choice towards the generation of entire classes of state-of-the-art OSC materials, e.g., thienothiophene small molecules[20] and thiophene polymers.[21] The use of side chain engineering, served to two main tasks other than improving solubility that are: (i) reducing the static and dynamic disorder in OSC materials, i.e., the formation of ordered crystalline domains as large as possible and building chemical structures resilient to phonon oscillations,[22,23] and (ii) changing the wettability and ion-conductive properties of the OSC material.[24–26]

1.2.2.1 Improving π-stacking and Orbital Overlap

The transport of charge in OSC is sensitive to the solid state ordering of polymer backbones and small-molecule cores which can be tuned by optimizing the intra- (for

polymers) and intermolecular non-covalent interactions. There are many possible chemical design strategies that have been adopted to improve the electrical properties of OSC materials for OFET applications, such as controlling the extension of the conjugation, replacing heteroatoms in the π-conjugated cores or introducing substituent side groups, as conveniently summarized by Bao et al.[27] A few representative examples were also recently summarized by McCulloch et al.[13] Here, we outline which methods can be utilized for the improvement of π-stacking interactions to achieve better intermolecular orbital overlap.

In polymers, the efficient interdigitation of side chains is key to attain a regular out-of-plane arrangement of vertically adjacent polymer chains resulting in optimal interchain spacing and close packing of the conjugated polymer backbones.[28] For instance, π-conjugated polymer chains can be brought into closer contact by π-stacking interactions driven by a "molecular docking" strategy, proposed by Pei et al.[29] This strategy consists in designing the monomeric unit by alternating small conjugated units (thiophene and bithiophene) with no side chains and larger aromatic cores (isoindigo) decorated with alkyl chains to form docking regions. The alternation of bulky structures hinders the stacking of similar regions and force the interaction of the two different regions through the docking cavities.

In small-molecule OSC, novel π-conjugated cores are being designed by small structural variations such as the "bent-shaped" geometry[30] or the further extension of the core conjugation.[31] Another possible approach, proposed by the group of Anthony, is to tune π-stacking interactions by using a benzodithiophene "universal crystal engineering core" containing two trialkylsilylethynyl groups that can be decorated by a variety of π-conjugated pendants.[32] These compounds are soluble and easy to crystallize for each of the screened pendants and yield molecular assemblies exhibiting planar π-stacking. Takimiya and colleagues developed a "disrupt and induce" strategy to rationally design the packing of molecular assemblies by favoring one interaction over another.[33] The β-methylthionation drives the acenedithiophene system to interact via the π–π stacking along the face-to-face direction instead of via the CH–π interaction along the edge-to-face direction. A combined side-chain positioning and isomerization of the aromatic core was also proposed by McCulloch and colleagues[34] as a crystal engineering strategy that combines theory and experiments.

1.2.2.2 Reducing Energetic Disorder

Charge transport properties in OSC materials, and especially in polymers, are strongly affected by both static and dynamic energetic disorder.[35] Static (losing translational symmetry) and dynamic (thermal vibration of the lattice) disorder contributions are closely correlated in OSC materials, thus often representing a crucial node in the modelling of charge transport properties.[36] Chemical design is essential for improving intermolecular interactions to address disorder effects and minimize the resulting impact on the transport of charge. For polymers, the key is to enhance intrachain transport by designing disorder-resilient backbones, while in small-molecule systems some specific phonon modes must be suppressed.[37]

In polymers, the main source of disorder (after the conformational disorder at the microscale in amorphous regions) is the conformational fluctuation of the backbone, that can be reduced by eliminating the torsion stress in the backbone.[38] The guidelines for the design of torsion-free structures include (i) the use of a minimal number of torsion susceptible linkages to connect (the larger the better) conjugated units collinearly, (ii) a torsion potential characterized by energetic minima at 180° or 0° with a steep profile and (iii) an optimized space filling by side-chain functionalization that avoids additional backbone torsion and guarantees close π−π contacts. Non-covalent S–F and S–O interactions are known to help planarizing π-systems[39] as well as other heteroatom interactions can predictably dictated the conformation of conjugated polymers.[40] More recently, it was found that the resilience to thermally induced backbone torsions and the substitution with bulky side chains governs the energy disorder landscape, hence relieving the strict requirement for backbone planarity.[41]

In molecular OSCs, the lattice thermal vibrations of large amplitude are detrimental to transport of charge, as these materials were already found to exhibit ideal charge transport properties in absence of thermal disorder, i.e., at low temperatures.[42,43] The long-axis sliding motion, for instance, is one of the phonon modes that contributes more importantly to the overall dynamic disorder, as revealed by computational methods targeting electron-phonon coupling combined with the experimental determination of low-frequency lattice vibrations.[44] A viable strategy to suppress these vibrations is to substitute side chains along the long axis, as it is done in e.g., C8-BTBT and C8-DNTT.[45] Alternatively, this long axis sliding motion can be suppressed by shaping the π-conjugated core so that HOMO is spread all over the core while preserving a molecular packing that yields balanced transfer integrals.[31]

1.2.2.3 Conferring Mixed Conductivity to OSC

Historically, the development of OSC materials for transistor applications has been focused on the improvement of electron conductivity, with poor attention to the introduction of ion transport.[18,21,46,47] During the past decade, the field of organic transistors has witnessed a rising interest in the exploitation of ionic and mixed ionic/electronic semiconductors.[48–50] The rise of iontronics is in part due to the recent difficulties in achieving OFET performances suitable to the market,[43,51] but also to the huge possibility of OECT devices for integrating electronics with biological systems.[14,52] Nowadays, a variety of strategies has been devised to achieve mixed conductivity in OSCs with the final (but not unique) aim of developing biocompatible materials for in-vivo applications.[53]

For polymeric systems, side-chain engineering is currently the most studied and viable route to modify the chemical properties of the polymer to interact with ions.[54] The replacement of alkyl side chains with glycolated ones in an electrically conductive backbone is a well-established method to transform a material for OFETs to a material for OECTs.[24] This approach has already been successfully applied to both p-type and n-type polymers based on, to name a few, polythiophenes,[25,26,55] bithiophene-co-thienothiophene,[56,57] bis-isatin[58] and isoindigo[59] backbones. The effect of the alkylene spacer in glycolated chains is also the subject of current investigation.[60] Side groups that are alternative to glycol-based chains are also being tested,[61,62] such as alkoxy, hybrid alkyl-glycol and charged (e.g., sulphonate and carboxylate) moieties.[63] Another route to achieve mixed conductivity is via blending with a polyelectrolyte[62] as in the case of PEDOT:PSS[64] or other PEDOT blends.[65] Remarkably, mixed conduction can also be achieved with no need for hydrophilic side chains or blending.[66]

For small-molecule OSCs, introducing an efficient mixed ionic/electronic transport without one detrimentally affecting the other, is not an easy task as the ubiquitous presence of water and oxygen can severely limit the electronic contribution via charge trapping.[67] General criteria for achieving ionic conduction by chemical design of small-molecule OSC are not yet well-established.[17] Among the most successful strategies for introducing a mixed conduction there is indeed the decoration with OEG side chains.[68] The OEG functionalization also works for n-type OECTs based on fullerene (C_{60}) derivatives.[69] The blending with polymers, such as polyethylene oxide is may also be exploited to improve OECTs based on small-molecule active materials.[68]

1.2.3 Charge Transport Properties of OSCs

The modelling of charge transport in OSC materials is not an easy task, as the complexity arising from their structural properties (see Section 1.3) requires a more detailed description of the electronic structure compared to inorganic semiconductors.[22] While a simpler band structure description (that do not consider electron-electron interactions) is usually sufficient for the latter, the modelling of OSCs often necessitates to include electron-electron scattering processes and the interaction of electrons with the crystal lattice (electron-phonon interactions).[44] The definition of new parameters that can be experimentally determined (by techniques complementary to those directly measuring of the device characteristics) has the purpose of taking into consideration all phenomena that effectively contribute to the behavior of some property. The charge carrier mobility, for example, is often described by expressions that are linked to related parameters, such as the charge hopping rate or the polaron binding energy, or that evidence some dependence on the temperature.[22] To further complicate the extraction of reliable OSC transport properties, the very same parameter can show large variations depending on the experimental technique or method, the process of sample fabrication, the interface with the other materials that compose the device and, ultimately, the environmental conditions.

The directionality of charge transport in OSC is a direct consequence of the molecular and crystalline structure of the material. One of the few examples of 3D isotropic charge transport is that of C_{60}, a spherical shaped molecule that can transport electrons in all spatial directions and thus bringing major benefits to OPV devices.[70] An efficient isotropic charge transport is also desired in OFET applications but while it is relatively easy to achieve isotropic in-plane charge transport in both polymers[71,72] and small-molecule OSCs,[73] the same cannot be stated for the out-of-plane transport. In fact, the crystal packing in OSC materials gives rise to charge transport which is more efficient along two crystal axis in the in-plane π-stacking direction, compared to the out-of-plane direction where the transport between adjacent layers of molecules is limited by poor orbital overlap in the third crystal axis direction.[22] Having a single dimensionality (1D) is also detrimental for charge transport, as OSC materials are defective rich. The presence of a defect would determine a dramatic loss in carrier mobility that can be avoided in materials exhibiting a 2D and 3D conductivity. In these latter materials, charge carriers follow alternative percolation pathways around defects. The strategies to characterize the charge transport anisotropy in single crystal

structures are well developed for electronic semiconductors,[74] but much more investigations should be carried out to improve our understanding of the structural dependence of ionic conductivity in OSC materials exhibiting mixed ionic/electronic conductivity.[64,75]

The aim of this subsection is to briefly introduce transistors, here exemplified by OFETs, and the two parameters that are commonly used to evaluate the performance, i.e., the charge carrier mobility, and the doping state, i.e., the threshold voltage, of the active OSC material.

1.2.3.1 Operation of Organic Field-Effect Transistors (OFETs)

The working principle of field-effect transistors, like OFETs, is the field-effect doping, i.e., the enhancement of the number of mobile charges within the OSC channel layer obtained via the application of a "gate" voltage through a dielectric layer. The role of the bias voltage applied to the gate electrode is to accumulate charges of a given sign on one side of the dielectric layer and, similarly to a parallel plate capacitor, to generate charges of opposite sign in the other side of the dielectric layer, where the OSC material is located. Depending on the polarity of the OSC (p- or n- type) a negative or positive gate potential is required to generate charge carriers. The charge transport properties of the OSC material can then be measured by recording the source-drain current (I_{DS}) either as a function of the source drain voltage (V_{DS}) at a constant gate bias (V_{GS}), i.e., the output curve, or as a function of V_{GS} at constant V_{DS}, i.e., the transfer curve. The current leaking from the gate to the source electrodes (I_{GS}) is called leakage current and its value should be typically a factor 100 lower than I_{DS}. This current must be minimized for two main reasons: (i) the leakage current dissipates power; hence, the device is more energy consuming if I_{GS} is high and (ii) the field-effect properties of the active material can be obscured by high I_{GS} as apparent I_{DS} modulations can wrongly result from I_{GS} modulations.

1.2.3.2 OFET regimes and Threshold Voltage (V_{TH})

In an ideal OFET device, there should be no charge accumulation at the interface when no V_{GS} is applied to polarize the dielectric aiming to generate free charge carriers in the active channel and turn the transistor in the ON state. Let's assume that the ideal device is in its OFF state at $V_{GS} = 0$, and thus a negative ($V_{GS} < 0$) or positive ($V_{GS} > 0$) can switch a p-type or n-type OFET device, respectively, to the ON state. In these conditions, the V_{GS} value associated with the device switching is 0, and it is referred to

as threshold voltage (V_{TH}). In real devices, charge carriers might be already significatively present at V_{GS} = 0 or an additional V_{GS} potential might be required to fill charge traps to before being able to accumulate free charge carriers. The condition of V_{TH} different from 0, may arise from structural defects, chemical impurities or doping. Positive or negative V_{TH} values can thus be associated to p-type or n-type doping in a semiconductive material of a given polarity.[76] In fact, as previously discussed, OFETs can be p-type, n-type or ambipolar. A p-type (n-type) will be in is ON state at $V_{GS} < 0$ ($V_{GS} > 0$). However, for a given OSC polarity, the device can operate in charge accumulation or charge depletion mode, depending on V_{TH}. The regulation of the working point of OFETs is an important requirement for their further implementation in commercial plastic electronics.[77]

OFETs can be operated in the linear or in the saturation regime, depending on the relative magnitude of the applied biases. When $|V_{DS}| < |V_{GS} - V_{TH}|$, the device is in the linear regime. When $|V_{DS}| > |V_{GS} - V_{TH}|$, the device is in the saturation regime. In between these two regimes, the condition $|V_{DS}| = |V_{GS} - V_{TH}|$ is called pinch-off. In the linear regime, $I_{DS}(V_{DS})$ is linear as the number of charge carriers in the conductive channel is solely governed by V_{GS}. V_{DS} just drives the charge carriers from one electrode to the other. As the magnitude of V_{DS} approaches that of V_{GS}, the pinch-off condition is achieved at equality. At pinch-off, the field-effect charge carriers in the region of the channel adjacent to the drain electrode are depleted. Across this depletion region, increasing in extension as V_{DS} further increases, I_{DS} is space-charge limited.[78] At V_{DS} above the pinch-off condition, I_{DS} does not increase anymore, thus reaching saturation.

1.2.3.3 Charge Carrier Mobility

The charge carrier mobility, μ, is the reference figure of merit for assessing the performance of OFETs. Higher μ values correspond to higher $I_{DS}(V_{GS})$ at a given V_{DS}. This parameter provides meaningful information only if the linearity of the transfer characteristics is respected, or equivalently, if the conductivity (σ) is a linear function of the carrier density (n), following the relationship $\sigma = \mu e n$, where e is the electron charge and μ does not depend on n.[79] The electrical properties of an OFET are modelled by the gradual channel approximation, which holds true if the relationship between the electric field (E0) at the electrodes is $E_{GS} >> E_{DS}$.[78] Under these assumptions, the mobility in the linear (μ_{lin}) and saturation (μ_{sat}) regimes can be expressed as:

$$\mu_{lin} = \frac{L}{WC_i V_{DS}} \left(\frac{\partial I_{DS}}{\partial V_{GS}} \right) \quad \text{(Equation 1.1)}$$

Which is applicable at $|V_{GS} - V_{TH}| >> |V_{DS}|$.

$$\mu_{sat} = \frac{2L}{WC_i} \left(\frac{\partial \sqrt{|I_{DS}|}}{\partial V_{GS}} \right)^2 \quad \text{(Equation 1.2)}$$

Which is applicable at $|V_{GS} - V_{TH}| < |V_{DS}|$. *L* and *W* are the channel length and width, respectively, C_i is the capacitance per unit area of the gate dielectric. These two equations are applicable when in the linear, $I_{DS}(V_{GS})$, and in the saturation, $|I_{DS}|^{1/2}(V_{GS})$, regime these expressions for the transfer characteristics are linear for a sufficiently large range of V_{GS} values. When these conditions do not hold true, many different correction strategies for the extraction of μ can be adopted.[79]

1.3 Solid-State Order in Organic Materials

The transport of charge carriers in organic materials is highly dependent on the solid-state arrangement of molecules. Not only the electronic coupling of adjacent molecules is controlled by the wavefunction overlap, but also the thin-film morphology (i.e., grain boundaries, structural defects, crystallinity) severely influences the performance of OSC devices. The crystal packing of OSC is primarily affected by the nature of the conjugated core and its substituents, but even when similar molecular structures are known it is very difficult to predict the solid-state organization of a novel OSC. The field of OSC crystal engineering aims to study how small chemical modifications can affect the intermolecular interactions underlying the crystal structure at the solid state to enable the design and synthesis of materials with desired properties. This kind of research applied to the transport properties of OSC is performed on materials that have slightly different crystal structure, but have similar molecular formula, electronic properties and self-assemble with the same kind of intermolecular interactions. Once a novel compound is designed, the fabrication of high-quality thin films relies on the optimization of deposition methods (in vacuum or in solution) which primarily depends on crystal nucleation and growth.[80] The thin-film morphology and microstructure become then the object of the primary efforts of the researcher developing a functional application for a specific OSC material.[81]

1.3.1 Inter- and intramolecular interactions

The self-assembly and packing of OSC molecules is mainly driven by intermolecular interactions. In the case of 1D polymers, intramolecular interactions also have an important role, due to the presence of numerous short- and long-range interactions among functional groups located along the polymer backbone. The nature of these interactions is generally weak, with the exception of H-bonding whose strength can be more than one order of magnitude larger than the other weak interactions. These forces are much weaker than the covalent interatomic bonds that characterize inorganic semiconductors, hence molecular order can be easily disrupted by thermal fluctuations that activates phonon modes contributing to thermal energetic disorder.[44] This disorder results in lower charge carrier mobilities compared to crystalline inorganic semiconductors. Among the intermolecular interactions, the most diffused and relevant for thiophene analogues are the π-π and C-H ··· π interactions. The π–π interaction is a dispersion force involving two (poly)cyclic molecules that reciprocally interact with the aromatic cloud of π electrons. The C-H ··· π interaction, instead, involves a H atom from the OSC core and the face of a π-conjugated system. Other types of weak intermolecular interactions, such as S ··· S, can support π-stacking[82] still without predominantly drive the crystalline self-assembly.[83] Halogen-based interactions (involving F in particular, F ··· F and F ··· S) were found to accelerate crystallization without significantly affecting the p-type polarity of anthradithiophene OSC derivatives.[84] H-bonding can also assist the crystallization of OSC, as demonstrated by the replacement of cyanovinyl and carboxylic groups with methyl groups leading to the loss of crystallization ability of an anthracene derivative.[85] Weak interactions can also control the polymer backbone conformation, as in the case of the S ··· O interaction between the thiophene S atoms and the glycol O atoms in pgBTTT, consequently enhancing the performance of the OECT device.[56]

The ensemble of these interactions governs the crystalline packing of OSC materials at the solid state. In turn, the OSC charge carrier mobility strongly depends on the formation of a conductive path that necessarily involves the charge transfer from one molecule to another. Slight changes in the molecular ordering can lead to significant variations in the orbital overlap with major consequences on charge transport. Certain non-covalent interactions offer a geometrical control over the self-assembly process, which is key in order to achieve a controlled, i.e., high, transfer integrals.[86] Controlling, the molecular orientation of, e.g., acene derivatives by a specific atomic substitution (H

with I) to exploit weak (I ··· I) interactions can increase the magnitude of transfer integrals.[87] Other interactions might have opposite effects on the transfer integrals of a class of derivatives, e.g., S ··· S vs S ··· π interactions in different OT compounds.[88]

1.3.2 Crystal Packing Motifs

OSC materials are constituted by (i) π-conjugated cores or backbones that determine the intrinsic optoelectronic properties and (ii) non-conjugated side groups that govern the solubility, crystalline packing, morphology, and microstructure of the thin film. In general, small-molecule thiophene analogues generally possess a 3D shape which is in most cases anisotropic. Platelet- or rod-shaped molecular species are the example of 2D and 1D anisotropy, compared to the 0D spherical shape (e.g., C_{60}) that would grant, in principle, the isotropy of the properties of materials. As a consequence, these OSC species adopt anisotropic crystalline packings that are reflected on the anisotropy of physical properties at the solid state, such as the carrier mobility. Thiophene analogues tend to assemble in a herringbone motif by forming crystalline structures in which 2D layers of molecules interact through C-H ··· π interactions where the electrostatic repulsion between π-conjugated cores is minimized. The DNTT core, for example, adopts a "face on edge" herringbone motif,[89] but also possesses C ··· S short contacts (with a closest distance of 3.3 Å) as many other analogue species such as BTBT[90], DN4T[31] and some of their derivatives. This is true for many of these small-molecule OSC species, but there are plenty of other spatial arrangements that molecules can assume. Few examples are shown in Figure 1.3.

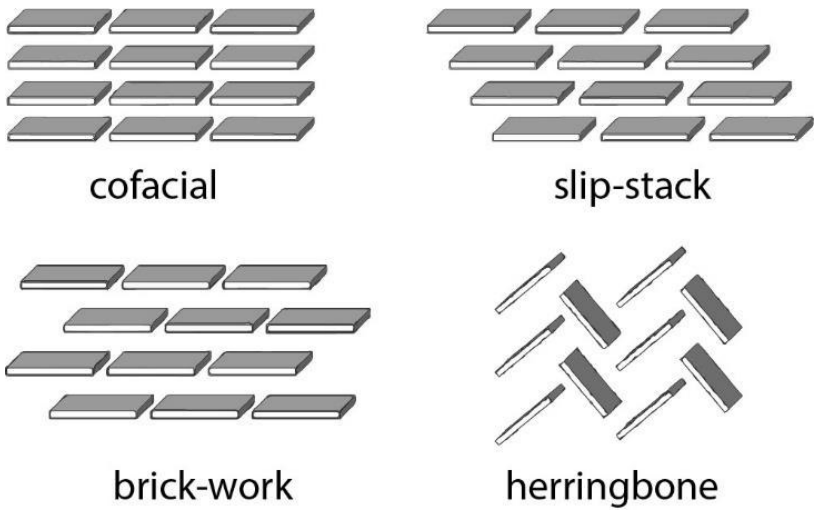

Figure 1.3: Examples of crystalline packing motifs.

Charge transport in these crystals occurs mainly via hopping through the individual molecular entities and particularly suffers the crystal discontinuity in correspondence of grain boundaries. The anisotropy in the orbital overlaps is detrimental for the overall mobility and band-like transport is observed at low temperatures and in single-crystal devices where dynamic disorder is minimized and grain boundaries are suppressed.[91,92] The situation is slightly different for 1D polymer OSC. One degree of freedom, the one along the backbone, is constrained to the conformational flexibility of the polymer chain. While on one side the intramolecular conductive pathway is limited by the continuity and length of the polymer chain, on the other side a long-range three-dimensional organization of the polymer must be granted for optimal charge transport through the entire bulk of the material. For example, regioregular poly(3-hexylthiophene-2,5-diyl), known as rr-P3HT, organizes at the solid state with lamellar structures in which the charge transport occurs both intramolecularly along the conjugated backbones and intermolecularly through the π-stacked structure of the backbones. The self-assembly results into 2D sheets that can assume one of two primary orientations with respect to the substrate: (i) edge-on, where the π-stacking direction is parallel to the substrate, or (ii) face-on, where the π-stacking direction is perpendicular to the substrate.[71] Having P3HT as a reference, researchers developed pBTTT that exhibits improved OFET performance thanks to more planar backbones and shorter inter-backbone distances that improved the polymer packing. In addition, a reduced density of alkyl side chains (compared to P3HT) enabled chain interdigitation to form more compact lamellar structures exhibiting large electronic couplings along the π-stacking direction.[93] There are, of course, regions of inhomogeneous disorder that represent the bottleneck of charge percolation among conductive crystalline domains.[94] The determination of the crystal structure in OSC materials is thus of utmost importance for the improvement of device performance and for the understanding and optimization of the charge transport properties that are found to significantly depend on the solid-state organization.[73]

1.3.3 Polymorphs

As previously mentioned, variations of molecular packing motifs are driven by chemical substitutions or functional groups influencing the charge distribution within the molecule, and thus changing the nature of the weak interactions or functioning as spacer groups by steric hindrance. However, an absolute control of the crystalline packing does not simply rely on the molecular structure design. Due to the relatively

poor directionality and low energy of weak interactions in such materials not only one energetically favored configuration may exist. Even though, in principle, only one structure is the thermodynamically most stable, it is very common to observe different packing motifs for the same molecular species, called polymorphs. Two polymorphs of the same molecule can exhibit significant differences in the electronic properties that in turn affect the performance of OFETs.[95] Even the substrate can induce the formation of different polymorphs that possess intrinsically different charge transport properties, as in the case of pentacene.[96]

Small molecular modifications or different processing protocols can lead to structural variations that might drive the crystallization towards one polymorph or another. Polymorph purity in thin films is thus an important issue to address in order to ensure that the physical properties observed can be only ascribed to one polymorph. Two different polymorphs of the same molecular species are considered as (and effectively are) two different materials. One possible a priori approach to study the different crystalline forms that a single chemical entity can adapt is polymorph screening. Polymorph screening is a crucial step in the development of drugs because each form has different physicochemical properties that can affect the biological activity and stability. For a given OSC compound, small structural variations can be critical for achieving the optimal OFET performance, hence, knowing about the existence of polymorphic forms can differentiate a promising material from one with mediocre properties. This approach requires a long process of solvent recrystallization at different evaporation rates and with different solvents, with a subsequent crystallographic analysis and resolution of the crystal structure.

Since this approach is quite time and resource expensive, it is more common to operate the other way round. The fabrication protocol of a given OSC is first optimized to give the best device performances by slightly varying the experimental fabrication conditions and once a working device is obtained. The crystallographic analysis is then run on the optimized thin-film morphology to ensure that no other polymorphic forms are present and, in the positive case, the eventual discovery continues with the isolation of the two forms to determine the most performing one. None of the two approaches is wrong or right, but the control of polymorphism must be always considered during the study of OSC materials due to the variety of polymorphs that can originate by a single molecular entity.[73]

1.3.4 Morphology and Microstructure

The development of high-performance OFET devices requires the assembly of the material phases by optimizing the charge injection and transport processes both at the molecular and device-size scales.[97] The morphology and microstructure of OSC thin films resulting from a fabrication protocol can dramatically differ when passing from solution or vacuum processed films as well as when considering the same deposition method with different processing parameters. The control of molecular arrangement at different length scales is a fabrication challenge that is made even more difficult by the weak intermolecular interactions that hold together the molecular entities of OSC materials. As a rule of thumb, a high crystallinity, the presence of large crystalline domains oriented in parallel, and an absence of structural defects are all sought-after properties that guarantee optimal optoelectrical OSC performance. All the synthetic efforts in the chemical design are generally directed to the enhancement of charge transfer properties, such as a better orbital overlap, an increased extension of the π-conjugated core and the formation of additional intermolecular interactions. The resulting change in the properties has to be counterbalanced with additional challenges in the re-optimization of film-forming properties, such as solubility and processability, and the unpredictable resulting large-scale morphology that might be detrimental to other transport properties. A strategic optimization of solution processed methods targeting morphology and microstructure is thus key for the successful application of OSC materials in device applications.[98]

The interfacing of the OSC material with the other device components thus requires considering several structural properties of the fabricated thin film. The aspects regarding density, dimension and orientation of the crystalline domains are discussed in Section 1.3.4.1. One way to access some partial information about how the thin film looks in the real space is by measuring its topography, as described in Section 1.3.4.2. Finally, the challenges related to grain boundaries, the borders between one crystalline domain and the other or, equivalently, the regions of disorder and discontinuity among the ordered structures, are presented in Section 1.3.4.3.

1.3.4.1 Crystallinity and texture

The processing method strongly influences the degree of crystallinity and texture of the OSC thin film.[80] Methods for OSC deposition are usually done in vacuum or in solution. Vacuum-based thermal deposition methods necessitate that the OSC sublimation

temperature is below the decomposition temperature of the molecule and they are more energy expensive than solution-based methods. Thermal evaporation is thus limited to molecules with relatively low molecular mass and polymer OSC molecules can be alternatively deposited in vacuum via electrospray deposition with limitations related to availability of suitable solvents and a sufficiently conductive sample substrate.[99] Solution-based deposition methods are instead limited by the solubility of the OSC molecule which are usually functionalized with side chain to increase the interaction with the solvent.

Thermal deposition methods yield nanometric-large crystalline domains due to the poor control of the crystallization rate and growth. Only the deposition rate and the substrate type, wettability and temperature are the optimization parameters that can be tuned. With such few parameters to be tuned, achieving an absolute thermodynamic control is quite challenging: the substrate temperature can be varied with precision to favor the migration and reorganization processes of the deposited molecules. However, the deposition rate, the parameter indicating the flux of molecules being deposited, can be barely reduced below 0.1 Å/s, a threshold value for the common deposition equipment. As a consequence, domains grow with random orientation in the direction parallel to the substrate and only epitaxial or wettability effects can be exploited to change the structural order in the direction perpendicular to the substrate. Many post-deposition methods have thus been developed to improve the crystallinity of the thin film, such as the use of an amorphous interlayer to promote a large-domain crystallization of the film by subsequent annealing after the OSC deposition,[100] but still there is no universal method to yield crystalline domains larger than ~ 10 μm and each OSC system is optimized separately. The main advantages of vacuum-based methods are related to the very clean surfaces and film uniformity, compared to the solution-based methods in which it is not always trivial to get rid of the solvent and of the amorphous fraction of the OSC deposited.

Solution-based methods, however, provide much finer control on the crystallinity and domain orientation. It is fair to note, however, that kinetic approaches, like spin-coating, offer a reduced degree of order at the supramolecular level.[101] While traditional spin coating and drop casting methods do not offer a specific directionality for the deposition, meniscus-guided coating is a class of scalable methods that exploit more thermodynamic conditions to induce long-range ordering of OSC molecules when suitably optimized.[102] Due to the intrinsic directionality of meniscus-guided deposition

method it is possible to obtain ultrathin films, down few layers,[103] of oriented single-crystal domains of millimeter size.[104] A striking result achieved by solution-based deposition method was the inkjet printing of C8-BTBT single-crystal films that were implemented in top-contact OFETs with mobilities exceeding 10 $cm^2 V^{-1} s^{-2}$.[105]

To sum up, the final aim of deposition methods for the fabrication of OSC thin films is to achieve (i) large enough (and possibly single-crystal) domains that no complicated alignment procedures must be done to integrate the device electrodes, (ii) a small dispersion of domain orientations, as the anisotropy of the charge carrier mobility may bring high device to device variability and (iii) controlled thin-film thickness to further reduce this variability.

1.3.4.2 Surface topography

Highly ordered crystalline structures of both small molecules and polymers are typically characterized by flat terraces with a height corresponding to the interlayer distance. Self-assembly in OSC materials gives rise to the peculiar phenomena of terrace formation whose surface topography can be easily recognized by the alternation of almost atomically flat areas and steep edge steps appearing in a similar way to a staircase structure. Some less ordered materials, containing regions of amorphous, show a much more disordered topography that do not easily correlates with other known properties of the OSC material. Where optical microscopy is not sufficiently resolved, AFM topography is useful for checking film continuity, the presence of nanometric cracks or holes in the film or to assess the dewetting processes that may occur in the thin film when it is exposed to the ambient atmosphere.

A widespread pitfall is to utilize simple AFM to infer structural information about the crystalline domains from simple topography imaging. While it might be tempting to associate the cracks and the dips in the film and the intergranular regions, it may not necessarily be always true (see Figure 1.4). It is fair also to note that there are other mapping techniques that offer greater insight into the size and orientation of crystalline domains[106] (also described in Section 2.3).

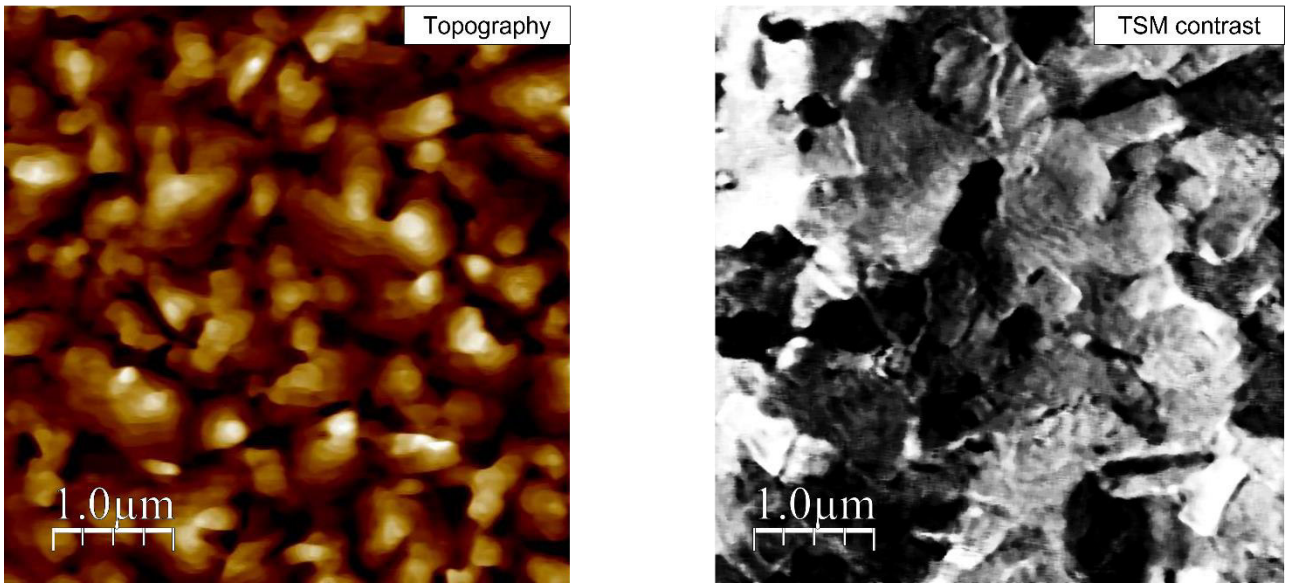

Figure 1.4: Topography and Transverse Shear Microscopy (TSM) images of a small-molecule thin film. The dark and bright area indicate regions with crystalline domains of different orientation. The images show that the identification of grain boundaries is not easily discernible from simple topography (Z-scale topography: 24 nm, Z-Scale TSM: 20 mV).

1.3.4.3 Grain boundaries

Grain boundaries are one of the most difficult regions to access in OSC materials. Grain boundaries are also complicated to describe accurately: while it is clear that they are located between adjacent crystalline domains, it is very challenging to study the structure of intergranular regions as well as to define their spatial extension within each grain.

For small-molecule OSC films, since crystalline domains are constituted by individual molecular entities that are spatially confined to either the ordered domain or the intergranular region, the impact of the grain boundary on the charge transport is quite severe, due to charge trapping and the formation of potential barriers.[107] Similar considerations can be done e.g., for sexithiophene films, where it has been observed that the chemical contamination of the boundary (e.g. adsorption of H_2O or O_2) may also modify the potential barrier.[108] By contrast, for OSC polymer films, individual chains may connect adjacent grains thus minimizing the effects of domain boundaries compared to what is observed for small molecules.[106] In all cases, the key for understanding resides in pushing the limits of resolution and sensitivity to study the arrangement of molecules and polymer chains in intergranular regions. Another possible approach, instead, avoids the problems associated with grain boundaries by directly depositing single-crystal thin films.

1.4 Electronic Properties of Metal/OSC Interfaces

One important property of OSC materials that marks a neat distinction with some metals and inorganic semiconductors is that no insulating oxide is formed upon exposure to ambient air.[109] Inert metals, that do not form a surface oxide, like Au, instead suffer from the accumulation of adventitious carbon.[110] None of those materials that are commonly employed in devices can form clean interfaces, unless a self-assembled monolayer (SAM) is deposited to passivate the surface of e.g., the metal or the oxide from further oxidation or contamination.[111,112] The formation of an interface between the electrode (usually a metal) and the OSC depends on the deposition method used to deposit the organic material and on the surface conditions of the electrode (fabrication and storage history). In organic electronics, metal/OSC interfaces are a prerequisite for the understanding of charge transport in devices. In most cases, the charge injection occurs at the metal/OSC interface: the alignment of the electronic energy levels of the two materials determines whether a device is working or not, and the correct interpretation of the device behavior starts from the evaluation of the contact.

This section focuses on the basic electronic properties of metals and OSCs to introduce the concept of metal-semiconductor interface. The physical quantities related to these electronic properties are useful to discuss the observed device behavior and were thus experimentally determined for all the functional systems reported in this thesis.

1.4.1 Electronic Structure of Metals

Metals are characterized by a chemical bonding (called metallic bonding) that is mediated by a cloud of delocalized electrons inside of a lattice of positively charged metal ions. Metals can be described in the simplest of the approximations as an ideal gas of free electrons that do not interact nor with each other nor with the atoms in the lattice.[113] More complex models were developed following the formalization of quantum mechanics,[114] that described the electron wavefunction as Bloch waves[115] providing the theoretical framework that constitutes the base for the modelling of electronic properties and charge transport at the solid state. Here, the work function of metals is defined and its relevance in device design and functioning is outlined with reference to organic electronics applications.

1.4.1.1 Work Function (WF)

When crossing the metal/vacuum interface, the electron experiences a difference in electrostatic potential arising from the dangling bonds of external metal atoms that generates an excess of electron density outside the metal surface and a deficiency of electron density within the metal.[116] This redistribution of charges, occurring at the surface via tunneling of electrons outside over a distance of ~ Å, generates a sheet of negative charges outside the metal and leaves a surface and sub-surface region of metal ions with an uncompensated positive charge.[117] The WF of a metal is the minimum energy that has to be supplied to the least bound electron to extract it from the bound state to the vacuum level (i.e., outside the metal). The Fermi level is a precisely defined thermodynamic quantity that corresponds to the electrochemical potential of electrons inside the material (E_F) which is a way to specify the energy of the least bound electron. The difference between the electrostatic potential energy of the electron in the space immediately outside the metal ($-e\Phi$) and E_F is the definition of WF ($WF = -e\Phi - E_F$).

The WF of metals have been already determined in the past for atomically clean surfaces with ultra-high vacuum equipment, but each of these values is specified for a particular crystal orientation, which is barely the case for polycrystalline electrodes in devices. For practical applications, these values are not particularly useful due to the high variability of the WF (even in the order of ≈ 1 eV) associated with multiple crystal orientation, surface roughness and composition and sample processing history.[117] The importance of precisely defining the interface of metals with the ambient responds to the urge of evaluating the composition and structure of the materials deposited on the electrode. Researchers developed different strategies to overcome the variability of the electrode properties, for example, by depositing the active material in the same deposition chamber of the metal or by depositing a SAM on the metal surface.[118] If none of these strategies is actuated, the surface of non-inert metals is quickly oxidized, and that of noble metals is covered by adventitious carbon contaminants.[119]

1.4.2 Electronic Structure of Organic Semiconductors

OSCs are not as simple as metals to describe. Metals are made of an (ordered) array of identical atoms that share a common cloud of delocalized electrons, while OSC materials are constituted by individual molecules whose structure is bound by strong covalent bonds and held together by weak non-covalent bonds at the solid state. The molecular character of OSC materials forces a description in terms of the frontier orbitals (HOMO

and LUMO) instead of expressing the electronic properties according to the band theory. However, the interaction of individual entities within a molecular crystal (or assembly of polymer chains) generates electronic bands and, depending on the degree of charge delocalization, one or the other description better represents the properties of the material. Whatever solid, in fact, presents a density of states and larger or narrower energy bands, despite strong localization of the electronic states observed in OSCs. Unfortunately, this localization limits the engineering of the band structure which is typically restricted to the addition of molecular dopants in the material.[120] At present, some approaches to tune the electronic properties of OSCs with continuity (as realized in inorganic semiconductors) are being investigated, even though the synthetic effort required to synthesize molecular equivalents with similar self-assembling properties poses an important challenge in organic electronics.[121]

Despite the π–π interactions along the stacks of conjugated cores in OSC materials (see Section 1.3), the charge cannot be localized over the entire volume of the material (which is also further limited by crystal defects and amorphous regions) and the bands are consequently narrow. However, the density of states of HOMO and LUMO is broadened by the presence of defective states and an increase in crystallinity results in sharper bands, but still featuring strong anisotropies arising from the molecular structure and packing directionality. Electrons in OSC materials do not move freely as in metals, but they always displace in the form of bound states.[122] Excitons, that are neutral quasiparticles consisting of bound state of an electron and an electron hole, are formed inside OSC crystals following e.g., the absorption of a photon, and possess a binding energy or about 0.1−1 eV, due to the relatively small dielectric constant of OSC materials.[123] Excitons in organic crystals are usually strongly polarized along crystallographic axes and can be transferred from one molecule to another.[124] This kind of quasiparticles is especially important in OLED and OPV applications.[125] Polarons, instead, are quasiparticles that comprise an electron displacing in a dielectric crystal and the spatial distortion of the lattice that is generated to screen the negative charge of the electron. The transport of charge in OSC is characterized by a strong interaction of the electron with phonons (electron-phonon coupling) that leads to the formation of polarons.[126] Band conductance can generally be obtained in OSC when temperatures are low and lattice vibrations are reduced, so that the effect of dynamic disorder is minimized.[45]

Without further discussing the fascinating complexity of OSC, the rest of the subsection is centered on the definition and the importance of the optoelectronic properties that determine the electrical behavior of p-type OSC materials, i.e., the ionization energy, the optical gap and the Fermi level.

1.4.2.1 Ionization Energy (IE)

The ionization energy (IE) of an OSC is the energy required to remove an electron from the material. According to the Koopmans' theorem, the first ionization energy of the isolated molecular system corresponds to the negative of the HOMO energy under the assumption of that the orbitals of the neutral molecule remain unaltered after the ionization.[127] The first principle calculation of HOMO energies can qualitatively correlate with experimental values with an error of less than 2 eV,[128] which provides IE values that are not sufficiently accurate for the optimization of the energy level alignment in devices (requiring precisions < 0.1 eV). At the solid state, the IE of OSC material is not a simple value, as for the isolated molecule, but multiple values arise from the anisotropy of ordered molecular assemblies similarly to what observed for different crystallographic orientations in metals.[129] There exists a surface dipole associated with molecular layers that is conceptually different from that observed in metals (see Section 1.4.1.1), as it is due to the anisotropy of both the molecular structure and the assembly that the OSC material forms.[129] Since the orientation-dependent polarization energy in the film controls the energetics of the assembly, changing the type of substrate can influence the interfacial order and the following growth of OSC thin films to obtain different IE and EA in the same material.[130] Substrates can also be functionalized with SAMs to induce a different morphology in the deposited material to attain orientation-dependent IE varying by, e.g., 0.7 eV in OT thin films.[131] Another approach alternative to the surface modification of substrates consists in exposing groups of different polarity to the surface termination of organic assemblies, such as replacing -H with -F atoms to tune the IE.[132] The IE of OSC materials can be nowadays determined in a variety of environments with different techniques (see Section 2.2).

1.4.2.2 The Band Gap (E_G)

Since the valence and conduction bands in metals are overlapping, there exists no gap between the two bands and many electrons can easily access a vacant electronic state at room temperature. In OSC materials, the energy difference between the top of the valence band (IE) and the bottom of the conduction band (EA) is called band gap (E_G,

or transport gap) and it considers the lowest energy levels of a single electron or hole in an uncorrelated state.[117] This gap is larger than the optical gap (here referred to as E_{OPT}) that instead is the energy corresponding to the absorption of a photon generating the lowest electronic transition (i.e., forming the exciton pair with lowest energy).[133] E_G is the relevant property for determining experimentally the carrier injection and extraction barriers, but the measurement of EA requires dedicated ultra-high vacuum equipment. When the latter is not available, E_{OPT} is used as an approximation for considerations on the energy level alignment, such as the doping level of the material which depends on the relative position of the Fermi level within the gap.

1.4.2.3 Fermi Level (E_F) and WF

Before defining the Fermi level (E_F), the vacuum level must be defined (E_{VAC}). As in the case of metals, E_{VAC} is the energy of the electron outside the solid surface at zero kinetic energy. This must not be confused with $E_{VAC}(\infty)$ that is not very useful for practical purposes (but important for theoretical ones).[134] While in metals E_F splits the continuum of occupied and unoccupied states hence collapsing IE and EA in the WF, in OSC materials there is no electronic state associated with E_F.[117] E_F statistical value that is found between IE and EA. In these materials, WF is defined as the difference of E_{VAC} and E_F and can be determined quantitatively via photoemission spectroscopy or Kelvin probe. The WF the depends on temperature, carrier density, density of states, and, finally, on the doping concentration, thus being an important indicator to evaluate the doping of a material.

1.4.3 Metal/OSC Junction

When the OSC is deposited on the electrode, an interface is formed. These metal/OSC junctions are the regions where charge is either injected to or extracted from the OSC. The successful displacement of charge carriers from one material to the other depends on energy barrier which forms at a metal/OSC junction originating from the mismatch of E_F in the metal and IE (EA) in a p-type (n-type) OSC. To follow the path of a charged particle through the source and drain electrodes via the conductive OSC channel in an OFET, the reader should consider all the processes of charge transfer that occur at the microscale. An accurate description of charge transport in functional devices starts from the understanding of the interface formation and its structural and electronic properties.

When the surface of metals is covered by organic molecules (or contaminants), the WF of the metal is altered due to the formation of an interface dipole arising from a transfer

of charge.[135] The direction of this charge transfer, and thus the variation of E_F in the metal, can be determined by knowing the WF and the IE of the isolated metal and OSC material. The two main contribution to this change are (i) the "pillow" effect, i.e., the metal WF decrease due to the compression of the metal wave function[136] and (ii) the effective charge transfer arising from the chemical interaction between the metal and the adsorbed material (e.g., SAMs).[137]

The critical aspects regarding metal/OSC junctions determine the functioning of devices. Once the interface is defined, the transfer of charge carriers is manly limited by the residual energy difference between the metal WF and the OSC IE, called Schottky barrier. This barrier can be reduced by proper metal/OSC energy level alignment to facilitate the injection of charge carriers from the into the OSC. The experimental values of OSC energy level then depend on the substrate used, as the interface dipole and charge transfer cause an interfacial charge redistribution that can extend to the bulk of the OSC, which is at the origin of band bending.[138]

1.4.3.1 Schottky Barrier

When a metal and an OSC material are brought into close contact to form an interface, an energetic barrier arising from the mismatch of the IE of the OSC and the effective WF of the coated metal is created.[139] This barrier is known as Schottky barrier and when its magnitude is above ~ 0.3 eV, the OFET physics is significatively impacted by charge injection.[140] In optimized devices, transport processes occurring nearby the contact in the bulk of the OSC are much more relevant and this barrier only minorly affects the device performance. However, it should be noted that an intrinsic Schottky barrier is present even when an ohmic contact is realized, with differences arising from the device configuration that can be mitigated by contact doping.[141] In fact, the same reasoning applied for Schottky barriers in OSC deposited on Au can be translated to atomically clean Au deposited on top of an OSC layer (i.e., in TC configuration).[142] The Schottky barrier can be quantified by current vs voltage and capacitance vs voltage characterization as well as via photoelectron emission spectroscopy and Kelvin probe techniques.[139] Its determination has an important role in controlling the contact resistance, as it will be discussed in Section 5.1.2.

1.4.3.2 Energy Level Alignment

In the past, it was very common to treat the energetics of vacuum level alignment in metal/OSC interfaces under the Schottky-Mott limit, hence disregarding the chemical

and physical interactions between the two components which is at the base of the device functioning.[143] The energy level alignment in metal/OSC junctions must be referenced to some invariant parameter. As evidenced by the WF anisotropy associated with different crystallographic facets, since E_F is the same within the metal and E_{VAC} depends on the crystal orientation, E_{VAC} cannot be used as an absolute reference.[138] For a formally correct positioning of E_{VAC}, the interface dipole must be quantified thus enabling the referencing to E_{VAC}.[144] During the process of junction formation, the chemical potentials of the metal and of the OSC are equalized as electronic charge is transferred from the material at higher potential to the one at lower potential, thus contributing to the dipole formation and, consequently, shift of E_{VAC}. The modelling of the energy level alignment at metal/OSC interfaces is already particularly challenging for strongly chemisorbed monolayer systems and it is far more complicated for "real" interfaces, even though some fruitful approaches exist.[145]

Many different strategies to optimize the energy level alignment in metal/OSC interfaces have been devised in the past two decades to facilitate the formation of ohmic contacts. One of the most common methods, that possesses some requirements and limitations about the choice of metal and monolayer-forming molecules, is SAMs.[111,137] Despite the additional tunneling barrier (represented by SAMs) put in series with the OSC space-charge barrier, OFET devices can benefit from the chemical modification of their interfaces.[146] As an alternative to SAMs, a universal method based on interlayers of strong donor and acceptor molecules for energy level alignment in metal/OSC interfaces was recently reported by Koch et al.[147] A similar (universal) method uses metal oxides to tune the WF of a variety of substrates for organic electronics.[148] Depending on the oxide WF and on the OSC energy levels, E_F can be differently pinned within the band gap to achieve three different regimes of alignment.[149] In general, reducing structural defects in the OSC thin film at the metal/OSC interface by electronically decoupling the two (e.g., by using an interlayer) is useful to minimize the number of electronic states within the band gap and thus improve charge injection.[150]

1.4.3.3 Band Bending

Except in cases where a molecular doping strategy is used, OSCs materials are intrinsic semiconductors having E_F at about midgap. E_G in OSC is also quite large (around 2 eV), hence the concentration of intrinsic carriers is relatively low. A charge redistribution occurs at the metal/OSC interface when the two materials are brought into contact. E_F is equalized by storing the charge at the interface, on the metal side, and inside a

depletion/accumulation region, within the OSC. However, if the OSC material is only slightly doped or undoped, free charge carriers are displaced from (even) micrometric distances from the interface.[145] Consequently, the energy level alignment shows a depth dependence, called "band bending", whose extent within the bulk of OSC is an important parameter to control electronic processes, such as charge injection/extraction, exciton dissociation and spin filtering, in OLED and OPV devices.[151,152]

Within the purpose of this thesis, the most relevant implications of band bending are related to the determination of E_F at OSC/metal interfaces via Kelvin probe techniques, as, at ≈ 2-10 nm from an interface, the WF corresponds to E_F of a monolayer of the OSC, while at larger thickness the WF converges to the E_F of the bulk OSC material.[153] One should also consider the effects of the tip size and probing depth when passing from macroscopic to microscopic Kelvin probe for the determination of the WF of the OSC.[154] The microscopic technique enables the electronic characterization of organic functional materials at the nanoscale by recording the surface potential of nanointerfaces in real device configurations.[155]

2 Experimental Tools for Organic Electronics

Materials science requires the utilization of many different experimental techniques to provide meaningful information about structure, composition, and various chemical and physical properties of the materials under study. Organic materials add a level of complexity to this characterization. While the protocols to control crystallinity in inorganic materials for electronics are relatively easy to implement due to the simplicity of the chemical structures and interactions involved, the same cannot be said for organic materials, as widely discussed in Section 1.3. This additional complexity must be then rationalized with experimental tools that can be simultaneously employed to provide useful pieces of information. It is a duty of the materials scientist to collect, interpret and reframe these data for describing the complexity of organic materials.

The scope of this section is to summarize the most relevant experimental techniques in the field of organic electronics and iontronics in light of the type of information that can be extracted from each of them. This summary does not aim to be completely exhaustive and comprehensive of all the known techniques, but it will list and describe those that are most useful for the interpretation of the experimental data reported in this thesis. The possibility of using different methods to extract and compare data related to the same (or similar) physical properties is a powerful approach that helps confirming the several hypotheses and assumptions that arise when describing such complex systems. The fundamental physics of the listed techniques are widely known to the scientific community and a detailed discussion of the basic working equations are outside the scope of this section. For the sake of simplicity, each subsection will be named after the properties of the materials, rather than on the techniques themselves. The interpretative empowerment of this section relies on the exemplificative comparison among different probing tools for the characterization of similar physical properties.

Some of the methods to determine the electrical properties of OSC are first described and related to the important multi-technique investigation of these materials in both thin-film samples and working devices. The electronic properties that control this performance can be then characterized and correlated to the crystallinity, morphology and surface thin-film properties. Not all the techniques listed have been actually used within this thesis work, but some of them are reported for the sake of comparison and for their relevance in the field of OSCs.

2.1 Electrical properties

The electrical properties of OSC materials are the final characteristics resulting from a long research process which comprises of synthesis, processing and device fabrication. The active OSC material is processed into a thin film supported on a conducting or insulating substrate for the determination of its electrical properties or assembled with other materials and integrated in a device to be characterized. Depending on the sample geometry and complexity, many physical quantities of relevance for electronics can be extracted with the measurement techniques developed. One should consider the OSC that has been assembled in a device as the result of the active material with its intrinsic properties, arising from processing, that is interfaced with all the other device components and within the surrounding environment of device operation. All these factors together enclose the essence of the measurement of an electrical property from an OSC material.

This section aims to compare the different techniques and the corresponding device geometries that can be employed to characterize the charge transport in OSCs. What all these techniques have in common is the characterization of the motion of electrons, disregarding the electronic properties, which are instead related to the energetic aspects of the electrons. Hence, the methods and instrumentation to determine the conductivity, the charge carrier mobility, the impedance, and other device parameters are discussed.

2.1.1 Electrochemical impedance spectroscopy (EIS)

While the sourcemeter is the ideal instrument to perform DC and pulse experiments, potentiostats and impedance meters dominate the world of electrochemistry and alternate current (AC) measurements. Electrochemical impedance spectroscopy (EIS) is a broad analytical and non-invasive technique for the electrical characterization of materials based on combined AC and DC inputs. EIS data correlates the electrical current and the applied voltage in the frequency domain. In fact, during the experiment the electrochemical system under study undergoes a small perturbation consisting of a sinusoidal signal of voltage (potentiostatic mode) or current (galvanostatic mode). The resulting set of data is a complex-valued function Z(f), called impedance (Z), as a function of the signal frequency (f). The fitting of EIS data can then be used to obtain some physical and microstructural properties of the system.[156]

The analysis of EIS spectra is done by fitting Z(f) with equivalent circuit models consisting of a combination of electrical elements, such as resistors, capacitors, inductors or other generalized impedance elements, and resulting in a finite circuit whose behavior can be analytically described by a mathematical expression. Knowing how to accurately fit an EIS spectrum is a skill that requires years of experience to be mastered, hence the fabrication of samples with a geometry that can be translated into a simple equivalent circuit is a clever choice to get started in the field. Concerning the use of EIS for the characterization of OSC materials, this technique is routinely used for the characterization of the capacitance of thin films, in particular when mixed conductors are involved as the product of carrier mobility and volumetric capacitance is a benchmarking parameter for OECT materials.[157] Alternatively, EIS can also be used to separate ionic and electronic resistive contributions in mixed conductors.[158] Furthermore, an energy resolved EIS method has been developed for OSC electronic structure mapping with energy resolution of ~ 100 meV and capable of providing some density of states parameters directly from the measured spectra.[159]

2.1.2 Conductive AFM (C-AFM)

Conductive AFM (C-AFM) is a scanning probe technique that is used to study the local electrical conductivity at the tip/sample point of contact while simultaneously measuring the surface topography. In C-AFM, a voltage bias is applied between the conductive tip and the electrode supporting the sample, which can be spatially arranged to study either the vertical or the lateral conductivity.

The sensitivity of the C-AFM measurement can be modified by using different operational amplifiers that are integrated in the C-AFM module or probe holder. These amplifiers require manual tuning and adjustment with a calibration resistor to check for a correct offset and sensitivity response. Based on the electrical current sensitivity, our AFM manufacturer distinguishes C-AFM from Tunneling AFM (TUNA) for the ability of its module amplifiers to measure ultra-low currents (< 1 pA). This increased sensitivity is fundamental for the electrical characterization OSC materials in which the basic conductivity is not sufficiently high when no field-effect enhancement is achieved in the conductive channel. Hence, three-terminal C-AFM setups can be realized with relative simplicity in order to control the lateral conductivity by field-effect, but in the case of vertical conductivity, the additional second electrode and oxide layer may complicate the effective sample geometry.

Basic C-AFM measurement can be performed in contact mode, but other modes that reduce the tip/sample interaction have been developed to enable C-AFM experiments in soft and particularly fragile samples. Among those techniques, Torsional Resonance TUNA and PeakForce-TUNA deserve to be mentioned for the several advantages that they bring to the imaging. Torsional Resonance TUNA imaging is performed with the tip kept in the near field while reducing both vertical and lateral tip-sample interactions by vibrating a torsional resonance mode of the cantilever (in addition to the fundamental resonance) and detecting the decrease in vibration amplitude to control the feedback loop.[160] PeakForce-TUNA combines the imaging capabilities of ScanAsyst and surface nanomechanics imaging (see Sections 2.4.1 and 2.5.1) with the electrical current measurement of TUNA.

C-AFM imaging was performed with a Bruker Dimension Icon setup operating in air, in contact mode. An MFP-3D AFM System (Asylum/Oxford Instruments) was also used for contact-mode C-AFM measurements. Either Pt/Ir coated SCM-PIT-V2 tips (tip stiffness: k = 3 N/m) or SCM-PIC-V2 tips (tip stiffness: k = 0.1 N/m) were employed.

2.1.3 Electrical properties: technique comparison

Electrical properties are at the core of the study of OSC devices. The techniques discussed in this section allow the researcher to determine the charge transport characteristics of OSC materials. The basic method to determine the mobility of an OSC is by characterizing the OFET device, but the mobility parameter extracted via the commonly used transistor equation is valid for a contact resistance approaching zero (the contacts must display Ohmic behavior) which is not always the case.[79] Hence, gated 4-point probe or transmission line method are two viable approaches to address contact resistance related issues. Depending on the geometry of the OFET, the in-plane (μ_{in}) or the out-of-plane (μ_{out}) mobility can be determined, the latter being trickier due to the requirement of a vertical transistor geometry.[161] Other device configurations different from the vertical OFET can be alternatively realized, such as samples for space charge limited current (SCLC) measurements,[162] a geometry that can be also adapted for C-AFM experiments.[163] Also EIS can be used to determine the charge carrier mobility, by taking the necessary precautions in the electrode, environmental condition and equivalent circuit selection.[162] All the above-reported techniques have in common the physical injection of charges from electrode contacts to the OSC film. The resulting mobility is governed by the effective transport of the carriers from one electrode to the

other, across the OSC/electrode interface, the OSC material and grain boundaries and all the sources of scattering present in the operational device.

Electrons require an electric field to displace within a material. An instrument combining a direct current (DC) power supply, a power source and a sensitive multimeter in the same unit that can apply variable voltage and/or currents and record electric signal via multiple channels is called sourcemeter. A sourcemeter can also incorporate a pulse generator and integrates all of these functions in the same housing. The sourcemeter is connected to the device to be characterized and, by forcing a voltage or a current through the circuit, it simultaneously measures the voltage and/or current in the device. For the measurement to be performed, a physical contact is here required. Depending on the type of experiment, two-, three- or four-terminal setups are needed to determine the electrical properties of the OSC films. These three different methods are discussed in this section with reference to the measurement techniques that have been specifically used throughout the thesis.

A Keithley 2636B SYSTEM SourceMeter was used for the electrical measurements.

- DC (two-terminal) measurements: Two-terminal DC measurements are the simplest type of experiment used to characterize the electrical response of a device. The application of a voltage to the source and drain electrodes enables the measurement of properties related to the device resistivity that also include the resistive contributions from the leads, hence being more representative of the real device operation, but adding additional unwanted contributions to the electrical properties of the material.
  Common two-terminal measurements include, for example, chronoamperometry (current vs time measurement at constant bias voltage) and current (I) vs voltage (V) curves (measurement of device resistivity by voltage sweeping).
- OFET (three-terminal) measurements: Three-terminal measurements employ a third electrode for the application of an additional bias voltage. OFET devices possess a gate electrode whose potential is changed to suppress or enhance the charge carrier density in the conductive channel. Transfer (gate voltage sweep at constant source-drain bias) and output (source-drain voltage sweep at constant gate bias) curves are transistor characteristic curves that are used to determine the OFET parameters such as charge carrier mobility, subthreshold slope and threshold voltage.

- 4-probe (four-terminal) measurements: Four-terminal measurements are generally useful when the intrinsic electrical properties of the OSC material have to be tested without any interference arising from the charge carrier injection electrodes. Four electrodes, or probes, are arranged in a line, for classical 4-probe measurement, or in a square for Van der Pauw measurements. For the line configuration, a bias voltage is applied at the external electrodes to force a constant current through the conductive channel while the two internal electrodes serve to record the potential drop at a known distance. The resistivity of the material is then obtained from the ratio of current value forced through the channel and the voltage drop measured between the two electrodes at a known distance.

Contact-free techniques have also been developed to study the potential of OSC materials for charge transport, without the need of fabricating the device. Time-resolved terahertz spectroscopy[164] and field-induced time-resolved microwave conductivity[42] are two techniques use THz and μ-waves radiation to study electron and hole transport in the bulk OSC material and at interfaces. Those techniques usually give mobility values in excess, as the oscillating motion of charges is limited in space (e.g., to the crystalline domains), with values approaching those recorded at low temperatures in the absence of electron-phonon coupling.[165] Alongside these techniques, the alternative approaches, such as two-terminal C-AFM, are very important for the study of OSC materials because they provide additional information on the mechanism, efficiency and limiting factors of charge transport at different length- and time-scales compared to the more traditional vertical junction and OFET geometries.

Complementary experiments that are especially important for OECTs or sensing devices are those that determine the capacitance of the OSC thin film. Capacitance-voltage profiling can be done with a sourcemeter equipped with a capacitance module, or, alternatively, capacitance measurements with EIS are straightforward for OSC thin films on a conductive substrate.[166]

2.2 Electronic properties

The "electronic" properties are distinct from the "electrical" ones because they focus more on the static and energetic aspects of the electron itself rather than treating the motion and behavior of the electron ensemble in a circuit. The energy state of the electrons in the OSC material, the available states within the electronic structure and

all the properties ruling the energy band alignment can be determined experimentally with a range of techniques that exploit electromagnetic radiation to excite or extract single electrons from their energy state, on one side, and voltage functions to displace electrons as a whole within a circuit in order to probe their overall behavior, on the other. The techniques falling in the first category use visible and UV light, as the characteristic energy of this type of radiation is similar to that of the electronic states, The techniques belonging to the second category use potentials in the order of few volts. The electronvolt (eV) is thus the energy scale typical of these experiments, those who determine the processes underlying the charge transfer and transport at the atomic scale.

2.2.1 Kelvin Probe Techniques

Kelvin Probe (KP) techniques are employed to experimentally determine the work function (or surface potential) of materials by measuring the electrostatic forces between the KP tip and the sample. When two materials having a different WF are contacted via an external circuit, an electrical current then flows through the circuit to equilibrate the chemical potential (or Fermi level) of the two materials (see the schematic representation in Figure 2.1 illustrating the working principle of the KP technique). The KP tip and the surface of the sample can be seen as the two plates of a capacitor. Opposite charges are generated on the capacitor plates because electrons flow from the material with lower Φ to the one with higher Φ. An electric field E is then formed between the two materials, correlated to the contact potential difference (CPD) of CPD = $\Phi_1 - \Phi_2$.

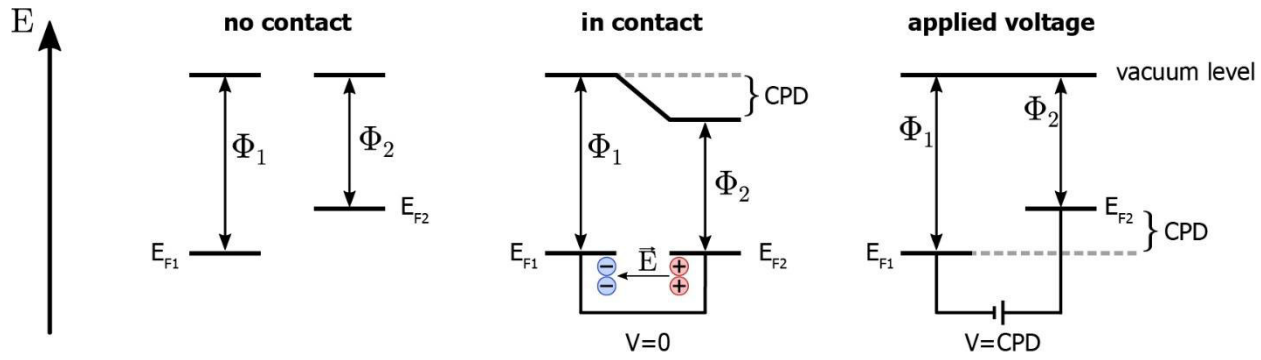

Figure 2.1: Energy levels in a KP experiment. No contact – the two materials have different Fermi levels (E_F) and hence different work functions (Φ_1 and Φ_2). In contact – an electric field E is formed when the materials are connected via an external circuit. Applied voltage – an external voltage corresponding to the CPD is applied.

When the two materials are contacted, an external $V_{CPD} = e(\Phi_1 - \Phi_2)$, where e is the elementary charge, can be applied to nullify the electric field. By measuring V_{CPD}, KP methods enable the measurement of the WF of unknown samples. By calibrating the WF of a reference electrode (Φ_{ref}), the WF of the unknown sample (Φ_s) can be determined via measurements of V_{CPD} with the equation $\Phi_s = \Phi_{ref} - V_{CPD}/e$. The experimental determination of V_{CPD} is done by nullifying the electrostatic interaction between the sample and the reference electrode.

Throughout the experiments reported in this thesis, the calibration of the probe was performed against a freshly cleaved highly oriented pyrolytic graphite (HOPG) surface, which is known to have a WF = 4.475 eV in N_2 environment,[167] at ambient conditions and with a correction for the non-zero RH.[168] Two different KP techniques have been used:

- Macroscopic KP: Macroscopic KP measurements were performed at ambient conditions using a 2-mm-diameter gold tip amplifier (Ambient Kelvin Probe Package from KP Technology, Ltd.).
- Kelvin Probe Force Microscopy (KPFM): KPFM imaging was performed with a Bruker Dimension Icon setup operating in air, in amplitude modulation tapping-lift mode, by using Pt/Ir coated SCM-PIT-V2 tips (tip stiffness: k = 3 N/m).

While both techniques can determine the same physical property, the type of information that can be obtained from the measurement is different. In fact, macroscopic KP data is averaged over a millimetric area at micrometric distances and KPFM probes submicrometric areas at nanometric distances, yielding a local estimate of the WF. For non-metal materials, the sampling depth is not simply limited to the Debye length (few Ångstroms) but can extend from tens to hundreds of nm within the bulk, depending on the material and on the KP probe type and size.[154]

2.2.2 Photoelectron Yield Spectroscopy in Air

Photoelectron Yield Spectroscopy in Air (PYSA) exploits the photoelectric effect to determine the photoelectron emission yield (proportional to the number of extracted photoelectrons) from a sample as a function of the incident light radiation energy. X-Ray and UV radiation are among the low-energy ionizing radiation, possessing the minimum energy required to excite electrons from a bound state in the material to an unbound state in the free-space vacuum level. For commercial PYSA instruments, the

primary choice is UV light as the determination of the energy level of shallow and frontier states does not require energies higher than UV. The main advantage of PYSA technique, compared to the other photoemission methods, is that it does not require a vacuum environment, thus avoiding all the delicate vacuum procedures and granting the characterization of a physical property in an environment more similar to that of device testing. Indeed, for air-stable OSC testing the processing and characterization environment is typically air, but for advanced optimization and final product fabrication a N_2-filled glovebox is generally preferred.

The photoelectric emission yield is related to the electronic properties of materials as it contains information about the binding energy of the most loosely bound electron and about the contamination layer situated above the electron-emitting surface.[169] The threshold energy value for electron emission, that is the WF for metals or the IE for OSC, is closely related to the onset energy of the photoelectron yield curve. It is possible to estimate the WF or the IE as the intersection of the tangents of the PYSA curve with the extrapolated baseline. The baseline at lower energies is fitted by using a flat line, while the PYSA curve is fitted by using a sloped line. It is generally easy to obtain reliable values from metals and p-type semiconductors or systems that are not easily oxidized in air. Due to a sampling depth for normal incidence of near UV light (200 nm – 250 nm) of around up to 10 nm (limited by the inelastic scattering of photoelectrons),[170] all materials having a sufficiently thin passivation layer (which usually has higher IE than the material located below) can be characterized. When the surface of the material is oxidized for more than 10 nm deep the experiment becomes meaningless. When the density of traps is so high to give a significant density of states or when the surface is covered by a material with smaller IE, than the parameter extraction becomes impossible or very tricky.

Photoelectron yield curves were collected using a Riken Keiki spectrophotometer (Japan) model AC-2 with energy step of 0.05 eV, a variable UV spot intensity of 10 to 500 nW, within an energy range of 3.4 to 6.2 eV. The final estimate for the energy threshold is known with error of ± 0.05 eV or less, depending on the homogeneity and air stability of the sample.

2.2.3 Ultraviolet photoelectron spectroscopy (UPS)

Ultraviolet photoelectron spectroscopy (UPS) is a technique based on the photoelectric effect that is used to characterize the electronic structure of material by probing its

surface with UV light. With this technique, it is possible to determine the WF of electronic and functional materials, by measuring the secondary-electron cut-off, and other physical quantities such as the IE and the EA (with an additional inverse photoemission experiment). The UPS measurement requires an ultra-high vacuum chamber (pressure < 10^{-8}-10^{-9} mbar) equipped with an electron energy analyzer. For laboratory equipment, the photoemission of electrons is usually stimulated with discharge lamps that produce radiation in the vacuum ultraviolet region, such as a He(I) UV source (21.2 eV). An alternative source for high-accuracy experiments is a monochromated synchrotron source. The light in synchrotron beamlines offer an easier control of light intensity and energy that is provided with little spread and that can be tuned at the facility to adapt the setup to the needs of the experiment. The sampling depth of UPS is limited to the first few nanometers (up to around 10 nm for normal light incidence) and might be decreased to become surface-specific by performing the measurement at grazing angles.

An advanced variation of UPS, called angle-resolved UV photoelectron spectroscopy, enables the mapping of the band structure of a material by determining energy and momentum of electrons. This technique is realized by using a setup that includes a sample manipulator that can rotate to position the sample at different emission angles with respect to the incoming beam.

2.2.4 Ultraviolet-visible (UV-Vis) spectrophotometry

UV-Vis spectrophotometry is an optical technique that works with light in the UV and visible range and can be employed in both transmission and reflectance mode to study the absorbance and reflectance of a variety of samples. In general, this technique is routinely used for quantitative analytical measurements of the concentration of unknown sample solutions, but it also finds many solid-state applications relevant of OSC materials. To cite a few, molecular electrochemical doping can be quantitatively studied thanks to the significant changes in the spectral features arising from the interaction between the dopant and the OSC,[171] the determination of the optical gap can constitute a useful input for a more accurate energy levels in the experimental electronic band structure,[172] and as a last example, a complementary tool for the characterization of OSC blends.[173]

UV-Vis spectra were collected using a Varian Cary 50 spectrophotometer equipped with an Oriel 68810 500 W Hg lamp in combination with an Oriel 77200 monochromator and a beam splitter to perform double beam experiments.

2.2.5 Electronic properties: technique comparison

All the techniques that have been discussed in this section provide complementary data about the electronic properties of OSC materials and the degree of detail that can be achieved is usually limited by the instrument availability and/or the need for such a deep characterization of the system. Here, experimental tricks for sample preparation and analysis are described alongside with pros and cons of each technique.

When a OSC device is fabricated having no information about how the energy levels of the active material match with that of the electrodes, the outcome can be dramatic resulting in devices with poor characteristics (and far from ideality) which require a more complicated performance assessment compared to simplified device models.[79] As a first prerequisite, the energetic barrier for charge injection should be as low as possible, meaning that the electrode WF should be matched with the HOMO(LUMO) of the p-type(n-type) OSC.[47]

The WF of the metal electrode or that of the OSC is an important parameter to determine the doping of the material based on how the Fermi level changes compared to the HOMO and LUMO levels. For metals, the WF can be quantified by means of KP, KPFM, PYSA and UPS. While the KP methods yield a WF value that is averaged over the sampled area of the surface, the optical methods give a minimum WF associated with the least bound electrons.[174] As a consequence, the former values are generally larger than the latter for metallic samples. In case a contamination layer (limited to a max 10 nm thickness) with different IE is present, KP methods resent of this contribution because of the averaging effect due to a complete sampling of the layer (and a sampling within the metal limited to the Debye length.[154] For optical methods the situation is different and two cases are distinguished: (i) the IE of the contamination layer is smaller than the metal WF, the metal WF discrimination is increasingly more difficult with an increasing thickness of the contamination layer and (ii) the IE of the contamination layer is larger than the metal WF, the electron signal from the metal is reduced as a function of the contamination layer thickness.

For OSC materials, where the sampling depth is different among the methods, there are supplementary precautions to take. Firstly, the sample must be electrically grounded to avoid charging. Charging issues are particularly critical for UPS and KP, while KPFM and PYSA are less subject to these problems due to the smaller number of charges involved in the measurement process, but a good grounding is always key to avoid the most common artifacts. If the OSC material is not sufficiently conductive itself, it must be supported on a conductive substrate. Secondly, the sampling depth and the environmental conditions are different among the techniques. Obviously, the vacuum environment guarantees that no external chemical species are interacting with the material, something that happens for ambient techniques. The two KP methods are basically different for the sampling area, which is related to the physical size of the probe, while the sampling area of the two optical techniques changes with the beam spot size. The sampling depth, as well, is larger for KP and KPFM (in the order of hundreds of nm)[154] and smaller for PYSA and UPS (usually less than 10 nm).[175]

The combination of KP, PYS and UV-Vis is very powerful and enables the drawing of the full energy level alignment diagram, with some exceptions where the use of UPS is necessary due to the intrinsic limitations of the PYS experiment.[176] Macroscopic KP is used to quantitatively determine the Fermi level of materials, while PYSA and UV-Vis provides estimates for IE and E_{OPT}, respectively, providing the necessary information to build the device energy diagram. EIS[159] and cyclic voltammetry[177] (CV) are alternatives to the above-discussed techniques, but their use is subject to experimental limitations, such as the use of non-solubilizing electrolyte, hence introducing a different environment for OSC characterization. CV can determine indirectly both IE and EA, but the measurements tend to underestimate the gap energies compared to those determined by optical means.[178]

KPFM is not so commonly employed for the determination of the energy level alignment because it is less practical than the macroscopic version when uniform wafer-scale films are characterized. Instead, KPFM is essential for the study of nanomaterials as the resolution of the AFM probes enables the WF characterization of nanometric (~ 50 nm) objects.[169] KPFM is one of the few techniques that can provide a direct estimate of the contact resistance of in-operando devices, where an external bias is applied to the device electrodes and the AFM probe is scanned over the conductive channel to measure the surface potential drop at the contacts.[179]

2.3 Crystallinity and solid-state structure

As broadly discussed in Section 1.3, the crystallinity of OSC materials at the solid state must be properly characterized to better identify the structural properties and the quality of the thin films for device applications. In recent years, a variety of characterization techniques has been developed aiming to assess the effect of crystal domain structure and orientation on the charge transport properties of OSC.[106] Some of these techniques has been employed within this Ph.D. work either directly or via scientific collaborations. The aim of this section is to briefly summarize these experimental approaches and critically evaluate their practicability with reference to the other known methods for the mapping of the grain size and orientation.

2.3.1 Polarized Optical Microscopy (POM)

Optical microscopy is routinely employed to qualitatively check the uniformity and continuity of organic thin films. The optical brightness changes as a function of the thickness, hence, by choosing a substrate giving a suitable optical contrast, it is also possible to distinguish the number of OSC layers in a terraced thin film via simple reflected bright-field optical microscopy. The information that can be obtain by optical microscopy, however, is not only limited to basic sample morphology. For the imaging of polycrystalline thin films, an important microscope setup uses two crossed polarizers (i.e., with perpendicular transmission directions). An optical microscope upgraded with two polarizers in the light path can probe the relative orientation of crystallites within the thin film, within the resolution dictated by light diffraction limits.

The incoming beam is linearly polarized by the first polarizer before reaching the sample. Thin films possessing crystalline anisotropy often exhibit birefringence, so the sample reflects the linearly polarized light into a beam with two different polarization components (the "slow ray" and the "fast ray"). After reflection, the two light components can be recombined via interference by passing through a second polarizer, called analyzer. When the two filters are cross-polarized, the light reflected from individual single crystals can be selectively enhanced or suppressed, giving an optical contrast for crystals of different orientation (similar considerations hold true for POM in transmission mode). Therefore, based on the brightness of the light reflected from different sample regions, the relative crystal orientations can be distinguished. A brightness change is observed if the sample is rotated in the microscope stage, as single-crystal domains with maximum brightness become dark when rotated by 45°.

Another rotation of 45° in the same direction brings the brightness back to the original intensity with a periodical trend. By contrast, amorphous films do not exhibit any brightness change upon sample rotation.

2.3.2 Transverse Shear Microscopy (TSM)

Atomic force microscopy (AFM) techniques include a versatile set of scanning probe tools that enable the characterization of surfaces at the nano- and microscale. Besides the most common use of AFM for the determination of the surface topography, there are many other surface properties that can be determined alongside with a simple height profile. TSM is a contact AFM mode that is a variation of the lateral force microscopy (or friction force microscopy) which differs from the latter for the scanning direction, changed from 90° to 0° with respect to the principal cantilever axis. When a sufficiently flat thin film of an anisotropic crystalline material is imaged under these scanning conditions, a frictional contrast due to the different orientation of crystalline grains can be observed.[180]

In TSM, the grain specificity arises from the frictional interaction between the tip and the interfacial molecules or chemical groups that are packed within grains of different orientations.[181] The AFM system detects this interaction in the photodetector as a cantilever twist by different amounts due to the shearing of the tip that depends on the crystallographic direction. It is worth noting that the trace and retrace TSM images show a contrast of opposite sign. This condition must be realized to ensure optimal TSM imaging conditions (which also requires a relative humidity (RH) < 20%) and minimizes the possibility of data misinterpretation due to artifacts. In addition, this technique conveniently provides two sets of data of opposite sign that can be processed via image math to enhance the small (5-20 mV) signal by subtracting one image to the other.

TSM measurements were performed in contact mode with a Bruker Dimension Icon setup operating in air at RH < 5% (under N_2 flux) by using nitride SNL-10 tips (variable tip stiffness: k = 0.06-0.35 N/m).

2.3.3 X-ray Diffraction (XRD)

X-ray diffraction (XRD) techniques comprehend a class of crystallographic methods based on the recording of the diffraction pattern of a monochromatic beam of X-rays through a crystal lattice. The samples can be either single- or polycrystalline in the form of crystal, powder or thin film and the technique is generally non-destructive. The

resolution of the diffraction pattern leads to the determination of the crystal structure, i.e., the precise spatial arrangement of the atoms within the unit cell, and many other crystallographic information. XRD techniques have very broad and versatile applications in many fields of science and medicine, and, nevertheless, the importance of XRD in organic materials research is not simply limited to the determination of the crystal structure of small-molecule and polymer OSCs, but it also extends to complementary structural properties that constitute fundamental information for the scientist.

For the sake of simplicity, each of the XRD techniques discussed here is treated separately in order to highlight when each method is particularly relevant and which peculiarities distinguish the sample data and preparation in a particular experimental setup. The outline begins with an elementary presentation of single-crystal XRD (SC-XRD) uses and applications to be compared with powder XRD (P-XRD). Other X-ray techniques relevant for OSC materials in the form of thin films are grazing-incidence wide-angle X-ray scattering (GIWAXS) and X-ray reflectivity (XRR). Small-angle X-ray scattering and the various other XRD techniques do not fit within this thesis, but still, the range of diffraction experiments that can be done for materials characterization with X-ray is anyhow impressive and it is not limited to the methods hereby described. It is worth mentioning here that besides XRD, in which X-ray photons elastically interact with electrons in the lattice, also neutrons can interact with the atomic nuclei, enabling a variety of neutron diffraction techniques complementary to XRD.

- Single-crystal XRD (SC-XRD): In a SC-XRD measurement, a single crystal of OSC material (typically small molecules) is mounted on a 3- or 4-circle goniometer that is rotated to position the crystal at selected orientations. A collimated beam of X-rays is directed onto the sample where it diffracts and a movable X-ray detector collects the diffraction intensity pattern which constitutes the experimental dataset. The resolution of the SC-XRD pattern results in the determination of the unit cell dimensions, bond lengths and angles and site occupancy, which can lead to the identification of a new polymorph or can serve as an input for the simulation of electronic and charge transport properties of the OSC material.
- Powder-XRD (P-XRD): Sometimes it is not possible to obtain single crystals by the nature of the OSC material (e.g., for polymers) or due to experimental complications. SC- and P-XRD are two complementary techniques, as the resolution of the crystal structure via P-XRD is only limited to particular systems

of moderate complexity. On the other hand, P-XRD not only constitutes an easy and viable option but can provide additional information regarding thin-film or powder samples. Investigations on phase analysis (e.g., identification of polymorphs), grain size and texture (e.g., preferred grain orientation) and crystalline/amorphous ratio can be performed on both small-molecule and polymer OSC materials.

- Grazing-incidence wide-angle X-ray scattering (GIWAXS): GIWAXS is particularly useful when the sample is in the form of a thin film. In GIWAXS, as in all the grazing-incidence techniques, the incidence angle of the X-ray beam on the sample surface is small. The surface specificity can be tuned by controlling the X-ray penetration depth which depends on the incidence angle. This aspect is very important for thin films, as in the standard 2θ scan a big fraction of the X-ray beam is lost into the substrate. The main advantage is the signal enhancement, counterbalanced by a loss in the in-plane spatial resolution.
- X-ray reflectivity (XRR): XRR does not qualify as a diffraction technique, but it is often associated with the other XRD techniques because of the many similarities of the experimental setup (especially with GIWAXS). XRR works over a small range of angles above the critical angle for total reflection of X-rays (which is typically around $2\theta \sim 0.1°\text{-}1°$). XRR instrumentation is optimized for achieving high angular precision in this range. At very small incidence angles, a beam of X-rays can be reflected by a flat sample such as a thin film, a sufficiently flat surface or multilayer films. XRR consists in measuring the intensity of X-rays in a specular geometry to obtain information about the surface roughness, the thickness of the thin film or of the distinct layers composing a multilayered film and material density. XRR highly benefits from a higher dynamic range when utilizing synchrotron radiation, as the reflectivity falls rapidly above the critical angle. XRR is also very important for the characterization of OSC materials as it is one of the few techniques with poor interaction with matter that can access buried interfaces.

2.3.4 Structural properties: technique comparison

In the following, advantages and disadvantages of the structural methods discussed in this section are outlined with reference to the other techniques that are known to give insight into the experimental mapping of crystalline domains. XRR and the other XRD techniques are left aside to focus on techniques that directly visualize crystalline

domains and molecular orientation. The molecular nature of OSC materials adds a level of complexity in the structural characterization, as the unit cell of crystalline inorganic materials is generally composed of few atoms bond by strong covalent bonds that are more difficult to damage, compared to weak intermolecular interactions.

Techniques based on electron beams require particular attention to avoid sample charging and damaging. High-resolution transmission electron microscopy (HR-TEM) enables the microstructural characterization of OSC materials with exceptional resolution by directly imaging individual polymer chains and determining their orientation.[182] A recently developed method based on the energy analysis of secondary electrons in a scanning electron microscopy (SEM) can combine the topography imaging capability with the mapping of localized molecular order in OSC polymers.[183]

Other viable options are represented by X-ray microscopy techniques, such as scanning transmission X-ray microscopy (STXM), but synchrotron radiation is needed because the photon energy must be tuned to select a core electron transition that corresponds to a transition dipole moment perpendicular to the structure of interest, that for OSC is e.g., the 1s → C=C π* transition, perpendicular to the plane of conjugated rings.[106] STXM was successfully applied to pentacene thin films by collecting each image with an X-ray exposure time of less than 10 ms per molecule, resulting in a negligible radiation damage.[184]

Conventional optical methods are limited by spatial resolution, but both OSC polymer[185] and small-molecule[186] systems characterized by sufficiently large domains can be successfully imaged via POM, even though, depending on the sample characteristics, the scattering of light in polycrystalline films can be an impeding factor. The necessary imaging conditions are realized when OSC cores or backbones are packed in such a way that the film exhibits dichroism and/or birefringence. Raman spectroscopy can thus be combined with POM to probe the molecular orientation of aligned OSC polymer films.[187]

Finally, scanning probe techniques, such as TSM and scanning near-field optical microscopy (SNOM), can probe microstructural properties with nanometric lateral resolution. TSM can only be applied for smooth, elastically compliant, and anisotropic crystalline films at relatively low RH (< 20%) for optimal contrast and on OSC surfaces that are sufficiently clean to maintain the sensitivity to the molecular orientation.[180]

The TSM contrast is less pronounced for relatively thick and rough films, although still visible as shown in Figure 1.4. SNOM is another alternative technique that exploits the near-field illumination by keeping the tip within one aperture length of the sample surface with a resolution (50–100 nm) set by the aperture size. Domain structure information regarding the local relative dichroism and dichroic orientation was obtained on spin-coated oligomeric OSC materials.[188]

2.4 Surface properties and composition

The properties of a material's surface are those which governs the nature of the interaction with the surrounding environment. These properties are also relatively easy to access because of their direct proximity to the probing tools, but the elusive nature of surfaces and the difficult spatial definition of a surface render the characterization of surfaces not always trivial. Contamination and amorphous layers are among the worst enemies of surfaces. For OSCs, the surface contamination is usually not a problem if the materials are vacuum processed. The issue of contamination much more critical for solution-processed films, where solvent residuals, impurities and amorphous material need to be avoided during processing as the techniques that can be used for post-processing removal usually deteriorate or destroy the active OSC film. Buried interfaces, which are more difficult to probe, are also object of the researcher's concern. More dramatically than surface properties (that mainly refer to the OSC/air interface), the interface properties control the behavior of the OSC material with respect to the other device components that may result in huge changes in device performance. The surface of OSCs is thus the primary access point for the non-destructive determination of many material properties (e.g., nanomechanics, composition, wettability).

In this section, the techniques that probe the properties of materials via its surface are briefly introduced and compared. Despite not being critical in the characterization of OSCs, these techniques are extremely useful for the optimization of the interface with other materials constituting the device components that must be integrated in the final device. The matching of surface properties of OSCs with metals, oxides and soft materials must go through an initial characterization of the isolated systems before the device assembling. By the end of this section, the strategic use of these techniques for the device optimization is outlined.

2.4.1 Nanomechanical characterization via AFM

The nanomechanical properties of a surface can be accessed via AFM. A qualitative assessment of the local mechanical inhomogeneity of the surface of materials is relatively easy to perform compared to a rigorous quantitative determination of physical parameters, such as the Young's modulus or the hardness. These properties require an accurate calibration and referencing to attain values comparable to those obtain with macroscopic stress and strain or indentation tests.

- Force volume: Force Volume (FV) imaging is the basic contact-mode technique for the determination of the nanomechanical properties of a surface via AFM. This technique combines the measurement of a force curve with topographic imaging and finally providing a height profile that corresponds to a user specified "trigger" force value for each pixel recorded. FV thus nearly simultaneously combines the information from topography and force curves into a single data set. This data set can be further processed by treating the tip-sample interaction with mathematical models returning semi-quantitative values for modulus, friction, adhesion and stiffness.
- Phase contrast imaging: During tapping mode AFM imaging, the phase shift of the cantilever oscillation is simultaneously measured, hence providing a phase contrast image. This signal corresponds to the phase lag between the driving force and cantilever response, and it is related to the viscoelastic properties of the sample and to the adhesion forces at the interface with the tip. For non-uniform samples, the phase contrast image indicates inhomogeneities in the nanomechanical properties of the surface that may result from a different sample composition.
- Nanoindentation: By using a diamond tip mounted on a stainless steel cantilever, the AFM can be used as a nanoindenter. Compared to the macroscopic indentation, AFM nanoindentation can probe the mechanical properties, such as the modulus or the hardness, of small volume samples at the nanoscale. The AFM is operated in contact mode by applying a user specified force for a defined amount of time before retracting the tip to image the depth and shape of the indentation. The topographic and force data is then analyzed to derive the nanomechanical properties of the surface.

Nanomechanical imaging was performed with a Bruker Dimension Icon setup operating in air in tapping or contact mode. The type of probe is specified with each experiment. For nanoindentation experiments, DNISP diamond tips are employed (tip stiffness: k = 225 N/m).

2.4.2 X-ray Photoelectron Spectroscopy (XPS)

X-ray Photoelectron Spectroscopy (XPS) is a surface-sensitive technique operating in ultra-high vacuum based on the photoelectric effect that is used to study the chemical composition of a solid surface (the sampling depth is around 5-10 nm), in the form of a thin film or powder, with a detection limit of around 0.1-1 at%. The photoelectrons from both deep and shallow levels are extracted from the surface of a sample by a soft X-ray beam and separated by an energy analyzer. The binding energy of the electrons is computed by subtracting the measured kinetic energy to the known energy of the X-ray photons. A spectrum reporting a quantity proportional to the electrons count as a function of the binding energy is then generated and the peaks associated with different elements analyzed.

Thanks to the wide availability of reference data for atomic sensitivity factors and binding energies (often provided by the instrument manufacturer), one can identify the elements present within the surface of a material and quantitatively determine its elemental composition. Additional information that can be derived by the XPS spectra regards the chemical state, the electronic structure and the density of states in the material. In fact, while the characteristic binding energy of the core electrons of each element can be found within a range of about ± 2 eV compared to the reference value for an atom forming only pure covalent bonds, this energy can be shifted if the atom is bound to other atoms with polar bonds. By knowing both the surface elemental composition and some additional chemical information about the sample, the XPS peaks of each element can be fitted to gain insight into the oxidation states and determine the relative fractions of each element associated with specific compounds or chemical species.

XPS spectra were collected at room temperature by using a ThermoScientific K-Alpha X-ray photoelectron spectrometer equipped with an Al X-ray source (1486.7 eV) at a working pressure of 10^{-8} -10^{-9} mbar. The spot of the wide elliptical X-ray beam was set at 400 μm. Survey spectra were recorded with a pass energy of 200 eV and with an

energy step of 1 eV. The spectra of the elements were recorded with a pass energy of 50 eV and an energy step of 0.1 eV.

2.4.3 Energy-Dispersive X-ray spectroscopy (EDX)

Energy-Dispersive X-ray spectroscopy (EDX) is a chemical analysis method that is usually coupled to an electron microscopy system to study the composition of a solid surface. This technique differs from XPS for the detected signal, which are X-rays instead of electrons, and by the much larger sampling depth (0.1-3 μm) arising from the higher penetration ability of X-rays. The detection limit is similar to that of XPS (0.1-1 at%), but an important part of the compositional information comes from the bulk of the material, hence dramatically reducing its surface sensitivity.

2.4.4 Water Contact Angle (CA)

Contact angle (CA) measurements represent a class of surface techniques that determine the angle of contact of a drop of liquid onto the surface of a solid, which is a measure of the wettability of a solid towards a liquid. Many different liquids can be used, but most of the experiments are performed with water. For this reason, the terms hydrophobic and hydrophilic are referred to a surface with poor wetting properties (if the measured contact angle is above 90°) or with good wetting properties (if the contact angle is below 90°), respectively.

2.4.5 Sum Frequency Generation (SFG)

SFG is a nonlinear optical technique that provides a signal only for non-centrosymmetric systems.[189] This technique can be implemented in the range of the infrared, making it a vibrational spectroscopy complementary to infrared and Raman. Differently from the other two more common techniques, SFG is an interface specific method, as it exploits the symmetry breaking that naturally occurs at an interface. With SFG, one can monitor, for example, the amount of water present at the interface between an oxide and an OSC by integrating the SFG signal corresponding to the O−H stretching mode (~ 3300 cm^{-1}).[190] Hence, SFG can be classified as one of the few experimental methods to access buried interfaces.

2.4.6 Surface properties and composition : technique comparison

The study of surface properties of OSC materials is somehow not as fundamental as the experimental methods that have been previously discussed. Most of the techniques

described here enable a fine determination of properties that well complement the electrical, electronic and structural characterization that is the base of organic electronics. Restricting the focus on the latter properties may be advantageous in the short and medium terms, but not all the experimental issues can be easily addressed with a reduced toolbox of techniques.

XPS, for example, may seem irrelevant techniques for the study of OSC, as the atomic composition of molecular compound is usually well-defined, but it provides significant information for OSC materials doping,[191] for chemical interactions at metal/OSC and organic/OSC interfaces[192] or for fractional composition in OSC blends.[193] When the sample is stable enough under electron beam, EDX can be combined with SEM and XPS to map the surface composition of samples covered with a layer as fragile as adventitious carbon contamination.[169] It would be quite challenging to assess the quality of OSC blends in the thin film if those compositional methods were not available.

The mismatch in the mechanical properties of OSC materials and traditional oxide substrates (such as SiO_2 and Al_2O_3) make a combination of them less suitable for micromechanical devices, but thanks to their soft mechanical character and the ability of some OSCs to exhibit a mixed conductivity, new promising fields such as organic bioelectronics are leading the future OSC research.[14] Still, micromechanical devices based on all plastic/organic materials hold great potential, but a better understanding of how the nanomechanical properties of OSC materials correlate with charge carrier mobility and morphology at the grain-scale and nanoscale is required.[194]

Water CA also represents a useful tool, especially when employed for quality check of SAM formation on metal and oxide surfaces. SAM are extremely important for two main reasons: (i) to change the surface wettability and enabling a fine tuning of surface properties for promoting optimal conditions for thin-film formation and (ii) to change the WF of electrodes for optimal charge injection. Alongside with the change of nanomechanical surface properties induced by the formation of a SAM, the variation in surface composition can be probed by XPS to give additional proof of the successful monolayer deposition.

2.5 Thin-film properties and topography

Thin films are by definition a layer of material with thickness ranging from one monolayer to several micrometers. During the process of dimensional shrinking of OSC

device size, controlling thin-film thickness is the basis for achieving device reproducibility. Each different thin-film fabrication method provides different ways of tuning the thickness and morphology which require a subsequent monitoring. OSCs are soft materials which exhibit an impressive variety of topographic features both at the nano- and microscale. A thin film of a crystalline small-molecule OSC has a complex topography arising from the step terraces, from regions of amorphous materials, from surface contaminants, from the crystalline domains and the relative grain boundaries. Similar features can be found in thin films of a polymer OSC, with increased complexity (in some cases) due to the more disordered nature of polymers that may yield alternating crystalline and amorphous regions in the same sample area. The experimental tools used to probe the surface and the bulk of thin films must be the least invasive possible to avoid the disruption of the weak intermolecular interactions that hold the material together.

In this section, the non-destructive techniques that are useful to characterize OSC thin films are presented with reference to the experimental thin-film properties (i.e., thickness, roughness and topography) that are the main object of investigation. The capability of the techniques discussed below is not limited to the measurement of those basic parameters but all of them find common ground within this context.

2.5.1 Atomic Force Microscopy (AFM)

Surface topography data can be collected via AFM by using different modes depending on the range of interactions involved in the measurement. The three main modes can be identified as contact, intermittent contact and non-contact modes. In contact mode, the interactions between the sample and the tip are measured by a continuous tracking of the displacement of the free end of the cantilever while the tip is in mechanical contact with the surface. In intermittent contact (tapping) mode, the cantilever is oscillated slightly below its resonance frequency and scanned across the surface while coming in close contact only intermittently. In non-contact mode, the cantilever is oscillated at slightly above its resonant frequency and scanned near the surface of the sample without contacting it.

One should choose the imaging mode alongside with the probe type depending on the sample characteristics, as the forces applied on the surface as well as shape and stiffness of the probe are crucial factors for optimal imaging. Depending on their purpose, tips are typically made of Si_3N_4 or Si and coated with Au, Pt/Ir or Al or left

uncoated. Here, I summarize the different probes that I have been using for the imaging of organic materials in devices divided by their mechanical property and the most suitable applications.

Probe name	Radius	f	k (N/m)	Mode	Purpose	Sample
DNISP	40 nm	50 kHz	225	C	Indentation	all
ScanAsyst-AIR	2-12 nm	70 kHz	0.4	T	Topography	OSC
SCM-PIC-V2	25 nm	10 kHz	0.1	C	C-AFM	OSC/Me/Ox
SCM-PIT-V2	25 nm	75 kHz	3	T	KPFM	OSC/Me/Ox
SNL-10 A	2-12 nm	70 kHz	0.35	C	TSM	OSC
SNL-10 D	2-12 nm	18 kHz	0.06	C	TSM	OSC
TESPA-V2	7 nm	320 kHz	37	T	Topography	Me/Ox

Table 2.1: List of AFM probes with properties and uses. The nominal value of the property of each probe is reported. The preferred (but not unique) imaging mode is indicated: T = tapping, C = contact. Suggested purposes and samples (Me = metal, Ox = oxide) are also reported.

For reliable measurements of additional AFM data such as electrical current, surface potential, friction force, etc. the surface topography must be devoid of significant artifacts. Hence, the choice of the correct probe is critical for each type of sample and imaging purpose. The aim of this section is to outline the reasons to choose a probe over another depending on the application.

For simple topography, vertical and lateral resolution as well as imaging stability with minimal force applied on the sample are prioritized. TESPA-V2 is a common choice for tapping mode, as it can be used with almost any substrate. However, this tip is very sensitive to surface contamination and tends to wear easily with soft samples due to the relatively high forces applied (its force constant is among the highest in AFM probes). For this reason, it is a very useful probe to nanopattern thin films via nanoscratching: setting the amplitude setpoint to 0 in tapping mode with this tip enables the scratching of ultrathin films, for e.g., the measurement of the thickness. TESPA-V2 has several advantages when imaging samples composed of different materials as the optimized imaging parameters for stiff samples, such as metal or oxides, work as well with soft surfaces. In addition, it is characterized by a rapid response in correspondence of steep features, which guarantees a good quality when imaging the surface of whole devices including the electrode, the OSC film and the dielectric. This tip can also be

conveniently used for phase contrast imaging that can be achieved by simple adjustment of the amplitude setpoint at values slightly below the minimum setpoint for tapping mode imaging. However, despite the large versatility of TESPA-V2, an optimal, more stable and durable imaging of isolated metal/oxide/OSC surfaces is achieved with other probes.

For instance, for the soft OSC materials a less stiff probe such as the ScanAsyst-AIR probe is more suitable due to the reduced forces applied on the surface. ScanAsyst probes are optimized for a proprietary Bruker mode that collects a force curve at every pixel in the image that is used as feedback signal. The software automatically controls the force applied on the sample by reducing the penetration depth and hence minimizing the interaction with the surface. On one side, this control is very helpful because only minimum operator input is required, but on the other side it is difficult to correct any imaging artifacts that the software does not perceive. Moreover, despite the huge potential of these proprietary Bruker modes (that can be also used to measure conductive AFM, KPFM and nanomechanical properties) they are still not very diffuse in the research community.

Some techniques, such as TSM, require a stable and continuous contact of the tip with the sample, as the friction forces must be present during imaging. Henceforth, an optimal contact-mode imaging must be achieved on the sample of interest. The SNL-10 series, having 4 tips with variable stiffness values < 0.35 N/m is a possible choice for TSM, as the applied force can be easily modulated with both the force setpoint and by changing the tip. The tip radius is quite low thus providing a good lateral resolution on soft OSC without significant thin-film damage or scratching.

For AFM modes involving the measurement of electrical properties, a conductive tip is usually required meaning that the inertness to contamination of Si_3N_4 or Si must be sacrificed to attain low resistivity with a metal covering, typically Pt/Ir or Au. Those metal covered tip possess larger tip radius and are more easily damaged or contaminated during imaging. Amplitude modulation KPFM imaging consists in two imaging steps: a height profile in tapping mode and a surface potential profile collected in lift mode. SCM-PIT-V2 has a sufficiently high stiffness to perform the tapping mode step and its Pt/Ir coating enables the detection of the surface potential. If this tip is used for contact mode C-AFM on OSC samples, the applied force is often too high to avoid sample damaging, consequently, a less stiff probe such as SCM-PIC-V2 is a better

choice. None of the two probes guarantees the same resolution offered by the probes previously described, but they represent a good compromise for having a conductive probe.

The main useful parameters that were obtained via AFM topography are the following:

- Thickness: after mechanically scratching the region of interest with a needle or with the AFM tip, the area of interest is scanned. For an easy image analysis, it is very important to align the scratch perpendicularly to the scanning direction and leave enough space for a reference plane. After proper plane subtraction, a mediated height profile (width of several pixels, to average both the reference plane and the film) is traced and the thickness value is obtained from the offset between baseline and film surface. For a statistically relevant thickness value, the procedure is repeated in different regions of the sample.
- Roughness: the surface roughness quantifies the amplitude of deviations of the real surface profile from an ideally flat profile. For roughness measurements, surface topography is directly imaged at the selected sample region within a defined scanning area. As roughness values depend on the chosen surface area, it is important to compare values obtained from identical area sizes, or to consider a renormalization factor before comparing. The roughness can be computed from a single AFM image as the average deviation from the medium plane (roughness average) or as the standard deviation (root mean square roughness, or R_{RMS}). Of the two, R_{RMS} is more sensitive to large deviations, as a single large peak or dip increases the RMS value more than the arithmetic mean value. The relative difference between the two is thus an indication of the inhomogeneity of the surface.
- Terrace step height: crystalline OSC films often possess a terraced topography and the terrace step height may represent a quantity to compare with the interlayer spacing obtained via XRD or to simply discriminate one material from another within a complex device. The most challenging aspects in terrace step height determination regard the correctness of the baseline flattening procedures and the uniformity and cleanliness of the exposed terrace surface. Once a sufficiently large terrace is found, the baseline is corrected (similarly to thickness determination) and the distance between two terraces is recorded. Factors that influence the measured values are the presence of a contamination layer, the

occurrence of different crystalline phases or an interfacial phase different from the bulk, a non-optimal preprocessing terrace levelling.

AFM experiments were performed on a Bruker Dimension Icon setup where not differently specified.

2.5.2 Profilometry

While not being a multidimensional mapping tool, profilometer is an alternative to AFM when the characterization of the height profile of features above 100-200 nm is needed. If steep height variations (such as those characterizing nanostructured surfaces done by lithography) are imaged via AFM, it is very easy to damage the tip or stress the piezo actuators. Note here that soft samples are not recommended for profilometer measurements as the poor control on the stylus force can easily damage the sample. The other advantages reside on the larger scan range on the order of cm (typically limited to less than 100 x 100 um^2 for AFM). Profilometer is mainly used in the semiconductor industry to determine thickness or roughness values over large areas as well as surface deformation or defects during quality checks.

- Thickness/roughness: In a similar way to AFM, the determination of the thin-film thickness/roughness is limited to the region probed by the stylus, hence information about the uniformity of the thin film must be obtained via optical microscopy or via sampling over different regions.

A KLA Tencor Alpha-Step IQ surface profiler was employed when thickness values above 100 nm were to be determined.

2.5.3 Ellipsometry

Ellipsometry is an analytical technique that works with light of wavelengths in the range of near UV and near IR. This technique can be used for the determination of the dielectrical properties of thin films by measuring the change of polarization of a beam of radiation transmitted or reflected by the material. Ellipsometry data is subject to fitting, similarly to EIS spectroscopy, as an analytical model is necessary to quantify the various parameters related to the property of the thin film. Among the material properties that it is possible to determine, thickness and dielectric function of the thin film are basic fitting parameters, but additional information about e.g., composition, roughness, crystallinity, doping concentration and electrical conductivity can also be

extracted by using variable angle spectroscopic ellipsometer (VASE) configuration.[195] This is another of the techniques that can be classified among the ones that can access experimental information about buried interfaces. Multi-layered films can also be analyzed by VASE consequently adding some complexity to the overall fitting procedure which requires previous knowledge of some material parameters to reduce the degrees of freedom.

2.5.4 Thin-film properties: technique comparison

The last section covering the experimental techniques regards the properties of OSC thin films that are not directly related to charge transport but provide a useful characterization contour that serves as a support to the previously discussed techniques. Thin film imaging and topography visualization is usually done in OSC materials via AFM, but also SEM can be used for the same purpose, if either very careful optimization of the electron flux and energy is done to avoid charging and damaging, or if a very thin Au coating is deposited before imaging.

Simple geometrical parameters can significantly change the response of devices. Ionic conductivity, for example, is found to scale proportionally with thickness,[196] a parameter can be determined punctually with AFM or profilometer or averaged over larger areas with VASE or XRR. The roughness of the substrate, as well, can influence the morphology of the thin film resulting in a larger density of grain boundaries in the OSC layer, consequently affecting the performance of OFETs.[197] Note here that XRR and VASE are two techniques that give complementary information and are both particularly suitable to study OSC thin films. It is quite common for models to require the dielectric function of the material as an input, but this information is often difficult to find in the literature or to determine from EIS measurements. XRR and VASE are both useful in this sense and can provide accurate data as long as the film is thicker than about 5 nm.[198]

3 Humidity Sensing based on Organic Semiconductors

3.1 Sensors

Sensors are devices that integrate the essence of external stimuli perception by capturing the changes in the surrounding environment. Life evolved to survive thanks to sensors that then inspired man-made devices mimicking the same functions observed in nature. Humans developed artificial sensor capable of transducing stimuli to a directly readable output. Artificial sensors are not only used by scientists to perform measurements during the experiments but are also widespread objects that improve our quality of life, both in our homes and in our offices. Sensors are everywhere: they can serve as safety detectors, thermometers and barometers help us to forecast the weather, the position, fuel and battery level sensors are fundamental parts of a vehicle, the camera of our phones is an optical sensor as well as the touchscreen itself is a capacitive sensor, just to name a few examples. In the need of information, all of these sensing devices serve their purpose of transducing a signal or stimuli. The transducing process involves two steps: (i) translating the external stimuli to a signal that is recorded by the device and (ii) quickly transmitting this signal to an output that can be easily read or interpreted by the operator. Artificial sensors can be used to quantify or to qualitatively assess information that might be inaccessible to our natural senses or that might be impossible to record with the necessary speed and accuracy that sensors can provide. Most sensing devices of today are integrated to electrical circuits; hence the output is preferentially transmitted via electrical signals. In general, sensors can potentially generate outputs in different forms such as optical, magnetic or mechanical and are referred to as "transducers". The more practical way the humans found based on the current technologies is to transduce the signals to a final electrical output. For the sake of example, electrical outputs are suitable for further computational processing of the data of for the subsequent visualization of a numerical value on a display, but other times a simple visual output, such as the change of color of a litmus paper, is chosen for practical reasons. The complex sensors that we use today are basically a system of multiple transducers that finally convert the signal to an electrical output.

In this chapter, an introduction on the humidity responsivity of thin-film materials that are currently being investigated will be presented. Organic small molecule materials will be then compared to highlight the different structural design strategies than can be adopted to confer the humidity sensitive properties to organic scaffolds of reduced

dimensions. This introductory section will, in fact, contextualize the present Ph.D. work on the sensing of humidity tuned by mixed electron/proton conduction exhibited by an organic small molecule. The detailed methods and characterization of humidity responsive chemiresistors based on a novel [1]benzothieno[3,2-b][1]-benzothiophene (BTBT) derivative equipped with hydrophilic oligoethylene glycol (OEG) lateral chains (OEG-BTBT) will be then provided. The scientific advances reported were published in early 2022,[190] and here reformulated to give a more comprehensive and linear story of the development of this humidity sensing system.

3.2 Humidity Responsive Thin-Film Materials and Devices

The aim of this section is to overview the materials for thin-film devices that have received the attention of researchers for humidity responsive applications. A brief introduction on the variety of different materials that can be used to sense the environmental humidity is first provided, before discussing in detail the state-of-the-art science behind humidity sensing with small organic molecules. Each of these different materials exemplify one particular aspect in the design of humidity sensitive materials. Low-dimensional materials, such as 0D (metallic nanoparticles, fullerene, etc.), 1D (carbon nanotubes, supramolecular fibers, etc.) and 2D (graphene and related materials), exhibit high surface-to-volume ratios and properties which are extremely susceptible to environmental changes, thus they represent ideal scaffolds as sensory materials. Their interaction with water molecule, occurring via recognition events through dipole-dipole interactions, can be controlled when the low-dimensional scaffold exposes hydrophilic groups, which can be grafted via chemical functionalization. This has been the case of 2D materials like graphene and transition metal dichalcogenides (TMDs). The latter, in view of their semiconducting nature, can be integrated in FET type of sensing devices. More precisely, TMDs are typically n-type semiconductors with electrical characteristics such as mobility and threshold voltage that are severely influenced by the RH.

Given that all hydrophilic components in the device can interact preferentially with water molecules via dipole-dipole interactions, a significant contribution can be expected to be originated from the SiO_2 substrate, which can exist in different forms including glass, porous silica or a thermally grown/native SiO_2 layer on a Si wafer. SiO_2 substrate can be chemically functionalized or treated with different physical inputs (e.g., ozone) to adjust such dipole-dipole interactions, thereby tuning the device response. When

investigating the performance of new materials for humidity-sensing applications, the role played by the substrate/active material interface is often neglected in the literature. Since thin-film devices are frequently supported on SiO_2 substrates, which possess an inherent moisture sensitivity,[199] it is a good practice to record the response of the bare substrate alongside with the characterization of the device, as thin-film sensors based on bare SiO_2 are known since decades.[200] The humidity sensing papers cited in Section 3.2, are conveniently summarized in Table 3.1 in Section 3.3.4.

3.2.1 Graphene-based Materials

Graphene is a 2D material that consists of an individual atomic plane of carbon atoms that are all sp^2 hybridized and are arranged in a hexagonal lattice, as if one single layer was isolated from graphite. When this material is free of defects, it exhibits excellent mechanical, thermal and electrical properties,[201] but it is very challenging to process. Hence, researchers have developed many different processing and production methods that can be easily scalable to an industrial level, such as the synthesis of graphene oxide (GO).[202] The advantage of graphene-based materials for humidity sensing is that both the pristine material, whose single-layer properties are easily affected by the surrounding environment, and the defective material, whose structural defects and of the terminal chemical groups are prone to interact with water molecules, made graphene-based humidity sensors an attractive field of research.[203]

When electric current or resistance is the output physical property of the sensor, it is referred to as "resistive-type". Yao et al.[204] studied the effect of water adsorption on the electrical properties of GO devices fabricated on Au interdigitated electrodes (IDEs) on 300 nm SiO_2 by both AC and DC methods. They showed that the electrical current in GO films is humidity responsive and the increased response at high RH is due to an enhanced ionic conductivity. Rathi et al.[205] followed the lattice doping approach by designing Li-doped and B-doped GO resistive-type humidity sensors, confirming that the presence of more water molecules increases the ion conductivity of the materials. The li-doped devices achieved a resistance change of almost 3 orders of magnitude over the RH range 11−97%.

When, instead, capacitance is the output physical property of the sensor, it is referred to as "capacitive-type". Bi et al.[206] fabricated a microscale capacitive GO-based humidity sensor increasing its capacitance by a factor 400 in the range 15–95% RH and with response times in the order of tens of seconds. Teradal et al.[207] developed

capacitive sensing devices based on a chemically functionalized porous GO material. The different polarity of the molecular units that reacted with the GO defects promoted the adsorption of different types of vapor molecules, consequently modulating the device selectivity among polar and non-polar species.

GO-based sensors, however, typically suffer from important drawbacks such as slow response and recovery. To address this issue, reduced GO devices were devised by Anichini et al.[208] who managed to overcome the intrinsic hydrophobic nature of this material by a simple chemical modification with hydrophilic moieties, i.e., triethylene glycol chains. This approach was then translated to organic electronics by synthesizing OEG-BTBT which is the core molecule of this thesis chapter.

3.2.2 TMDC-based Materials

TMDC materials are atomically thin 2D materials of the type MX_2, where M is a transition-metal element and X is a chalcogen element. The typical structure of a monolayer consists of one layer of metal atoms that is sandwiched between two layers of chalcogen atoms. Molybdenum disulfide, MoS2 is the prototypical TMDC material, whose optoelectronic properties have been discovered only recently,[209] compared to its long historical use as a lubricant. Being a semiconducting material rich in structural defects, its properties can be tuned in functional electrical devices.[210] Due to its ability of detection of a variety of analytes at room temperature, MoS_2 has been studied as a possible active material for miniaturized gas sensing at room temperature, with several other advantages as a high specific surface area and its compatibility with emerging flexible devices.[211]

MoS_2 devices can operate as field-effect transistors with humidity sensing function. In fact, TMDC materials can easily reach mobilities above 10^2 cm^2 V^{-1} s^{-1} while also being particularly sensitive to moisture.[212] This phenomenon can be directly exploited by utilizing the most sensitive form of the material, that is a large-area, uniform single-layer MoS_2, and testing the transistor performance at different RH. Zhao et al.[213] observed a shift in the threshold voltage of the device by reversibly changing the RH between 0% and 35% so that the device resistance changed by a factor higher than 10^4 at 35% RH. Of course, the limited RH range in which the devices are effectively operational is quite restrictive but it proves how the transistor characteristics of field-effect responsive material can abruptly change by a variation in RH. The factors that can strongly influence the performance of such devices are the number of MoS_2 layers

and the gate bias, as found by Yang et al.[214] In their experiment, the on-state current of the tri-layer MoS_2 transistor was found to be heavily dependent on the RH, while for the six-layer MoS_2 transistor the on-state current remained nearly unchanged as a function of RH, indicating the importance of the number of MoS_2 layers. Another investigation was performed by Late et al.[215] who compared the humidity sensing performance of two-layer and five-layer MoS_2 devices, but reported contrasting results due to a lack of control of the gate voltage, further confirming the importance of the transistor characterization when a humidity sensing device is based on field-effect responsive materials.

3.2.3 Self-assembly in Humidity Sensing

OSC molecules self-organize into ordered supramolecular structures at the solid state by forming weak non-covalent bonds. OEG-BTBT, an OSC material which self-assembles into 2D-layered films will be the main object of focus in the whole chapter. In this section, instead, we introduce the reader to the possible approaches for achieving organic 1D structures for humidity sensing[216–218] and how to eventually exploit multidimensionality in sensing.[219]

One molecular design strategy consists in the coupling of two large electroactive π-conjugated donor-acceptor cores into an amphiphilic dyad.[216] An ultrasensitive system of 1D fibers can be obtained by self-assembly on surface this dyad. Its molecular structure can be seen as an oligothiophene (OT) backbone, functionalized with hydrophobic chains, and a perylenediimide moiety, functionalized with hydrophilic chains, connected by a conformationally rigid ethynylene space. The specific interaction of functional groups having similar chemical properties within the molecular structure gives rise to a sub-nm phase segregation between hydrophobic and hydrophilic moieties resulting in a high degree of order at the supramolecular level. The coating of these micrometric fibers on the SiO_2 substrate is characterized a partial coverage of both the Au IDEs and the oxide that provide a great interaction with water at the applied voltage of 5V, leading to a change of the current signal by seven orders of magnitude and a state-of-the-art response speed of 26 ms.

Squillaci et al. also exploited a similar hierarchical self-organization strategy by devising a naphthalenediimide (NDI) derivative decorated with aminoacidic groups.[217] The attachment of tyrosine moieties to the imide N atoms of the conjugated core are known to be critical for the self-assembly behavior, leading to a consequent variation of the

OSC material properties, such as the charge carrier mobility. The self-assembly relies on the interaction of the carboxylic acid groups capable of forming H-bonds and on the competitive π-π stacking of both the cores and the phenyl groups from the tyrosine. In this case, the uniform coverage offered by the tightly packed tubular 1D structures, displaying a high aspect ratio (width of about 40 nm and length of several μm), results in the increase of the n-type mobility to a maximum of 10^{-3} cm^2 V^{-1} s^{-1} at 50% RH due to a threshold voltage shift similar to what presented in Section 3.2.2. The source-drain voltage in these devices operating at environmental humidity is kept below 2 V while the gate voltage is swept between ± 60 V, reaching currents of hundreds of μA in the conductive channel.

Another great example of self-assembly control via weak non-covalent interactions in OSC material is that of a symmetric OT bearing OEG side chains.[218] The molecular organization is purely driven by the π–π stacking between the conjugated backbones, opposed to the interaction between OEG side chains, and occurs directly in solution, thus offering a major opportunity for tuning the properties of the fiber before deposition. The change in current response observed in 2-terminal devices at a low 1 V source-drain bias is, in this case, only limited to a factor 10^2 in the 15−90% RH range, probably due to the reduced SiO_2 substrate coverage of the deposited fibers.

A final example, exploiting a similar self-assembly in solution prior to deposition, regards the formation of 3D porous networks of Au nanoparticles that were chemically interconnected by dithiolated OEG chains.[219] By monitoring optical plasmonic properties of the nanoparticle suspension, the cross-link reaction was quantitatively followed, thus enabling a precise evaluation over the reaction process. Using OEG linkers of different molecular length (4 and 6 ethylene glycol chains) the sensitivity of the nanoparticle 3D network could be modulated by the different swelling behavior of the hydrophilic groups.

3.3 Engineering of e^-/H^+ Transport for Humidity Sensing

In this section, a novel BTBT derivative equipped with hydrophilic OEG side chains (OEG-BTBT was synthesized and integrated as an active material in humidity sensitive chemiresistors. The development of systems that are capable of responding to environmental changes, such as RH, requires designing and assembling highly sensitive and efficiently transducing materials. Such a difficult challenge can be only mastered by the disentanglement of the role played by each device component. In this way, a

high performance responsive system can be achieved by optimizing the synergistic contribution of all functional elements. OEG-BTBT humidity sensitive chemiresistors can electrically transduce subtle changes in ambient RH with high current ratios (> 10^4) at low bias voltages (2 V), thus reaching a state-of-the-art performance.

To elucidate the role of each device constituent (active material, electrodes, substrate and interfaces) a multiscale structural, spectroscopical, and electrical characterization was performed. At the molecular scale, the BTBT core promotes the self-assembly of (semi)conducting crystalline thin films, while the OEG side chains are prone to adsorb ambient moisture. In fact, these chains act as hotspots for H-bonding with atmospheric water molecules that can locally dissociate when a bias voltage is applied, resulting in a mixed electronic/protonic long-range conduction throughout the film. Water molecules can then access the humidity-sensitive sites of the SiO_2 substrate surface thanks to the structural defects within the film and to the peculiar orientation of OEG-BTBT molecules at the interface with the substrate, whose hydrophilicity can be tuned for an improved device response. A synergistic chemical engineering of materials and interfaces is thus achieved and it is found to be key for designing highly sensitive humidity-responsive electrical devices whose mechanism relies on the interplay of electron and proton transport.

The relevance of this approach relies on the widespread use of SiO_2 as a device substrate whose hygroscopic properties can be tuned a priori before the deposition of the active material. For an effective exploitation of the synergistic effect, it is very important for the active material to be a not too good electrical conductor nor too good ionic conductor, as this cooperative effect might become secondary if other transport processes are dominant. Hence, a balance of these two properties in mixed ionic-electronic conductors is desirable to gain advantage from this synergy.

3.3.1 Relevance of Humidity-Responsive Materials

The development of humidity-responsive materials and technologies has accordingly experienced a rapid expansion over the past few years.[220,221] Applications typically include sensors for humidity monitoring and humidity-driven actuators.[220] Materials and systems designed to smartly respond to humidity changes frequently undergo a modification of their size (viz. swelling or shrinking) due to of chemical/physical processes triggered by water uptake or release via evaporation.[220] Very frequently though, electrical control or readout are extrinsic elements to such materials and

systems, being implemented only a posteriori.[220] On the other hand, some other technologies are designed to display high sensitivity in their electrical response to humidity changes as a result of electrical processes (ionic or electronic).[222] Importantly, the direct electrical transduction enables facile device integration with other electronic components to develop advanced applications.[221]

Humidity-responsive materials and devices must be rationally designed both to maximize physical interactions with atmospheric water molecules and to efficiently translate such interactions into useful electrical responses. Humidity-responsiveness can be granted to organic, inorganic, and hybrid materials via *ad hoc* synthesis of functional systems decorated with appropriate chemical groups.[222] Functional humidity-sensitive moieties, which act as active sites for interactions with atmospheric water molecules, include hydroxyl, carboxyl, and nitro groups, quaternary ammonium, sulfonate, or phosphonium salts as well as vinyl alcohol and ethylene glycol units.[223] Electrical transduction occurs by exploiting the ability of such functionalized materials to transport or accumulate charges, electronic or ionic species, whose behavior is influenced by their interaction with atmospheric water molecules. In this framework, humidity-responsive materials and devices can be designed and optimized to feature high performance via the in-depth understanding of the influence of the adsorbed water on such electronic/ionic conduction processes.

3.3.2 OEG-BTBT Chemiresistors

The as-synthesized OEG-BTBT molecules (Figure 1.2a) were deposited as thin films onto SiO_2 test patterns from OEG-BTBT suspensions at concentrations ranging from 1 to 30 mg/mL, depending on the desired film thickness. OEG-BTBT suspensions were freshly prepared by dissolving the synthesized powder in chloroform ($CHCl_3$) prior to use. The OEG-BTBT/$CHCl_3$ mixtures are regarded as suspensions, and not solutions, as the Tyndall effect was observed by shining a red laser light in a transparent vial containing the mixture. OEG-BTBT suspensions at were spin-casted on both bottom-contact (BC) and top-contact (TC) SiO_2 test patterns at 2000 rpm, 2500 rpm/s for 30 s. BC test patterns having 30-nm thick Au IDEs onto a 10-nm-thick indium-tin oxide (ITO) adhesive layer with a channel length (L) of 5 μm and a total width (W) of 10 mm were purchased from the Fraunhofer Institute for Photonic Microsystems, IPMS, Dresden, Germany. These samples, after sonication in acetone (5 min) and isopropanol (5 min) are referred to as "bare SiO_2".

The geometry of the fabricated OEG-BTBT chemiresistors is shown in Figure 3.1a. The molecular film cast onto SiO_2 from 10 mg/mL suspensions exhibits an average thickness of 90 nm. The surface topography of OEG-BTBT crystalline thin films shows regions with heights above 100 nm, similar to lamellar structures, organized in small domains, as shown in Figure 3.1b. This kind of morphology is found in other thienoacenes thin films.[224] The root-mean-square roughness (R_{RMS}) of the films is about 46 nm (calculated from a 25 μm × 25 μm area). OEG-BTBT solutions spin casted from chloroform form continuous films both on SiO_2 and Au. This deposition method guarantees a responsive film with the homogeneous morphological characteristics over channel and electrode surfaces. This film continuity can be observed in the SEM image reported in Figure 3.2a. To further analyze the structural properties of the films, thinner films of a nominal thickness of 6 nm were imaged (see Figure 3.2b). In this way, the limitations related to the relatively moderate roughness of 90-nm-thick films are avoided. Here, we note that the interfacial layer is characterized by the platelet morphology and terraced topography that is commonly observed for BTBT derivatives.

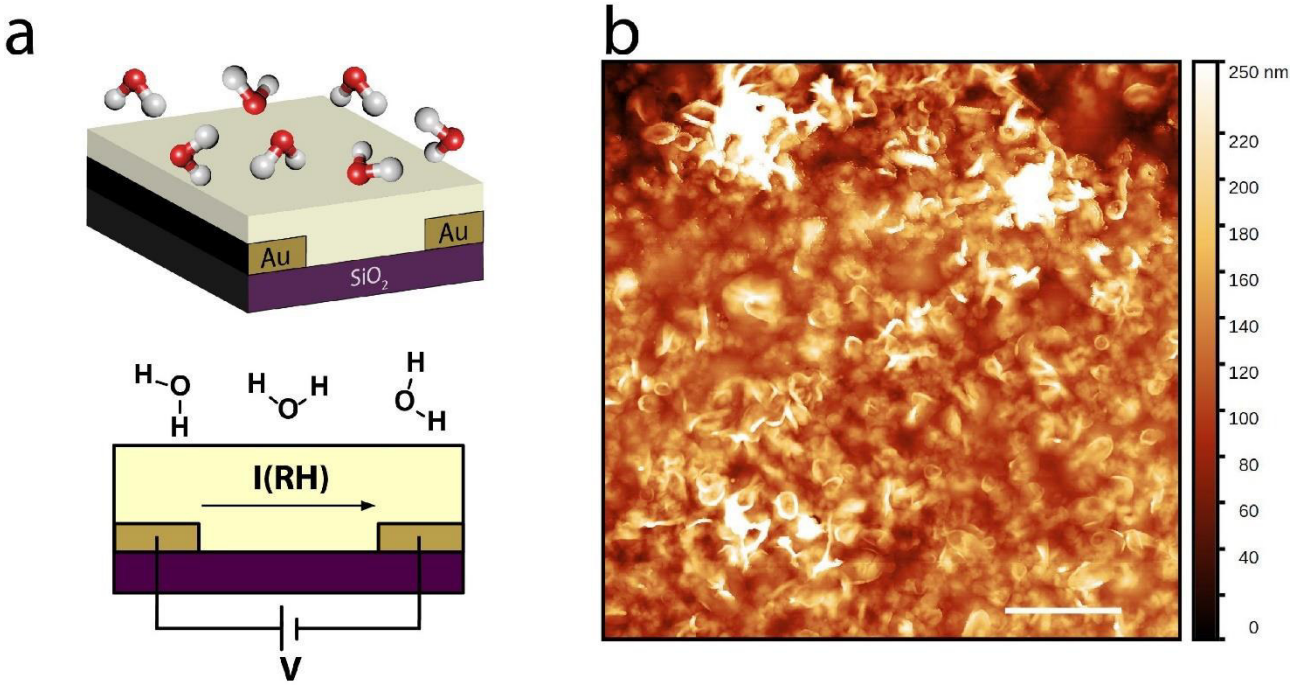

Figure 3.1: Sketch of the OEG-BTBT humidity-responsive chemiresistor and AFM topography of the OEG-BTBT thin film. (a) The RH-sensitive device current I(RH) is recorded upon application of a constant DC bias (V). (b) AFM height image of the spin-cast OEG-BTBT film surface deposited on SiO_2. R_{RMS}: 46 nm, lateral scale bar: 5 μm.

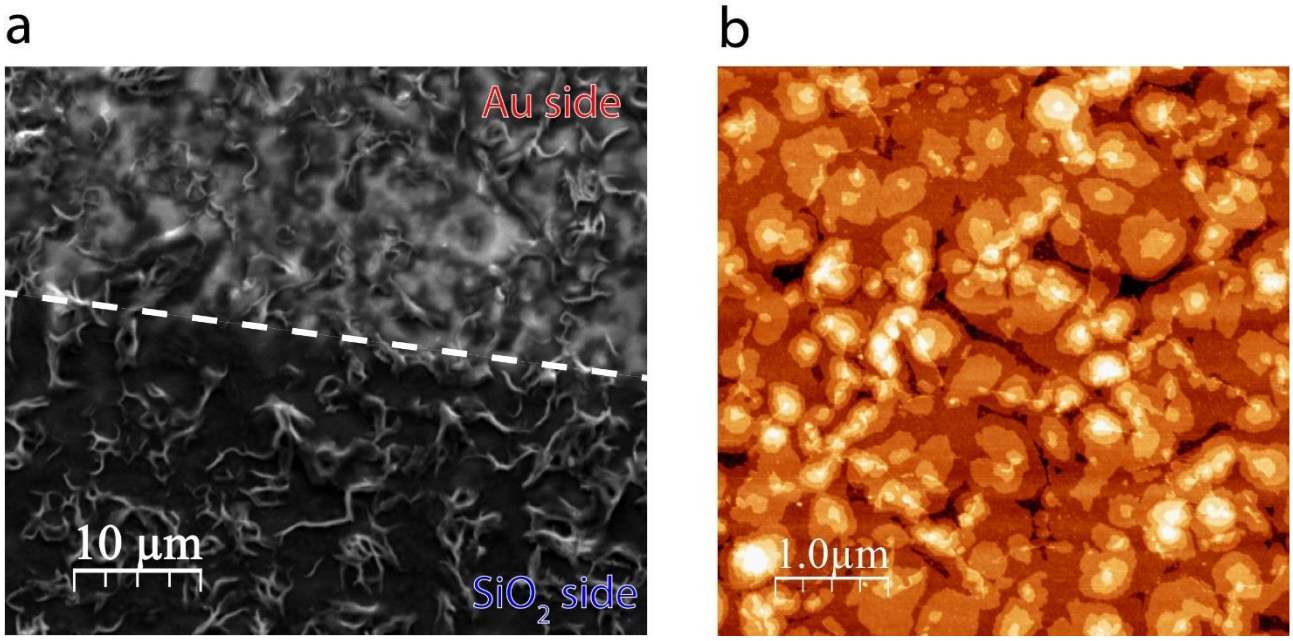

Figure 3.2: SEM and AFM imaging of an OEG-BTBT film. (a) SEM imaging on bottom contact (BC) Au test patterns used for the electrical measurements. Film thickness: 90 nm. (b) AFM height image of the spin-cast OEG-BTBT film surface deposited on SiO_2. Z-scale: 11 nm, R_{RMS}: 1.7 nm; nominal film thickness: 6 nm. Adapted with permission from reference.[190] Copyright © 2022 American Chemical Society.

3.3.3 Electrical Characterization of OEG-BTBT/SiO_2 Chemiresistors

The humidity response of OEG-BTBT chemiresistors was measured at a 2 V bias step while recording the device current I(RH) for an interval of 10 s at different levels of RH. Organic electronic devices that operated under a prolonged application of a voltage bias are often affected by current-drifting problems,[225] especially in the presence of elevated humidity,[226] hence, the application of pulsed measurements is useful to avoid these issues. It is also much more energetically convenient for sensing applications. By applying a 2 V bias to the chemiresistors at different RH levels, a short initial capacitive transient current is observed,[227] followed by a near steady-state response (Figure 3.3a). As displayed in Figure 3.3a, I(t) curves are noisy for RH below 30% and the signal detection limit (DL), of ca. 5 pA, is reached at RH ≈ 10% in our experimental setup. The current increases monotonically with RH. The device I–V characteristics (reverse voltage sweep) are also sensitive to the change in RH and a marked capacitive hysteresis, increasing with RH, is observed within a ± 2 V window (Figure 3.3b). This hysteresis also increases in magnitude when the voltage scan rate is increased from 440 to 2410 mV/s, indicating a strong capacitive contribution in the device response. This hysteresis is probably related to charge trapping effects concerning the water present at the interface with proton blocking Au electrodes or the dielectric.[228]

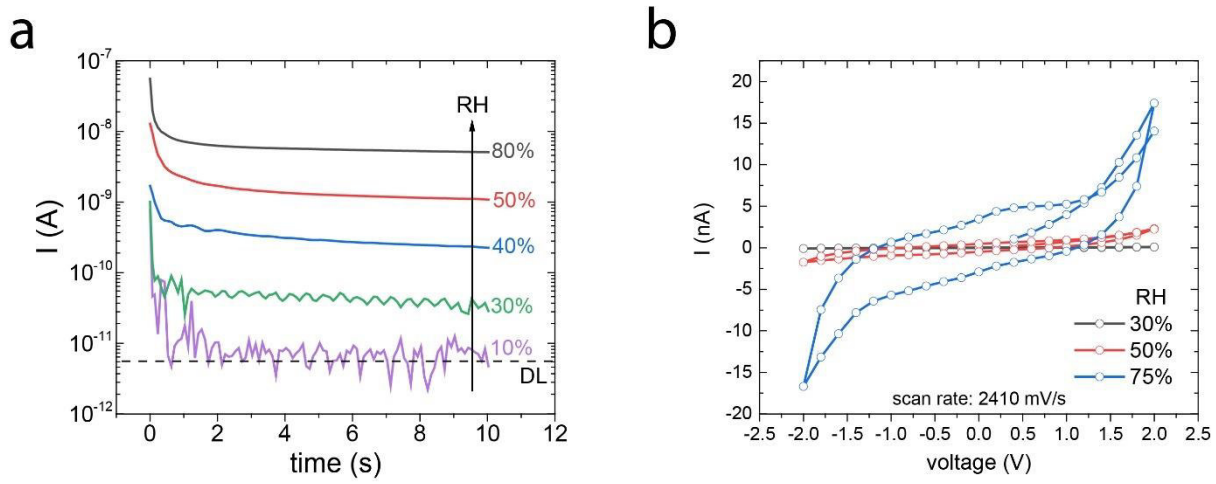

Figure 3.3: Electrical performance of RH-responsive OEG-BTBT/SiO_2 chemiresistors in BC configuration. The devices were fabricated onto bare SiO_2 substrates. Device channel length: L = 5 μm. (a) chronoamperometric response of devices at different RH levels. The current detection limit (DL) is indicated with a dashed black line. (b) I−V curves measured at different RH at fast sweep rates (2410 mV/s). Reprinted with permission from reference.[190] Copyright © 2022 American Chemical Society.

3.3.3.1 Device response and recovery times

From the $I_{DS}(t)$ response of chemiresistor under variable RH conditions one can estimate the device response (τ_g) and recovery (τ_d) time constants. OEG-BTBT devices are capable to quickly and reversibly react to short (Figure 3.4a) and long (Figure 3.4b) intermittent RH changes obtained via a pulsed flow of humid air directed on the sample surface. With the assistance of a commercial electrovalve (U.S. Solid 12 V DC ¼" G Solenoid Valve), the devices have been exposed to a train of humid-air pulses of humid air. I(t) was then measured at a constant 2 V bias. Rough estimates for τ_g and τ_d were obtained from Figure 3.4a. These parameters were obtained as the difference between the initial and final values of the growth and decay of I(t). While τ_g was determined from the onset of I(t) increase and the maximum I(t) value, τ_d is related to the start of I(t) decay and the subsequent stabilization of the current, as illustrated in the inset of Figure 3.4a. With this rough procedure, the response time τ_g is estimated to be ~ 300 ms, while the device recovery time τ_d is ~ 1 s.

For a more accurate and reliable determination of the chemiresistor response dynamics, the time constants have also been estimated from I(t) curves obtained upon a prolonged exposure of the sample to the flux of humid air (Figure 3.4b). A non-linear growth equation (Equation 3.1) can be employed to fit both the growth and the decay of I(t) to estimate the τ values. Equation 3.1 is expressed as a current (I_0) and time (t_0) offsets,

a pre-exponential factor (A) that differentiate between for growth (−) and decay (+) behavior, and, finally, the time constant (τ).

$$\boldsymbol{I = I_0 + A \cdot e^{-\frac{t-t_0}{\tau}}} \qquad \text{(Equation 3.1)}$$

The time constants for OEG-BTBT devices employing TC and BC electrode configurations are: $\tau_{g,TC}$ ~ 400 ms, $\tau_{d,TC}$ ~ 150 ms, $\tau_{g,BC}$ ~ 500 ms, $\tau_{d,BC}$ ~ 200 ms. These values are calculated as the average of least three τ values obtained from the fitting of individual current vs time pulse profiles. Devices possessing a reversible response and recovery behavior that occurs at comparable τ values are fast enough for most humidity sensing applications.

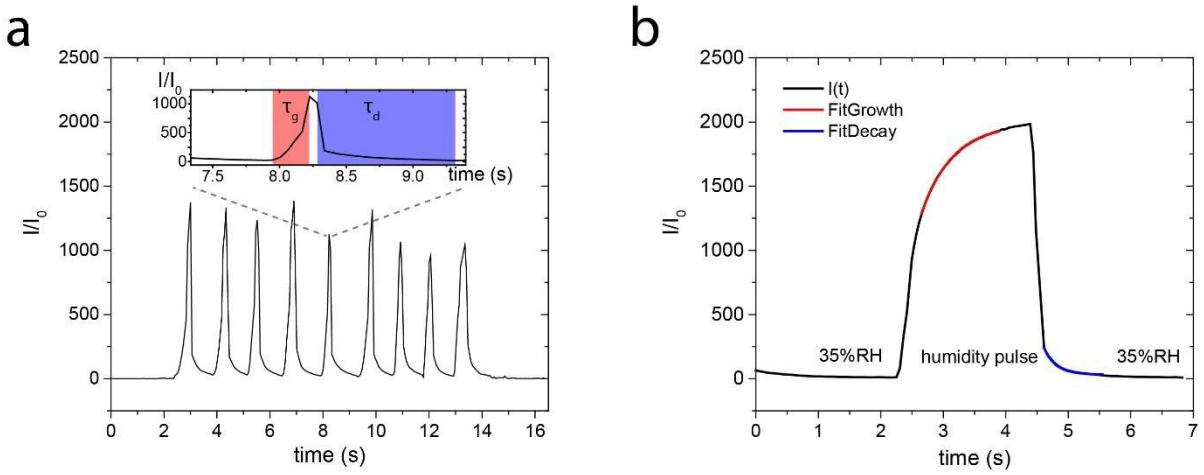

Figure 3.4: Determination of response (τ_g) and recovery (τ_d) times in OEG-BTBT devices. (a) Normalized I(t) (I/I_0) response of devices when exposed to a train of short (<1 s) humid air pulses at 2 V bias. Inset: Magnification of a pulse profile illustrating a rough method to estimate the time constants. (b) $I/I_0(t)$ response to a single long (>1 s) pulse at RH ≈ 35%. The curves obtained by fitting of the I(t) data during the growth (red) and the decay (blue) of $I/I_0(t)$ are also reported. Reprinted with permission from reference.[190] Copyright © 2022 American Chemical Society.

3.3.3.2 Selectivity of OEG-BTBT chemiresistors towards vapors of solvents

Among the fundamental properties of sensors there is selectivity. Depending on the analyte, many different selectivity tests can be performed to evaluate sensor poisoning substances or interferents. Since the response of OEG-BTBT sensors towards water is dominated by protonic transport, protonated solvents and solvents exposing functional groups that can easily interact with water or protons were investigated. The I(t) response of the chemiresistors to water was recorded in ambient air, while I(t) curves for organic solvents (and the blank) were recorded in a water free environment (N_2-

filled glove box, [H_2O] < 1 ppm, [O_2] < 10 ppm). The current response of our chemiresistors is highly selective for water molecules, as shown by I(t) measurements (constant |2 V| bias) performed in saturated environments of methanol, ethanol and diethyl ether (Figure 3.5a). The exposure of OEG-BTBT chemiresistors to vapors of those solvents only produces a minor current response.

Among the three solvents tested in these experiments, diethyl ether only induced a minor current enhancement compared to the blank, as the lack of intrinsic H-interactions with OEG side chains had the lowest impact on the chemiresistor response. The exposure to vapors of ethanol (more polar) led to a 10-fold (compared to blank) increase in I(t), facilitated by the interaction of the alcoholic group with glycol groups. Only the presence of methanol significantly increases the recorded current, in the nA range, thanks to its reduced dimensions and the proton of the -OH group. Although provoking a much less marked current response compared to water, methanol also forms H-bonds and can more easily permeate the film compared to ethanol. As a reference, the current response observed in devices operated in a saturated water environment reached tenths of μA. In fact, water molecules can donate not only one (like methanol or ethanol) but two hydrogen bonds, thus being able to form proton conductive networks between OEG side chains located at adjacent OEG-BTBT molecules.

The direct comparison of the effect of the different solvents on the device response is done by defining a normalized sensitivity parameter. Firstly, the recorded current is referred to a common blank (e.g., I(solvent)/I(blank): selectivity ratio in Figure 3.5b). Secondly, this ratio is divided by the vapor pressure of the solvent to give the normalized selectivity. OEG-BTBT chemiresistors are found to be at least a factor ~ 10^3 more selective for water than for the other solvents. A peculiar behavior can be observed if pulses of the organic solvents (or pure N_2) are directed to the in-operando device at 60% RH. Negative peaks of current are recorded (Figure 3.5c-f), hence suggesting that the solvents competitively interact with binding sites of water, thus disrupting the proton percolation networks within the organic film. For methanol, these spikes are particularly intense as its adsorption competition with water comes into play. Methanol interacts with OEG side chains hence competitively adsorbing to them against water.

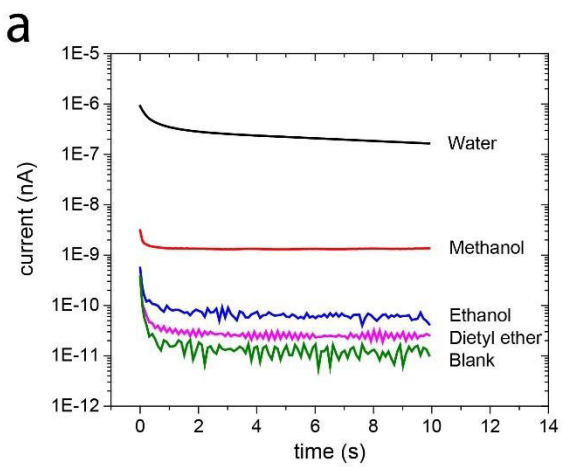

b

Solvent	Vapor pressure (Torr)	Current (A)	Selectivity ratio	Normalized selectivity ($Torr^{-1}$)
Water	17.54	1.8×10^{-7}	1.5×10^{4}	8.6×10^{3}
Methanol	97	1.3×10^{-9}	1.1×10^{2}	1.1×10^{0}
Ethanol	43.9	6.2×10^{-11}	5.1×10^{0}	1.2×10^{-1}
Dietyl ether	442	2.5×10^{-11}	2.1×10^{0}	4.7×10^{-3}

Blank current: 1.2×10^{-11} A

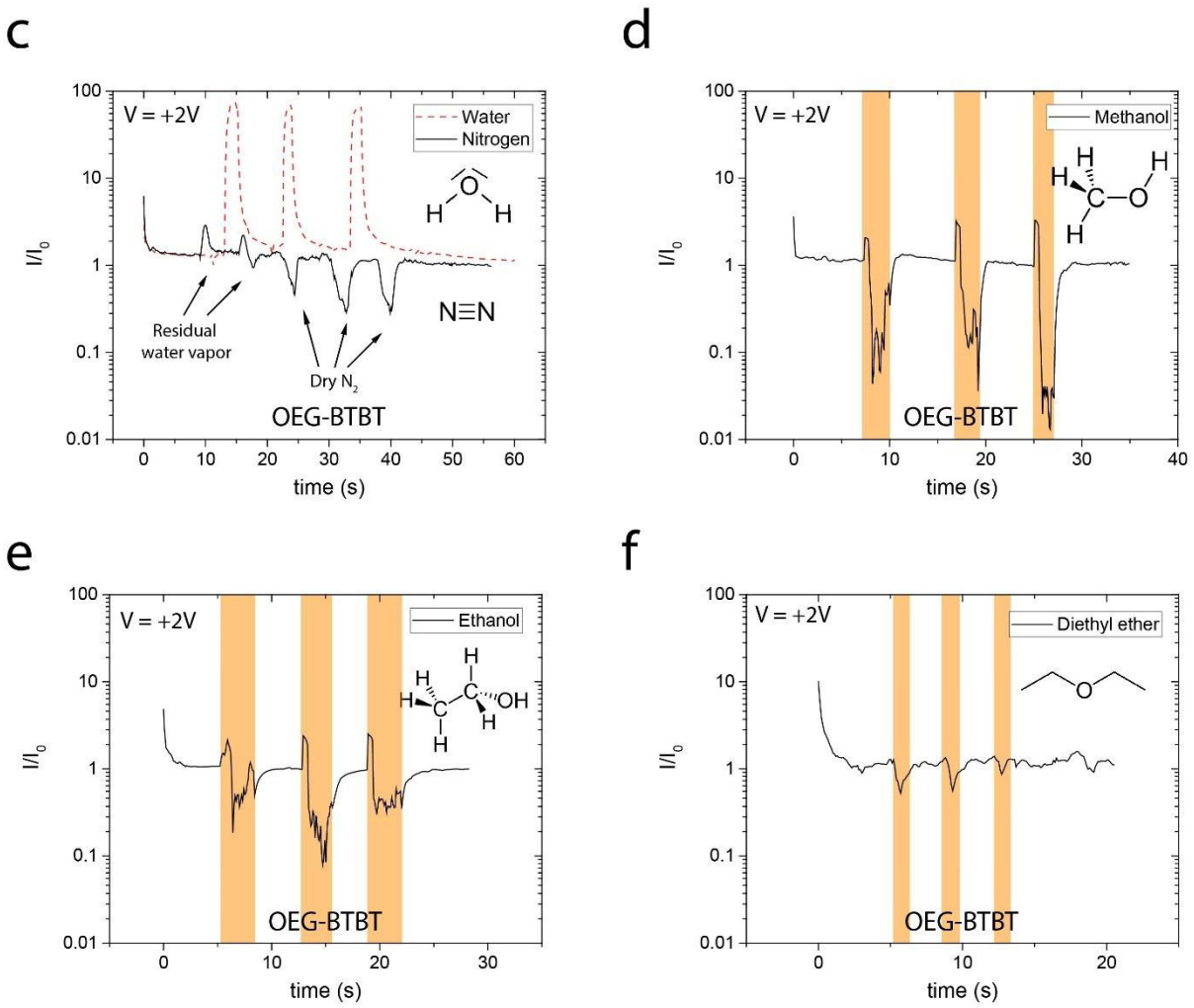

Figure 3.5: Selectivity of the OEG-BTBT devices towards different vapors upon the application of a 2 V bias. (a) Chemiresistor transient current measured in a saturated environment of the indicated solvent. Table (b): selectivity of OEG-BTBT devices to different solvent vapors. (c) Current response when exposed to humid air (dashed red) and dry N_2 (solid black) pulses at 60% RH. Current response when exposed to vapors of (d) methanol, I ethanol, (f) diethyl ether at 60% RH. Reprinted with permission from reference.[190] Copyright © 2022 American Chemical Society.

3.3.3.3 Humidity calibration curves of OEG-BTBT/SiO_2 chemiresistors

Calibrating the chemiresistor response to variation of the environmental humidity is a fundamental part in the development of a sensor. Repeated measurements of I(t) curves at a constant bias (2 V) were performed by a Keithley 2636B SourceMeter unit on devices placed inside a hermetic chamber containing a N_2 atmosphere. A flux of pure N_2 or water-saturated vapor in N_2 was purged into the chamber to reach the desired RH. The reference RH level inside the was recorded with a commercial humidity sensor (Sensirion SHT31 Smart Gadget) that could be connected to the smartphone to give real-time values. Each I(RH) curve was built by individual averaged values obtained from I(t) curves at the steady state. The humidity in the chamber was increased at 10% RH steps up to 80% RH and then decreased back to 10% RH with the same RH step. The single data points of the I(t) curve are averaged by the sourcemeter for a time interval of 100 ms. I(RH) was extracted from the I(t) curve only after reaching equilibrium, a condition that was generally verified after 10 s (see Figure 3.6a). As illustrated in the figure, the resistive and capacitive contributions were from the I(t) profile, to extract via areal integration the resistive current (I, blue) and capacitance (C, red) values at different RH levels.

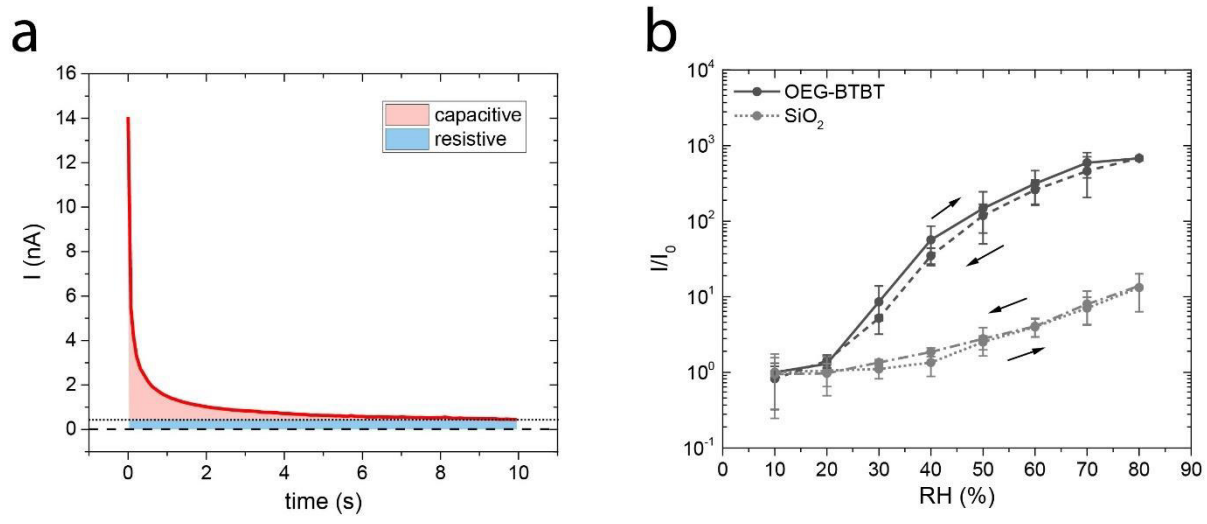

Figure 3.6: Chronoamperometry I(t) and humidity calibration curves of OEG-BTBT chemiresistors. (a) Example of the OEG-BTBT chemiresistor transient current upon a 2 V step bias. The capacitive and resistive contributions in the device response are highlighted as light red and light blue areas, respectively. (b) Normalized current (I/I_0) response as a function of RH for BC OEG-BTBT/SiO_2 devices (solid line) and bare SiO_2 (dotted line) samples. The arrows illustrate the forward and backward data collection upon the RH increase and decrease (dashed and dash-dotted lines indicate values measured while decreasing the RH). L = 5 um, bias voltage: ± 2 V. Adapted with permission from reference.[190] Copyright © 2022 American Chemical Society.

The I(RH) response of OEG-BTBT devices (black) and uncoated (bare) SiO_2 test patterns (gray) is shown in Figure 3.6b. Each point in the curve corresponds to the I(t) values that were averaged over a time interval of four or more seconds, after I(t) stabilization, in all cases occurring after t > 5 s. A normalized current (I/I_0) was defined as the ratio between the measured current (I) and the device initial response (I_0), i.e., at RH = 10%. The reversible current modulation in OEG-BTBT/SiO_2 devices spanned three orders of magnitude ($I/I_0 \approx 10^3$) upon changing the RH from 10% to 80%. No substantial hysteresis was observed for such BC devices (L = 5 μm) operating under pulsed bias, as the current at a given I(RH) for both the forward and backward curves lays within the experimental error.

3.3.4 Substrate Effect on the Response OEG-BTBT Chemiresistors

In this study, and in many other cases where thin-film devices are fabricated, the active material is frequently deposited on SiO_2 substrates, which is often considered as chemically inert (for most applications) and electrically insulating, but it actually exhibits an inherent moisture sensitivity.[199] In fact, the surface of SiO_2 itself can interact with atmospheric water molecules thanks to the presence of silanol groups.[229] Despite the experimental evidence and the numerous reports regarding the sensitivity of SiO_2 to humidity, the role played by the substrate is often neglected when investigating new materials for humidity sensing (Table 3.1).

Material & Reference	SiO_2 thickness	Full substrate coverage	%RH range	DC Voltage (V)	Control Sample
AuNPs/OEG[219]	230 nm	yes	5-82.5	0.5	yes
OT/OEG[218]	230 nm	no	5-87.5	1	no
NDI[217]	230 nm	almost	pulse	2	no
OT/NDI[216]	230 nm	no	0-75	5	no
SiO_2[200]	200/400 nm	yes	17-98	-	yes
GO[204]	300 nm	no	15-95	¼	no
GO[207]	bulk	almost	6-97	-	no
GO[205]	bulk	almost	10-95	10	no
GO[206]	bulk	yes	15-95	1	no
rGO[208]	bulk	yes	0-98	2	no
MoS_2[214]	270 nm	no	11-97	0.05	no
MoS_2[215]	300 nm	no	4-84	1.5	no
MoS_2[213]	300 nm	yes	0-35	0.5-2	no
This work	230 nm	yes	10-80	2	yes

Table 3.1: Selection of papers reporting humidity responsive thin-film/2D materials devices fabricated on SiO_2 substrates. The thickness of the SiO_2 substrate, the use of a control sample, the complete coverage of the substrate by the active material, the RH range and the applied voltage are listed in the table. Abbreviations: AuNPs: Au nanoparticles, rGO: reduced GO, MoS2: mono- and few-layer molybdenum disulfide.

However, the electrical properties of SiO_2 can dramatically change if water condensates on the surface.[230,231] Elucidating the role of the substrate helps avoiding data misinterpretation or the overestimation of the device figures of merit and helps clarifying the humidity-response mechanism.

3.3.4.1 Interface Engineering in OEG-BTBT chemiresistors

Devices consisting of bare SiO_2 substrates reversibly respond to RH changes, as seen in Figure 3.6b, light gray curves. For untreated bare SiO_2, the response is significantly inferior to that of the OEG-BTBT chemiresistors fabricated on that same substrate ($I/I_0 \leq 10$ in the range 10−80% RH). The magnitude of this response can be modulated via the modification of the SiO_2 surface through some treatments that change the surface wettability, such as UV/ozone exposure[232] and alkylsilane functionalization.[233] As previously mentioned, water molecules are known to adsorb mainly at the SiO_2 surface silanol sites.[234] This process results in the formation of a network of molecules that is driven by H-bonding,[235] and a uniform water layer (of thickness of a few monolayers) thus grows as a function of RH.[236] The extent of this network can severely change both on the base substrate and within the film when more or less hydrophilic sites are present on the supporting surface, as the substrate wettability was proven to affect the depth distribution profile of the adsorbed water within thin films of hygroscopic materials.[237]

Hydrophilic (UV-SiO_2) and hydrophobic (ODTS-SiO_2) surfaces were obtained via UV/ozone exposure (5 min, Novascan PDS Pro Series system) and octadecyltrichlorosilane (ODTS) functionalization, respectively. The ODTS SAM treatment was done on UV-SiO_2 substrates inside a N_2-filled glove box. ODTS SAMs were grown by immersing the UV-SiO_2 substrates in a toluene solution of ODTS (10 µL in 10 mL) heated at 60 °C for 1 h, and then left at room temperature for 12 h to cool down. The ODTS-coated substrates were then rinsed with toluene and dried at 60°C for 1 h under N_2.

By increasing the hydrophilicity of the SiO_2 surface via UV/ozone the water CA drops from a value of CA ≈ 55° to a value below 10°. This change in the affinity of the surface to water can be ascribed to the increased number of water-sensitive groups exposed by SiO_2. The responsivity of bare UV-SiO_2 and of the respective OEG-BTBT devices is enhanced by a factor ~ 5 compared to devices fabricated on bare SiO_2 (see Figure 3.7a). OEG-BTBT/UV-SiO_2 devices reach $I/I_0 > 10^3$ for RH levels increasing from 10% to 80%. By contrast, the humidity response of both OEG-BTBT-coated and uncoated devices

fabricated on ODTS-SiO_2 (CA ≈ 110°) is significantly reduced and detectable currents are recorded only above RH > 40% (Figure 3.7a). Due to the hydrophobic treatment, water molecules find much less sites for the interaction with SiO_2 and only the surface groups corresponding to ODTS SAM defects remain available. In fact, the amount of water present at the SiO_2/OEG-BTBT interface effectively controls the performance of the chemiresistors, as the trends observed in the humidity calibration curves are reflected in the SFG measurements performed at variable RH levels on treated substrates (Figure 3.7b). For these measurements, 50 nm-thick OEG-BTBT films were prepared onto quartz substrates of optical grade modified by either UV/ozone or ODTS. The different surface wettability affects how many water molecules can be accommodated at the interface between OEG-BTBT and the SiO_2 substrate. The integrated SFG signal increases more rapidly for films fabricated on onto hydrophilic substrates compared to films on hydrophobic SiO_2.

To sum up, the reason why the water reaching the interface via permeation through the organic film governs the device I(RH) response is that a more efficient network for the percolation of H^+ upon the voltage bias is formed when water molecules are present to bridge gaps between hopping sites in the material.[238] The formation of silanol groups mediated by water occurs spontaneously on SiO_2 surfaces at room temperature, adding up new sites for proton conduction to the overall conductive network.[239]

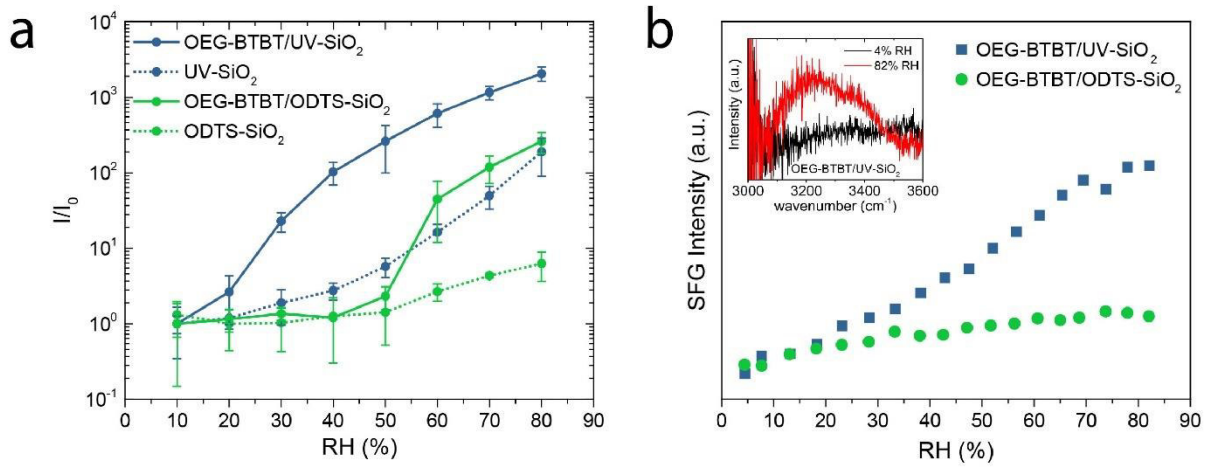

Figure 3.7: Humidity curves of OEG-BTBT chemiresistors on modified SiO_2 substrates and amount of water at the interface. OEG-BTBT thin films are fabricated on UV-SiO_2 and ODTS-SiO_2 substrates. (a) Current response of OEG-BTBT devices fabricated on treated SiO_2 (solid lines) and bare substrates (dotted lines). L = 5 um, bias voltage: ± 2 V. For OEG-BTBT/ODTS-SiO_2 and ODTS-SiO_2 devices, the current reaches the instrumental DL at RH ≤ 40%. (b) SFG integrated intensity of the 3300 cm^{-1} O−H stretching band (Inset: SFG spectrum of the OEG-BTBT/UV-SiO_2 interface at low (4%) and high (82%) RH). SFG measurements performed by A. Greco. Adapted with permission from reference.**[190]** Copyright © 2022 American Chemical Society.

Hence, the improved humidity sensing capability of OEG-BTBT thin films deposited onto hydrophilic SiO_2 can be explained in these terms. By and large, the dramatic influence of the interface wettability to the overall performance of OEG-BTBT chemiresistors demonstrated how the synergy between a hygroscopic molecular film and a humidity responsive substrate can bring major benefits to the sensing of humidity.

3.3.5 Mixed Conductivity in OEG-BTBT

Demonstrating the different conductive character of OEG-BTBT chemiresistors at different RH levels was proven by gathering complementary information from multiple characterization techniques. The data collected from OFET, SFG, EIS and chemiresistor measurements were put together to support the claim that in the limit of low humidity OEG-BTBT devices fabricated on hydrophobic SAM-treated SiO_2 substrates can operate as hole-transporting transistors, while in the range of finite humidity (10−80%) the designed OEG-BTBT chemiresistors can be utilized as humidity sensors.

3.3.5.1 TFTs based on OEG-BTBT – Hole conductivity

The μ_{in} of OEG-BTBT was determined from bottom-gate bottom-Au-contact three-terminal devices fabricated on a hydrophobic SAM-treated metal oxide dielectric. Both solution-processed (Solution-TFT) and vacuum-processed (Vacuum-TFT) transistors were fabricated on SiO_2 for this purpose. The electrical characteristics of OEG-BTBT devices were recorded in a N_2-filled glovebox ($[H_2O] < 1$ ppm, $[O_2] < 10$ ppm) using a Keithley 2536A SourceMeter or at ambient conditions with an Agilent 4155B Semiconductor Parameter Analyser. Since vacuum-processed transistors showed the best performance, the transistors ultimately design to exhibit the best hole mobility performance are fabricated via vacuum evaporation on Al_2O_3 substrates. Transfer curves are reported in Figure 3.8.

OEG-BTBT devices on SiO_2: The substrate (and gate electrode) is a conductive Si wafer coated by 230-nm (Solution-TFT) or 300-nm (Vacuum-TFT) thermally grown SiO_2 treated with ODTS. C = 15 nF/cm^2 (230 nm) or 11.4 nF/cm^2 (300 nm) is the areal capacitance of the dielectric SiO_2 layer. The source and drain electrodes are a symmetric couple of Au IDEs (L= 2.5 μm, W = 10 mm for Solution-TFT; L = 5 μm, W = 1 mm for Vacuum-TFT). Solution-TFTs were obtained via spin-coating of OEG-BTBT/$CHCl_3$ suspensions at 2000 rpm, 2500 rpm/s for 30 s yielding around 100-nm-thick films. Vacuum-TFTs were obtained via thermal evaporation of the OEG-BTBT powder yielding

thin films of nominal thickness ≈ 30 nm under high vacuum (p ≈ 2 × 10^{-6} mbar). The electrical characteristics of OEG-BTBT devices were recorded in a N_2-filled glovebox ([H_2O] < 1 ppm, [O_2] < 10 ppm) using a Keithley 2536A SourceMeter (Solution-TFT) or with an Agilent 4155B Semiconductor Parameter Analyser (Vacuum-TFT). The μ_{in} values were extracted from Equation 1.2 with a data input from transfer curves in the saturation regime. The hole μ_{in} of these devices was estimated to be μ_{in} ≈ 5 × 10^{-8} and 3 × 10^{-5} cm^2 V^{-1} s^{-1} for Solution-TFT and Vacuum-TFT, respectively. Solution-TFTs exhibit V_{TH} ≈ -15 V, while for Vacuum-TFTs V_{TH} ≈ -55 V.

OEG-BTBT devices on Al_2O_3: The substrate (and gate electrode) is a conductive Si wafer coated by 30-nm thermally grown Al_2O_3 treated with n-tetradecylphosphonic acid (TPA). C = 186 nF/cm^2 is the areal capacitance of the dielectric Al_2O_3 layer. Source and drain are a couple of Au electrodes (L = 50 μm, W = 500 μm). Since the IE of OEG-BTBT thin films is 5.54 ± 0.03 eV (as determined by PYSA), treating Au electrodes with perfluorobenzenethiol (PFBT) offers an improved alignment. The WF of the Au electrode was adjusted from 4.8 ± 0.1 eV (bare Au) to 5.5 ± 0.1 eV (Au-PFBT). OEG-BTBT thin films of nominal thickness ≈ 12 nm were obtained via thermal evaporation on the substrate kept at 100°C under high vacuum (p ≈ 2 × 10^{-6} mbar). The μ_{in} values were extracted from Equation 1.1 with a data input from transfer curves in the linear regime. The hole μ_{in} of these devices was estimated to be μ_{in} ≈ 1 × 10^{-3} (PFBT functionalization) and 3 × 10^{-5} cm^2 V^{-1} s^{-1} (bare Au). Both type of devices exhibited V_{TH} ≈ -1 V.

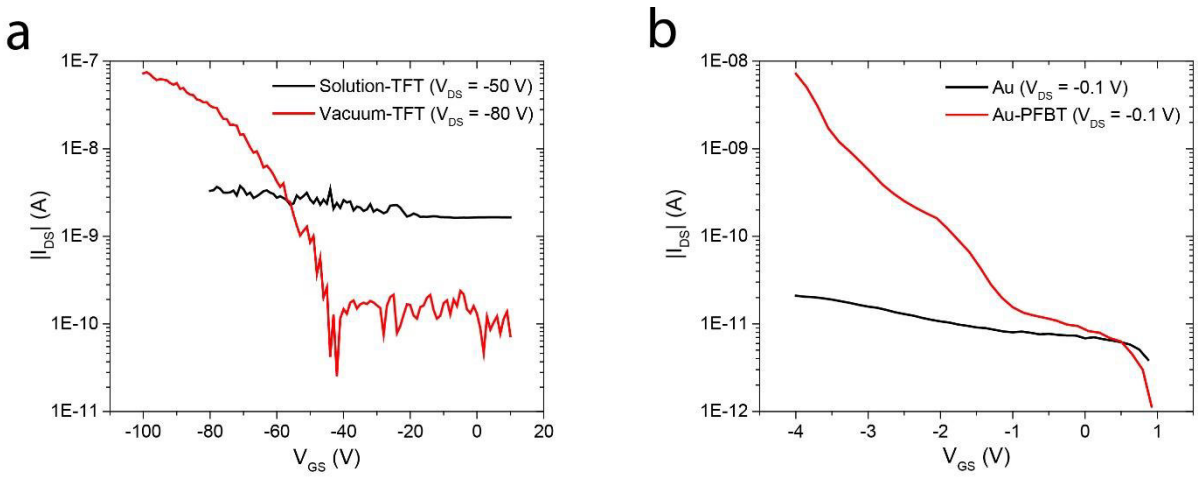

Figure 3.8: Transfer curves of OEG-BTBT TFTs. (a) Transfer curves of OEG-BTBT/ODTS-SiO_2 devices recorded in a N_2-filled glove box in the saturation regime. Vacuum-TFT measurement performed by M. Gicevičius. (b) Transfer curves of OEG-BTBT/TPA-Al_2O_3 devices recorded in the linear regime at ambient conditions (RH = 55%). The applied V_{DS} is reported in the figure. Reprinted with permission from reference.[190] Copyright © 2022 American Chemical Society.

While the relatively high V_{TH} values of OEG-BTBT/SiO_2 devices suggest that significant charge carrier trapping phenomena are occurring at the OSC/dielectric interface, the μ_{in} value of OEG-BTBT/Al_2O_3 devices fabricated on PFBT-treated Au electrodes indicates that an efficient hole transport can be achieved even at ambient conditions in the presence of humidity (RH = 55%).

3.3.5.2 EIS of OEG-BTBT devices – Mixed conductivity

Impedance measurements were performed at room temperature on TC devices fabricated on UV-SiO_2 by applying an AC voltage of 0.1 V amplitude over a 100 kHz – 100 Hz frequency range with a Metrohm Autolab PGSTAT128N potentiostat. EIS spectra were recorded with one of the device terminals connected to the potentiostat working electrode and the other terminal was connected to both the coupled reference and counter electrode. The sample real (Z'), imaginary (Z'') impedance and phase (θ) were collected at low (10%) and high (97%) RH. Autolab NOVA software was used for data collection and analysis. OEG-BTBT and C8-BTBT devices were compared to show the differences between a mixed hole/H^+ conductor (OEG-BTBT) and a structurally similar hole conductor (C8-BTBT). Three independent measurements were recorded for each sample and experimental condition. EIS measurements and equivalent circuit fitting were performed by S. Gullace and the final data interpretation was done with the help of Dr. R. Furlan De Oliveira. The EIS spectra are reported in Figure 3.9.

The capacitive response is predominant for both OEG-BTBT and C8-BTBT at 10% RH (Figure 3.9), with OEG-BTBT being characterized by a more verticalized Z'' vs Z' trace and θ ≈ -90° within the whole frequency range measured, as it can be observed from the Nyquist plots (Z'' vs Z') and Bode plots (phase). These results indicates that at low RH levels OEG-BTBT is particularly more capacitive than its alkylated counterpart. A broad incomplete semicircle in the Nyquist plots (Figure 3.9a,c) indicates a large resistance contribution to the response of both films, which is more prominent for OEG-BTBT. At almost dry air conditions and in the absence of a proper field-effect gating, both materials are poor electronic conductors. The instrumental noise at low frequency is due to the limitations of the potentiostat at high impedance.

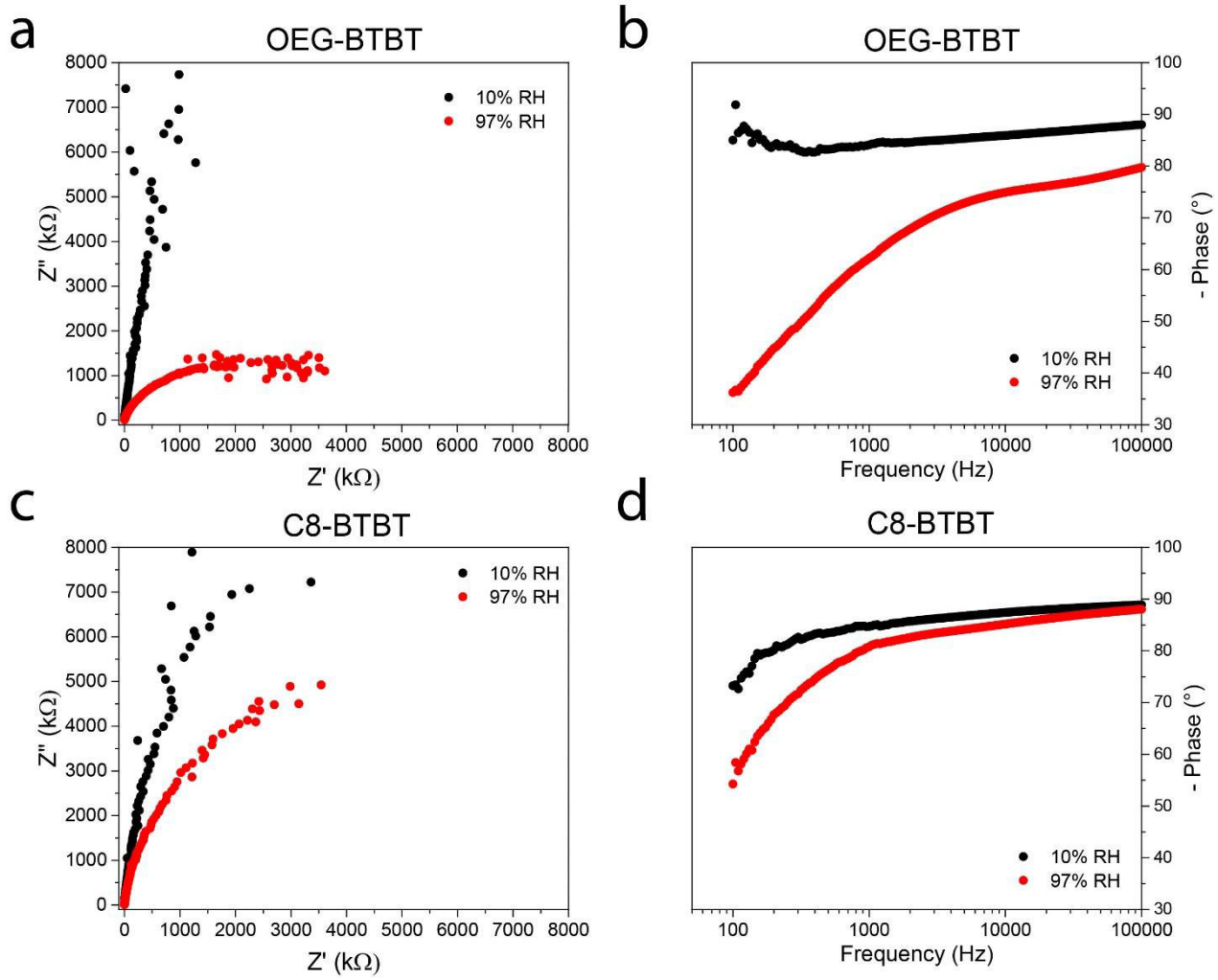

Figure 3.9: EIS measurements for OEG-BTBT and C8-BTBT thin-film two-terminal devices at low (10%) and high (97%) RH. Nyquist plots (a, c) and Bode phase plots (b, d). Device channel length: L = 100 μm. AC voltage applied: 0.1 V and frequency range 100 kHz – 100 Hz.

At 97% RH, the Nyquist plot of OEG-BTBT devices shows a depressed semicircle and θ values < 30° at low frequency values (< kHz) that typically characterize charge conduction processes.[240] These processes are probably ascribed to the transport of heavy charged (ionic) species in the bulk[241] acting together with electronic species. As the ionic contribution appears only in humid air and the molecular structure of OEG-BTBT does not contain any ionic species, this conduction process is ascribed to protons that are dissociated from the adsorbed atmospheric water. In fact, the SFG measurements reported previously (Figure 3.7b) indicate that increasing amounts of water can be adsorbed within the OEG-BTBT film at increasing RH. Instead, in this wet environment, C8-BTBT devices still show a significant capacitive contribution that is coupled to a large electrical resistance, suggesting that the electronic conductivity is not effectively activated without the aid of a gate electrode and moisture only slightly changed the thin-film conductive properties.

3.3.5.3 OEG-BTBT chemiresistors – H^+ conductivity

Another set of measurements supporting the claim of efficient ionic conductivity in OEG-BTBT chemiresistors is given by the thickness-dependent current observed in both BC and TC devices. More conventional ways of directly measuring proton conductivity as a function of RH rely on the use of palladium hydride electrodes[242] or other methods involving deuterated water.[243] The first method requires the know-how of measurements in a reducing environment of 5% H_2 in N_2. The use of deuterated water vapor requires some expertise as well to avoid isotopic exchange with environmental water and the precise control of the RH level might not be granted by the commercial sensor that has been employed throughout the experiments, rendering it difficult to compare the behavior of chemiresistors exposed to the two water isotopes.

The I(RH) curves were thus collected from 90-nm ("thin") and 260-nm-thick ("thick") films deposited onto UV- SiO_2 (Figure 3.10). The current pathways in BC and TC devices are essentially different because of the particular electrode geometry and injection areas. In BC devices, the current flows in close vicinity to the OSC/substrate interface up to a volume defined by the channel W and L and the thickness of electrodes, while TC devices the current is preferentially flowing close to the OSC/air interface.[244]

Chemiresistors with thin, 90 nm, OEG-BTBT films showed similar I/I_0 trends in the 10−80% RH range for both electrode layouts. In fact, current is less dependent on the position of electrodes in thinner films as it flows more uniformly throughout the volume of the channel. These devices reach almost the same I/I_0 at 80% RH indicating that the humidity sensitive sites might have reached saturation both in the film and at the buried substrate interface.[237] For thicker (260 nm) OEG-BTBT films, the electrode configuration affects the I/I_0 response that is increased by a factor ≈ 200 for TC and ≈ 50 for BC devices. When a H^+ transport is considered, the conductivity is expected to increase with RH (because of increased water adsorption) and film thickness (for an increased number of proton sites).[196] Interestingly, at RH below 40%, the response of thick (260 nm) BC devices is larger than TC devices as the hydrophilic OSC/UV-SiO_2 interface can adsorb and supply H^+ more effectively. By contrast, at RH above 40%, H^+ conduction is facilitated by the larger contribution of adsorbed water molecules in proximity of the OSC/air interface, as the substrate contribution becomes less important.[245]

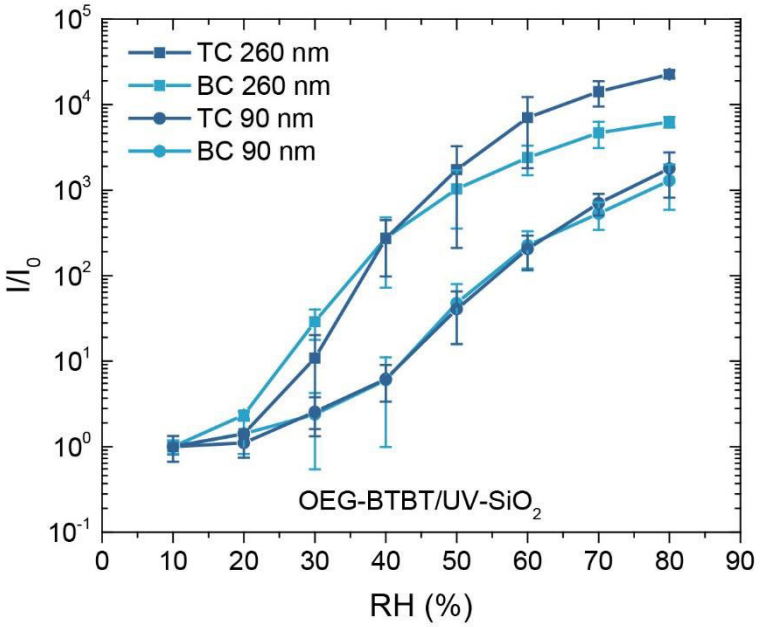

Figure 3.10: Effect of organic film thickness and electrode configuration on the OEG-BTBT chemiresistor humidity response. Comparison between the I(RH) curves of BC and TC devices made of OEG-BTBT films with thickness of around 90 nm ("thin") and 260 nm ("thick"). Error bars correspond to the standard deviation acquired for n ≥ 3 devices. Device channel length: L = 60 μm. RH range: 10−80%. Voltage bias applied: 2 V. Reprinted with permission from reference.[190] Copyright © 2022 American Chemical Society.

3.4 Conclusions and Outlook

Thin films of OEG-BTBT have been deposited on Au IDEs-prepatterned SiO_2 substrates to fabricate humidity-sensitive chemiresistors with state-of-the-art sensitivity. OEG-BTBT is a novel BTBT derivative that has been designed to combine the properties of hygroscopicity and semiconductive hole transport. Via a spin-coating deposition method, this molecule self-assembles on SiO_2 substrate into semiconducting films that can electrically respond to changes in RH, outperforming many other similar devices based on organic or 2D materials. Within the RH range of study (10−80%), the conductivity of our chemiresistors fabricated on hydrophilic UV-treated SiO_2 experience changes up to a factor ~ 2×10^4 when the thin-film thickness and electrode configuration are optimized. The fast and reversible chemiresistor response to increasing and decreasing ambient humidity levels was evaluated together with the characterization of a remarkable selectivity towards interfering organic solvent vapors. In fact, OEG-BTBT thin films exhibit a mixed electron/H^+ conducting behavior that is controlled by environmental humidity conditions and substrate wetting properties and arising from the interaction between the OEG side chains and molecular vapors that can

dissociate with the formation of protons. Evidence of proton transport was given by a combination of EIS measurements and changes in the chemiresistor electrical properties as a function of thickness and humidity. Thanks to a multiscale characterization of our samples, it can be concluded that the observed device behavior derives from a synergistic combination of the molecular design of the material and the interfaces of the chemiresistor. The transduction of RH changes with major sensitivity enables the use of OEG-BTBT thin films for many electronic applications requiring an improved responsivity to water vapor. Future developments could aim towards the exploitation of this novel compound in devices operating at ambient conditions and wet environments of relative humidity as high as 80%.

4 Optically Switchable Organic Electrochemical Transistors

4.1 Organic Electrochemical Transistors (OECTs)

Iontronics is the key discipline underlying bioelectronics that aims to control the ionic/electronic character of active materials for interfacing devices with biological tissues and living systems. With increasing importance of nanofluidic devices in and beyond the biomedical field, consisting in studying and modelling of the nanoscale behavior of fluids and ionic species transported at the nanometric scale,[246] the field of bioelectronics experienced a boost in its development. These research efforts resulted in the nanofabrication of devices and sensors employing nanofluidics[247] and enabling the study of *in vitro* systems.[248] Among OSCs, conjugated polymers and polyelectrolytes exhibiting mixed conductivity represent the current state-of-the-art materials for electrical biointerfacing.[14,249] Despite being challenging for scientists to study and to characterize in depth, the interface of the object of interest (e.g., for bioelectronics, living cells) represents the first access point for man-made devices to enable signal transfer across the cell membrane. For this purpose, the need for biocompatible materials is essential and OSC materials represent a natural choice to interact with the biological interface due to the structural similarity between organic materials and biomaterials. All the findings on organic interfaces that were gathered by researchers in the past decades constitute the base for the development of integrated organic/bio-organic systems.[109] The stakes at play are huge: we can already aim to communicate with living cells to sense its vital parameters or actuate functions in-vitro,[248] the intensive effort towards efficient drug delivery in living tissues can be enabled by the electrochemical signaling driven by OECTs[250] with the future perspective of targeting the mechanisms underlying the expression and release of macro(bio)molecules and being able to find new therapeutical approaches by locally monitoring disease states.[109] The development of biocompatible systems that can work with or respond to multiple inputs such as electronic stimuli, ionic gradients, light pulses and mechanical stresses with long-term stability at physiological conditions is thus a prerequisite for the full integration of man-made electronics with the human body.[251,252]

Within this context, OECTs represent an important type of devices that are currently at the edge of organic electronics research, even though their first discovery is relatively old, dating back to the mid-eighties.[253] The typical structure of an OECT consists of an

OSC material that is directly in contact with the source and drain electrodes, defining the channel, and an electrolyte (usually a water solution of a salt at physiological concentrations), in which a third, gate, electrode is immersed. To change the conductivity of the active material, an electrochemical (EC) doping is induced by injecting ionic species from the electrolyte to the OSC film, hence enabling the transistor switching function. With reference to source as the grounded electrode, anions or cations can selectively diffuse into the channel causing a change in electrical conductivity by controlling the gate voltage. The applied drain voltage can then move the electronic or ionic charge carriers present within the OECT channel.

4.1.1 Electrical characterization of OECT devices

The operation of OECTs is linked to the electrochemical doping of the channel, which is a different phenomenon from the field-effect enhancement of the charge carrier density in the channel of an OFET. The figures of merit that represent the materials properties must then be adapted to the diverse working principle of OECT, as the simple use of the charge carrier mobility does not grasp the physics of the OECT device comprehensively. OECT devices also require a more complex setup compared to conventional planar OFETs. In fact, the addition of a non-solid or semi-solid electrolyte often requires a spatial confinement. Having a microfluidic system would be the optimal choice, as is avoids issues with solvent evaporation, thus granting a continuous flux of solution at a constant and stable concentration. By contrast, it is not always easy to fabricate the microfluidic setup nor to adapt the previously existing experimental setup for electrical characterization to the microfluidic cell.

In this subsection, the figures of merit of OSC materials for OECTs are discussed alongside with how to determine these parameters experimentally. In addition, particular attention will be given to the experimental setup for the electrical characterization of OECTs, as tiny variations in the device geometry and components can severely affect the device performance.

4.1.1.1 State of the art of OECTs

Researchers in the field of bioelectronics devised new methods and adapted already existing models derived from the conventional OFET mathematical description. The steady state and transient behavior of OECTs were described via simple analytic expressions that in some cases closely resemble that of OFETs and in other cases must

keep into account the additional phenomena of ionic transfer and motion.[254] The charge carrier mobility (μ) cannot capture alone the complexity of the mixed ionic/electronic transport properties of the OSC active material in the channel of OECT devices. As the capacitance of the channel measures the ability of the material to store ions, the volumetric capacitance, or capacitance per unit area, (C*) this parameter also governs the transconductance of the transistor and must then be included within the figures of merit for the evaluation of OECT performance.[255] Remarkably, the use of EIS is found to be essential in the characterization of OECT materials as it proves to be an important tool for the evaluation of capacitive and resistive elements within OECT devices.[166] By combining information from DC and AC methods, the product μC* is a powerful benchmarking parameter for OECT devices.[157]

The working principle of OECTs can be well understood by comparing it to the behavior of a transistor consisting of a thin film of an OSC polymer (a modified P3HT where the side chains terminate with a -COOH group) where ions can permeate within the bulk from a polyelectrolyte that is gated from top.[256] Depending on the gate bias, this transistor can operate in three different regimes: (i) at a relatively low gate voltage, the device behavior resembles that of a conventional OFET. (ii) for a relatively high gate bias, an intermediate regime was identified (fast switching speeds (10^{-2} s) and high current density (10^3 A/cm^2) in which the charge transport occurs via few OSC monolayers). (iii) at higher gate voltages, the device operates in a slow regime that involves a volumetric (3D) charge transport with the entire bulk of the OSC.[256] The transconductance of state-of-the-art OECTs is in the range of mS, even though it vanishes at frequencies higher than 1 kHz, while typical OFETs possess lower transconductance, but they can be operated at higher frequencies.[52] Further investigations, led to the understanding of the role of the side chain for controlling the mode of operation of organic transistors, as, for example, alkoxylated polymers can show a combination of interfacial and bulk doping enabling an important design strategy for OECTs.[24]

The current performance of OECTs already enables their use into functional devices and applications. Until now, individual transistor devices have been developed and the field mainly focused on the figures of merit.[157] Still, bioelectronics needs more optimization in the device stability,[257] due to the particular environment of living systems, and more testing for both bioelectronic circuits [258] and *in-vivo* applications.[259]

4.1.1.2 Experimental setup for OECTs

The setup for OECT characterization comprises a thin film of OSC deposited on an insulating substrate where the entire active channel is covered by an electrolyte that can be liquid, solid or semisolid (gel-like).[260,261] For the working principle of OECTs, a mobile ionic species must be present inside the electrolyte and should be able to be reversibly transferred in and out of the OSC channel upon the application of a variable gate voltage. If the electrolyte is solid there is no need for spatial confinement, but in case the electrolyte is not self-confined, the use of a supporting structure, such as a "pool" made of an inert material (e.g., PDMS) must be used to obtain a stable measurement. For testing purposes, a simple drop of electrolyte might be sufficient, but continuous evaporation of the solvent occurs thus changing the concentration of the solution. In principle, the operation of the OECT should not depend on the concentration once a sufficient amount of salt is provided, however, some reports show a significant concentration dependence on the recorded electrical current, highlighting how the setting up of OECTs measurements is very delicate.[262] For the sake of example, the most common electrolyte solutions contain 0.1 M concentration of a salt, like NaCl or KCl, in order to have a value comparable to the physiological concentration of salt.

Another important aspect regards the optimization of the geometrical parameters of the device components.[263] Firstly, the surface area of the gate electrode should be maximized (at least tenfold) compared to the area of the active channel and conductive components that are exposed to the electrolyte environment.[264] To fulfill this requirement, one possible option is to curl up a Pt wire immersed in the electrolyte, or better, to utilize a dense inert metallic grid with submillimetric holes to highly increase the surface area of the gate electrode. Alternatively, one can minimize the exposed channel area by covering the entire device with an inert coating and then subsequently opening a window to contact the electrolyte.[52] Secondly, the thickness of the film can significantly influence the recorded current, since the electrical response of an OECT is volumetric. In fact, the channel capacitance is proportional to the channel thickness and the electrochemical doping occurs within the entire channel volume.[255] Thirdly, the use of a reference electrode is highly recommended, as in all electrochemical experiment the absolute potential of the system can fluctuate up to hundreds of mV. A practical choice is to immerse a simple Ag/AgCl electrode after a suitable process of coating.[265] Having in most cases an electrolyte containing chloride, the Ag/AgCl electrode is directly immersed in a solution where it is electrochemically stable.

Finally, the device can be connected to a sourcemeter/potentiostat, ideally with a total of four channels to connect source, drain and gate electrodes, together with a reference electrode for the monitoring of the absolute potential of the electrolyte. Knowing this potential is critical for the determination of the gate electrode potential during the measurement of transfer characteristics.

4.2 Optically Switchable OECTs

Multiresponsive and multifunctional devices based on organic materials are a promising part of an emerging interdisciplinary field that unites the effort of scientists from physics, chemistry, biology, medicine and engineering.[266–268] Optoelectronic control approaches in organic bioelectronics are still relatively unexplored, with some reports regarding the study of photocapacitive and photofaradaic processes in photoelectrodes based on OSC materials,[269] the use of photocapacitors to control the activity of living cells by acting as electrodes for extracellular stimulation,[270] or by interfacing traditional light-based devices such as organic LEDs, solar cells photodetectors to living systems.[271] The use of optical tools represents a viable strategy combining minimal invasiveness with the potential to yield fast and low power photonic devices. Light-based smart healthcare for diagnostics and therapeutics is already widespread in clinics, although the realization of functional items that can be directly worn by or implanted in patients is still very limited.[266] There are plenty of opportunities to develop new (photo)chemical approaches for the realization of bioelectronic devices based on OSC materials.[272] These bioelectronic and neuromorphic devices may then be self-powered by transparent photovoltaics integrating a power supply in close vicinity, implemented for example, as an artificial skin.[273]

Switchable bioelectronics can thus be seen as a subfield of bioelectronics that is mainly focused on studying all the bioelectrochemical processes that aim to mimic and control biological systems with the aid of external stimuli.[274] Interface is probably one of the most challenging aspects for the implementation of switchable bioelectronics as a fine regulation of interfacial properties is required for the integration, biocompatibility, mechanical flexibility of devices.[274,275] Photoswitchable biomaterials were pioneered by Willner in the past few decades,[276,277] and molecular photoswitches,[278] in particular, can be designed to be integrated with biological systems[279] and/or interact with bioelectronic materials as stimuli-responsive blocks to generate dynamic interfaces.[274]

Within this context, the blending of molecular photoswitches with OECT polymer represents a novel strategy for controlling the device operation.

4.2.1 Designing Optically Switchable OECTs

The road towards optically switchable OECT devices, i.e., using light to modulate the electrical response of OECT, is still unexplored. Having an additional tool to remotely control the device operation in living systems other (than the gate) and with the minimum invasiveness, such as light, is highly desirable. Some OSC materials possess bandgap energies comparable to that of visible and UV light, meaning that they can absorb light. The phenomenon of photoconductivity is thus quite common and it is often exploited in photodiodes and phototransistors.[280] In general, photoconductive OSC materials experience an increase of the conductivity upon light irradiation, but the opposite process is much less common.[281] Polymer OSC materials, with their highly and extended π-conjugated chains often possess photoconductive properties, although it is challenging to completely quench the electrical conductivity with light. Hence, one possible approach to target this conductivity modulation is via the blending of molecular photochromic additives into OSC polymer matrices.[282] Among the photoswitching molecules that can be used for imparting an additional light responsive nature to the OSC polymer, spiropyran (SP) is a first choice for the design and tuning of dynamic materials.[283] The SP derivatives possess two stable forms at room temperature: the neutral closed ring configuration is called spiropyran, and the zwitterionic open ring configuration is named merocyanine (MC). Both forms coexist at room temperature but the relative population of the two forms depends on the environmental conditions (e.g., the compound is in the form of powder, solution in diverse solvents or thin film) and on the functional groups attached to the SP switching core. It is possible to reversibly switch between the SP and the MC form by irradiating the sample containing an SP species with either visible (~ 530 nm) or UV (~ 365 nm) light. Monochromatic light from LEDs is usually preferred to have a better control over the matching between the absorption wavelength of the SP/MC system and to limit photodegradation. UV light induces the opening of the SP ring promoting the formation of the MC form, while visible light and thermal energy promote the closing of the ring.

On the other hand, a suitably designed OSC polymer for OECTs must be chosen as a matrix for blending with the spiropyran, based on the molecular affinity between side chains of the spiropyran and the polymer. Since a common choice for OECT polymer

side chain is either OEG[26] or alkyl chains,[284] due to the relative ease of the polymer synthesis, the increased molecule solution processability and the positive effects on the structural arrangement of the polymer,[56] we focused our attention on pgBTTT. Its structure consists in a BTTT backbone decorated by OEG chains (Figure 1.2d). While the pgBTTT polymer has been kindly provided by Prof. Iain McCulloch, the target spiropyran functionalized with OEG chains (OEG-SP) was synthesized in our group by Dr. W. Danowski. The chemical structure of OEG-SP is shown in Figure 4.1.

In the following sections, a complete multiscale characterization of the OEG-SP/pgBTTT blend is provided. Firstly, the photophysical, UV-Vis, characterization of the switching properties of the blend are discussed. Secondly, the electrical characteristics of the OECT transistors made with optically switchable blends are reported. After that, the electronic properties of the blend upon reversible electrochemical doping and UV photoswitching are studied and, finally, the main conclusions about this first example of optically switchable OECTs are drawn.

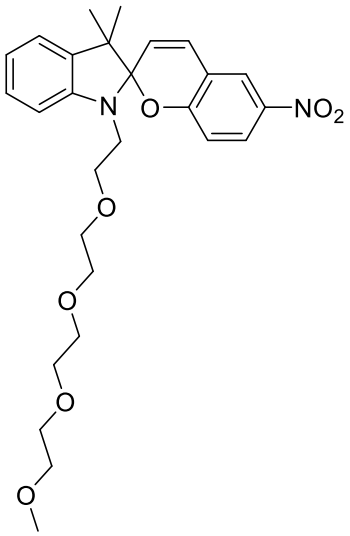

Figure 4.1: The chemical structure of OEG-SP. The compound was synthesized by W. Danowski.

4.2.2 Photophysical characterization of OEG-SP/pgBTTT blends

UV-Vis spectrophotometry provides a convenient way to monitor the photoswitching properties of the SP/MC system. All photoswitching and photocurrent experiments were performed in a dark room. Two different LEDs were employed for the illumination of the sample: one emitting light in the near UV and the other emitting a brilliant green light. The 365 nm UV-LED is a ThorLabs M365L2 operating at 700 mA with a power output of 3 W. The 530 nm green LED is a ThorLabs M530F1 operating at 1000 mA with a power

output of 5 mW. These two LEDs can be controlled by a programmable driver that selectively switch on and off the LED lights.

As a first experiment, the photophysical properties of the OEG-SP photoswitch were determined in solution. Since all the solution casting methods to deposit the OSC polymer blend films utilize $CHCl_3$ solutions, the stability and switching capability of OEG-SP was characterized in $CHCl_3$ solution. However, it is necessary that the SP/MC system is also able to show switching properties at the solid state, hence 1 mg/mL $CHCl_3$ solutions of OEG-SP were drop casted onto quartz substrates. Figure 4.2a shows that the relative population of the close and open ring forms in the SP/MC system can be modified by irradiation with a UV LED (~ 3 minutes). The appearance of the strong absorption band at about 560 nm is typical of the MC form, as well as the weaker absorption band at about 390 nm. These two features can be used as a fingerprint for the identification of the MC form in the polymer blend. By observing the pgBTTT spectrum in Figure 4.2b (black curve partially overlapped with the red curve), one can notice that pgBTTT has a very strong absorption band at about 600 nm, a value which is almost overlapping with that of MC. This is also confirmed by the color similarity of pgBTTT and MC solutions in $CHCl_3$. The polymer possesses an electric blue color, while the photoswitching molecule exhibits a brilliant violet-blue color.

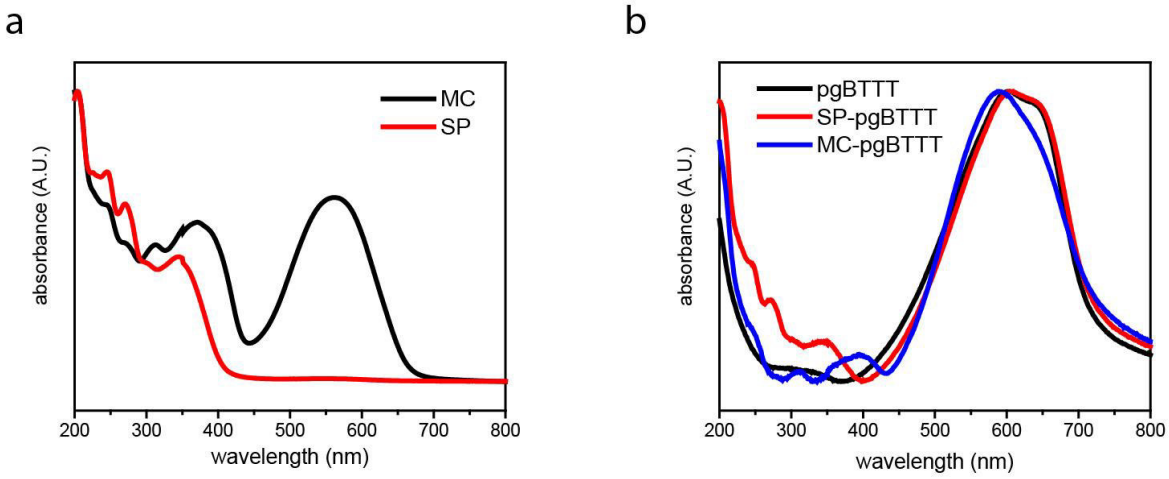

Figure 4.2: UV-Vis spectra of the SP/MC system, pgBTTT neat polymer and the 20% m/m blend. (a) the SP/MC system. Absorbance spectra of a thin film of SP drop casted from a 1 mg/ml $CHCl_3$ solution on quartz before and after (MC) irradiation with a 365 nm UV LED. (b) neat pgBTTT and OEG-SP/pgBTTT 20% m/m blends. Absorbance spectrum (pgBTTT) of a thin film of neat pgBTTT drop casted (1 mg/ml $CHCl_3$) on quartz. Absorbance spectra of the OEG-SP/pgBTTT blend before (SP-pgBTTT) and after (MC-pgBTTT) irradiation with a 365 nm UV LED. The spectra have been normalized by the intensity of the maximum peak in the range 550–650 nm. The spectra were collected by L. Cusin.

To prove the solid-state switching of OEG-SP within the blend it is thus necessary to identify at least two spectral regions where the absorption signal from the open MC form does not completely overlap with the pgBTTT spectral features. For the 20% m/m OEG-SP/pgBTTT blend as well, the two absorption spectra were collected before and after UV light irradiation for about 3 minutes. The major difference between the SP-pgBTTT and the MC-pgBTTT spectra (Figure 4.2b) is found at around 400 nm, where neat pgBTTT provides minimal spectral interference and the MC peak (blue curve) is at its maximum value, whereas the absorption of both pgBTTT and SP-pgBTTT thin films is minimum. A closer observation to the spectra reveals that the peak shape of neat pgBTTT, characterized by a shoulder at around 650 nm, is unaltered in the SP-pgBTTT form, but significatively changes in the MC-pgBTTT form by shifting the peak maximum to a lower wavelength.

4.2.3 OECT fabrication and thin-film characterization

OECT devices were fabricated on ultraflat quartz-coated glass substrates supplied by Ossila. Au source, drain and coplanar gate electrodes were deposited via thermal evaporation of a 2 nm Cr underlayer + 40 nm Au layer deposited at 0.1 Å/s at a base pressure of around 10^{-7} mbar and maximum pressure during deposition of 10^{-5} mbar. The channel parameters are W = 300 µm and L = 30 µm, yielding a channel area of around 9×10^{-3} mm^2, while the coplanar gate electrode had a rectangular shape of 3 × 4 mm^2, providing a gate to channel area ratio of around three orders of magnitude. The design and configuration of the electrodes were realized with CleWin layout editor. The final substrates with nanopatterned electrodes were designed and fabricated by P. A. Livio.

Before the polymer deposition, the substrates were treated via UV-ozone (5 min) using a Novascan PDS Pro Series system to improve the polymer adhesion (except where differently indicated). Thin films of the pure polymer were deposited on the substrate via drop casting (0.3 mg/mL in $CHCl_3$) or via spin coating (10 s, 2500 rpm, 2000 rpm/s, 0.05 mg/mL in $CHCl_3$) at room temperature. For polymer blends, the same processing parameters were employed but spiropyran derivatives were added to the solution to give a 20% m/m pgBTTT/SP blend at a fixed pgBTTT concentration. For concentrations above 0.3 mg/mL in $CHCl_3$, a polymer suspension was formed and many visible particles of polymer remained suspended in the solvent even after overnight stirring at 40 °C.

The active channel in OECT devices was fabricated via drop-casting to obtain thin films of thickness above 30 nm. The topography of films of the neat pgBTTT polymer and of the blend is shown in the AFM height images reported in Figure 4.3. These drop-casted films have a thickness of ≈ 60 nm for the neat polymer and of ≈ 30 nm for the blend. The surface of neat pgBTTT is characterized by numerous aggregates that may correspond to aggregated polymer, while the polymer blend shows a much smoother surface that indicates that the OEG-SP additive helps solubilizing the polymer aggregates and partially controls the thin-film morphology (the roughness over 2 × 2 μm^2 areas is R_{RMS} ≈ 10 nm for pgBTTT and R_{RMS} = 3.2 nm for OEG-SP/pgBTTT).

Finally, as a last step of the fabrication the channel area was isolated by mechanical scratching of the deposited film to minimize the leakage current effects. Remarkably, pgBTTT (and the blend) can be processed via spin coating of diluted solutions to yield ultrathin films of polymer. The characterization of such a system enables the investigation of interfacial effects, such as electronic properties at the OSC/electrode or at the OSC/dielectric interfaces.

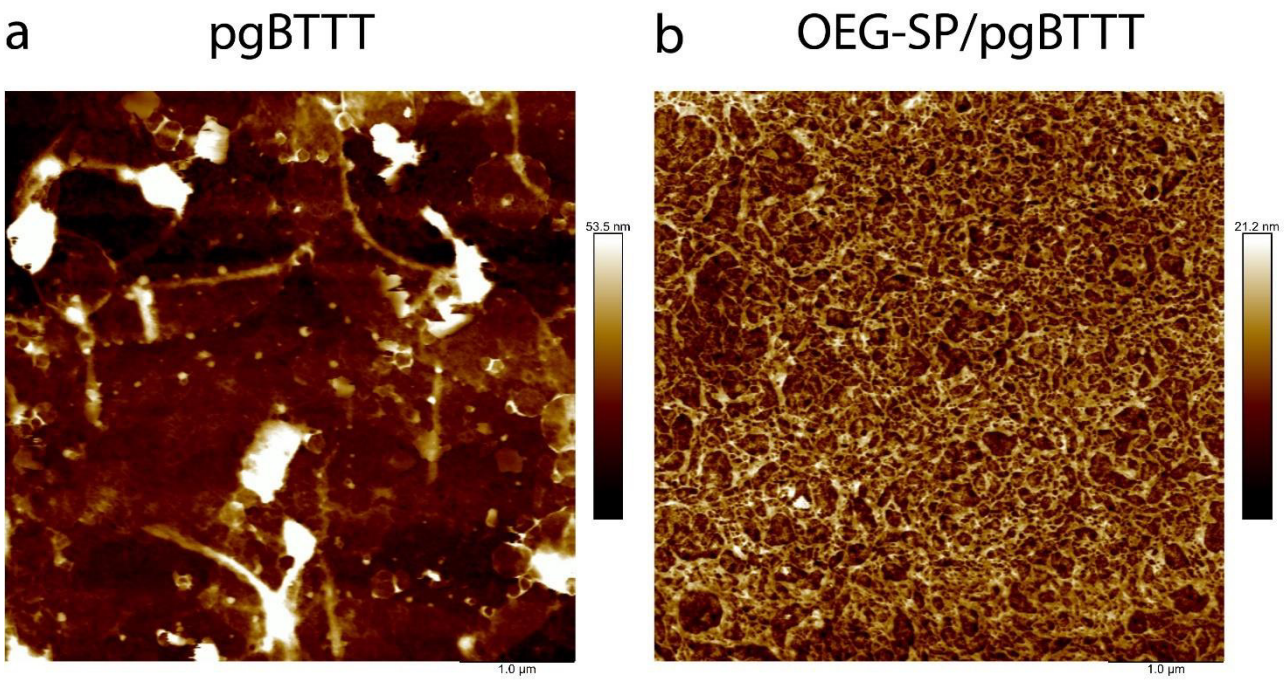

Figure 4.3: AFM height image of drop-casted films of neat pgBTTT and OEG-SP/pgBTTT 20% m/m blends. Both films are deposited on a SiO_2 substate from 0.3 mg/mL $CHCl_3$ suspensions. Image size: 5 × 5 μm^2. (a) neat pgBTTT, Z-scale: 53.5 nm, thickness: 60 nm, R_{RMS}: 10 nm (b) OEG-SP/pgBTTT, Z-scale: 21.2 nm, thickness: 30 nm, R_{RMS}: 3.2 nm. R_{RMS} is computed from 1 × 1 μm^2 regions.

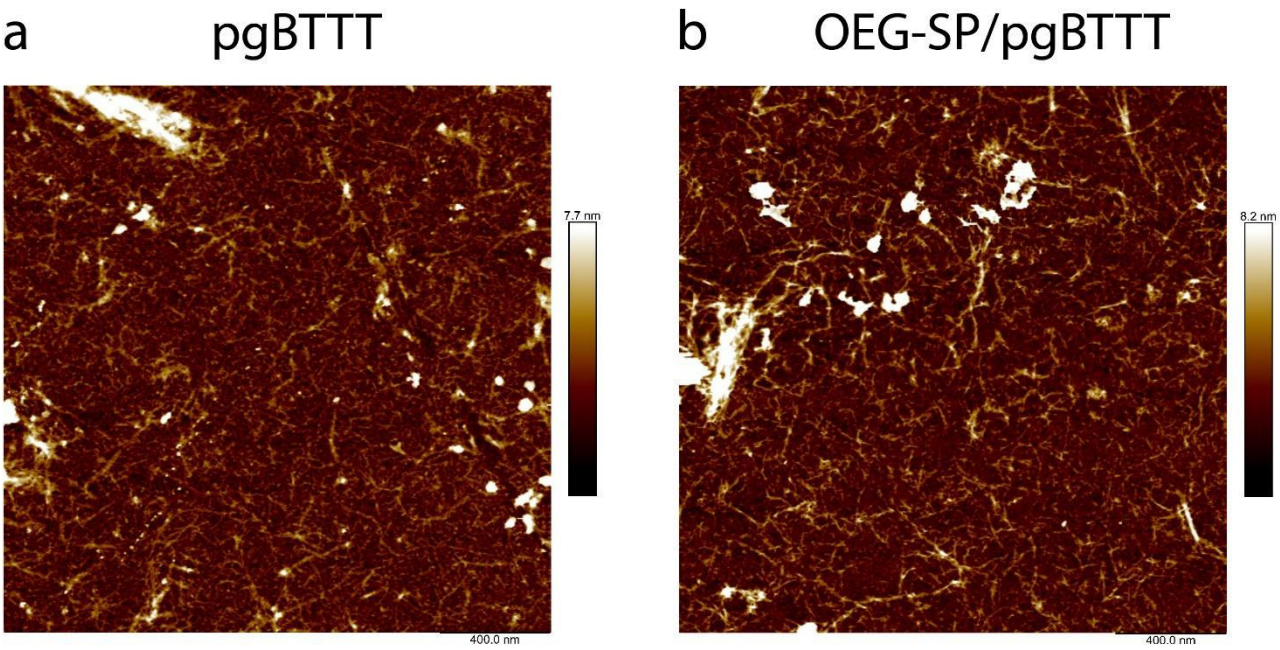

Figure 4.4: AFM height images of the spin-casted films of neat pgBTTT and OEG-SP/pgBTTT 20% m/m blends. Both films are deposited on a quartz substate from 0.05 mg/mL $CHCl_3$ solutions. Image size: 2 × 2 μm^2. (a) neat pgBTTT, Z-scale: 7.7 nm, thickness: 1.7 nm, R_{RMS}: 0.8 nm (b) OEG-SP/pgBTTT, Z-scale: 8.2 nm, thickness: 3.0 nm, R_{RMS}: 0.9 nm.

Thinner films obtained via spin coating are continuous, as shown by the AFM images reported in Figure 4.4, and have a thickness below 5 nm. Both surfaces show similar features, such as elongated, wire-like structures, that are all interconnected and completely cover the substrate. Some thicker regions associated to polymer aggregates (of much smaller size compared to the thicker films) are present in both samples. Such a similar topography suggests that the formation of the first interfacial layers is still driven by polymer/substrate interactions, with poor contribution from the additive. The film thickness slightly increases following the addition of OEG-SP from around 2 nm to 3 nm, still leaving the surface roughness unaltered.

4.2.4 Electrical Characterization of Optically Switchable OECTs

The characterization of optically switchable blends requires particular attention due to the possible photoconductivity of the polymeric matrix. The neat polymer might exhibit some degree of photoconductivity if its absorption properties overlap with the light utilized for the photoswitching of the SP additive. In addition, the advantage of adding a photoswitching elements resides on the prolonged subsistence of the electrical properties in one or in the other switching state, hence the long-term stability of the states and the degradation of the switching properties over time must be determined.

In this section, the photocurrent properties of the neat pgBTTT thin films are first investigated, as the timescales that characterize the photocurrent rise and decay represent the starting point for the further implementation of the optical switching properties of the blend. The entity of the photoswitching capability and the electrical stability of the photoswitching blend are then addressed.

4.2.4.1 Photocurrent in neat pgBTTT

Thin films of pgBTTT respond to the irradiation of light at the wavelengths that are used for the SP photoswitching. The study of the photocurrent response has been done on thicker (60 nm) films fabricated via drop casting of a 0.3 mg/mL solution of pgBTTT in $CHCl_3$ on a UV-treated prepatterned quartz substrate. The electrical measurements were carried out on OECT devices by using a Keithley 2636B SourceMeter unit. The two Au electrodes served as source and drain and were connected with micromanipulators to the probe station. A 0.5M NaCl solution in water served as the electrolyte with the gate (Pt grid) and reference (AgCl coated Ag wire) electrodes immersed. The electrolyte was contained in a PDMS pool in order to electrically isolate it from the testing probes and to increase the volume compared to a simple drop of electrolyte.

The neat pgBTTT OECT devices were first characterized in dark conditions. The transfer characteristics in the saturation regime are shown in Figure 4.5a. pgBTTT OECTs possess a channel depth (d) of 60 ± 5 nm and a channel aspect ratio (W/L) of 10. The threshold voltage (V_{TH}) is -50 ± 40 mV with ON currents reaching ~ 0.4 mA at a gate voltage (V_{GS}) of -0.5 V, and ON/OFF current ratios of ~ 10^4. Compared to state-of-the-art devices, the V_{TH} is shifted towards less negative values (-50 vs -250 mV), the absolute ON currents (vs 4 mA) and ON/OFF current ratios (10^4) are one order of magnitude lower. These differences can be explained by the different thickness (a factor 2 smaller) and by the UV-ozone treatment. Since the absolute current measured in a OECT device depends on the thickness, a lower ON current is expected and the ON/OFF ratio is affected by this loss of one order of magnitude in the absolute current. The UV-ozone treatment, instead, can influence the doping state of the polymer by providing free silanol sites and fixed charges that can interact with the OSC material and shift the V_{TH} towards more positive values.[285]

The pgBTTT OECTs were also tested under continuous light irradiation with the 530 nm LED. The transfer and the associated transconductance (g_m) curves are reported in Figure 4.5b.

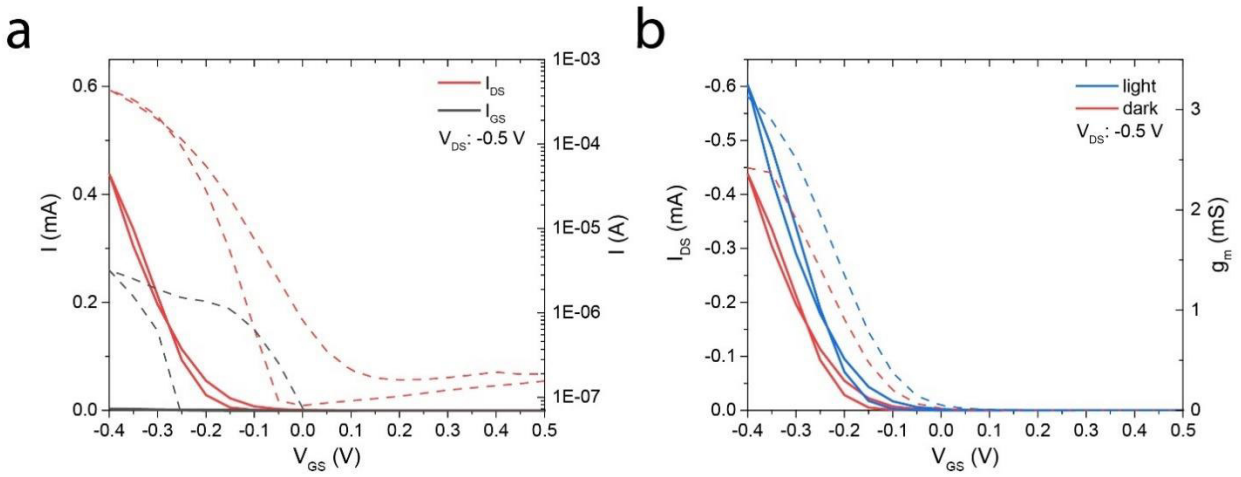

Figure 4.5: Transfer characteristics of pgBTTT OECTs and photocurrent response. V_{DS} was set at -0.5V, the sweep rate is 100 mV/s with a voltage step of 0.05 V. (a) Transfer and leakage curves of pgBTTT OECT devices recorded in the saturation regime in 0.5M NaCl in dark conditions. Solid and dashed curves are reported in linear and logarithmic scale, respectively. (b) Transfer characteristics of pgBTTT OECT devices in dark and under illumination with 530 nm light from a green LED. The transconductance (g_m) is also reported with a dashed line.

The values of g_m peak at 3.1 and 2.4 mS for the light and dark curves, respectively (at V_{GS}: -0.4 V and V_{DS}: -0.5 V). In fact, continuous illumination of the thin film causes an increase of the maximum ON current to about 0.6 mA, which corresponds to about 30% of photocurrent contribution relative to the current measured in the dark. While the shape of the transfer curve under irradiation remains almost unaltered, a V_{TH} shift of about +50 mV is consistently observed. With the parameters extracted from the transfer curves, the mobility-volumetric capacitance product (μC*) can be estimated from the transconductance, if the operation and the geometrical OECT parameters are known.[157]

$$g_m = \frac{Wd}{L}\mu C^*(V_G - V_{th}) \qquad \text{(Equation 4.1)}$$

For the OECT devices shown in Figure 4.5, W/L is 10 and d is 60 nm. A fair comparison of the g_m must be done at a common overdrive $V_{GS} - V_{TH}$ value. Hence, μC* products are compared at $V_{GS} - V_{TH}$ = -0.35 V, μC* giving 114 and 133 F cm^{-1} V^{-1} s^{-1} for dark and light curves, respectively. This value is about a factor 5 lower than the reference value for pgBTTT is a similar device configuration,[56] the value might differ due to the use of a different gate material.[264] To evaluate the timescale of the process of photoexcitation of charge carriers, the growth and decay of the photocurrent was monitored as a function of the illumination time, i.e., a chronoamperometry $I_{DS}(t)$ at device operation conditions (V_{GS}: -0.4 V and V_{DS}: -0.5 V) while turning on and off the 530 nm LED was performed (see Figure 4.6a).

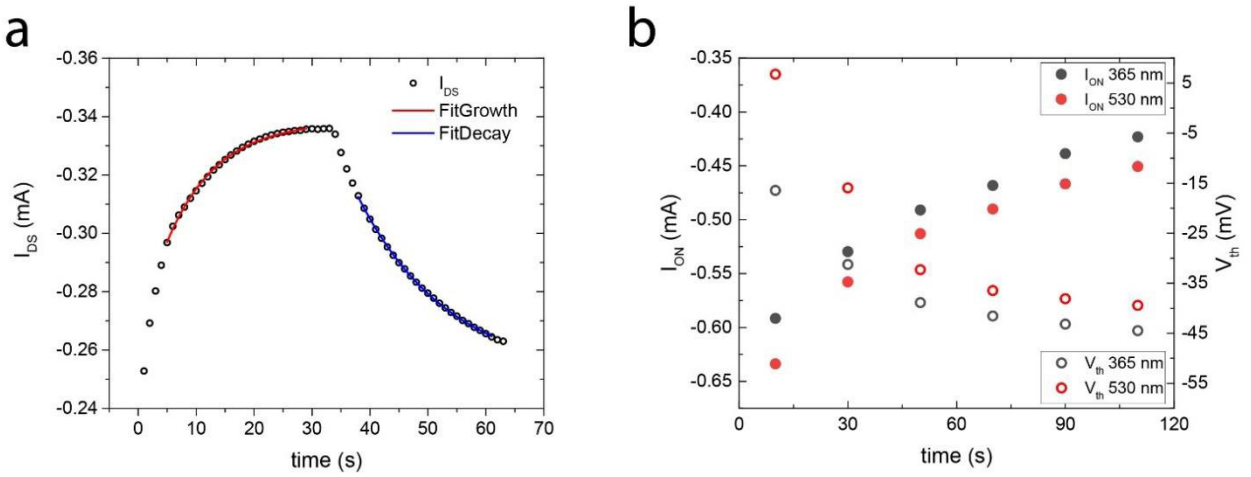

Figure 4.6: Photocurrent response of neat pgBTTT OECTs. (a) OECT current response during and after continuous illumination with a 530 nm LED. The curves obtained by fitting of the I(t) data during the growth (red) and the decay (blue) of the current are reported in the same graph. (b) Decay of I_{ON} and V_{TH} characteristics after photoexcitation of the pgBTTT OECT by irradiation with 365-nm and 530-nm LEDs.

From the $I_{DS}(t)$ response of OECT under different light conditions one can estimate the photocurrent growth (τ_g) and decay (τ_d) time constants. The $I_{DS}(t)$ response can be fit by a non-linear growth/decay equation equivalent to that reported in Section 3.3.3.1 (Equation 3.1) and estimate τ values during the growth and the decay of the transient photocurrent curve. The photocurrent τ values for pgBTTT OECTs are $\tau_g = 9 \pm 1$ s and $\tau_d = 16 \pm 2$ s, meaning that it takes a maximum time period of around one minute (a period $> 3\tau$) for the pgBTTT system to stabilize once a steady light condition is set during device operation. Since the photocurrent decay time is more critical than the current growth, the stabilization of the transfer characteristics as a function of time has been also determined. The time constants associated with the decay of photocarriers when the OECT is periodically switched on and off might differ from the ones obtained for continuous device operation. It is thus very important to verify if photogenerated carriers have different relaxation dynamics when the device is in the OFF state for some time during device switching.

Firstly, the pgBTTT OECT system was photostimulated for 2 minutes with either the 365 nm or the 530 nm LED to reach a steady state. Secondly, after switching off the light source, OECT transfer curves were consecutively collected every 20 s to determine the time dependence of the maximum ON current and of the V_{TH} values. Since every transfer curve starts at positive V_{GS} values (in the OFF state) and the maximum ON current value is obtained at around 10 s, these measurements have a time resolution of 20 s and an

initial time offset of 10 s. The maximum ON currents and V_{TH} values extracted during transfer characteristic measurements performed for 2 minutes are reported in Figure 4.6b. The data have been fitted with the non-linear decay equation previously described (Equation 3.1 adapted) and the resulting τ_d fitting parameters are shown in Table 4.1.

Sample	I_{ON} 365 nm	I_{ON} 530 nm	V_{TH} 365 nm	V_{TH} 530 nm
τ_d	60 ± 10 s	45 ± 6 s	26.8 ± 1.5 s	27 ± 4 s

Table 4.1: Decay time constants (τ_d) for I_{ON} and V_{TH} OECT parameters at V_{GS} = -0.4 V and V_{DS} = -0.5 V.

For an intermittent operation of the pgBTTT OECT devices, it is found that the decay time of the photocurrent is around one minute in the worst of the cases. Whatever change in the device ON current provoked by OECT irradiation with UV or visible light at the wavelength of the tested LEDs persists for the first minute, after which the value of the current has already decreased by at least 63% of the original value.

4.2.4.2 Substrate effect on ultra-thin pgBTTT OECTs

To test the effective influence of the substrate treatment in the modulation of the V_{TH}, ultra-thin pgBTTT films have been spin casted on clean (5 min sonication in acetone and then isopropanol) and on UV-treated prepatterned quartz substrates from 0.05 mg/mL solutions of pgBTTT in $CHCl_3$. OECT devices fabricated on clean quartz are referred to as "pgBTTT/SiO_2", while those fabricated on UV-treated quartz are referred to as "pgBTTT/UV-SiO_2". The resulting films have an average thickness of 1.4 nm (R_{RMS}: 0.8 nm) and 1.7 nm (R_{RMS}: 0.8 nm) for pgBTTT/SiO_2 and pgBTTT/UV-SiO_2, respectively.

Upon a low V_{DS} bias of -0.01 V, an ON/OFF ratio > 10^4 is achieved for both devices, with ON currents a factor ~ 3 times lower for the non-treated substrate at V_{GS}: -0.2 V (transfer curves in Figure 4.7). This change in performance cannot be simply explained by a different thickness, which can only account for ≈ 25% of the observed current. One reason is the different V_{TH}: about +300 mV and +400 mV for SiO_2 and UV-SiO_2 substrates, respectively. These values are significatively shifted from the V_{TH} (-50 mV) of thicker (> 50 nm) films on SiO_2 substrates, indicating that thinner pgBTTT films (down to 2 nm thickness) possess different doping characteristics from those shown previously (Figure 4.5). One possible explanation is that the equilibrium value for V_{TH}, controlled by substrate effects or ion diffusion from the electrolyte, is more susceptible to change in thinner films, providing a way to control V_{TH} via the channel depth.

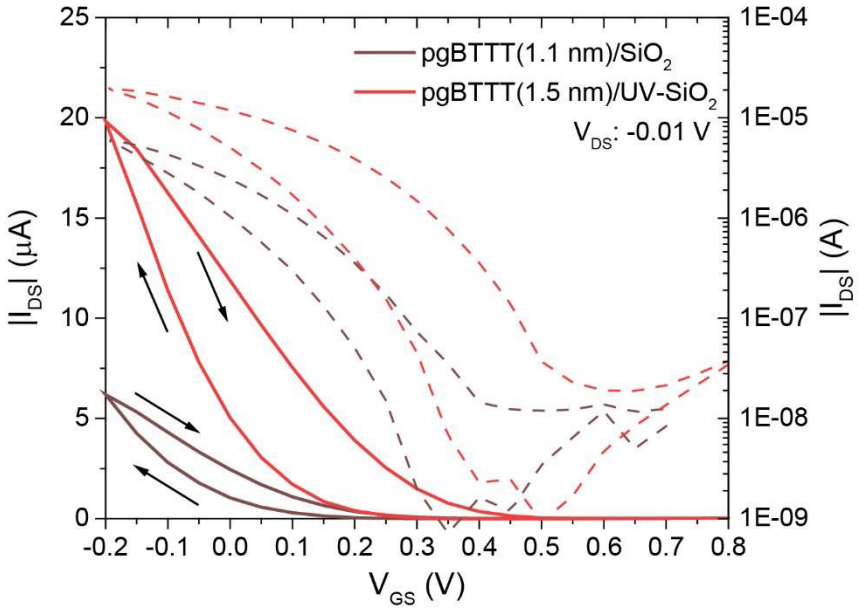

Figure 4.7: Transfer curves of pgBTTT OECT devices recorded in the linear regime (V_{DS}: -0.01 V) in 0.5 M NaCl at ambient conditions. The OECT devices were fabricated on clean quartz (SiO_2, brown) and UV-treated (UV-SiO_2, red) substrates via spin coating of 0.05 mg/mL pgBTTT solutions in $CHCl_3$. Voltage sweep rate: 100 mV/s. Linear (solid) and logarithmic (dashed) scales, the applied V_{DS} and the arrows illustrating the voltage sweep direction are reported in the figure.

Cicoira et al., in fact, found that the V_{TH} of PEDOT:PSS OECTs (depletion mode devices) was increasing with thickness, meaning that a more intense gate voltage was needed to dope the material (and thus deplete the charge carriers in the channel) at a larger channel thickness.[286] An increase of the ON/OFF current ratio for devices having thinner films was also found.[286] For a fair comparison, g_m values at the same $V_{GS} - V_{TH}$ ($V_{GS}(SiO_2)$: -0.15 V, V_{GS}(UV-SiO_2): -0.05 V), 3.4 μS and 6.4 μS for SiO_2 and UV-SiO_2 substrates, respectively, are considered. Under these premises, the differences in performance between the two substrates are not as pronounced as it seemed from a simple comparison of the maximum ON current.

Another relevant difference is that OECTs fabricated on UV-SiO_2 substrates showed a more marked hysteresis compared to the untreated samples, as it is better seen in the logarithmic scale plots in Figure 4.7. This phenomenon may arise from a capacitive contribution in the device response likely due to ion-trapping effects at the dielectric interface,[190] promoted by the formation of dangling silanol bonds produced via UV-ozone.

The data about neat pgBTTT devices that was collected in these last two subsections will serve as a reference (i.e., the blank sample) for the photophysical and electronic properties of OEG-SP/pgBTTT blends.

4.2.4.3 Photoswitching in OEG-SP/pgBTTT blends

Photoswitching experiments were also performed by using 365 nm and 530 nm LEDs. Devices fabricated from blends of 20% m/m OEG-SP/pgBTTT (0.3 mg/mL of pgBTTT in $CHCl_3$) were obtained via drop casting on UV-SiO_2 prepatterned quartz substrates. Transfer curves were collected from OEG-SP/pgBTTT OECT devices operating in 0.5 M NaCl electrolyte solution and, in between each measurement, alternately irradiated with either the UV (2 minutes) or the green LED (5 minutes) (Figure 4.8a).

The decrease in I_{ON} is about 20% of the initial value when the OECT is illuminated with UV light and I_{ON} recovery of more than 10% is observed upon illumination with visible (green) light. The I_{ON} of the OECT experiences an overall negative drift that do stabilize only after a few cycles, even though the current recovery associated with the switching to the SP form slowly continue to degrade (Figure 4.8b).

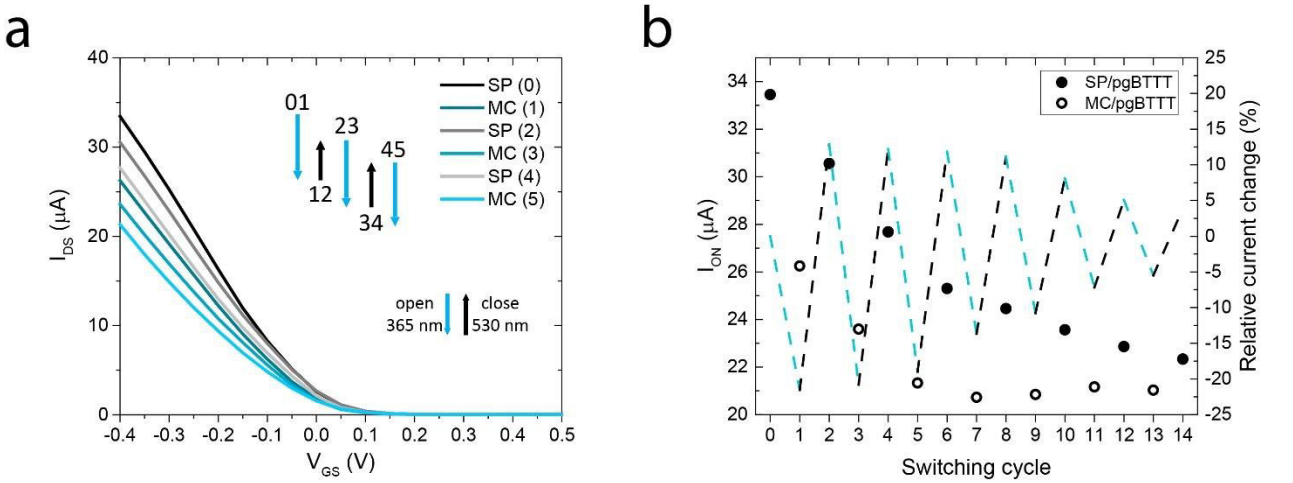

Figure 4.8: Photoswitching properties of OEG-SP/pgBTTT blends. V_{DS}: -0.5 V, 0.5 M NaCl electrolyte. Voltage sweep rate: 100 mV/s. (a) Transfer curves of OECT devices based on the polymer blend collected after the first three complete open/close cycles. Even and odd numbers refer to the closed (SP) and open (MC) state, respectively. The blue (downward, 365 nm LED) and black (upward, 530 nm LED) arrows indicate the optical switching between two states. For a more immediate visual interpretation, the length of the arrow is proportional to the change in current caused by the SP switching. (b) I_{ON} data for 14 switching operations (full, SP, and empty, MC, circles). The relative change in I_{ON} after each switching operation is indicated by a dashed line (light blue: SP opening, black: MC closing).

In fact, after around the 5th cycle of switching between the SP and MC forms, signs of photofatigue start to appear as it is commonly observed for non-immobilized SP.[287] The presence of the aqueous environment is also a factor that may contribute to the MC degradation due to hydrolysis.[288] A 57% loss in the initial signal after the 12th cycle of switching[287] is comparable to the 66% reduction observed (from 21.5% to 7.2% I_{ON} modulation). Overall, the I_{ON} of the OECT decreases by 40% due to photofatigue, with the concomitant gradual loss of the photoswitching capability.

Before further discussing the stability and degradation aspects of these OECTs, a performance comparison of the blend devices with the neat pgBTTT devices (previously reported in Figure 4.5) is provided in Figure 4.9. Table 4.2 compares the OECT characteristics. The V_{TH} of OECTs based on the OEG-SP/pgBTTT blend is +220 ± 30 mV, higher than that of neat pgBTTT devices (-50 mV) and with opposite sign. As from the forward sweep curves, those V_{TH} values indicate that blend OECTs are already in the on-state at V_{GS} = 0. The μC* product decreases from 113 to 7 F cm^{-1} V^{-1} s^{-1} due to the polymer blending with the SP species, as well as the ON/OFF ratio that decreases by about a factor of 10. The photoswitching capability of the OECT hence comes at the price of a reduced device performance.

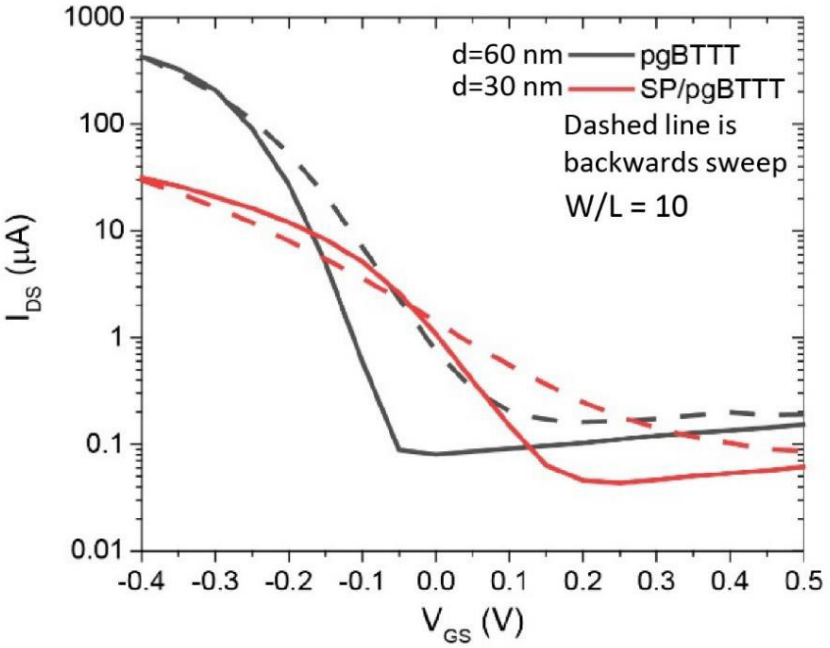

Figure 4.9: Performance comparison between neat pgBTTT and OEG-SP/pgBTTT (SP-pgBTTT) BC-Au OECTs. The OECT devices were fabricated on UV-SiO_2 substrates via drop casting of 0.3 mg/mL mixtures in $CHCl_3$. The transfer (forward, solid, and backward, dashed, sweep) curves are reported in logarithmic scale. V_{DS} = -0.5 V. Voltage sweep rate: 100 mV/s.

Parameter at $V_{GS} - V_{TH}$=-0.35 V	pgBTTT (d = 30 nm)	SP/pgBTTT (d = 60 nm)
μC* (F cm^{-1} V^{-1} s^{-1})	113	7.1
V_{TH} (V)	-0.05	+0.22
ON/OFF	5×10^3	6×10^2

Table 4.2: OECT figures of merit for neat pgBTTT and blend OEG-SP/pgBTTT devices.

4.2.4.4 Electronic properties of pgBTTT thin films

With the aim of clarifying the differences between the neat and the blend polymer, the characterization of the electronic properties of the two materials helps to understand how the doping state affects the OECT performance. Combining multiple techniques, such as KP, PYSA and UV-Vis spectrophotometry, is very important in the study of OECT materials, because their optoelectronic properties can radically change during the device operation, as seen in spectroelectrochemistry experiments performed on pgBTTT thin films.[56] How the electronic energy levels are modulated during the electrochemical doping of the material is also key to rationalize the OECT operation. Macroscopic KP and PYSA are two techniques that are performed at the solid/gas interface while electrochemistry experiments are run in a salt electrolyte. Remarkably, the effects of ionic doping in pgBTTT remain even after bias disconnection. Hence, the electronic properties of the films in the doped and undoped states were investigated via KP and PYSA before and after doping the polymer in a 0.1 M NaCl electrolyte solution. PYSA measurements were performed at a light spot intensity of 500 nW.

Thin films of pgBTTT of variable thickness were fabricated via drop casting (0.3 mg/mL in $CHCl_3$) on ITO-coated quartz and on Au substrates. The UV-Vis spectrum of these films is characterized by a strong absorption ascribed to a π−π* optical transition,[56] that peaks at about 602 nm (see Figure 4.2) with the absorption onset at 717 nm resulting in an optical gap of E_{OPT} = 1.73 eV. The reversible doping of pgBTTT thin films immersed in an NaCl electrolyte solution is characterized by a color change (the maximum absorption of the polymer redshifts from about 600 nm to 900 nm) from an electric blue tint to a pale shade that tends to transparency. The IE and the Fermi level of the polymer were measured for the polymer as deposited and after the processes of doping and dedoping on ITO substrates. The results are summarized in Table 4.3.

No significative variation of the IE is observed upon doping and dedoping processes, suggesting that the presence of Cl^- ions within the bulk of pgBTTT is not distorting the energetic landscape of the π-conjugated system. By contrast, the Fermi level is shifted towards the HOMO by almost 0.3 eV when Cl^- ions are intercalated, indicating that the material undergoes a p-doping. The incorporation of negative ions via electrochemical intercalation generates hole carriers in the pgBTTT backbone thus increasing the overall conductivity of the material.

Sample		ITO	pgBTTT as deposited	pgBTTT (V_{GS}: -0.5 V)	pgBTTT (V_{GS}: +0.5 V)
Property	IE (eV)	5.04 ± 0.03	5.29 ± 0.05	5.32 ± 0.05	5.28 ± 0.03
	E_F (eV)	4.81 ± 0.02	4.50 ± 0.01	4.79 ± 0.06	4.54 ± 0.03

Table 4.3: IE and E_F of pgBTTT on ITO before and after doping (V_{GS} = -0.5 V) and dedoping (V_{GS} = +0.5 V) experiments in 0.5 M NaCl. The experimental parameters of substrate (ITO) and pgBTTT thin films were measured in ambient air and averaged for n ≥ 3 samples.

The IE of pBTTT is about 5.1 eV,[284,289] and the measured values for pgBTTT are found to be around 5.3 eV. This value is in contrast with that reported by Hallani et al.[56] (4.73 eV), but such a low value of IP was only obtained by P3AT derivatives with no electron withdrawing groups.[290] It is instead more common to find larger IP values when a alkyl chain is replaced by a OEG chain, as in the case of C8-BTBT and OEG-BTBT which possess IE of ≈ 5.20 eV[291] and 5.54 eV,[190] respectively, as determined by PYSA.

To evaluate the effect of UV irradiation on the two material components, further KP and PYSA experiments were performed upon 5-minute UV illumination (see Table 4.4).

Sample		pgBTTT	OEG-SP
Before UV	IE (eV)	5.33 ± 0.06	5.68 ± 0.01
	E_F (eV)	4.46 ± 0.02	4.58 ± 0.02
After UV	IE (eV)	5.33 ± 0.05	5.65 ± 0.03
	E_F (eV)	4.51 ± 0.01	4.41 ± 0.02

Table 4.4: IE and E_F of pgBTTT on Au and OEG-SP before and after 5 min irradiation with a UV LED at 365 nm.

The illumination of pgBTTT via a UV LED does not significatively affect the energy levels of the polymer, indicating its stability towards 365 nm light irradiation. The spiropyran itself has IE and E_F values higher than the polymer, but, on the contrary, the merocyanine form (OEG-SP after UV, OEG-MC) is more n-doped by about 0.2 eV compared to OEG-SP. Note here that during the PYSA experiments the spiropyran sample underwent no significant color change upon UV irradiation (about 5 minutes). Instead, after illumination with a UV LED at 365 nm for the same period of time it completely turned to a dark violet color.

Finally, the electrochemical and the UV photoswitching experiments were carried out together on the polymer blend deposited onto ITO substrates (Table 4.5). The IE and E_F values for neat pgBTTT films are reported again for reference.

Sample		pgBTTT	pgBTTT/SP	pgBTTT/MC	pgBTTT/MC*
V_{GS}: 0 V	IE (eV)	5.29 ± 0.05	4.96 ± 0.05	4.99 ± 0.04	
	E_F (eV)	4.50 ± 0.01	4.45 ± 0.03	4.48 ± 0.03	
V_{GS}: -0.5 V	IE (eV)	5.32 ± 0.05	5.11 ± 0.01	4.95 ± 0.03	4.94 ± 0.01
	E_F (eV)	4.79 ± 0.06	4.59 ± 0.02	4.46 ± 0.01	4.55 ± 0.01

Table 4.5: IE and E_F of pgBTTT and the photoswitching blend on ITO upon electrochemical doping (V_{GS} = -0.5 V) in 0.5 M NaCl and photoswitching experiments. For pgBTTT/MC at V_{GS} = -0.5 V the photoswitching was performed after electrochemical doping (*: the electrochemical doping was done on the switched pgBTTT/MC film). The experimental parameters were measured in ambient air and averaged for n ≥ 3 samples.

The primary effect of the blending is to reduce the IE of the blend compared to the neat polymer. Since OEG-SP is a compound with IE higher than pgBTTT, the 0.3 eV reduction in the blend IE cannot be ascribed to the 20% m/m presence of the photochrome, also because the addition of such a compound would not change the minimum IE of the material to whom the PYSA technique is sensitive. Such a change in electrical properties from the neat polymer to the blend might be due to different structural properties of the blend, e.g., increased chain disorder or a different crystalline packing. Asides from this major change, it is remarkable that the IE – E_F difference (related to the doping character of the material) remains around 0.5 eV before and after EC doping of the blend, but also when the blend is photoswitched via UV, indicating that there is already an accumulation of charge carriers at 0 V, in agreement with the V_{TH} values determined previously (refer to Table 4.2).

The effects of UV photoswitching are evident in the EC-doped blend, as the 0.15 eV shift in the IE (towards a more oxidized material), ascribed to the EC doping, is neutralized by the conversion of the OEG-MC form in the blend (reducing effects on the material). Note here that due to the relatively high solubility of the OEG-MC form in the water electrolyte, accurate IE and E_F values were collected when the photoswitching experiment was performed after the electrochemical doping step. The 0.15 eV change in IE causes a variation in the charge injection due to a different injection barrier at the Au/polymer interface that could be responsible for the photomodulation observed on OEG-SP/pgBTTT devices.

4.3 Conclusions and Outlook

A first example of optically switchable OECT devices has been fabricated starting from the blending of a well-known mixed conductor, such as pgBTTT, and a versatile photochromic derivative based on a spiropyran core decorated with OEG chains. The bottom contact devices obtained via drop-casting of neat pgBTTT exhibited state-of-the-art performance, with minor mobility and ON/OFF current ratio losses due to different device geometries. Similar devices, based on a blend of pgBTTT and OEG-SP, were demonstrated to modulate the OECT ON current by a factor 30% upon illumination with 365 nm UV light. The addition of the device photoswitching capability came with a further decrease in OECT mobility and ON/OFF ratio of about one order of magnitude with the switching property decaying after about six switching cycles due to photofatigue and causing and the irreversible I_{ON} negative drift occurring over time that stabilized at about 10-12 switching cycles. In fact, the OEG-MC form might easily interact with the water environment by being partly solubilized by the electrolyte and brought into solution. Further improvements to this system could be implemented by a better chemical design of the OEG-SP core, that could involve structural modifications of the switching core to limit the aggregation of molecules in the MC form as well as modifying the side chains to reduce the detrimental interaction with water.

Once these stability issues are addressed, understanding the mechanism underlying the changes in OECT current, such as those occurring during reversible photoswitching, is key to the development of a reliable photoswitching system. The determination of the energy levels (such as IE, WF, E_F, optical gap, etc.) was found to give important insights into the process of doping and dedoping induced by the EC switching as well as the changes of the electronic states due to UV illumination. The decrease in the ON current

of OEG-SP/pgBTTT devices observed upon UV illumination could be explained by a reversible variation of the hole injection barrier resulting from a 0.15 eV shift of the IE of the blend.

Besides the electronic properties, there are many other aspects to investigate in order to understand the complexity of the observed behavior. A very important characteristic of OECTs based on pgBTTT is the structural ordering of the polymer backbone and side chains, which can dramatically influence the device performance.[56] The switching from SP to MC may induce structural changes that can be evaluated by a structural XRD analysis. Compared to the neat pgBTTT OECTs, there is a clear change in the device behavior upon irradiation as the pure polymer exhibited photocurrent enhancements (only) for both UV and visible light (Figure 4.6b). The UV photocurrent quenching in the blend, instead, might suggest that more fundamental processes might be involved in the formation/depletion of charge carriers. This seminal work finally outlines the major challenges that need to be overcome to introduce optical switching properties in materials and drives the path towards the integration of these light-sensitive properties in bioelectronic devices for their future development.

5 Vertical Conductivity in Small-Molecule OFETs

The interest in developing OSC materials during the last 45 years can be mainly attributed to the discovery of the semiconductive properties of doped polymers.[1] In the following years, OSC materials showed great potential for low cost fabrication of OFETs over large areas.[46] In applications requiring ease of processing on different substrates and ease of tuning of the (opto)electronic properties of the active material, OFET devices represent a valid alternative to their inorganic counterpart thanks to the wide tunability of the molecular structure of OSC small molecules, oligomers and polymers. In the very last decade, most of the research efforts towards the development of OFETs have been focused on the improvement of the charge carrier mobility, although the transit frequency did not experience a significative enhancement, remaining far below 1 GHz.[51] Of all the OFET characteristics, this latter parameter (determining whether or not a device can be used for fast switching electronics) has received little attention, even though it is fundamental for the operation of short-channel transistors. Hence, the future scaling-up of OFETs into commercial electronics hangs on the successful overcoming of the current performance and stability limitations. Among the objectives for this decade, three main challenges have been identified: (i) minimizing the contact resistance in devices channel lengths below 1 μm, (ii) if the velocity of carriers is limiting the transit frequency, the channel length might be decreased to values below 100 nm, (iii) the large-area nanofabrication of OFETs with sufficient device-to-device uniformity and thin-film homogeneity.[51]

One of the factors affecting the contact resistance in OFETs is the out-of-plane conduction.[292] The charge carrier mobility value that is generally reported in OFET devices is the in-plane mobility, originating from the horizontal transistor geometry. OSC materials, however, undergo self-assembly with the π-stacking direction oriented either parallel (face-on) or perpendicular (edge-on) to the normal of the substrate surface. The solid-state assembly can determine significant differences in the extracted carrier mobility, as in the case of P3HT, showing a mobility anisotropy of factor ≈ 100.[71] In the past decades, new OSC structures have been designed and optimized while having in mind this "lateral" device geometry. Despite being crucial for the transfer of charge carriers between the source and drain electrodes and the conductive OSC channel in both planar and staggered geometries, the charge transport in the vertical direction has been poorly studied as thinner and thinner (down to monolayer) OSC films became the main object of investigation. The issues regarding contact doping and

charge injection are still to be addressed in these ultrathin-film devices, whose critical factors played so far only a minor role in OFET research.[293] The processing and fabrication methods for the best performing OSC materials reported until now have been devised for OFETs built with this traditional lateral configuration, even though an alternative approach involving a vertical OFET configuration is recently gaining popularity to overcome some of the challenges listed above.[161] To bring further progress to the field, a deeper understanding of the phenomena occurring at the OSC/electrode interface is a prerequisite to an advanced design of materials and devices.

This chapter proposes the characterization of unconventional electronic properties (e.g., the vertical conductivity) of thin films based on small-molecule OSCs via an approach involving scanning probe microscopy and other techniques that can locally and macroscopically reveal the electronic states of the electrode and the OSC materials. The core of this work resides on the use of C-AFM for the mapping of the electrical current in thin films grown on Au exhibiting a sufficiently uniform topography with oriented terraces. Many complementary techniques were also employed to investigate the electronic properties governing the process of charge injection, such as KP and PYSA. Moreover, a focus on the effects of environmental contamination on bare Au is included in the initial part of the chapter to address the uncertainty in the positioning of the Fermi level of the electrode (the WF of Au can change by 1 eV depending on its fabrication and storage conditions).[117] Aspiring to reunify some of the past works by using an original approach, a method of analysis of the vertical conductivity harmonizing multiple information from different techniques is the final aim of this chapter.

5.1 Charge Transport Properties in OFETs

As discussed throughout this thesis, OSC materials possess conductive properties that can be reversibly modulated by orders of magnitude via the application of external stimuli, such as a gate voltage, a light pulse or ionic doping. This switching characteristic is at the base of transistor devices. In the past decades, new OSC materials with mobilities exceeding 10 $cm^2 V^{-1} s^{-1}$ have been synthesized and characterized but it appears that the field reached its maximum potential. Stretchable OFETs are currently under development but the technologic challenges are still numerous and the actual applications very limited.[294] As a consequence, the interest of companies in OSCs for logic operations started to fade[43] and recent claims of record mobilities started to be

doubted by a great part of the organic electronics community who also tried to standardize the methods for the assessment of mobility.[79]

Nowadays, many contact and contact-free methods for the evaluation of the charge transport properties in OSC materials are available (see Section 2.1) but, among them, the most practical and widespread is by characterizing an OFET. Not only the device itself provides a straightforward measurement of the charge carrier mobility, but it also serves as a primary component of plastic electronics circuitry.[295,296] The traditional lateral OFET configuration is more accessible to standard nanofabrication protocols that require particular attention when vertical geometries are used instead.[297] In both cases, the mechanisms underlying the charge injection at the metal/OSC interface are still challenging to understand and to model computationally,[298,299] as the structural properties of buried interfaces are complicated to access. One way to circumvent these limitations is by planning stepwise experiments where the thickness of OSC material is increased progressively to monitor the changing of properties during the interface formation.[143]

This section analyzes the performance of OSCs by comparing the figures of merit of OFETs or other devices in which the material is integrated. These devices are specifically designed for the study of either vertical or lateral conductivity. The electrical properties are also measured locally with C-AFM.

5.1.1 Vertical and Lateral Mobility in OSC

OSC materials present highly anisotropic charge transport properties, as previously outlined in the introductory chapter. The device configuration and geometry are thus designed to exploit at best the intrinsic characteristics of the material, so that the maximum performance is achieved in the optimized device with high operational and environmental stability.[300] Since μ in state-of-the-art lateral OFETs has reached a seemingly insurmountable plateau, researchers were forced to explore novel unconventional routes for the improvement of conductivity, such as light-vacuum strong coupling[301,302] or chiral-induced spin selectivity effect,[303,304] but these attempts would require much more involvement of the scientific community to prove that such an effortful molecular design and device fabrication provides the sufficient and cost-effective improvements.

One of the most promising routes at the moment of writing is the development of vertical OFETs (VOFETs) that are devices in which the three electrodes are vertically stacked, with two electrodes at the two extremes and a third ("permeable") electrode sandwiched in between.[297] The working mechanism of some VOFETs geometries is similar to that of lateral OFETs, but in some other cases the functioning is remarkably different.[305] All the OSC materials developed until now are very good conductors in plane, but only few of them possess also a good out-of-plane conductivity (as outlined in Section 1.2.3). Although vertical devices require more sophisticated nanofabrication, the full potential of VOFETs is still to be uncovered but recent results are encouraging.[306] The tools to determine the vertical conductivity are already available for most of the groups that study lateral OFETs, hence it is just a matter of paradigm change to move the interest of organic electronic researchers to this relatively novel field.[307]

The key to succeed in OSC material design for device application is first by achieving isotropic transport of charge. For lateral OFETs, the in-plane isotropy is prioritized,[308–310] but VOFETs require a much more balanced lateral and vertical charge transport.[311] A second step is to be able to optimally dope the target OSC material to improve charge injection and extraction at the contact but also the charge transport in the channel.[312] Doping approaches targeting the improvement of well-established OSC materials for transistor applications recently experienced several advances that regard not only the device performance and stability, but also the environmental sustainability and the biocompatibility of materials and processes.[313] The control of thin-film morphology and doping in rubrene-based devices yielded record vertical hole mobilities and reliable operation on flexible substrates, proving that the 1 GHz frequency (obtained for a diode device) is a realistic objective for VOFETs.[314]

The current state of the art in the determination of μ from device-like samples is mainly represented by OFET mobilities. The mobility extraction from other types of device measurements requires a careful choice of electrodes or particular geometrical requirements.[162] Contact-free techniques were also discussed in Section 2.1. C-AFM enables the local measurement of μ, but being in the space-charge-limited current (SCLC) regime is a prerequisite that can be challenging to achieve.[163] In addition, the basics of mobility anisotropy determination are described with reference to the relative techniques and models used.

5.1.1.1 OFETs

In a simplistic perspective, depending on the OFET geometry, either the vertical (VOFET) or the lateral mobility (OFET) are determined. In lateral OFETs, the determination of mobility anisotropy can be done with high angular resolution provided that a single-crystal device is fabricated.[315,316] In polycrystalline devices, grain orientation can significatively affect the overall mobility, as grain boundaries can severely limit the transport of charge between adjacent crystalline domains.[186] The grain size is a critical aspect in the fabrication lateral OFETs, as the process of ordered assembly of OSC materials can be easily altered by the substrate roughness and the deposition parameters, consequently affecting the performance.[80] In VOFETs, the entire device thickness (comprising the electrodes) can be easily kept below the micron,[317] hence the grain size is not particularly relevant for thin films based on OSC that are used for lateral OFETs since their growth is smooth in the vertical (short) direction.[318] For an optimization of the vertical mobility, new chemical design strategies are being adopted to improve the electronic coupling in the vertical direction.[319]

Regarding the figures of merit, the lateral and vertical OFETs share common features, but some of those differ quite significatively due to the intrinsic characteristics of device geometries and working principles. VOFETs, for example, are compared based on current density (J) and ON/OFF current ratio.[161] Areal current density are meaningful for vertical transistors, where the section of the active channel is well defined, but for lateral transistors it is not so trivial to define the lateral section of charge transport, which is not simply defined by the thin-film thickness. An example of electrochemical VOFET reached operational J values > 1 MA cm^{-2} for about one hour and an ON/OFF ratio of ~ 10^8.[320] Generally, traditional VOFETs exhibit J values around 1 A cm^{-2} in a dual-base configuration[321] or a few orders of magnitude smaller.[161] However, leakage currents (nA range) higher than lateral OFETs (< pA range) correspond to these higher current densities in VOFETs.[322] Lateral-channel OFETs are mostly compared in terms of field-effect mobility, which is currently standing at $\mu \approx 20$ cm^2 V^{-1} s^{-1},[43] being still an important parameter for VOFETs (where vertical mobilities are still below 1 cm^2 V^{-1} s^{-1}),[297] but not as practical as J for direct comparison. ON/OFF current ratios are also usually reported for lateral OFETs, as values above 10^6 are desired for a clean device switching.[43]

Transit frequency is a parameter that regards both lateral and vertical OFETs and has a great importance for applications in high-speed electronics.[51] The operation frequency of VOFET already easily reaches the MHz range,[323] with an example of transit frequency of 40 MHz.[324] By contrast, low-voltage lateral OFETs are still struggling to achieve transit frequencies in the order of 10 MHz.[293] Due to the current limitations on the device switching frequencies, remarkable progress has been done on OFETs by transferring the state-of-the-art performances to nanometric devices on flexible substrates.[325,326]

5.1.1.2 C-AFM

Depending on sample preparation, C-AFM can be performed in lateral or vertical geometry thus enabling the investigation of both the in-plane and the out-of-plane charge transport. By controlling the substrate wettability, the assembly of organic molecules at the solid state can be driven towards an edge-on or a face-on arrangement. In the lateral configuration, a metal electrode of finite size is deposited on top of the OSC thin film, and the C-AFM tip is contacted at a known distance from this electrode to record the lateral current. In the vertical configuration, the electrode is deposited on the whole substrate and then coated by the OSC thin film. In this latter case, the C-AFM tip can be contacted at any region that is uniformly coated by the OSC and the film thickness must be known.

C-AFM studies of OSC materials have been pioneered by Frisbie, who reported point-contact current measurements on sexithiophene thin films in both vertical[327] and lateral[328] configurations. The OSC channel potentiometry[329] and single grain boundaries[108] were then studied on the same OSC system upon application of a gate bias. The advantage of the C-AFM technique, other than being able to select where to perform I−V curves via a point and shoot method, is that it can provide a current mapping at constant bias.[330] C-AFM is useful, for example, when the sample has a non-uniform conductivity like the conductive/insulating lamellae of PEDOT:PSS films[331] or the fibrillar structures in P3HT films.[332] This technique is thus unique for its capability of mapping not only the electrical, but also the mechanical properties of surfaces as a function of the temperature.[333] The applications of C-AFM in organic electronics are not only limited to thin films,[334] but also SAMs on metals can be studied.[335] C-AFM investigations in lateral geometry enable also the OFET characterization in a three-terminal setup, with the possibility to perform the transmission line method (TLM) at

different probe locations without the necessity of an additional electrode nanofabrication step.[336] C-AFM was used to demonstrate the (unusual) lack of dependence of OFET performance on the OSC grain size that was ascribed to unusually conductive grain boundaries.[337]

Further modelling of the (vertical configuration) C-AFM measurements on thin films enabled the correct determination of μ_{out} by SCLC measurements.[163] Rigorously asymmetric I−V curves are measured in this regime, granted by asymmetric electrodes, one of which (either the substrate or the AFM tip) is electron/hole blocking.[338] For a planar SCLC geometry, the Mott-Gurney law (Equation 5.1) can be used to fit the diode-like J vs V curves to extract the charge carrier mobility.

$$\boldsymbol{J = \frac{9}{8}\varepsilon\varepsilon_0\mu\frac{V^2}{L^3}} \qquad \text{(Equation 5.1)}$$

Where ε is the relative dielectric constant of the OSC layer, ε_0 is the vacuum permittivity, V is the applied bias and L is the channel length. For this law to be applied, the carrier injection into the OSC material must dominate the transport behavior so that a space charge region is formed within the channel. This expression can be adapted to C-AFM measurements for a more accurate determination of the mobility by adding semi-empirical parameters:[163]

$$\boldsymbol{J = \alpha\varepsilon\varepsilon_0\mu e^{0.89\gamma\left(\frac{V}{L}\right)^{\frac{1}{2}}}\frac{V^2}{L^3}\delta\left(\frac{L}{D}\right)^{1.6}} \qquad \text{(Equation 5.2)}$$

Where α is a prefactor (8.2), δ is an empirical dimensionless parameter (7.8), D is the estimated diameter of the tip-substrate contact area and, there is some dependence on the field, γ ≠ 0, otherwise, γ is 0.[163] This model have been successfully applied, e.g., to conjugated polymer films[339] or to ordered face-on assemblies of phthalocyanines.[340] Equation 5.2 can be further adapted to include the built-in potential[338] and different contact mechanics models to obtain an analytical expression.[341] More complex models can also include the thickness dependence.[342]

C-AFM is a particularly suitable technique to study the out-of-plane conductivity, as the combination of local imaging and electrical contacting at the nanoscale avoids the problem of pinholes and electrical shorting when a top electrode is fabricated on an OSC thin film or when a Hg drop is used in molecular junctions.[343] With this technique, it

was possible to investigate the effect of the length of the alkyl chain in junctions comprising thin films of molecular assemblies.[344] The magnitude of the current recorded via C-AFM can be useful to discriminate between horizontally and vertically oriented crystalline domains in acene-based OSC thin films.[345] A comprehensive study on the application of C-AFM for the determination of the vertical mobility at the nanoscale in organic electronics, by Button and Mativetsky,[341] also proposed a method for high-resolution mapping of μ. Since the solid-state packing at the nanoscale well correlates with the out-of-plane hole mobility, morphological features in crystalline thin films can be easily associated to charge transport pathways.[346]

It is fair to note that C-AFM measurements typically require humidity controlled environments, as the environmental RH can promote local chemical reactions (e.g., in GO)[347] that can alter the electrical properties of the material. Another limitation of the technique regards the control of the applied force and the effective electrical contact area.[348] Since the contact-mode operation alters the tip shape and composition over time, the contact setpoint and the applied bias should be kept to minimum values to avoid current fluctuations and improve the overall accuracy of the measurement.[349] The ensemble of these factors contributes to increase the experimental uncertainty, hence a wide I−V curve sampling is required to estimate the electrical properties reliably.

5.1.1.3 Other Device Configurations

The determination of μ_{out} is not only limited to vertical OFETs and C-AFM. Conventional SCLC,[163] time of flight (ToF) and charge extraction by linearly increasing voltage (CELIV) measurements[332] are other common methods in organic electronics.

- SCLC: Due to the relative simplicity of the experimental setup (the active material sandwiched between two asymmetric electrodes) SCLC measurements are performed in solids since the fifties.[350] Deviations from the ideal SCLC regime are, for example, indicative of charge trapping.[351] Maximum care must be taken when comparing SCLC and OFET mobilities as they might differ by few orders of magnitude.[352]
- ToF: ToF requires both electrodes to be injection-blocking and the same sample can be used to measure both electron and hole mobilities.[162] The electric field dependence of the mobility[353] or its thermal dependence[354] can also be determined.

- CELIV: In a similar way to ToF, CELIV also requires both electrodes to be injection-blocking and both hole and electron μ values can be extracted from the same sample.[162] Extraction current transients can provide σ and n and reveal the field dependence.[355] In CELIV, σ and μ are not influenced by contact barriers found in the SCLC setup.[356]

5.1.2 Contact Resistance in OFETs

Contact resistance (R_C) represents another key parameter contributing to the overall performance of OFETs, and it is highly relevant in the framework of out-of-plane conductivity. A comprehensive review of the literature addressing the minimization of the contact resistance in OFETs (to width-normalized R_C values < 100 Ω cm) has been recently published by Klauk et al.[293] The need for consistently reporting R_C as a standard figure of merit of OFETs (alongside with reporting L and the parasitic gate-to-contact overlaps) is key to the further development of OFETs. This parameter has been steadily optimized in the past decades[292] towards driving the speed of devices above the GHz threshold.[357]

In a functional device, R_C is the resistive contribution of the contacting metal/OSC interfaces which arises from a complex convolution of injection and extraction barriers (refer to Section 1.4.3 about metal/OSC junctions), electrode and organic thin-film morphologies, the area of injection, the carrier density at the contacts and other parameters.[293] Another important parameter related to R_C is the transfer length (L_T), which is the average critical distance travelled by charge carriers above which they are transferred to the contact. This parameter is easier to model for TC configuration than for BC: the growth of OSC molecules in the contact region (metallic) is generally different from that in the channel region (dielectric). Hence, the electrical properties of injection and channel areas are comparable in TC configuration, but different in BC.[358] Reducing L_T below the length of the contact (L_C) in lateral OFETs can also cause current overcrowding and an increase of R_C, with significant impact on the effective μ and on the transit frequency.[359]

By decreasing L, the study of the origin of R_C to describe the contact behavior of OFETs by a model encompassing the complexity of organics devices becomes increasingly important.[358] The V_G dependence of R_C must also be taken into account as e.g., R_C usually decreases with increasing V_G in staggered TC OFETs, due to field-induced lowering of OSC channel and bulk resistivities.[360] Nonidealities and instability in the

OFET behavior are often arising from R_C issues or structural defects, hence the improvement of μ implies the realization of Ohmic contacts and the consequent elaboration of doping or blending strategies for addressing these issues.[361] A correct extraction of R_C and μ requires the identification of injection and bulk limitations to ensure that the experimental conditions for the use of conventional methods and techniques for the extraction of these parameters are fulfilled.[362] Moreover, simple approaches, such as lowering of the contact deposition rate,[363] or more elaborate ones involving a different device design, such as tuning the saturation coefficient in source-gated OFETs,[364] are the necessary tools to ultimately achieve contacts with an optimized charge injection.

The engineering of the active interfaces in organic electronics thus represents a central part in the device optimization process.[365] Besides the methods listed above, the general approach involves the doping of contacts either at the bulk OSC level or at the metal/OSC interface.[120] The effective doping of OFET devices has not yet been extensively explored due to the difficulties in controlling dopant diffusion, but it remains a fundamental strategy for defining the charge injection barrier and V_{TH}.[366] The molecular nature of organic compounds requires doping methods that are compatible with the physicochemical properties of soft materials. Hence, the realization of doping in organic electronics occurs via mixing with molecular dopants to form doped molecular assemblies via two main mechanisms: ion-pair and ground-state charge transfer complexation.[171] The quantitative doping of active materials enables a much improved device stability and avoids detrimental effects arising from ambient processing which may cause an unwanted performance variability.[313]

Changing the carrier density and the energy level alignment at the interface has profound consequences on R_C.[293] Incorporating a thin injection layer of e.g., an electron acceptor between the metal contact and a p-type OSC, despite apparently introducing an additional barrier to the transport of charges, improves the contact properties of lateral OFETs by reducing R_C compared to the unmodified device.[367] The doping of contacts, consisting of an interlayer of a material different from that of the active channel or the same material with different doping properties, can be directly transferred to VOFET devices in which the reduction of L_T is key to not only improve charge injection, but also to attain short transport paths for an ideal device operation.[368] Small L_T values are useful to avoid short channel effects, like high direct (source-drain) leakage currents and low I_{DS} modulation, that often affect VOFETs. If on

one hand a large injection barrier increases R_C, on the other hand it was shown that the modification of one of the electrodes (e.g., the source electrode) can reduce the direct leakage.[369] Methods that can provide a fine tuning of the electrode WF are thus necessary for the optimal trade-off of injection barrier and the resulting leakage current and R_C, e.g., graphene derivatives (like rGO) yield electrodes whose WF can be tuned with continuity in VOFETs.[370]

5.2 Interfacial properties of OSC on Metal Electrodes

The electronic properties of metal/OSC interfaces are far from the simple combination of the properties of these two components alone, as widely discussed in Section 1.4. Many other properties of OSCs are influenced by the underlying metal (or dielectric) substrate at the level of the interface,[109] hence why the multiscale characterization of the system under investigation is crucial for understanding the processes occurring at the microscopic scale. When studying systems that result from the coupling of two materials with very different properties, such as a metal and an OSC, the starting point is to consider the stability of the materials in the environment(s) of processing and of device operation. For instance, the sources of environmental contamination might differ between the two components and the assessment of the possible ways of degradation must be performed (or known) prior to the assembly of the coupled system. The same is true for other solid-state properties that play a role in the functioning of the final device, e.g., the energy levels or the degree of structural order of the atomic and molecular components.

This section aims to highlight all these aspects by showing to which extent the properties of the coupled system are comparable to those of the separate entities. Major attention is dedicated to the visualization of the surface topography, morphology and contamination to understand their correlation with electronic properties. A consistent part of this section contains experimental data that is my personal work although literature was also referenced for completeness.

5.2.1 Metal Electrode

Electrodes are often based on metals,[109] even though other type of conducting materials are being explored for this purpose, including polymers,[371] graphene,[372] carbon nanotubes,[373] metal oxides,[374] with the goal of overcoming the limitations associated with metallic materials, such as optical transparency, in organic

electronics.[375,376] Among metals, Au is probably the most popular and widely used material for metal electrodes in p-type OFETs and it thus serves as a reference for the study of this class of OSC. One of the reasons of its popularity, besides its moderate chemical inertness to most solvents, resistance to corrosion and the instability of its surface oxide at ambient conditions, is that its work function (WF) can be tuned almost continuously in a wide range with quite simple and straightforward procedures.[111,377] The determination of its electronic, morphological and other basic properties as a function of the crystalline orientation, sample characteristics, preparation and treatments is readily available in the literature and conveniently provides a consolidated platform for further applications in devices.[378–380] Despite being widely employed in many scientific contexts, the dynamics of Au surface properties are not completely understood.

By choosing Au as a representative material for metal electrodes, this subsection exemplifies the factors that one has to consider for utilizing metals in OFETs and to determine the charge transport properties of OSC in general. A novel perspective on the understanding of the Au surface contamination is here reported alongside with the structural and energetic aspects that characterize the surface of this metal at ambient processing conditions. Another key interpretation of these results is related to the contamination of the conductive AFM tip that occurs during measurement conditions as it is of utmost importance for both KPFM and C-AFM.

5.2.1.1 Surface Topography and Morphology

The topography of Au surface in electrodes is a result of the method of deposition, the substrate and the post-deposition treatments chosen. Polycrystalline films exhibit many surface defects, such as grain boundaries, and individual grains are oriented in different crystallographic directions.[381] The surface of those films can be imaged with dedicated scanning tunneling microscopy (STM) equipment, but ambient AFM techniques can only barely reach the sufficient lateral resolution to map the terraces. By contrast, ideal systems such as Au samples exhibiting oriented crystalline facets, e.g., Au(111) on mica, possess atomically flat surfaces and large terraces that are suitable to study the formation of surface contamination and SAMs.[380,382] Exemplificative images of Au(111) and polycrystalline Au surface topography are shown in Figure 5.1.

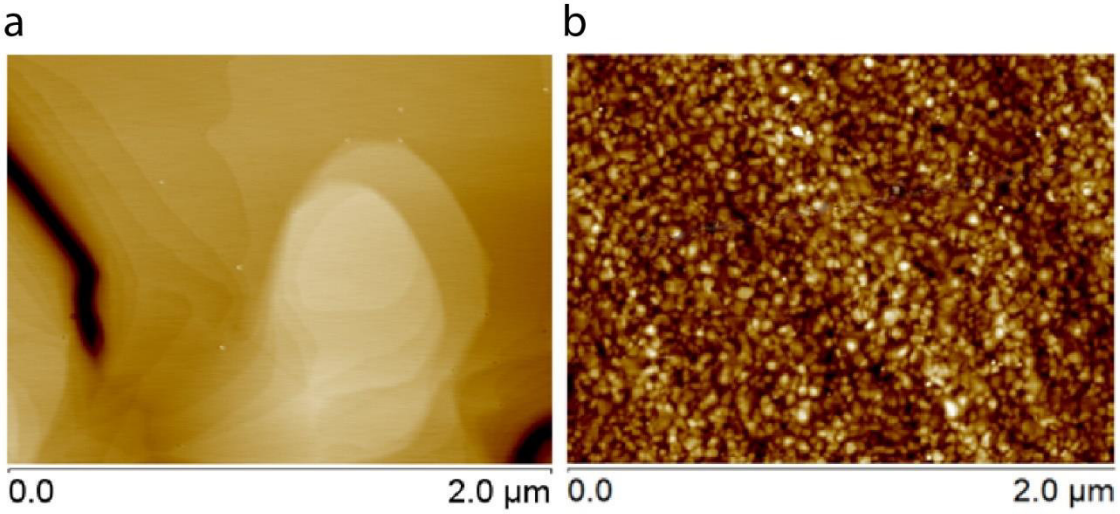

Figure 5.1: Tapping mode AFM topography of clean (a) Au(111) on mica and (b) polycrystalline Au on SiO_2 collected at ambient conditions. Z-scale: (a) 15 nm, (b) 13 nm.

Molecularly smooth Au thin films are mainly fabricated by vacuum deposition,[380] which requires a high vacuum environment, but sometimes a clean Au surface is needed at ambient conditions, hence template stripping can be used instead.[383] The control over the topography and morphology of these films can be tuned via the substrate or the deposition parameters.[384] Further surface treatments have different effects on the surface topography. Surface cleaning by ion bombardment, for example, disrupts the surface flatness as defective features appears after the treatment.[385] Annealing procedures, like flame annealing, can cure these damaged surfaces or increase the flat surface area of contaminated Au thin films while efficiently removing contaminant species.[386] Other surface cleaning techniques, such as plasma treatments, have an impact on the roughness of gold film surfaces.[387,388] To sum up, depending on the application, many tools are available to tune the surface morphology and topography.

The surface of atomically clean Au is hydrophilic and relatively inert, but molecular species of organic origin tend to absorb on it and completely cover it within a few minutes of exposure to ambient air due to its high surface energy when pristine.[389] The driving force for the formation of SAMs is that the same that governs the contamination of the surface, but the nature of the bond is different and still object of debate.[390] The Au surface is far from being intact upon adsorption of molecules, which is another factor affecting the surface topography. The topography of a clean Au(111) sample is dynamically affected by the process of contamination, as it undergoes a structural rearrangement of the terraces that sees step edges with a small curvature radius disappearing by being included within the surface.[169] A structural rearrangement is also observed when alkanethiol SAMs are formed.[391] Remarkably, the morphology

of gold also affects the air stability of SAM.[392] All these phenomena provide an outline of the complexity of gold surfaces and show that fabrication procedures of electrodes can have a strong impact on the surface morphology of the film and, consequently, on the OSC materials that are deposited onto it.

5.2.1.2 Surface Contamination

Environmental contamination mediated by adventitious carbon regards not only the surface of gold and inert metals but also that of aluminum,[393] copper and metal alloys.[394] Understanding the surface dynamics of Au is thus the starting point for the further generalization of the impact of adventitious carbon contamination on the morphological and electronic properties of metal electrodes. This contamination starts as a simple uniform layer but evolves over time with the formation of aggregates.[169] The process of airborne contamination was found to occur in two phases: (i) a rapid initial phase, taking place within the first minutes and completing in about one hour, in which carbon contaminants are adsorbed, and (ii) a slow subsequent phase involving the formation and growth of contaminant aggregates that migrate on the surface. The height and lateral size of these aggregates can reach values higher than 15 nm and 100 nm, respectively, thus significatively influencing the substrate roughness and the wettability properties of the contaminated Au surface. The surface topography of both Au(111) and polycrystalline Au is affected by the adventitious carbon in a similar way, as shown in Figure 5.2.

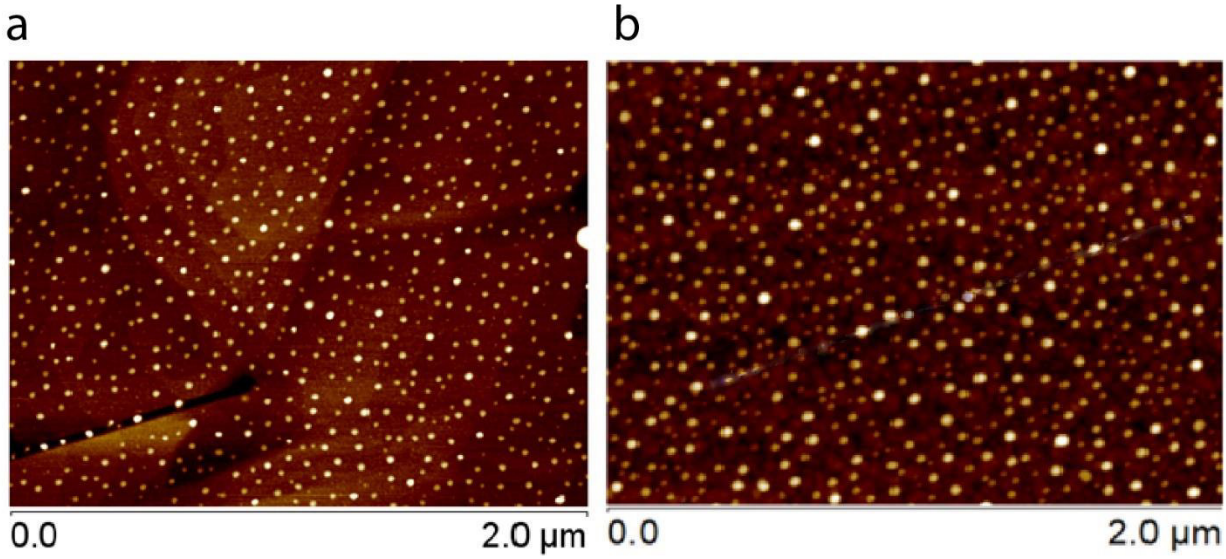

Figure 5.2: Tapping mode AFM topography of (a) Au(111) on mica and (b) polycrystalline Au on SiO_2 collected at ambient conditions after 1 week of exposure to ambient air. Z-scale: (a) 11 nm, (b) 15 nm.

5.2.1.3 Electronic Properties: WF

As previously mentioned, different crystalline orientations can lead to large shifts in the WF for the same metal (~ 1 eV), as observed in the emblematic example of atomically clean tungsten, W(111) and W(110), surfaces that possess WF of 4.47 eV and 5.25 eV, respectively.[395] The presence of adventitious carbon can lead to WF changes over time of 0.5 eV within the same identical surface.[169] When the variation in the sample WF are relatively small (e.g., from different crystallographic orientations in Au[396] and Ag)[397] the effect of the environment should be considered and the complete removal of adventitious carbon is a fundamental part of the preparation protocol.

The methods for the determination of the energy levels have been introduced in Section 2.2. Here, KP and PYSA have been employed to measure the WF of Au samples. The WF estimated via PYSA from the onset of the photoelectron yield (PY) spectra, which is directly correlated to the minimum photon energy required to extract an electron from the metal. KP, instead, provides a measurement of the contact potential difference (CPD) that reflects the difference in WF between the KP tip and the sample. By calibrating the tip WF via an HOPG reference, the sample WF is known. Both KP and PYSA are operated in ambient air (KP equipment can also be used in e.g., vacuum or nitrogen environments) hence the measurements can be affected by the environment.

Obtaining an atomically clean metallic surface in air is quite challenging, as even the noble metals (i.e., Au, Pt and others) interact quickly with water, oxygen and the carbon species present in the ambient. Template-stripped Au films can immediately generate a clean hydrophilic surface as soon as the mica substrate is removed, so that the properties of "clean" Au can be practically studied without the need of vacuum processing.[383] WF and CPD do not coincide in absolute value due to the intrinsic differences in the measurement techniques, but the recorded curves exhibit a similar trend, as shown in Figure 5.3. During the first 15 minutes these values quickly decrease to reach a minimum after about one hour, due to the process of contamination, to then slowly increase again and partially recovering the starting values due to an equilibration process involving the Au surface and its layer of contamination.[169]

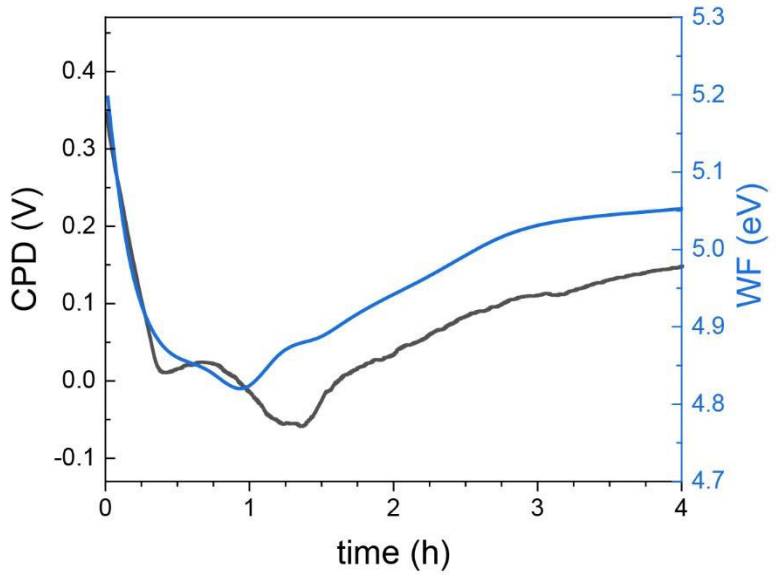

Figure 5.3: CPD (black, KP) vs WF (blue, PYSA) curves collected from template-stripped Au(111) at ambient conditions. The tip calibration WF for CPD measurements is Φ_{ref} = 4.83 eV.

The process of contamination of metals, here exemplified by Au, is believed to occur in two distinct phases: during the starting phase the surface of Au is covered by airborne adsorbed species within minutes and a process of surface reorganization occurs until the growth and aggregation of clusters of contaminants dominates the surface dynamics. If the Au surface is stored before its subsequent use, these two phases can be controlled by considering the storage environment as a reactor containing a defined number of contaminant species.

When the surface is stored in an open ambient, the air is an infinite source of contaminants and the adsorption of new species with subsequent aggregation occurs indefinitely with a process that may took even a month to reach equilibrium and it is subject to the fluctuation of environmental conditions. By contrast, the storage in a closed, sealed, container is characterized by a drop in the concentration of contaminants (even in non-vacuum-sealed containers). At some point, the concentration of contaminant is not sufficient for further adsorption and only the aggregation of clusters occurs, with no further nucleation. The WF decreases during this process as the contaminants migrate to aggregates which decrease in number. The surface thus reorganizes to a condition similar to that observed during the first hour of contamination, with few sparse aggregates and a large (contaminated but not aggregate-covered) surface area characterized by a decreasing WF.

This open-close cycling process, highlighting how the contamination process is slowed down by the storage in sealed containers which is typically adopted in worldwide laboratories, is shown for a polycrystalline Au sample in Figure 5.4. The data for Au(111) can be found in Figure 7 of the main text of the paper published in Advanced Materials Interfaces (DOI: 10.1002/admi.202100068).[169] Aggregation of contaminant clusters dominates nucleation when the Au sample is stored in the closed container. A similar behavior in the WF of polycrystalline Au samples was observed. The PYSA measurement provides not only an estimate of the sample WF, but also contains information about the thickness of the overlayer covering the electron-emitting surface.[398,399] Thicker layers of carbon contaminants reduce the amount of electrons detected in the PYSA measurements, hence resulting in the decrease of the absolute PY. The square root of the PY is plotted as a function of the incident photon energy. The slope of the linear fitting used to extract the onset is eventually related to the amount of carbon contaminants adsorbed on the surface. From Figure 5.4, the decaying trend of the PYSA spectra slope thus indicates that contaminant aggregates nucleate and grow, reaching an almost steady-state condition after ≈ 10 days, while the WF can still be modulated by about 0.1 eV by opening and closing storage cycles.

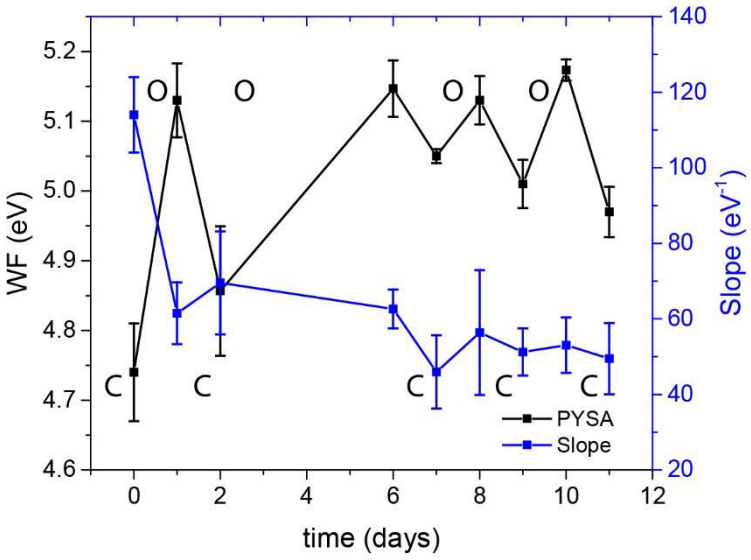

Figure 5.4: WF (black squares) versus PY slope (blue squares) changes of a polycrystalline Au sample upon cycles of exposure to ambient conditions and closing in a glass container. O and C letters in the graph indicate the storage conditions (O = open laboratory air; C = closed in a glass container).

5.2.1.4 Electronic Properties: WF tuning

Tuning the WF of Au electrodes can be accomplished by the chemisorption of suitably designed SAMs or over/underlayer deposition of a contact dopant. The most common SAMs are based on thiolated molecules,[400] yet recently some alternative molecular scaffolds have been proposed including N-heterocyclic carbenes[401]. The interlayer method involves either the use of strong donor (or acceptor) organic compounds,[147] polymers[376] or transition metal oxides.[374] In this thesis work, only the SAM approach was employed, which will be the focus of this subsection.

The tunneling barrier correlated with the presence of a SAM between the active material and the electrode affects R_C which increases exponentially as a function of the molecular length of alkanethiols.[402] This trend is true also for fully conjugated molecular wires such as oligophenyleneimine SAMs.[403] The increase in the measured C-AFM current resulting from a reduction of effective thickness induced by conformational photoswitching of a thiol-based azobenzene SAM further confirms the interdependence of the tunneling barrier and the molecular length.[404] Henceforth, short SAM-forming molecules are preferred for OFET applications, as the tunneling contribution to the overall resistivity can be minimized. Thiol-based SAMs are usually deposited from solution due to the good solubility of thiols in most organic solvents. It should be noted that low concentrations, in the order of ≈ 1 μM, are sufficient to yield complete monolayers of octadecanethiol on Au, with higher concentrations making the absorption process quicker.[405] The adsorption reaction is electrochemically reversible, as the selective desorption of the SAM-forming molecules can be exploited to remove the SAM from one of the two electrodes to give a pristine Au surface and enable the fabrication of asymmetric electrodes at ambient conditions.[406]

Some of the most studied thiols for Au electrode functionalization are conveniently listed in the table below (Table 5.1). With the exception of hexadecanethiol (C16SH), that decreases the WF of Au, similarly to other n-alkanethiols, only SAMs yielding Au surfaces with WF values above 5 eV were considered, as those are of higher interest for studies on p-type OSC. Lower WF values are already provided by ambient-contaminated Au surfaces, hence, the use of simple n-alkanethiols has been typically limited to pioneering studies on SAMs, and low-WF (~ 4 eV) metal electrodes (Al, Cu, Ag) can be used instead.

Compound	WF_p (eV)	WF_k (eV)	CA (°)
PFBT	5.50*	5.55*	81.8[407]
PFDT	5.64*	5.94*	117.9[118]
C16SH	4.05*	4.10*	115-105[408]
NBT	5.20[409]	-	43.2[409]-61.9[118]
FBT	5.21[410]	-	81.8[409]
HBT	5.22[409]	-	30.9[409]
MBA	4.95*	-	81.8[407]

Table 5.1: WF and CA of a selection of Au surfaces coated by thiol-based SAM. Literature values are followed by the reference. Values that were experimentally determined by the author are denoted by an asterisk. WF_p = determined via PYSA, WF_k = determined via KP. Instrumental error is below 0.05 eV.

5.2.2 Organic Semiconductors

Before studying the coupled system of OSC and the metal electrode, the surface properties of OSC thin films on flat and inert oxide substrates (such as SiO_2 and Al_2O_3 on Si wafers) are investigated. The thin films of OSC reported in this section were fabricated via thermal evaporation by F. Modesti.

5.2.2.1 Surface Topography and Morphology

Thin films of OSC grow forming polycrystalline structures if no particular deposition techniques are adopted, as outlined in Section 1.3.4. It is a common mistake to identify the grain boundaries from the topography AFM image of organic thin films as the apparent border regions defined by height minima. Each apparently monocrystalline domain is frequently composed of multiple subdomains possessing different crystalline orientation (see Figure 5.5).

The DNTT thin film in Figure 5.5 was thermally deposited (at 0.1 Å/s, 100 °C) on Al_2O_3 substrates treated with TPA. DNTT is one of the best film forming OSCs due to the good film continuity, characterized by a relatively flat and ordered terraced topography on oxide substrates, thus resulting in low roughness. The surface topography of these thin films is also characterized by the diffuse presence grain boundaries defining the microcrystalline domains (regions with lateral size around 1 μm). The solid-state order in polycrystalline OSC films is of central importance, as an additional source of resistance in OFETs is charge transport through grain boundaries.[411] Nevertheless, the dimension of these topographic domains (here referred to as apparent domains or grains) is still indicative of the maximum size of the crystalline domains in the thin film.

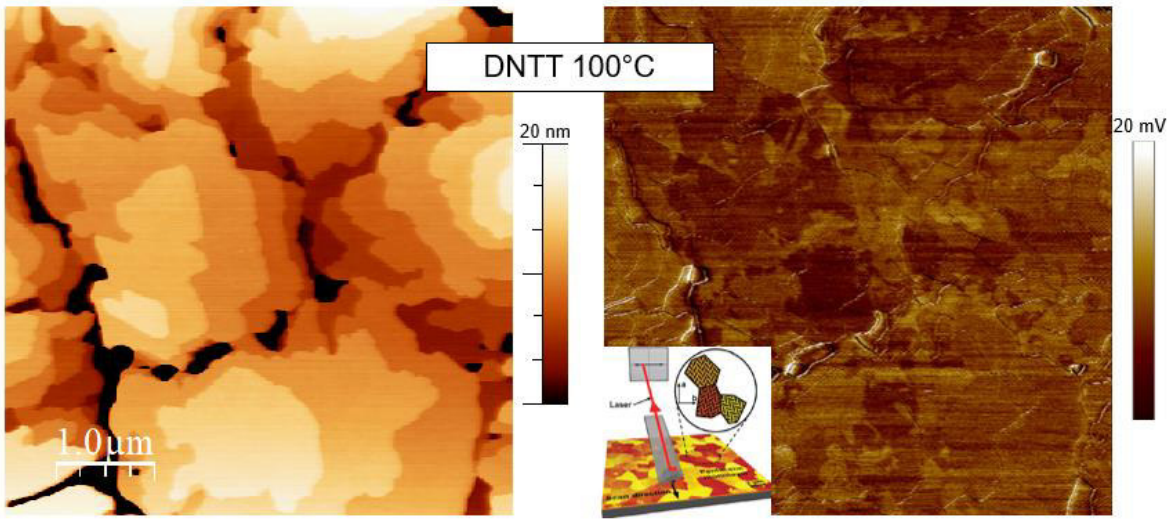

Figure 5.5: Topography and TSM images of a DNTT thin film thermally evaporated at a substrate temperature of 100°C. The TSM contrast indicates sample regions of domains possessing a different crystalline orientation thus highlighting the actual grain boundaries.

The prediction of the topography of thin films based on small-molecule OSC resulting from structural variations is still a challenging task for theoreticians, given that even the correct prediction of crystalline motifs based on the molecular structures is a hard task. Anyway, if a compound is available and can form films via thermal deposition, the empirical approach is quite rapid and practical and a screening of the resulting topography is easily done. A variety of AFM images collected on thin films of small-molecule OSC, reported in Figure 5.6, compares the surface topography upon slight molecular structure changes. One of the most successful modifications in terms of device performance, stability and processability is the attachment of alkyl side chains to conjugated thiophene-based cores, such as DNTT[412] and BTBT[90] derivatives.[413]

One peculiarity of n-alkylated derivatives is that thermally-evaporated thin films are characterized by a terraced topography, like their non-alkylated counterparts, but tend to form tall lamellar structures that stand out from the surface by tens of nm.[224] This behavior is here exemplified by C8-DNTT (a) and C12-DBTTT (b), the alkyl derivative of dibenzothiophenothieno[3,2-b]thiophene (DBTTT). The substitution of tert-butyl (tBu) side chains to these two cores (e) causes the complete disappearance of lamellae for DBTTT (but not a dramatic increase in the apparent domain size) and a partial, but significant, reduction for DNTT also characterized by larger terraces. Lateral functionalization of DNTT with chiral chains (d), synthesized by M. Volpi, provides terraces as large as those in DNTT, but very fragile films and OFET performances not as good as C8-DNTT (the study of this chiral compound is still undergoing). The tBu-

thiophene derivatives of BTBT (c) show the most disordered topography with the presence of numerous aggregates and terraces of reduced dimensions. Finally, in (f), further extension of the conjugated core is also detrimental to the surface topography, that is dramatically less ordered for the non-alkylated DN4T and isoDN4T.

Poor control of the morphology is characteristic of vacuum processed films. When molecules are soluble enough, optimized solution processing methods offers major film quality and excellent device properties.[105] Correlating thin-film morphology with device performance is nowadays necessary to publish, as it provides a supplementary means of comparison among different deposition methods.[80] This approach is often key to discriminate multiple novel compounds deposited by the same technique.[414] Hence, by locally observing and identifying the crystallization mechanisms of OSC molecular assemblies a fine control of the thin-film morphology can be ultimately achieved.[415]

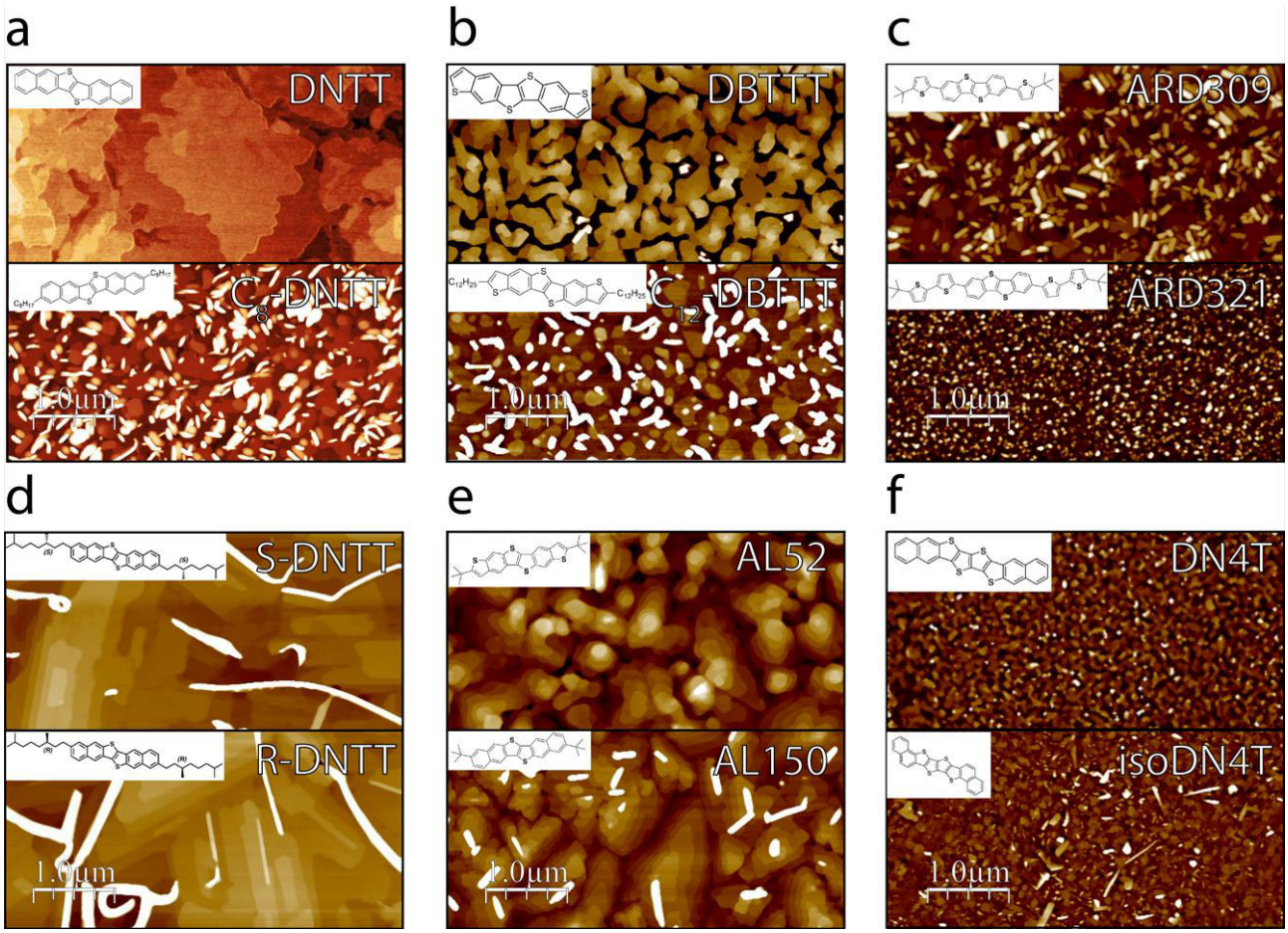

Figure 5.6: Topography images of thermally evaporated small-molecule OSC thin films. (a) DNTT (T: 70, Z: 15) vs C8-DNTT (T: 100, Z: 35), (b) DBTTT (T: 70, Z: 45) VS C12-DBTTT (T: 70, Z: 20), (c) ARD309 (T: 130, Z: 70) vs ARD321 (T: 130, Z: 30), (d) S-DNTT (T: 100, Z: 70) vs R-DNTT (T: 100, Z: 70), (e) tBu-DBTTT or AL52 (T: 130, Z: 25) vs tBu-DNTT or AL150 (T: 130, Z: 30), (f) DN4T (T: 100, Z: 35) vs isoDN4T (T: 100, Z: 100). Substrate temperature (T) values are expressed in °C and Z-scales (Z) in nm.

5.2.2.2 Surface Contamination

One of the great advantages of OSCs is that they form clean interfaces with many materials and they are also able to preserve this cleanliness in ambient environment.[109] Thermally-evaporated thin films deposited from high-purity compounds exhibit outstandingly clean surfaces (see Figure 5.6) that are suitable to be investigated by AFM techniques, but realizing similar samples via solution processing requires much more optimization. The problem of residual surface contamination in solution-processed films is generally not critical for device operation, but local characterization techniques might be completely hindered by the presence of a contamination layer (e.g., TSM).

Surface contamination in OSC thin films results from a poor optimization of the deposition parameters, from solvent or solution contamination and degradation, or from difficult evaporation of the solvent and/or incomplete crystallization with formation of amorphous.[416] The continuous improvement of solution processing technologies is currently focused towards a better molecular alignment but more fundamental aspects, like understanding the solution drying process and the effects of environment (e.g., temperature, RH etc.), still pose relevant questions about the reproducibility of the OSC thin films.[417]

5.2.2.3 Electronic Properties: IE and E_F

Within the work of this thesis, PYSA has been employed on both powder and thin-film OSC materials. Thanks to the properties of surface cleanliness and environmental stability of benzothiophene small-molecule derivatives, the IE can be usually determined with a precision below 0.05 eV with average values that persist over months of storage at variable ambient conditions. A variety of IE from small-molecule OSC is summarized in Table 5.2.

The most remarkable trends that emerge from this table are: (i) the functionalization with a n-alkyl lateral chain decreases the IE compared to the naked core and (ii) tBu functionalization increases this value instead. E_F has also been determined via macroscopic KP on small-molecule OSC deposited on thin films to verify the doping state of the materials deposited. The determination of E_F is not essential for determining the energy level alignment, as the IE is the crucial parameter governing the charge injection barrier at metal/OSC interfaces. The KP technique requires the sample to be sufficiently conductive, hence the E_F measurements were carried out on OSC thin films supported

on Au substrates. However, as discussed in Section 1.4, it is known that the E_F value of OSCs on metals is affected by the interaction with the substrate. The following section, Section 5.2.3, addresses the changes in OSC material properties arising from the formation of the metal/OSC junction.

Class	Compound	IE_p (eV)	IE_t (eV)
DN4T	DN4T	5.27 ± 0.02	4.85 ± 0.01*
	isoDN4T	5.22 ± 0.01	4.95 ± 0.01*
	C8-DN4T		4.94 ± 0.01
	C10-DN4T		4.97 ± 0.05
DNTT	DNTT	-	5.16 ± 0.04
	C8-DNTT	-	4.94 ± 0.01
	tBu-DNTT (AL150)	-	5.38 ± 0.01
	S-DNTT	5.23 ± 0.01	5.19 ± 0.01
	R-DNTT	-	5.23 ± 0.01
	S+R-DNTT	-	5.23 ± 0.01
BTBT	C12-BTBT	-	5.21 ± 0.04
	C7-BTBT	5.28 ± 0.02	-
	tBuC6-BTBT (I)	5.78 ± 0.03	-
	tBuC6-BTBT (II)	5.57 ± 0.03	-
	OEG-BTBT	-	5.54 ± 0.03
DBTTT	DBTTT	-	5.13 ± 0.01
	C12-DBTTT	-	5.10 ± 0.01
	tBu-DBTTT (AL52)	-	5.31 ± 0.01
perylene	OMT	5.07 ± 0.05	-
	TMP	5.27 ± 0.05	-
	OMP	5.43 ± 0.02	-

Table 5.2: Ionization energies of a selection of small-molecule OSC as determined by PYSA. IE_p: powder, IE_t: thin film. All the IE_t values were collected from thin films on dielectric substrates except for * = PEDOT:PSS substrate. S+R-DNTT indicates a sample obtained by co-sublimation of S- and R-DNTT. OMP, TMP and OMP indicate terrylene and perylene derivatives. tBuC6-BTBT is reported as two polymorphic forms (I and II).

5.2.3 Organic Semiconductors on Au

Depositing the OSC material on the rougher surface of a metal, i.e., Au, compared to that of SAM-treated SiO_2 and Al_2O_3, can severely affect the thin-film morphology, the self-assembly and the solid-state electronic properties. Some degree of improvement can be achieved by also functionalizing the Au surface with a SAM, also providing major advantages regarding charge injection. However, reaching the same thin-film properties and quality both on Au and on the dielectric substrate by either thermal evaporation or solution processing is not only important from a device perspective but also for the characterization of the fundamental properties of OSC, that might significantly differ from one morphology to another.

With the aim of assessing the impact of the changes occurring at the level of the substrate/OSC interface due to roughness and substrate wettability properties, this section discusses the formation of OSC interfaces on Au with reference to SAM-treated metal oxides. Further considerations on the energy levels in the coupled metal/OSC systems are then included in the discussion.

5.2.3.1 Surface Topography and Morphology

In the previous section, a variety of surface topography images was collected on different film forming OSC molecules deposited via thermal evaporation (see Figure 5.6). Among all of these, DNTT and chiral-DNTT showed the best film forming properties, by exhibiting large terraces in both cases and showing a reduced number of lamellar structures in the latter case. These two molecules are hereby used to exemplify the changes in morphology occurring when moving from a (flatter) metal oxide surface to a (rougher) metal surface.

In Figure 5.7a, the evolution of the topography of a 10-nm-thick film of DNTT upon substrate changes is reported. A thickness of 10 nm is not always sufficient to completely cover the substrate if the growth process is characterized by a Volmer-Weber or Stranski-Krastanov modes. Dewetting phenomena at ambient conditions are also a relevant issue of DNTT thin films which tend to restructure by forming islands on SAM-treated dielectric substrates in the hour timescale.[418] Thin films on PFBT-treated gold surfaces showed a much better coverage compared to those on bare Au. The presence of some taller features surrounded by the substrate (darker areas) suggest that dewetting processes might be occurring also on thin films on metal. This phenomenon is much more pronounced for bare Au substrate than for PFBT ones, as it can be observed in Figure 5.7a.

Another interesting example of substrate-induced morphology is that observed on (thicker) 50-nm-thick R-DNTT films. While µm-large lamellar structures are evident on TPA-Al_2O_3 substrate, those features completely disappear in the bare Au sample, that is characterized by few sparse aggregates and much smaller apparent grains with terraces that are not perfectly parallelly oriented to the substrate, due to templating effects of the substrate (Figure 5.7b).

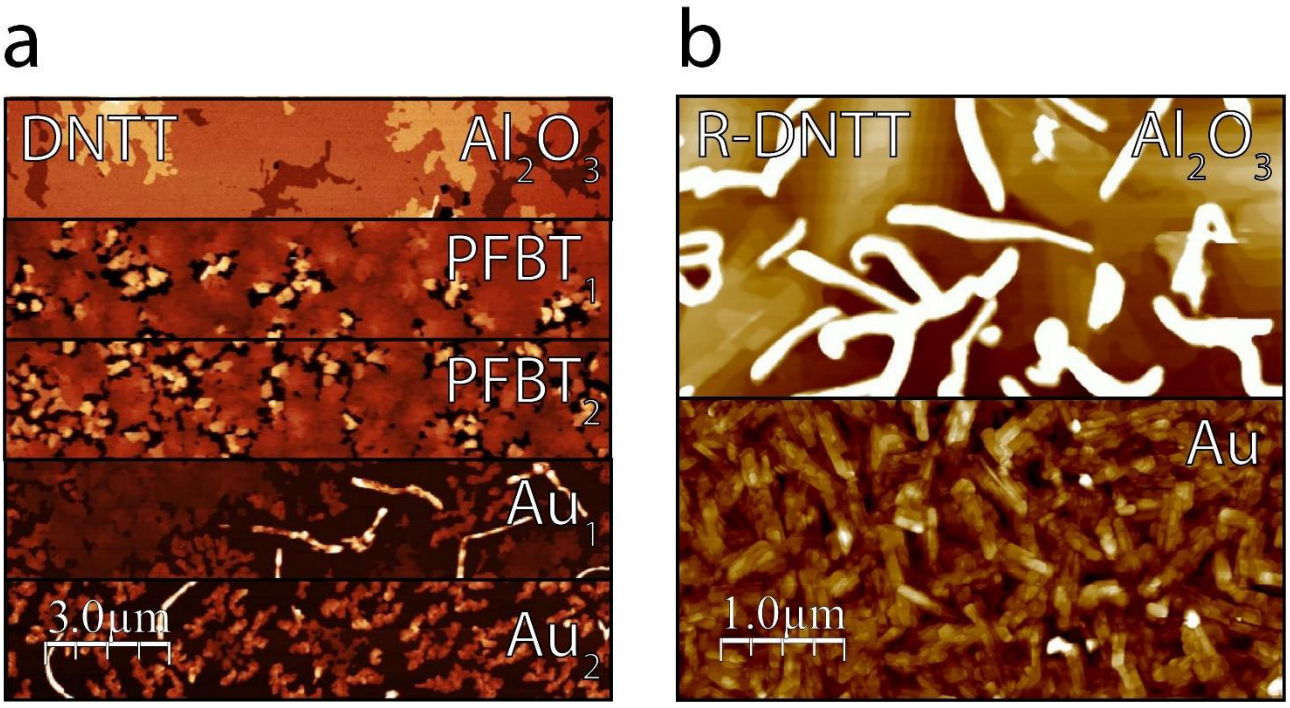

Figure 5.7: Topography images of (a) 10-nm DNTT and (b) 50-nm R-DNTT thin films fabricated via thermal evaporation on different substrates held at 70°C. Substrates: (a) Al_2O_3: TPA-Al_2O_3, Z: 12, $PFBT_1$: PFBT-Au on Al_2O_3, Z: 35, $PFBT_2$: PFBT-Au on SiO_2, Z: 40, Au_1: Au on Al_2O_3, Z: 100, Au_2: Au on SiO_2, Z: 90, (b) Al_2O_3: TPA-Al_2O_3, Z: 85, Au: Au on Al_2O_3, Z:35. Z-scales (Z) are expressed in nm.

5.2.3.2 Electronic Properties: Energy Level Alignment

Morphological changes and interaction with the substrate influence the energetics and the solid-state ordering of the OSC thin film.[419] The E_F of different DNTT and DBTTT derivatives has been measured on conductive Au substrates having a reference WF of about 4.9 eV. IE values from both Au and dielectric substrates are also reported together with an estimate of E_G (from literature) to assess the doping state of the films. This set of data is summarized in Table 5.3.

A distinct trend in the magnitude ordering of IE and WF values can be identified, as $IE_d > IE_{Au} > E_F$ for each of the p-type OSC compounds. All the molecules reported in the table assemble in crystal structures characterized by vertically standing elements on dielectric substrates, even though a first interfacial layer of flat-lying molecules can be observed in thermally-evaporated films, e.g., DNTT.[420] The use of thiol-based SAM helps to drive the growth of small-molecules OSC directly with an upright orientation, without a wetting layer, as in the case of pentacene.[421] It is no doubt, however, that bare Au surfaces induce an interfacial dipole in small-molecule OSC thin films that decreases the effective IE of the OSC in relatively thin films compared to the bulk

value.[422] This explains why IE_d > IE_{Au}, as at the IE/WF conditions in Table 5.3 OSC bands are bent,[423] while E_F being smaller than IE is trivial (see Section 1.4). By comparing the E_F values with the optical gap, all OSC are characterized by a significative p-type character (the E_F values are typically at ≈ 0.3−0.5 eV higher than IE, while midgap is at ≈ 1.2 eV higher energies).

Class	Compound	IE_d (eV)	IE_{Au} (eV)	E_F (eV)	E_G (eV)
DNTT	DNTT	5.16 ± 0.04	5.04 ± 0.03	4.76 ± 0.04	2.36[424]
	C8-DNTT	4.94 ± 0.01	4.87 ± 0.03	4.66 ± 0.02	2.92[412]
	tBu-DNTT (AL150)	5.38 ± 0.01	5.33 ± 0.01	4.76 ± 0.03	-
	S-DNTT	5.19 ± 0.01	-	4.74 ± 0.01	-
	R-DNTT	5.23 ± 0.01	-	4.75 ± 0.01	-
DBTTT	DBTTT	5.13 ± 0.01	5.10 ± 0.01	4.74 ± 0.01	2.94[425]
	C12-DBTTT	5.10 ± 0.01	4.94 ± 0.01	4.58 ± 0.01	≈2.8[426]
	tBu-DBTTT (AL52)	5.31 ± 0.01	5.20 ± 0.01	4.81 ± 0.01	-

Table 5.3: IE and E_F values of a selection of small-molecule OSC as determined by PYSA and macroscopic KP. IE_d: dielectric substrate (SAM-treated Al_2O_3 or SiO_2), IE_{Au}: Au substrate. E_G values were estimated from UV-Vis spectra reported in the literature.

5.3 Determination of the Vertical Conductivity in OSC Materials

Charge injection and contact resistance issues in OFETs are of central importance for the downscaling even after a decade of intense and dedicated research.[51,423] The modulation of charge injection in OFETs is a trade-off between the electrode WF and the tunneling barrier that is typically controlled by the functionalization of electrodes with SAMs. For example, in polymer-based devices having width-normalized R_C in the range of 10^3−10^6 Ω cm, the OSC HOMO/Au WF energy level mismatch (and not the tunneling barrier due to the length of the SAM-forming molecule) dominates the injection.[407] The extraction of lateral and vertical conductivity values (and other parameters such as R_C) are often difficult from a unique device geometry, hence different device configurations need to be fabricated to get better estimates for each of these parameters. Within this context, SAM functionalization of electrodes represent a powerful strategy to design devices with peculiar electrical characteristics.

As outlined in Section 5.1, injection-blocking electrodes are often a strict requirement in the techniques for the determination of the vertical conductivity and, in particular, to perform C-AFM measurements in the SCLC regime. SCLC has been often used in the literature to model I−V curves measured via C-AFM, as the analytical treatment of local electrical data is relatively easy to perform if collected in the SCLC regime.[163] Quantitatively determining the vertical μ of OSCs via C-AFM is especially important as it provides a parameter for comparison in molecular assemblies where slight structural

modifications can have an impact on the overall device properties. However, particular care has to be taken when current spreading effects are relevant in the system under study so that a supplementary calibration step is required.[427]

Many research groups applied C-AFM to study the out-of-plane conductivity of OSC materials and the literature is rich of examples spanning from small molecules to polymers. The increasing chain length in P3AT derivatives was found to decrease the transversal μ value in single polymer nanofibers deposited on Au.[428] In a similar system, constituted of single crystals of 3-hexyl-thiophene octamers, the anisotropy of the charge transport was demonstrated via C-AFM.[429] When the current was measured directly in the vertical configuration, the observed tunneling behavior (along the conjugated backbones, through more than 100 nm) was ascribed to the hopping processes at the interface between two neighboring molecules. When, instead, the AFM tip was displaced at micrometric distances from the electrode, the SCLC regime was achieved, as the limiting step in the charge transport was that occurring in the π-stacking direction. SCLC regime was successfully attained in thinner (12 nm) P3HT films when C-AFM was performed in lateral configuration at low (≈ μm) distances from the electrodes, while the I−V curves were linear at larger (≈ 50 μm) distances.[430] SCLC measurements can still be successfully performed on samples as thin as 4 nm, as demonstrated by our group on perylenecarboxydiimide-based nanostructures deposited via Langmuir-Blodgett.[431] Single crystals of rubrene derivatives have also been screened by C-AFM with the aim of identifying promising OSCs obtained by structural modifications.[432] Recently, Mativetsky et al. utilized the μ mapping to quantify the spreading of lateral current in the vertical C-AFM configuration, pushing the technique a further step beyond the current state of the art.[433]

In the next section, out-of-plane conductivity measurements of DNTT and C8-DNTT thin films performed via C-AFM will be presented and discussed.

5.3.1 Vertical conductivity in DNTT thin films

For out-of-plane current measurements, the C-AFM equipment was run with the TUNA module, enabling the detection of current variations as low as 1 pA. C-AFM experiments were performed at ambient conditions under a constant N_2 flux to keep the RH levels below 5%. Thin-film samples of OSCs were fabricated on ultraflat Si wafers exposing a 30-nm-thick Au layer covering the underlying SiO_2 or Al_2O_3 oxide layers. The Au surface, that was treated with a PFBT SAM deposited from a diluted 10 μM ethanol solution prior

to OSC deposition, was grounded to the sample holder of the instrument where the voltage bias was applied.

The current mapping of the DNTT/Au-PFBT system is shown in Figure 5.8. In both thin (10 nm) and thick (25 nm) films there are regions where the tip goes in contact with the substrate (darker in the topography image, brighter in the current image). The tip in contact with Au is short-circuited, hence the current amplifier reaches saturation. The dynamic range of the current amplifier, and in turn the C-AFM image equalization, were optimized to show the best contrast highlighting the slight current changes arising from the non-uniformity of the sample thickness. Regions of maximum height in (a) correspond to minima of current in (b). The maxima in the lateral current scale reported in (b) indicates the indicative maximum current recorded in OSC regions.

A drop in current intensity (by a factor of ~ 10) was indeed observed when passing from 10 to 25-nm-thick films, as expected for the additional resistance due to the supplementary layers. Thin films grown on Au-PFBT/Al_2O_3 have a slightly more continuous and uniform topography compared to Au-PFBT/SiO_2 thus being more advantageous for a stable C-AFM imaging and I−V characterization.

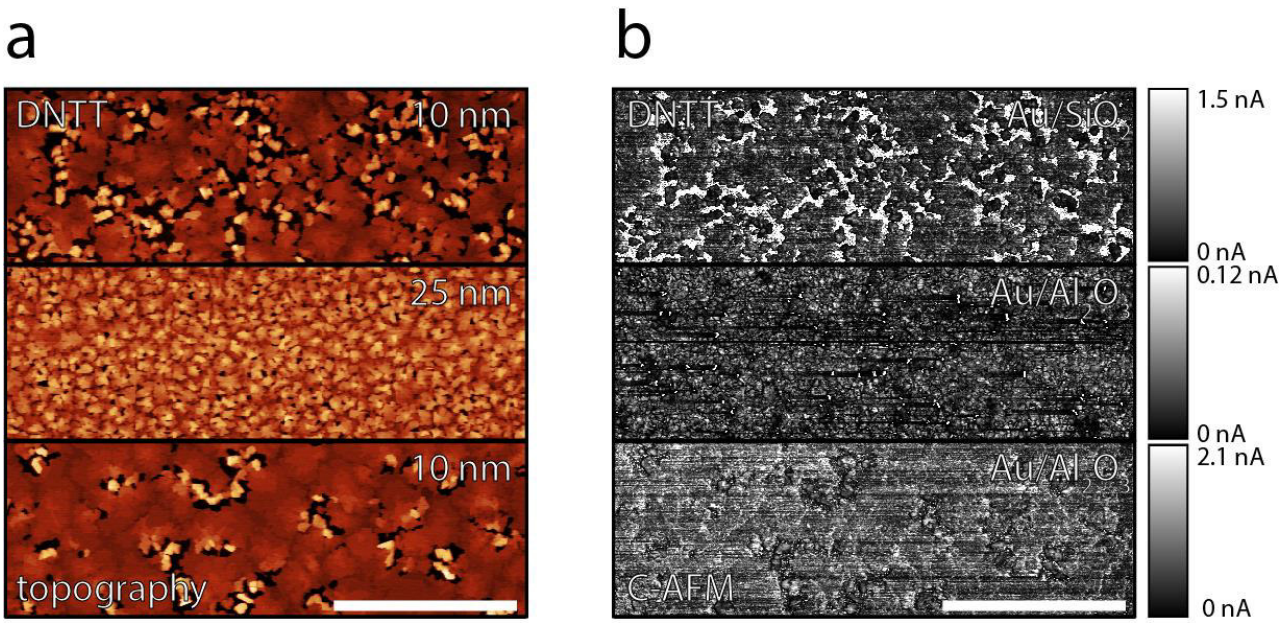

Figure 5.8: Topography (a) and C-AFM (b) images of DNTT thin films fabricated via thermal evaporation at a substrate temperature of 70°C. From top to bottom: 10-nm film on PFBT-Au/SiO_2, Z: 40; 25-nm film on PFBT-Au/Al_2O_3, Z: 40; 10-nm film on PFBT-Au/Al_2O_3, Z: 35. Z-scales (Z) are expressed in nm. Sample bias: 0.1 V. Au: PFBT-Au. Scale bar: 5 μm.

A set of (at least 50) I–V curves were collected in different regions of each sample by displacing the tip over a 5 x 5 array of points separated by 200 nm in a 1 × 1 μm^2 area. After that, curves characterized by a poor contact and/or tip/substrate short circuits were excluded from the analysis, with an average rejection ratio of 50%. The resulting averaged I–V curves (of samples shown in Figure 5.8) are reported in Figure 5.9.

The current response of DNTT thin films on PFBT-Au is asymmetric and characterized by a good injection at positive sample bias. The choice of depositing the OSC on PFBT-Au affected both the surface topography (as seen in Figure 5.7a) and the charge injection, as asymmetric contacts are needed to perform SCLC measurements. Knowing that the WF of the Pt/Ir tip of SCM-PIC-V2 probes is about 4.9 eV and that the WF of PFBT-Au is around 5.5 eV, the degree of curve asymmetry depends on the IE of the OSC studied. In the case of DNTT, the effective injection barrier for holes is smaller at the SAM-treated electrode/OSC interface (IE ≈ 5.2 eV for the oriented film at the solid state) than at the interface with the tip, as evidenced by the I–V curves reported in Figure 5.9.

The positive side of the I–V curves is then plotted in logarithmic scale in Figure 5.9b to extract the power coefficient associated with the I(V) dependence. The linear part at small voltage bias was also fitted by linear regression. The results of the I–V curve fitting are summarized in Table 5.4.

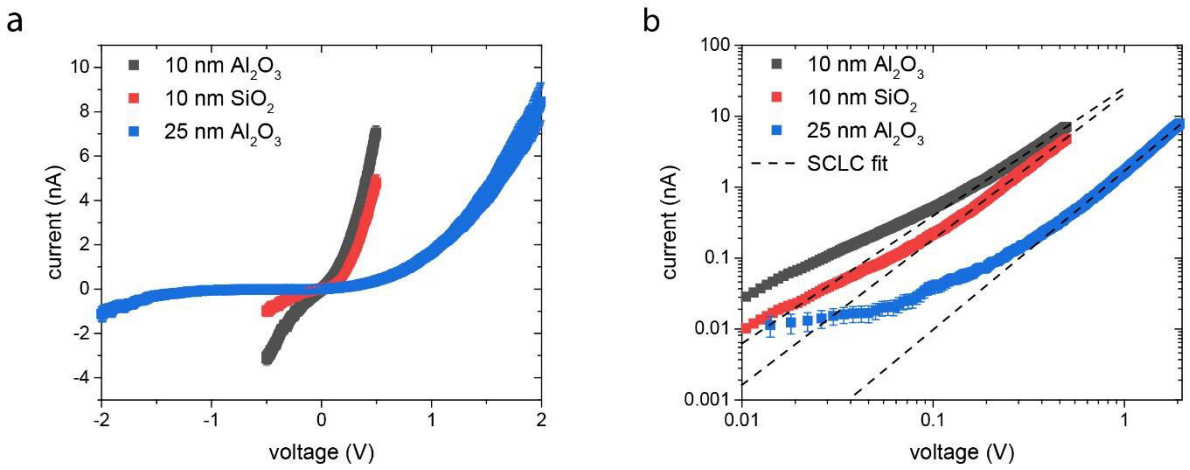

Figure 5.9: I-V curves measured using C-AFM on DNTT thin films plotted in (a) linear and (b) logarithmic scale. The linear plot highlights the I–V asymmetry characteristic of SCLC regime. The logarithmic plot is used to extract the slope in the SCLC region. Each curve is obtained from an average of at least 20 individual curves. The 1 nA/V amplifier and forces < 5 nN were employed. The standard deviation is indicated by error bars. Voltage is sample bias.

Sample	Linear	SCLC
10 nm Al_2O_3	1.05 ± 0.01	1.87 ± 0.01
10 nm SiO_2	1.08 ± 0.01	2.04 ± 0.01
25 nm Al_2O_3	1.01 ± 0.03	2.22 ± 0.01

Table 5.4: Power coefficients of linear and SCLC regions extracted from linear regression of the averaged I–V curves collected from DNTT thin films. The reported uncertainties, determined as the statistical fitting error, are rounded to the hundredth.

Both linear and SCLC regimes are attained within a relative discrepancy of 10% with respect to the ideal cases of linear slope = 1 and SCLC slope = 2. No intermediate regimes or trap filling regions appear to be present for this system. The out-of-plane mobility can thus be extracted by using Equation 5.1 or 5.2. All the experimental parameters contained in the equations must be estimated somehow.

The contact area between the C-AFM tip and the sample surface can be estimated with the method described by Ginger et al.[163] Assuming around 0.5 nm of tip indentation from the deflection error signal (larger deformation would probably destroy the film at these low thickness values ≈ 10–25 nm) and a hemispherical shape at the apex of the SCM-PIC-V2 probe (nominal tip diameter of 25 nm), the circular contact patch has diameter of ≈ 10 nm and the resulting contact area is ≈ 78 nm^2. This value should be seen as an upper limit, as typically only a small fraction (< 10 nm^2) of this area effectively contributes to the transport of charge.[348] The relative dielectric constant of DNTT was determined to be around 1.96 via VASE. The computed μ_{out} parameters are reported in Table 5.5.

Sample	μ_{out} Mott ($cm^2\ V^{-1}\ s^{-1}$)	μ_{out} Corr ($cm^2\ V^{-1}\ s^{-1}$)
10 nm Al_2O_3	1.3×10^{-1}	2.8×10^{-3}
10 nm SiO_2	9.5×10^{-2}	2.0×10^{-3}
25 nm Al_2O_3	1.4×10^{-1}	5.8×10^{-4}
Average	$(1.3 \pm 0.2) \times 10^{-1}$	$(1.8 \pm 1.1) \times 10^{-3}$

Table 5.5: Out-of-plane mobilities of DNTT thin films. The words "Mott" and "Corr" refer to the original Mott-Gurney law (Equation 5.1) or the corrected version (Equation 5.2).

The out-of-plane mobilities found by C-AFM are only slightly lower than the in-plane μ value of 0.6 $cm^2\ V^{-1}\ s^{-1}$ reported by Klauk et al.[434] from TC OFET measurements fabricated via thermal sublimation on a similar TPA-treated Al_2O_3 dielectric substrate operated at low voltages. Since DNTT compounds are typically showing μ_{in} values in excess of 1 $cm^2\ V^{-1}\ s^{-1}$ due to optimal in-plane orbital overlap,[20] it is reasonable to hypothesize that the transport in the out-of-plane direction is limited by poorer transfer integrals in the direction perpendicular to the π-stacking.

It is worth noting that the basic Mott-Gurney relationship provides much more consistent values than its corrected counterpart, as the relative deviation for the first set of μ is ≈ 20%, while it is ≈ 60% for the second set of data. Quantitatively determining μ_{out} requires the determination of the thickness dependence to further verify the validity of the two equations used here.

5.3.2 Vertical conductivity in C8-DNTT thin films

DNTT derivatives possessing n-alkyl side chains have the major advantage of an improved solution processability while maintaining high hole mobility, but at the cost of a reduction in the orbital overlap between layers of molecular assemblies. One possible strategy to quantify the impact of this structural change on the charge transport is by determining μ_{out} in DNTT and Cn-DNTT thin films via C-AFM. Having already estimated the μ_{out} of DNTT in the previous section, here the two systems are directly compared to evaluate to which extent side chains can limit the out-of-plane charge transport.

The C-AFM mapping of evaporated DNTT and C8-DNTT on the same substrate (Au-PFBT on ODTS-SiO_2) and with comparable thickness (≈ 10 nm) is reported in Figure 5.10.

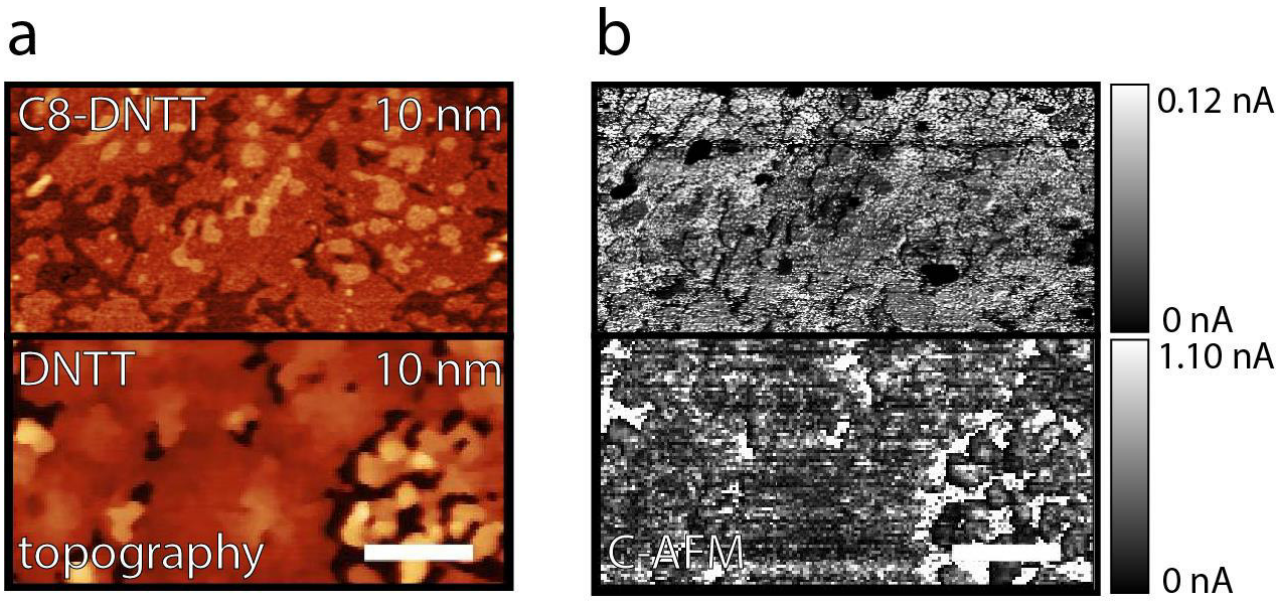

Figure 5.10: Topography (a) and C-AFM (b) images of C8-DNTT and DNTT thin films fabricated via thermal evaporation. C8-DNTT was deposited at a substrate temperature of 100 °C. DNTT was deposited at a substrate temperature of 70 °C. (top) 10-nm film of C8-DNTT on PFBT-Au/SiO_2, Z: 20; (bottom) 10-nm film of DNTT on PFBT-Au/SiO_2, Z: 40. Z-scales (Z) are expressed in nm. Brighter regions in the C-AFM mapping correspond to higher current values. Sample bias: 0.1 V. Scale bar: 5 μm.

The topography images highlight the major uniformity of the C8-DNTT film, which presents a wider terraced morphology compared to DNTT, despite exhibiting a rougher surface due to substrate-induced effects. Note that, for 10-nm-thick films, about 3 vs 6 molecular layers of C8-DNTT and DNTT, respectively, are constituting the films. The cracks present on the DNTT film, which give access to the substrate (as seen from the saturation in the current image), and regions where dewetting phenomena are evident, are not found in the C8-DNTT film. In the C8-DNTT film, topographical features better correspond to the observed current mapping whereas, in the DNTT film, the correlation between thicker regions and lower currents is not clearly evident. These differences in the electrical behavior can be ascribed to current spreading phenomena that are present in the DNTT film. Here, charges can be easily transported in-plane to find less resistive vertical pathways but, instead, current spreading is significatively limited by alkyl chains in C8-DNTT as a direct vertical charge transport is the least resistive way unless more conductive defects are present.

A C-AFM current vs voltage dataset was collected from 10-nm-thick C8-DNTT and DNTT films deposited on Au-PFBT/ODTS-SiO_2 substrates and reported in Figure 5.11. The charge injection in C8-DNTT has an opposite behavior compared to DNTT, as observed in Figure 5.11a. In fact, the injection of holes occurs from the tip in C8-DNTT (at negative sample bias) and from the gold electrode in DNTT (at positive sample bias).

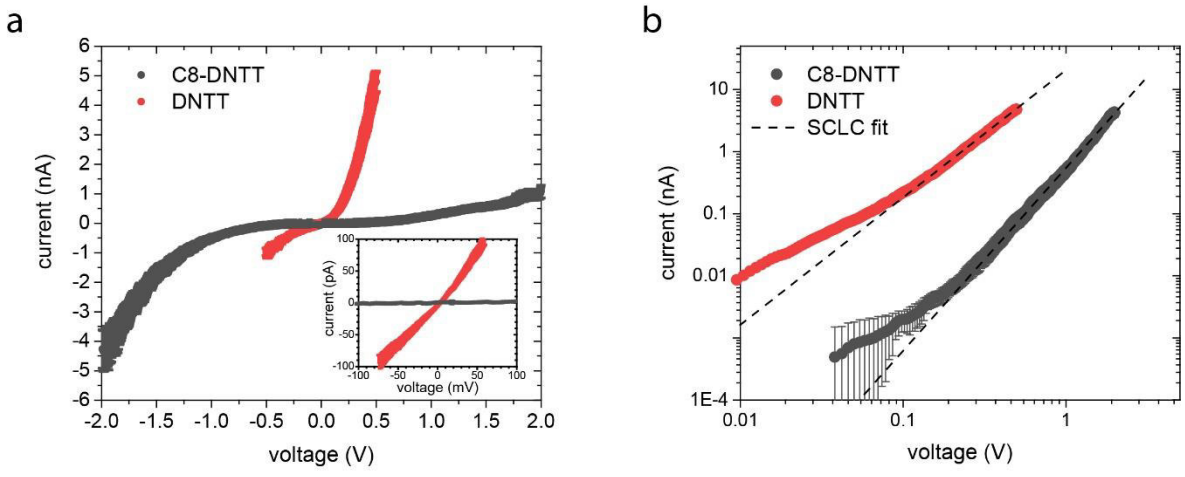

Figure 5.11: I-V curves measured using C-AFM on C8-DNTT and DNTT thin films deposited on Au-PFBT/ODTS-SiO_2 plotted in (a) linear and (b) logarithmic scale. The linear plot highlights the I−V asymmetry. A magnification of the low-voltage region is shown in the inset graph. The logarithmic plot is used to extract the slope in the SCLC region. Each curve is obtained from an average of at least 20 individual curves. The 1 nA/V amplifier and forces < 5 nN were employed. The standard deviation is indicated by error bars. Voltage is sample bias.

While for DNTT holes are efficiently injected from the high WF electrode, for C8-DNTT (low IE material, IE = 4.94 eV) the large energy mismatch limits the injection from Au-PFBT (WF ≈ 5.5 eV). This low IE value better matches with the tip WF (around 4.9 eV) facilitating the injection of holes from the AFM tip. However, the I−V characteristics of C8-DNTT in the high voltage range, expected to be in the SCLC regime, are not as ideal as in DNTT. The slope of the linear fit (2.94) significatively deviates from 2, indicating the possible presence of charge traps.[351] As a consequence, it would not be formally correct to use the SCLC model to compare to quantitatively compare μ_{out} of DNTT and C8-DNTT. A value of out-of-plane conductivity can be alternatively extracted from the I−V curves obtained by C-AFM, by determining the conductance in the linear region of a I(V) plot and converting it into conductivity. The out-of-plane conductivities of these two OSC materials as determined via linear fitting of the C-AFM I−V curves (in the range ± 100 mV) are about 2×10^{-3} S/m and 1×10^{-1} S/m for C8-DNTT and DNTT, respectively. These values account for a factor 50 reduction in vertical conductivity due to alkyl chains. One way to improve the out of plane conductivity of such promising OSC compounds is by fine tuning the thin-film morphology.[435]

To further investigate this system, highly crystalline C8-DNTT thin films were fabricated via blade coating on Au/SiO_2 substrates in collaboration with M. Gicevičius at the University of Cambridge. Blade coating techniques enable fine control of the number of layers deposited on the substrate after careful optimization of the solvent, concentration and substrate temperature and wettability, so that even a single C8-DNTT monolayer could be deposited on ODTS-SiO_2 to yield OFET devices with superior performance.[436]

With the aim of studying the vertical conductivity, smooth C8-DNTT thin films characterized by few layers exhibiting large terraces (with size in the order of 10 μm) on Au substrates were fabricated, as shown in Figure 5.12a-b, The current mapping collected at -3 V sample bias (Figure 5.12c) shows a neat current contrast among the different layers, with the current amplifier being saturated at -20 nA in regions where the Au substrate is exposed, and intermediate current values recorded with decreasing intensity as a function of the thin-film thickness. Distinct layers are found at different heights with reference to the substrate (Figure 5.12d) and the average step height (3.42 nm) well matches with the expected interlayer distance value obtained from diffractometry (3.36 nm).[412]

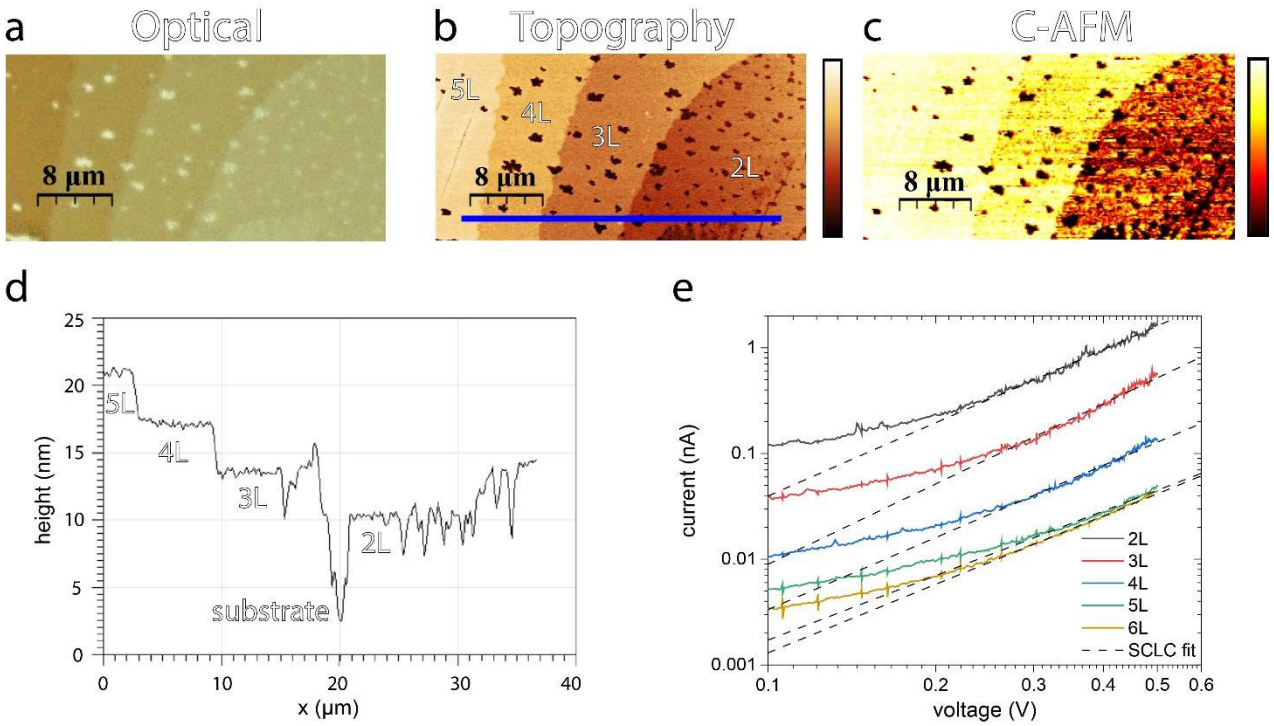

Figure 5.12: C-AFM characterization of blade coated C8-DNTT films on Au. (a) Optical image of the scanned area. (b) AFM topography indicating the number of molecular layers and the height profile region (blue solid line). Darker regions correspond to the Au substrate. Z-scale: 30 nm (c) Current mapping collected at -3 V sample bias. Black regions correspond to the shorted Au substrate. Z-Scale : -20 nA. (d) Height profile as indicated by the solid blue line in (b). The experimental interlayer distance is 3.42 nm versus a refence value of 3.36 nm.[412] (e) I–V curves measured using C-AFM as a function of the number of C8-DNTT layers. The curves were collected with an Asylum Research MFP-3D AFM System (Maxwell Centre, University of Cambridge) and plotted in a logarithmic scale. The sixth layer (6L) is not indicated in the AFM images, but it is located to the left side of the fifth layer (5L).

A complete I–V characterization of this sample was not only possible via collecting individual curves as a function of the number of layers (Figure 5.12e), but also by recording multiple C-AFM images (as that in Figure 5.12c) at different sample bias values providing a comprehensive dataset of [I, V, number of layers]. This dataset is currently being analyzed by M. Gicevičius for the development of an analytical model to extract μ_{out} from the C-AFM characterization of such molecular systems. Here, the analysis is limited to the extraction of mobility values from the I–V curves.

The I–V curves reported in Figure 5.12e, obtained from blade-coated C8-DNTT samples, follow a much more ideal behavior compared their thermally deposited counterparts. In fact, for the thickness values explored the average slope of the SCLC fitting is 2.25 ± 0.18, indicating that the thin-film fabrication method can influence on the formation of interfacial charge traps that are drastically reduced in those blade-coated samples. Table 5.6 lists the μ_{out} values that were determined for each thickness.

Sample	μ_{out} Mott ($cm^2 V^{-1} s^{-1}$)	μ_{out} Corr ($cm^2 V^{-1} s^{-1}$)
2L	3.0×10^{-2}	8.3×10^{-4}
3L	4.1×10^{-2}	6.3×10^{-4}
4L	4.1×10^{-2}	4.0×10^{-4}
5L	3.9×10^{-2}	2.7×10^{-4}
6L	3.7×10^{-2}	2.0×10^{-4}
Average	$(3.8 \pm 0.5) \times 10^{-2}$	$(4.7 \pm 2.6) \times 10^{-4}$
DNTT Thermal	$(1.3 \pm 0.2) \times 10^{-1}$	$(1.8 \pm 1.1) \times 10^{-3}$

Table 5.6: Out-of-plane mobilities of blade-coated C8-DNTT thin films. The average mobility values of DNTT are reported for comparison. The words "Mott" and "Corr" refer to the original Mott-Gurney law (Equation 5.1) or the corrected version (Equation 5.2).

The agreement between the mobility values extracted from different number of layers is quite remarkable as it highlights how good the model fits the data. Thanks to a direct height measurement (AFM topography), the thickness (L) of the film is known with sufficiently high accuracy to yield coherent results even with a dramatical mathematical dependence such as the third power (L^3). The non-corrected version of the Mott-Gurney law provides a final μ_{out} average value with a precision of the first decimal figure, $(3.8 \pm 0.5) \times 10^{-2}$ cm^2 V^{-1} s^{-1}, while only one significant figure is known in the other case, $(4.7 \pm 2.6) \times 10^{-4}$ cm^2 V^{-1} s^{-1}. These μ_{out} values are a factor 3.5 and 3.8, respectively, lower than the corresponding average values for DNTT, suggesting that in molecular assemblies with long-range solid state ordering the transport of charge in the vertical direction is quite effective even if there are "insulating" regions of alkyl chains. Note, however, that there is no control in the doping state of the two compounds that could be affected by the measuring environment (ambient air at low < 5% RH) that might change the amount of free charge carriers even in the absence of a gate voltage.

5.4 Conclusions and Outlook

I–V measurements and current mapping of the vertical conductivity have been performed via C-AFM on DNTT and C8-DNTT thin films. For the correct interpretation of the C-AFM data, a preliminary analysis involving the determination of the OSC and metal electronic energy levels as well as their surface topography on different substrates was necessary. In fact, understanding the electrical behavior of these films, as probed via C-AFM, requires the knowledge of the WF of the electrodes, one of which must be a blocking electrode (to perform the measurements in the SCLC regime) and the other one must inject the majority charge carrier (holes in this case). In addition, not only the knowledge of the IE of the OSC is necessary, but also its E_F could provide further insight into the energy level alignment at the interface. The integration of band bending

into the data interpretation, however, would require a dedicate study of the interface formation with a careful determination of the E_F dependence with the OSC thickness. More importantly, the previous determination of the surface topography can help discriminating thin films that forcedly require the electrical characterization via I–V curves, averaged on a data collection in random sample position, from thin films where the current mapping can also provide combined I(V) data as a function of the number of layers. Such an experimental approach is very useful to prove the validity of the mathematical model employed for the extraction of μ_{out} values or to obtain multiple mobility values that can provide a consistent statistic from an individual sample, as in the case of the C8-DNTT layers.

Thanks to C-AFM, measuring the vertical mobility in a sample geometry that could be easily comparable or adaptable to that of an operating OFET is made possible. It has been demonstrated that C-AFM is a viable method to compare the transport of charge in the out-of-plane direction in small-molecule OSC thin films. It was found that the original Mott-Gurney law can give much more consistent μ_{out} values in the nanometric thickness range (5 nm < L < 15 nm) compared to its corrected version that seemed to better describe μ_{out} in films with thickness above 50 nm.[163] The out-of-plane mobilities of DNTT and C8-DNTT are determined by C-AFM to be in the 10^{-1}–10^{-2} cm^2 V^{-1} s^{-1} range which is significatively higher than typical values (10^{-3}–10^{-5} cm^2 V^{-1} s^{-1}), even though after the law correction the values are reduced to a more realistic range of 10^{-3}–10^{-4} cm^2 V^{-1} s^{-1}. Such a discrepancy might also be explained in terms of the absence of grain boundaries for our films, that can be present instead for thicker films, causing an enhancement of the recorded current.

Despite the absolute μ_{out} values obtained, the power of this method relies on the direct comparison of the materials' conductivity in similar experimental conditions. Further investigations of small-molecule OSC thin films by C-AFM might be important for the future development of VOFETs where the vertical conductivity plays a major role in the device operation. Validating this C-AFM method for a variety of OSC might enable a quicker screening of candidate compounds in VOFETs without the need of fabricating such complex structures for the purpose of testing the electrical properties of the material.

6 Conclusions and Outlook

In this thesis, different classes of OSC materials have been employed as active materials in functional devices, namely humidity sensors (a small molecule, OEG-BTBT) and OECTs (a polymer blend of pgBTTT and OEG-SP). The study of OSC compounds bearing OEG side chains has been proven to be important for both fundamental aspects, such as understanding the interaction between environmental water and substrate/active OSC material, and applicative purposes, as glycolated chains promote protonic and ionic conductivity to operate e.g., humidity sensors or OECTs. The investigation of the electrical properties of OSC materials was not only limited to these types of devices. C-AFM measurements were performed to estimate the out-of-plane charge carrier mobility of representative small-molecule (DNTT) derivatives. Organic electronics is currently witnessing a rising interest in developing methods for the experimental determination of the out-of-plane mobility. This parameter is not only important for conventional device geometries, such as thin film transistors and solar cells, but because of the emergence of novel device configurations, it is nowadays pivotal for geometries such as vertical OFETs. Hence, the selection of well-referenced OSC materials is important for giving useful additional indications to the scientific community to attain a more complete picture of charge transport in OSCs. The proposed C-AFM approach is complementing our current knowledge about the anisotropic electrical characteristics of OSC materials.

In Chapter 3, the reported findings on OEG-BTBT-based humidity sensors bring a new perspective on the design of organic materials. The electrical performance of bottom-contact humidity-sensitive chemiresistors could be improved by optimizing the substrate wettability, the thin-film thickness and electrode configuration to ultimately achieve a state-of-the-art sensitivity. The synergy between the substrate and the active material was found to govern the performance of these devices which relied on a mixed electron/proton conductivity. Such an improvement could not be achieved in purely hole conductive materials (e.g., C8-BTBT) as the conduction of protons was found to be essential for the exploitation of this effect. The mixed electron/H^+ conducting behavior, in fact, arose from the local dissociation of environmental water molecules into protons occurring in close vicinity to the OEG side chains and at the interface with substrate and/or electrodes. Towards the application of small organic molecules for humidity sensing purposes, the ability of OEG-BTBT to efficiently transduce changes in RH via a

mixed conductivity mechanism represents an important point in the development of iontronic devices.

In this regard, bioelectronics is a rapidly emerging field that requires many new materials exhibiting both ionic and electronic conductivity. The side-chain modification with OEG groups is a valuable strategy in both humidity sensing and bioelectronics fields. For instance, the well-studied polymer pBTTT was adapted to achieve major mixed conductivity properties by substituting alkyl side chains with OEG chains in the π-conjugated backbone of BTTT, giving a polymer named pgBTTT. In Chapter 4, a first example of optically switchable OECT devices has been fabricated starting from the blending of pgBTTT and a versatile photochromic derivative based on a spiropyran core, that was functionalized as well by a OEG side chain (OEG-SP). The ON current in these devices was modulated of a factor 30% by alternating UV and visible light irradiation during operation. Introducing the photoswitching functionality to these OECTs had an additional cost in terms of performance, as both the mobility and ON/OFF ratio decreased of about one order of magnitude. This switching property was maintained for about 6 switching cycles, after which the combined effects of photofatigue and solubilization of the OEG-MC form into the water electrolyte caused the alteration of the correct device functioning. Despite those drawbacks, important indications on improving the chemical design of the photoswitching element are discerned. Further structural modifications could be aimed towards reducing the interaction with water and promoting a more specific interaction with the blending polymer. The future understanding the mechanism underlying the changes in current that occur during reversible photoswitching will be then the starting point for assembling a reliable photoswitching system. The implementation of light-modulated systems in devices with promising applications in bioelectronics (OECTs) holds, in fact, a great potential in the development of multiresponsive and multifunctional materials that could radically change some medical and therapeutic approaches.

In Chapter 5, more fundamental aspects of charge transport in OSC materials are investigated through the estimation of the out-of-plane mobility of DNTT derivatives via C-AFM. In the community of organic electronics, the current design of OSCs has been mainly developed for the maximization of μ_{in}, with poor regard to μ_{out}. This is especially true when considering OFETs, whose conventional device geometry is planar and OSC molecules typically assemble edge-on when deposited on dielectrics. The fabrication of devices where the charge is transported with a current flowing in the direction

perpendicular to the substrate, instead, presents several technological challenges. The active material in OFETs must exhibit a high charge carrier mobility in the direction imposed by device geometry, but this is not the only parameter to be optimized for their commercial application in consumable electronics. Experimental tools that specifically target single electrical current contributions are highly valuable in the development of semiconductive systems. C-AFM mapping of the vertical conductivity in DNTT and C8-DNTT thin films provided combined I(V) data as a function of the number of layers that is useful, for example, to study charge injection and transfer to the active channel. The comparison of μ_{out} values of the alkyl- and non-functionalized version of DNTT extracted from this dataset highlighted a minor loss in the efficiency of the out-of-plane transport of holes for C8-DNTT compared to DNTT. The alkyl side-chain functionalization is one of many synthetic approaches which are currently explored to devise OSC materials that could bring the OFET technology to a point that is convenient for industrial research. In addition, the developed method, which considers the mobility extracted from 2- to 6-layer-thick films of OSC, provided consistent results as a function of the thickness, thus confirming the validity of the equations used to model the system. The power of this method also relies on the direct comparison of the conductivity of OSC materials in similar experimental conditions. Further validation of this C-AFM method will pave the way for the future development of VOFETs by facilitating the screening of OSC materials.

Each of the experimental chapters reported in this thesis is targeted at contributing to address grand challenges in organic electronics. Since efficient conductive pathways are made possible by a strategic molecular design, correlating the electrical properties of OSC with their chemical structure is fundamental for the future development of the field. The versatility granted by organic scaffolds is unique in the world of functional materials thanks to wide possibilities offered by the tuning of solid-state properties by devising chemical structures that assemble via intermolecular interactions. To this end, the past several decades of research in organic electronics evidenced the necessity of a multitechnique approach to identify and harness the key points in the development of new materials for devices. Devising alternative strategies combining the expertise of several groups with the aim of investigating OSC materials is nowadays crucial for the progress of this technology. The experimental work presented here is in fact the result of the many successful scientific collaborations that enabled these investigations from the synthesis of the basic materials to the further in-depth analysis of materials'

properties. So far, diverse aspects of supramolecular chemistry have been investigated to promote the advancement of functional devices ranging from sensing devices with applications in living systems to opto(electronic) devices for logic operations.

In the near future, concerted efforts from experts in these fields will be aimed towards the merging of these two worlds to be able to fully integrate *in-silico* electronics into living systems. This thesis proposes the supramolecular approach as an additional tool towards the achievement of multifunctionality in organic materials. For the interfacing of OSCs to biological systems, the target device should be able to present electrolytes as an integral part of their structure that actively contributes to its functioning. This task can be achieved by designing the OSC material at the molecular level to transport both ionic and electronic carriers, without being negatively affected (or its functioning compromised) by the water (or another solvent) environment. The studied materials studied were shown to be excellent vehicles of electronic/ionic charge carriers when in contact with water vapor (OEG-BTBT) or a NaCl water solution (pgBTTT). Applying these materials in sensors (e.g., humidity sensors) or transistors (e.g., OECTs) is of great importance for the growing bioelectronics community that can find novel and inspiring approaches to fabricate devices with specific functionalities.[14]

On the other hand, in a nearer future, our findings represent a solid reference to the scientific community that will help to extend our current understanding of the relationship between supramolecular solid-state organization and mixed ionic/electronic conductivity. On a more fundamental view, the reported materials represent examples of solid-state molecular assemblies that interact with the environment (water vapor, light, ions, electric field, etc.) and transduce an input signal into an electrical output. A deeper study of such architectures could give more insight into charge transport mechanisms to improve our knowledge on the origin and coexistence of ionic and electronic carriers. Investigating novel organic mixed ionic/electronic conductors is currently a priority in the field of bioelectronics, which necessitates the improvement of transconduction properties of materials for OECTs.[437] Understanding how electronic charge injection and ionic conduction are related by a thorough study of structure–property relationships is thus of primary importance. There are plenty of options to implement scanning probe techniques (such as C-AFM, KPFM and others) to explore electronic and ionic conductivity in these systems. Our research was limited to state-of-the-art small-molecule OSCs, but many groups are trying to fill this gap, highlighting once again the contribution that AFM-related techniques can offer to fundamental

research. This thesis finally proposes diverse solutions that enclose all the above-mentioned approaches towards the progress of the field.

7 References

[1] C. K. Chiang, C. R. Fincher, Y. W. Park, A. J. Heeger, H. Shirakawa, E. J. Louis, S. C. Gau, A. G. MacDiarmid, Phys. Rev. Lett. **1977**, 39, 1098.

[2] N. Thejo Kalyani, S. J. Dhoble, Renew. Sustain. Energy Rev. **2012**, 16, 2696.

[3] H. Sirringhaus, Adv. Mater. **2014**, 26, 1319.

[4] O. Inganäs, Adv. Mater. **2018**, 30, 1800388.

[5] S. Yuvaraja, A. Nawaz, Q. Liu, D. Dubal, S. G. Surya, K. N. Salama, P. Sonar, Chem. Soc. Rev. **2020**, 49, 3423.

[6] M. Carroli, A. G. Dixon, M. Herder, E. Pavlica, S. Hecht, G. Bratina, E. Orgiu, P. Samorì, Adv. Mater. **2021**, 33, 2007965.

[7] H. Ling, S. Liu, Z. Zheng, F. Yan, Small Methods **2018**, 2, 1800070.

[8] J. Song, H. Lee, E. G. Jeong, K. C. Choi, S. Yoo, Adv. Mater. **2020**, 32, 1907539.

[9] A. Pron, P. Rannou, Prog. Polym. Sci. **2002**, 27, 135.

[10] S. Z. Bisri, S. Shimizu, M. Nakano, Y. Iwasa, Adv. Mater. **2017**, 29, 1607054.

[11] C. Wang, H. Dong, W. Hu, Y. Liu, D. Zhu, Chem. Rev. **2012**, 112, 2208.

[12] W. Wang, A. D. Schlüter, Macromol. Rapid Commun. **2019**, 40, 1800719.

[13] H. Bronstein, C. B. Nielsen, B. C. Schroeder, I. McCulloch, Nat. Rev. Chem. **2020**, 4, 66.

[14] G. Malliaras, I. McCulloch, Chem. Rev. **2022**, 122, 4323.

[15] M. C. Morvant, J. R. Reynolds, Synth. Met. **1998**, 92, 57.

[16] S. L. Bidinger, S. Han, G. G. Malliaras, T. Hasan, Appl. Phys. Lett. **2022**, 120, 073302.

[17] C. J. Kousseff, R. Halaksa, Z. S. Parr, C. B. Nielsen, Chem. Rev. **2022**, 122, 4397.

[18] S. Allard, M. Forster, B. Souharce, H. Thiem, U. Scherf, Angew. Chem. Int. Ed. **2008**, 47, 4070.

[19] Z. B. Henson, K. Müllen, G. C. Bazan, Nat. Chem. **2012**, 4, 699.

[20] K. Takimiya, I. Osaka, T. Mori, M. Nakano, Acc. Chem. Res. **2014**, 47, 1493.

[21] H. Dong, C. Wang, W. Hu, Chem. Commun. **2010**, 46, 5211.

[22] V. Coropceanu, J. Cornil, D. A. da Silva Filho, Y. Olivier, R. Silbey, J.-L. Brédas, Chem. Rev. **2007**, 107, 926.

[23] C. B. Nielsen, A. Giovannitti, D.-T. Sbircea, E. Bandiello, M. R. Niazi, D. A. Hanifi, M. Sessolo, A. Amassian, G. G. Malliaras, J. Rivnay, I. McCulloch, J. Am. Chem. Soc. **2016**, 138, 10252.

[24] A. Giovannitti, D.-T. Sbircea, S. Inal, C. B. Nielsen, E. Bandiello, D. A. Hanifi, M. Sessolo, G. G. Malliaras, I. McCulloch, J. Rivnay, Proc. Natl. Acad. Sci. **2016**, 113, 12017.

[25] M. Moser, L. R. Savagian, A. Savva, M. Matta, J. F. Ponder, T. C. Hidalgo, D. Ohayon, R. Hallani, M. Reisjalali, A. Troisi, A. Wadsworth, J. R. Reynolds, S. Inal, I. McCulloch, Chem. Mater. **2020**, 32, 6618.

[26] J. W. Onorato, Z. Wang, Y. Sun, C. Nowak, L. Q. Flagg, R. Li, B. X. Dong, L. J. Richter, F. A. Escobedo, P. F. Nealey, S. N. Patel, C. K. Luscombe, J. Mater. Chem. A **2021**, 9, 21410.

[27] J. Mei, Y. Diao, A. L. Appleton, L. Fang, Z. Bao, J. Am. Chem. Soc. **2013**, 135, 6724.

[28] I. McCulloch, M. Heeney, C. Bailey, K. Genevicius, I. MacDonald, M. Shkunov, D. Sparrowe, S. Tierney, R. Wagner, W. Zhang, M. L. Chabinyc, R. J. Kline, M. D. McGehee, M. F. Toney, Nat. Mater. **2006**, 5, 328.

[29] T. Lei, Y. Cao, X. Zhou, Y. Peng, J. Bian, J. Pei, Chem. Mater. **2012**, 24, 1762.

[30] T. Okamoto, C. P. Yu, C. Mitsui, M. Yamagishi, H. Ishii, J. Takeya, J. Am. Chem. Soc. **2020**, 142, 9083.

[31] R. Jouclas, J. Liu, M. Volpi, L. Silva de Moraes, G. Garbay, N. McIntosh, M. Bardini, V. Lemaur, A. Vercouter, C. Gatsios, F. Modesti, N. Turetta, D. Beljonne, J. Cornil, A. R. Kennedy, N. Koch, P. Erk, P. Samorì, G. Schweicher, Y. H. Geerts, Adv. Sci. **2022**, n/a, 2105674.

[32] A. J. Petty, Q. Ai, J. C. Sorli, H. F. Haneef, G. E. Purdum, A. Boehm, D. B. Granger, K. Gu, C. P. Lacerda Rubinger, S. R. Parkin, K. R. Graham, O. D. Jurchescu, Y.-L. Loo, C. Risko, J. E. Anthony, Chem. Sci. **2019**, 10, 10543.

[33] C. Wang, D. Hashizume, M. Nakano, T. Ogaki, H. Takenaka, K. Kawabata, K. Takimiya, Chem. Sci. **2020**, 11, 1573.

[34] H.-Y. Chen, G. Schweicher, M. Planells, S. M. Ryno, K. Broch, A. J. P. White, D. Simatos, M. Little, C. Jellett, S. J. Cryer, A. Marks, M. Hurhangee, J.-L. Brédas, H. Sirringhaus, I. McCulloch, Chem. Mater. **2018**, 30, 7587.

[35] Z. Shuai, H. Geng, W. Xu, Y. Liao, J.-M. André, Chem. Soc. Rev. **2014**, 43, 2662.

[36] G. Gryn'ova, K.-H. Lin, C. Corminboeuf, J. Am. Chem. Soc. **2018**, 140, 16370.

[37] S. Fratini, M. Nikolka, A. Salleo, G. Schweicher, H. Sirringhaus, Nat. Mater. **2020**, 19, 491.

[38] D. Venkateshvaran, M. Nikolka, A. Sadhanala, V. Lemaur, M. Zelazny, M. Kepa, M. Hurhangee, A. J. Kronemeijer, V. Pecunia, I. Nasrallah, I. Romanov, K. Broch, I. McCulloch, D. Emin, Y. Olivier, J. Cornil, D. Beljonne, H. Sirringhaus, Nature **2014**, 515, 384.

[39] K. J. Thorley, I. McCulloch, J. Mater. Chem. C **2018**, 6, 12413.

[40] G. Conboy, H. J. Spencer, E. Angioni, A. L. Kanibolotsky, N. J. Findlay, S. J. Coles, C. Wilson, M. B. Pitak, C. Risko, V. Coropceanu, J.-L. Brédas, P. J. Skabara, Mater. Horiz. **2016**, 3, 333.

[41] V. Lemaur, J. Cornil, R. Lazzaroni, H. Sirringhaus, D. Beljonne, Y. Olivier, Chem. Mater. **2019**, 31, 6889.

[42] Y. Tsutsui, G. Schweicher, B. Chattopadhyay, T. Sakurai, J.-B. Arlin, C. Ruzié, A. Aliev, A. Ciesielski, S. Colella, A. R. Kennedy, V. Lemaur, Y. Olivier, R. Hadji, L. Sanguinet, F. Castet, S. Osella, D. Dudenko, D. Beljonne, J. Cornil, P. Samorì, S. Seki, Y. H. Geerts, Adv. Mater. **2016**, 28, 7106.

[43] G. Schweicher, G. Garbay, R. Jouclas, F. Vibert, F. Devaux, Y. H. Geerts, Adv. Mater. **2020**, 32, DOI 10.1002/adma.201905909.

[44] G. Schweicher, G. D'Avino, M. T. Ruggiero, D. J. Harkin, K. Broch, D. Venkateshvaran, G. Liu, A. Richard, C. Ruzié, J. Armstrong, A. R. Kennedy, K. Shankland, K. Takimiya, Y. H. Geerts, J. A. Zeitler, S. Fratini, H. Sirringhaus, Adv. Mater. **2019**, 31, 1902407.

[45] S. Illig, A. S. Eggeman, A. Troisi, L. Jiang, C. Warwick, M. Nikolka, G. Schweicher, S. G. Yeates, Y. H. Geerts, J. E. Anthony, H. Sirringhaus, Nat. Commun. **2016**, 7, 1.

[46] C. d. Dimitrakopoulos, P. r. l. Malenfant, Adv. Mater. **2002**, 14, 99.

[47] E. J. Meijer, D. M. de Leeuw, S. Setayesh, E. van Veenendaal, B.-H. Huisman, P. W. M. Blom, J. C. Hummelen, U. Scherf, T. M. Klapwijk, Nat. Mater. **2003**, 2, 678.

[48] G. Tarabella, F. M. Mohammadi, N. Coppedè, F. Barbero, S. Iannotta, C. Santato, F. Cicoira, Chem. Sci. **2013**, 4, 1395.

[49] J. Rivnay, R. M. Owens, G. G. Malliaras, Chem. Mater. **2014**, 26, 679.

[50] J. M. Leger, Adv. Mater. **2008**, 20, 837.

[51] U. Zschieschang, J. W. Borchert, M. Giorgio, M. Caironi, F. Letzkus, J. N. Burghartz, U. Waizmann, J. Weis, S. Ludwigs, H. Klauk, Adv. Funct. Mater. **2020**, 30, 1903812.

[52] J. Rivnay, S. Inal, A. Salleo, R. M. Owens, M. Berggren, G. G. Malliaras, Nat. Rev. Mater. **2018**, 3, 1.

[53] J. Tropp, J. Rivnay, J. Mater. Chem. C **2021**, 9, 13543.

[54] J. Mei, Z. Bao, Chem. Mater. **2014**, 26, 604.

[55] P. Schmode, A. Savva, R. Kahl, D. Ohayon, F. Meichsner, O. Dolynchuk, T. Thurn-Albrecht, S. Inal, M. Thelakkat, ACS Appl. Mater. Interfaces **2020**, 12, 13029.

[56] R. K. Hallani, B. D. Paulsen, A. J. Petty, R. Sheelamanthula, M. Moser, K. J. Thorley, W. Sohn, R. B. Rashid, A. Savva, S. Moro, J. P. Parker, O. Drury, M. Alsufyani, M. Neophytou, J. Kosco, S. Inal, G. Costantini, J. Rivnay, I. McCulloch, J. Am. Chem. Soc. **2021**, 143, 11007.

[57] A. Savva, R. Hallani, C. Cendra, J. Surgailis, T. C. Hidalgo, S. Wustoni, R. Sheelamanthula, X. Chen, M. Kirkus, A. Giovannitti, A. Salleo, I. McCulloch, S. Inal, Adv. Funct. Mater. **2020**, 30, 1907657.

[58] X. Chen, A. Marks, B. D. Paulsen, R. Wu, R. B. Rashid, H. Chen, M. Alsufyani, J. Rivnay, I. McCulloch, Angew. Chem. Int. Ed. **2020**, anie.202013998.

[59] Z. S. Parr, J. Borges-González, R. B. Rashid, K. J. Thorley, D. Meli, B. D. Paulsen, J. Strzalka, J. Rivnay, C. B. Nielsen, Adv. Mater. **2022**, 34, 2107829.

[60] M. Moser, Y. Wang, T. Cecilia Hidalgo, H. Liao, Y. Yu, J. Chen, J. Duan, F. Moruzzi, S. Griggs, A. Marks, N. Gasparini, A. Wadsworth, S. Inal, I. McCulloch, W. Yue, Mater. Horiz. **2022**, 9, 973.

[61] Y. He, N. A. Kukhta, A. Marks, C. K. Luscombe, J. Mater. Chem. C **2022**, 10, 2314.

[62] B. D. Paulsen, S. Fabiano, J. Rivnay, Annu. Rev. Mater. Res. **2021**, 51, annurev.

[63] S. P. O. Danielsen, G. E. Sanoja, S. R. McCuskey, B. Hammouda, G. C. Bazan, G. H. Fredrickson, R. A. Segalman, Chem. Mater. **2018**, 30, 1417.

[64] J. Rivnay, S. Inal, B. A. Collins, M. Sessolo, E. Stavrinidou, X. Strakosas, C. Tassone, D. M. Delongchamp, G. G. Malliaras, Nat. Commun. **2016**, 7, 11287.

[65] S. Inal, J. Rivnay, A. I. Hofmann, I. Uguz, M. Mumtaz, D. Katsigiannopoulos, C. Brochon, E. Cloutet, G. Hadziioannou, G. G. Malliaras, J. Polym. Sci. Part B Polym. Phys. **2016**, 54, 147.

[66] J. Surgailis, A. Savva, V. Druet, B. D. Paulsen, R. Wu, A. Hamidi-Sakr, D. Ohayon, G. Nikiforidis, X. Chen, I. McCulloch, J. Rivnay, S. Inal, Adv. Funct. Mater. **2021**, 31, 2010165.

[67] H. T. Nicolai, M. Kuik, G. a. H. Wetzelaer, B. de Boer, C. Campbell, C. Risko, J. L. Brédas, P. W. M. Blom, Nat. Mater. **2012**, 11, 882.

[68] Z. S. Parr, R. B. Rashid, B. D. Paulsen, B. Poggi, E. Tan, M. Freeley, M. Palma, I. Abrahams, J. Rivnay, C. B. Nielsen, Adv. Electron. Mater. **2020**, 6, 2000215.

[69] C. G. Bischak, L. Q. Flagg, K. Yan, C.-Z. Li, D. S. Ginger, ACS Appl. Mater. Interfaces **2019**, 11, 28138.

[70] H. Kang, W. Lee, J. Oh, T. Kim, C. Lee, B. J. Kim, Acc. Chem. Res. **2016**, 49, 2424.

[71] H. Sirringhaus, P. J. Brown, R. H. Friend, M. M. Nielsen, K. Bechgaard, B. M. W. Langeveld-Voss, A. J. H. Spiering, R. a. J. Janssen, E. W. Meijer, P. Herwig, D. M. de Leeuw, Nature **1999**, 401, 685.

[72] J. J. Brondijk, W. S. C. Roelofs, S. G. J. Mathijssen, A. Shehu, T. Cramer, F. Biscarini, P. W. M. Blom, D. M. de Leeuw, Phys. Rev. Lett. **2012**, 109, 056601.

[73] M. Mas-Torrent, C. Rovira, Chem. Rev. **2011**, 111, 4833.

[74] J. Chen, C. K. Tee, M. Shtein, D. C. Martin, J. Anthony, Org. Electron. **2009**, 10, 696.

[75] A. M. Nardes, M. Kemerink, R. a. J. Janssen, J. a. M. Bastiaansen, N. M. M. Kiggen, B. M. W. Langeveld, A. J. J. M. van Breemen, M. M. de Kok, Adv. Mater. **2007**, 19, 1196.

[76] S.-Y. Kim, J. Hwang, Y. J. Kim, H. J. Hwang, M. Son, N. Revannath, M.-H. Ham, K. Cho, B. H. Lee, Adv. Electron. Mater. **2019**, 5, 1800805.

[77] P. Cosseddu, J.-O. Vogel, B. Fraboni, J. P. Rabe, N. Koch, A. Bonfiglio, Adv. Mater. **2009**, 21, 344.

[78] Z. A. Lamport, H. F. Haneef, S. Anand, M. Waldrip, O. D. Jurchescu, J. Appl. Phys. **2018**, 124, 071101.

[79] H. H. Choi, K. Cho, C. D. Frisbie, H. Sirringhaus, V. Podzorov, Nat. Mater. **2017**, 17, 2.

[80] A. A. Virkar, S. Mannsfeld, Z. Bao, N. Stingelin, Adv. Mater. **2010**, 22, 3857.

[81] Z. He, K. Asare-Yeboah, Z. Zhang, S. Bi, Org. Electron. **2022**, 103, 106448.

[82] Y. Sun, L. Tan, S. Jiang, H. Qian, Z. Wang, D. Yan, C. Di, Y. Wang, W. Wu, G. Yu, S. Yan, C. Wang, W. Hu, Y. Liu, D. Zhu, J. Am. Chem. Soc. **2007**, 129, 1882.

[83] S. Tsuzuki, H. Orita, N. Sato, J. Chem. Phys. **2016**, 145, 174503.

[84] S. Subramanian, S. K. Park, S. R. Parkin, V. Podzorov, T. N. Jackson, J. E. Anthony, J. Am. Chem. Soc. **2008**, 130, 2706.

[85] R. Li, W. Hu, Y. Liu, D. Zhu, Acc. Chem. Res. **2010**, 43, 529.

[86] A. Troisi, G. Orlandi, J. Phys. Chem. A **2006**, 110, 4065.

[87] A. Matsunaga, Y. Ogawa, D. Kumaki, S. Tokito, H. Katagiri, J. Phys. Chem. Lett. **2021**, 12, 111.

[88] J. Shi, L. Xu, Y. Li, M. Jia, Y. Kan, H. Wang, Org. Electron. **2013**, 14, 934.

[89] S. Haas, Y. Takahashi, K. Takimiya, T. Hasegawa, Appl. Phys. Lett. **2009**, 95, 022111.

[90] H. Ebata, T. Izawa, E. Miyazaki, K. Takimiya, M. Ikeda, H. Kuwabara, T. Yui, J. Am. Chem. Soc. **2007**, 129, 15732.

[91] T. Hamai, S. Inoue, S. Arai, T. Hasegawa, Phys. Rev. Mater. **2020**, 4, 074601.

[92] J. Cho, T. Higashino, T. Mori, Appl. Phys. Lett. **2015**, 106, 193303.

[93] E. Cho, C. Risko, D. Kim, R. Gysel, N. Cates Miller, D. W. Breiby, M. D. McGehee, M. F. Toney, R. J. Kline, J.-L. Bredas, J. Am. Chem. Soc. **2012**, 134, 6177.

[94] S. D. Kang, G. J. Snyder, Nat. Mater. **2017**, 16, 252.

[95] O. D. Jurchescu, D. A. Mourey, S. Subramanian, S. R. Parkin, B. M. Vogel, J. E. Anthony, T. N. Jackson, D. J. Gundlach, Phys. Rev. B **2009**, 80, 085201.

[96] S. Schiefer, M. Huth, A. Dobrinevski, B. Nickel, J. Am. Chem. Soc. **2007**, 129, 10316.

[97] A. Salleo, R. J. Kline, D. M. DeLongchamp, M. L. Chabinyc, Adv. Mater. **2010**, 22, 3812.

[98] Y. Diao, L. Shaw, Z. Bao, S. C. B. Mannsfeld, Energy Environ. Sci. **2014**, 7, 2145.

[99] J. C. Swarbrick, J. B. Taylor, J. N. O'Shea, Appl. Surf. Sci. **2006**, 252, 5622.

[100] M. A. Fusella, S. Yang, K. Abbasi, H. H. Choi, Z. Yao, V. Podzorov, A. Avishai, B. P. Rand, Chem. Mater. **2017**, 29, 6666.

[101] S. J. Rinehart, G. Yuan, M. D. Dadmun, Soft Matter **2020**, 16, 1287.

[102] Z. Lu, C. Wang, W. Deng, M. Tehinke Achille, J. Jie, X. Zhang, J. Mater. Chem. C **2020**, 8, 9133.

[103] B. Peng, S. Huang, Z. Zhou, P. K. L. Chan, Adv. Funct. Mater. **2017**, 27, 1700999.

[104] R. Janneck, P. Heremans, J. Genoe, C. Rolin, Adv. Mater. Interfaces **2018**, 5, 1800147.

[105] H. Minemawari, T. Yamada, H. Matsui, J. Tsutsumi, S. Haas, R. Chiba, R. Kumai, T. Hasegawa, Nature **2011**, 475, 364.

[106] C. R. McNeill, J. Polym. Sci. Part B Polym. Phys. **2011**, 49, 909.

[107] S. Yogev, R. Matsubara, M. Nakamura, Y. Rosenwaks, Org. Electron. **2010**, 11, 1729.

[108] T. W. Kelley, C. D. Frisbie, J. Phys. Chem. B **2001**, 105, 4538.

[109] M. Fahlman, S. Fabiano, V. Gueskine, D. Simon, M. Berggren, X. Crispin, Nat. Rev. Mater. **2019**, 4, 627.

[110] P. Swift, Surf. Interface Anal. **1982**, 4, 47.

[111] S. Casalini, C. A. Bortolotti, F. Leonardi, F. Biscarini, Chem. Soc. Rev. **2017**, 46, 40.

[112] A. Ulman, Chem. Rev. **1996**, 96, 1533.

[113] P. Drude, Ann. Phys. **1900**, 306, 566.

[114] A. Sommerfeld, Z. Für Phys. **1928**, 47, 1.

[115] F. Bloch, Z. Für Phys. **1929**, 52, 555.

[116] N. D. Lang, W. Kohn, Phys. Rev. B **1971**, 3, 1215.

[117] A. Kahn, Mater. Horiz. **2016**, 3, 7.

[118] D. Boudinet, M. Benwadih, Y. Qi, S. Altazin, J.-M. Verilhac, M. Kroger, C. Serbutoviez, R. Gwoziecki, R. Coppard, G. Le Blevennec, A. Kahn, G. Horowitz, Org. Electron. **2010**, 11, 227.

[119] T. L. Barr, S. Seal, J. Vac. Sci. Technol. A **1995**, 13, 1239.

[120] B. Lüssem, M. Riede, K. Leo, Phys. Status Solidi A **2013**, 210, 9.

[121] M. Schwarze, W. Tress, B. Beyer, F. Gao, R. Scholz, C. Poelking, K. Ortstein, A. A. Günther, D. Kasemann, D. Andrienko, K. Leo, Science **2016**, 352, 1446.

[122] R. Ghosh, F. C. Spano, Acc. Chem. Res. **2020**, 53, 2201.

[123] A. Dkhissi, Synth. Met. **2011**, 161, 1441.

[124] K. Feron, X. Zhou, W. J. Belcher, P. C. Dastoor, J. Appl. Phys. **2012**, 111, 044510.

[125] S. R. Forrest, Philos. Trans. R. Soc. Math. Phys. Eng. Sci. **2015**, 373, 20140320.

[126] J.-F. Chang, H. Sirringhaus, M. Giles, M. Heeney, I. McCulloch, Phys. Rev. B **2007**, 76, 205204.

[127] T. Koopmans, Physica **1934**, 1, 104.

[128] P. Politzer, F. Abu-Awwad, Theor. Chem. Acc. **1998**, 99, 83.

[129] S. Duhm, G. Heimel, I. Salzmann, H. Glowatzki, R. L. Johnson, A. Vollmer, J. P. Rabe, N. Koch, Nat. Mater. **2008**, 7, 326.

[130] H. Yoshida, K. Yamada, J. Tsutsumi, N. Sato, Phys. Rev. B **2015**, 92, 075145.

[131] M. Timpel, M. V. Nardi, G. Ligorio, B. Wegner, M. Pätzel, B. Kobin, S. Hecht, N. Koch, ACS Appl. Mater. Interfaces **2015**, 7, 11900.

[132] I. Salzmann, S. Duhm, G. Heimel, M. Oehzelt, R. Kniprath, R. L. Johnson, J. P. Rabe, N. Koch, J. Am. Chem. Soc. **2008**, 130, 12870.

[133] J.-L. Bredas, Mater. Horiz. **2013**, 1, 17.

[134] D. Cahen, A. Kahn, Adv. Mater. **2003**, 15, 271.

[135] X. Crispin, V. Geskin, A. Crispin, J. Cornil, R. Lazzaroni, W. R. Salaneck, J.-L. Brédas, J. Am. Chem. Soc. **2002**, 124, 8131.

[136] H. Vázquez, Y. J. Dappe, J. Ortega, F. Flores, J. Chem. Phys. **2007**, 126, 144703.

[137] G. Heimel, L. Romaner, E. Zojer, J.-L. Bredas, Acc. Chem. Res. **2008**, 41, 721.

[138] H. Ishii, K. Sugiyama, E. Ito, K. Seki, Adv. Mater. **1999**, 11, 605.

[139] Y. Xu, H. Sun, Y.-Y. Noh, IEEE Trans. Electron Devices **2017**, 64, 1932.

[140] H. Sirringhaus, Adv. Mater. **2005**, 17, 2411.

[141] K. Noda, Y. Wada, T. Toyabe, Org. Electron. **2014**, 15, 1571.

[142] W. Osikowicz, M. P. de Jong, S. Braun, C. Tengstedt, M. Fahlman, W. R. Salaneck, Appl. Phys. Lett. **2006**, 88, 193504.

[143] A. Kahn, N. Koch, W. Gao, J. Polym. Sci. Part B Polym. Phys. **2003**, 41, 2529.

[144] G. Witte, S. Lukas, P. S. Bagus, C. Wöll, Appl. Phys. Lett. **2005**, 87, 263502.

[145] S. Braun, W. R. Salaneck, M. Fahlman, Adv. Mater. **2009**, 21, 1450.

[146] A. Vilan, D. Cahen, Chem. Rev. **2017**, 117, 4624.

[147] T. Schultz, D. Lungwitz, E. Longhi, S. Barlow, S. R. Marder, N. Koch, Adv. Funct. Mater. **2021**, 31, 2010174.

[148] M. T. Greiner, M. G. Helander, W.-M. Tang, Z.-B. Wang, J. Qiu, Z.-H. Lu, Nat. Mater. **2012**, 11, 76.

[149] L. Chai, R. T. White, M. T. Greiner, Z. H. Lu, Phys. Rev. B **2014**, 89, 035202.

[150] M. Oehzelt, N. Koch, G. Heimel, Nat. Commun. **2014**, 5, 4174.

[151] Q. Bao, S. Braun, C. Wang, X. Liu, M. Fahlman, Adv. Mater. Interfaces **2019**, 6, 1800897.

[152] H. Wang, P. Amsalem, G. Heimel, I. Salzmann, N. Koch, M. Oehzelt, Adv. Mater. **2014**, 26, 925.

[153] H. Ishii, N. Hayashi, E. Ito, Y. Washizu, K. Sugi, Y. Kimura, M. Niwano, Y. Ouchi, K. Seki, Phys. Status Solidi A **2004**, 201, 1075.

[154] A. Liscio, V. Palermo, O. Fenwick, S. Braun, K. Müllen, M. Fahlman, F. Cacialli, P. Samorí, Small **2011**, 7, 634.

[155] A. Liscio, V. Palermo, P. Samorì, Acc. Chem. Res. **2010**, 43, 541.

[156] F. Ciucci, Curr. Opin. Electrochem. **2019**, 13, 132.

[157] S. Inal, G. G. Malliaras, J. Rivnay, Nat. Commun. **2017**, 8, 1767.

[158] R. A. Huggins, Ionics **2002**, 8, 300.

[159] V. Nádaždy, F. Schauer, K. Gmucová, Appl. Phys. Lett. **2014**, 105, 142109.

[160] L. Huang, C. Su, Ultramicroscopy **2004**, 100, 277.

[161] Y. Chen, Y. Yao, N. Turetta, P. Samorì, J. Mater. Chem. C **2022**, 10, 2494.

[162] A. Kokil, K. Yang, J. Kumar, J. Polym. Sci. Part B Polym. Phys. **2012**, 50, 1130.

[163] O. G. Reid, K. Munechika, D. S. Ginger, Nano Lett. **2008**, 8, 1602.

[164] Z. Jin, D. Gehrig, C. Dyer-Smith, E. J. Heilweil, F. Laquai, M. Bonn, D. Turchinovich, J. Phys. Chem. Lett. **2014**, 5, 3662.

[165] N. Karl, Synth. Met. **2003**, 133–134, 649.

[166] D. A. Koutsouras, P. Gkoupidenis, C. Stolz, V. Subramanian, G. G. Malliaras, D. C. Martin, ChemElectroChem **2017**, 4, 2321.

[167] W. N. Hansen, G. J. Hansen, Surf. Sci. **2001**, 481, 172.

[168] A. Liscio, V. Palermo, K. Müllen, P. Samorì, J. Phys. Chem. C **2008**, 112, 17368.

[169] N. Turetta, F. Sedona, A. Liscio, M. Sambi, P. Samorì, Adv. Mater. Interfaces **2021**, 2100068.

[170] H. Kanter, Phys. Rev. B **1970**, 1, 522.

[171] I. Salzmann, G. Heimel, M. Oehzelt, S. Winkler, N. Koch, Acc. Chem. Res. **2016**, 49, 370.

[172] J. C. S. Costa, R. J. S. Taveira, C. F. R. A. C. Lima, A. Mendes, L. M. N. B. F. Santos, Opt. Mater. **2016**, 58, 51.

[173] A. C. Jakowetz, M. L. Böhm, A. Sadhanala, S. Huettner, A. Rao, R. H. Friend, Nat. Mater. **2017**, 16, 551.

[174] J. S. Kim, B. Lägel, E. Moons, N. Johansson, I. D. Baikie, W. R. Salaneck, R. H. Friend, F. Cacialli, Synth. Met. **2000**, 111–112, 311.

[175] Y. Ozawa, Y. Nakayama, S. Machida, H. Kinjo, H. Ishii, J. Electron Spectrosc. Relat. Phenom. **2014**, 197, 17.

[176] R. J. Davis, M. T. Lloyd, S. R. Ferreira, M. J. Bruzek, S. E. Watkins, L. Lindell, P. Sehati, M. Fahlman, J. E. Anthony, J. W. P. Hsu, J. Mater. Chem. **2011**, 21, 1721.

[177] N. Elgrishi, K. J. Rountree, B. D. McCarthy, E. S. Rountree, T. T. Eisenhart, J. L. Dempsey, J. Chem. Educ. **2018**, 95, 197.

[178] J. Sworakowski, Synth. Met. **2018**, 235, 125.

[179] K. P. Puntambekar, P. V. Pesavento, C. D. Frisbie, Appl. Phys. Lett. **2003**, 83, 5539.

[180] V. Kalihari, E. B. Tadmor, G. Haugstad, C. D. Frisbie, Adv. Mater. **2008**, 20, 4033.

[181] K. Puntambekar, J. Dong, G. Haugstad, C. D. Frisbie, Adv. Funct. Mater. **2006**, 16, 879.

[182] M. Brinkmann, C. Contal, N. Kayunkid, T. Djuric, R. Resel, Macromolecules **2010**, 43, 7604.

[183] R. C. Masters, N. Stehling, K. J. Abrams, V. Kumar, M. Azzolini, N. M. Pugno, M. Dapor, A. Huber, P. Schäfer, D. G. Lidzey, C. Rodenburg, Adv. Sci. **2019**, 6, 1801752.

[184] B. Bräuer, A. Virkar, S. C. B. Mannsfeld, D. P. Bernstein, R. Kukreja, K. W. Chou, T. Tyliszczak, Z. Bao, Y. Acremann, Chem. Mater. **2010**, 22, 3693.

[185] M. Statz, S. Schneider, F. J. Berger, L. Lai, W. A. Wood, M. Abdi-Jalebi, S. Leingang, H.-J. Himmel, J. Zaumseil, H. Sirringhaus, ACS Nano **2020**, 14, 15552.

[186] J. Rivnay, L. H. Jimison, J. E. Northrup, M. F. Toney, R. Noriega, S. Lu, T. J. Marks, A. Facchetti, A. Salleo, Nat. Mater. **2009**, 8, 952.

[187] H.-M. Liem, P. Etchegoin, K. s. Whitehead, D. d. c. Bradley, Adv. Funct. Mater. **2003**, 13, 66.

[188] S. Kuehn, P. Pingel, M. Breusing, T. Fischer, J. Stumpe, D. Neher, T. Elsaesser, Adv. Funct. Mater. **2011**, 21, 860.

[189] A. G. Lambert, P. B. Davies, D. J. Neivandt, Appl. Spectrosc. Rev. **2005**, 40, 103.

[190] N. Turetta, M.-A. Stoeckel, R. Furlan de Oliveira, F. Devaux, A. Greco, C. Cendra, S. Gullace, M. Gicevičius, B. Chattopadhyay, J. Liu, G. Schweicher, H. Sirringhaus, A. Salleo, M. Bonn, E. H. G. Backus, Y. H. Geerts, P. Samorì, J. Am. Chem. Soc. **2022**, 144, 2546.

[191] H. Hintz, H. Peisert, H.-J. Egelhaaf, T. Chassé, J. Phys. Chem. C **2011**, 115, 13373.

[192] I. G. Hill, D. Milliron, J. Schwartz, A. Kahn, Appl. Surf. Sci. **2000**, 166, 354.

[193] K. Zhang, T. Marszalek, P. Wucher, Z. Wang, L. Veith, H. Lu, H.-J. Räder, P. M. Beaujuge, P. W. M. Blom, W. Pisula, Adv. Funct. Mater. **2018**, 28, 1805594.

[194] V. Panchal, I. Dobryden, U. D. Hangen, D. Simatos, L. J. Spalek, I. E. Jacobs, G. Schweicher, P. M. Claesson, D. Venkateshvaran, Adv. Electron. Mater. **2022**, 8, 2101019.

[195] J. A. Woollam, B. D. Johs, C. M. Herzinger, J. N. Hilfiker, R. A. Synowicki, C. L. Bungay, Proc. Vol. 10294 Opt. Metrol. Crit. Rev. **1999**, 1029402.

[196] D. K. Paul, R. McCreery, K. Karan, J. Electrochem. Soc. **2014**, 161, F1395.

[197] M. Geiger, R. Acharya, E. Reutter, T. Ferschke, U. Zschieschang, J. Weis, J. Pflaum, H. Klauk, R. T. Weitz, Adv. Mater. Interfaces **2020**, 7, 1902145.

[198] S. Zollner, Y. Liang, R. B. Gregory, P. L. Fejes, D. Theodore, Z. Yu, D. H. Triyoso, J. Curless, C. Tracy, AIP Conf. Proc. **2005**, 788, 166.

[199] M. S. Haque, H. A. Naseem, W. D. Brown, J. Electrochem. Soc. **1997**, 144, 3265.

[200] R. S. Jachowicz, S. D. Senturia, Sens. Actuators **1981**, 2, 171.

[201] K. S. Novoselov, A. K. Geim, S. V. Morozov, D. Jiang, M. I. Katsnelson, Iv. Grigorieva, Sv. Dubonos, andAA Firsov, nature **2005**, 438, 197.

[202] D. R. Dreyer, S. Park, C. W. Bielawski, R. S. Ruoff, Chem. Soc. Rev. **2010**, 39, 228.

[203] C. Lv, C. Hu, J. Luo, S. Liu, Y. Qiao, Z. Zhang, J. Song, Y. Shi, J. Cai, A. Watanabe, Nanomaterials **2019**, 9, 422.

[204] Y. Yao, X. Chen, J. Zhu, B. Zeng, Z. Wu, X. Li, Nanoscale Res. Lett. **2012**, 7, 363.

[205] K. Rathi, K. Pal, ACS Omega **2017**, 2, 842.

[206] H. Bi, K. Yin, X. Xie, J. Ji, S. Wan, L. Sun, M. Terrones, M. S. Dresselhaus, Sci. Rep. **2013**, 3, 2714.

[207] N. L. Teradal, S. Marx, A. Morag, R. Jelinek, J. Mater. Chem. C **2017**, 5, 1128.

[208] C. Anichini, A. Aliprandi, S. M. Gali, F. Liscio, V. Morandi, A. Minoia, D. Beljonne, A. Ciesielski, P. Samorì, ACS Appl. Mater. Interfaces **2020**, 12, 44017.

[209] A. Splendiani, L. Sun, Y. Zhang, T. Li, J. Kim, C.-Y. Chim, G. Galli, F. Wang, Nano Lett. **2010**, 10, 1271.

[210] S. Ippolito, A. G. Kelly, R. Furlan de Oliveira, M.-A. Stoeckel, D. Iglesias, A. Roy, C. Downing, Z. Bian, L. Lombardi, Y. A. Samad, V. Nicolosi, A. C. Ferrari, J. N. Coleman, P. Samorì, Nat. Nanotechnol. **2021**, 16, 592.

[211] R. Kumar, W. Zheng, X. Liu, J. Zhang, M. Kumar, Adv. Mater. Technol. **2020**, 5, 1901062.

[212] Z. Yu, Z.-Y. Ong, S. Li, J.-B. Xu, G. Zhang, Y.-W. Zhang, Y. Shi, X. Wang, Adv. Funct. Mater. **2017**, 27, 1604093.

[213] J. Zhao, N. Li, H. Yu, Z. Wei, M. Liao, P. Chen, S. Wang, D. Shi, Q. Sun, G. Zhang, Adv. Mater. **2017**, 29, 1702076.

[214] H. Yang, S. Cai, D. Wu, X. Fang, Adv. Electron. Mater. **2020**, 6, 2000659.

[215] D. J. Late, Y.-K. Huang, B. Liu, J. Acharya, S. N. Shirodkar, J. Luo, A. Yan, D. Charles, U. V. Waghmare, V. P. Dravid, C. N. R. Rao, ACS Nano **2013**, 7, 4879.

[216] M. A. Squillaci, L. Ferlauto, Y. Zagranyarski, S. Milita, K. Müllen, P. Samorì, Adv. Mater. **2015**, 27, 3170.

[217] M. A. Squillaci, G. Markiewicz, A. Walczak, A. Ciesielski, A. R. Stefankiewicz, P. Samorì, Chem. Commun. **2017**, 53, 9713.

[218] M. A. Squillaci, A. Cipriani, M. Melucci, M. Zambianchi, G. Caminati, P. Samorì, Adv. Electron. Mater. **2018**, 4, 1700382.

[219] M. A. Squillaci, M.-A. Stoeckel, P. Samorì, Nanoscale **2019**, 11, 19319.

[220] Y. Park, X. Chen, J. Mater. Chem. A **2020**, 8, 15227.

[221] H. Farahani, R. Wagiran, M. N. Hamidon, Sensors **2014**, 14, 7881.

[222] Z. Chen, C. Lu, Sens. Lett. **2005**, 3, 274.

[223] M. A. Najeeb, Z. Ahmad, R. A. Shakoor, Adv. Mater. Interfaces **2018**, 5, 1800969.

[224] R. Hofmockel, U. Zschieschang, U. Kraft, R. Rödel, N. H. Hansen, M. Stolte, F. Würthner, K. Takimiya, K. Kern, J. Pflaum, H. Klauk, Org. Electron. **2013**, 14, 3213.

[225] M. Tello, M. Chiesa, C. M. Duffy, H. Sirringhaus, Adv. Funct. Mater. **2008**, 18, 3907.

[226] S. Park, S. H. Kim, H. H. Choi, B. Kang, K. Cho, Adv. Funct. Mater. **2020**, 30, 1904590.

[227] J. Wünsche, Y. Deng, P. Kumar, E. Di Mauro, E. Josberger, J. Sayago, A. Pezzella, F. Soavi, F. Cicoira, M. Rolandi, C. Santato, Chem. Mater. **2015**, 27, 436.

[228] T. Cramer, A. Campana, F. Leonardi, S. Casalini, A. Kyndiah, M. Murgia, F. Biscarini, J. Mater. Chem. B **2013**, 1, 3728.

[229] P. A. Thiel, T. E. Madey, Surf. Sci. Rep. **1987**, 7, 211.

[230] J. H. Anderson, G. A. Parks, J. Phys. Chem. **1968**, 72, 3662.

[231] M.-H. Seo, H.-H. Yang, K.-W. Choi, J.-S. Lee, J.-B. Yoon, Appl. Phys. Lett. **2015**, 106, 053701.

[232] H. Baumgärtner, V. Fuenzalida, I. Eisele, Appl. Phys. A **1987**, 43, 223.

[233] S. R. Wasserman, Y. T. Tao, G. M. Whitesides, Langmuir **1989**, 5, 1074.

[234] G. J. Young, J. Colloid Sci. **1958**, 13, 67.

[235] J. Yang, S. Meng, L. Xu, E. G. Wang, Phys. Rev. B **2005**, 71, 035413.

[236] D. B. Asay, S. H. Kim, J. Phys. Chem. B **2005**, 109, 16760.

[237] K. Ito, M. Harada, N. L. Yamada, K. Kudo, H. Aoki, T. Kanaya, Langmuir **2020**, 36, 12830.

[238] K. D. Kreuer, Solid State Ion. **2000**, 136–137, 149.

[239] J. A. Schaefer, F. Stucki, D. J. Frankel, W. Göpel, G. J. Lapeyre, J. Vac. Sci. Technol. B Microelectron. Process. Phenom. **1984**, 2, 359.

[240] J. R. Macdonald, Impedance Spectrosc. **1992**, 20, 289.

[241] V. F. Lvovich, in Impedance Spectrosc., John Wiley & Sons, Ltd, **2012**, pp. 1–21.

[242] H. Morgan, R. Pethig, G. T. Stevens, J. Phys. [E] **1986**, 19, 80.

[243] L. Glasser, Chem. Rev. **1975**, 75, 21.

[244] L. Merces, R. F. de Oliveira, H. L. Gomes, C. C. Bof Bufon, Org. Electron. **2017**, 49, 107.

[245] T. Kawamoto, M. Aoki, T. Kimura, T. Mizusawa, N. L. Yamada, J. Miyake, K. Miyatake, J. Inukai, Jpn. J. Appl. Phys. **2019**, 58, SIID01.

[246] L. Bocquet, Nat. Mater. **2020**, 19, 254.

[247] Y. Hou, X. Hou, Science **2021**, DOI 10.1126/science.abj0437.

[248] C. Pitsalidis, A.-M. Pappa, A. J. Boys, Y. Fu, C.-M. Moysidou, D. van Niekerk, J. Saez, A. Savva, D. Iandolo, R. M. Owens, Chem. Rev. **2022**, 122, 4700.

[249] I. B. Dimov, M. Moser, G. G. Malliaras, I. McCulloch, Chem. Rev. **2022**, 122, 4356.

[250] R. Avila, C. Li, Y. Xue, J. A. Rogers, Y. Huang, Proc. Natl. Acad. Sci. **2021**, 118, e2026405118.

[251] M. Berggren, E. D. Głowacki, D. T. Simon, E. Stavrinidou, K. Tybrandt, Chem. Rev. **2022**, DOI 10.1021/acs.chemrev.1c00390.

[252] S.-H. Sunwoo, S. I. Han, H. Joo, G. D. Cha, D. Kim, S. H. Choi, T. Hyeon, D.-H. Kim, Matter **2020**, 3, 1923.

[253] H. S. White, G. P. Kittlesen, M. S. Wrighton, J. Am. Chem. Soc. **1984**, 106, 5375.

[254] D. A. Bernards, G. G. Malliaras, Adv. Funct. Mater. **2007**, 17, 3538.

[255] J. Rivnay, P. Leleux, M. Ferro, M. Sessolo, A. Williamson, D. A. Koutsouras, D. Khodagholy, M. Ramuz, X. Strakosas, R. M. Owens, C. Benar, J.-M. Badier, C. Bernard, G. G. Malliaras, Sci. Adv. **2015**, 1, e1400251.

[256] A. Laiho, L. Herlogsson, R. Forchheimer, X. Crispin, M. Berggren, Proc. Natl. Acad. Sci. **2011**, 108, 15069.

[257] J. Chen, W. Huang, D. Zheng, Z. Xie, X. Zhuang, D. Zhao, Y. Chen, N. Su, H. Chen, R. M. Pankow, Z. Gao, J. Yu, X. Guo, Y. Cheng, J. Strzalka, X. Yu, T. J. Marks, A. Facchetti, Nat. Mater. **2022**, 21, 564.

[258] R. B. Rashid, X. Ji, J. Rivnay, Biosens. Bioelectron. **2021**, 190, 113461.

[259] A. Nawaz, Q. Liu, W. L. Leong, K. E. Fairfull-Smith, P. Sonar, Adv. Mater. **2021**, 33, 2101874.

[260] Z. Yi, G. Natale, P. Kumar, E. Di Mauro, M.-C. Heuzey, F. Soavi, I. I. Perepichka, S. K. Varshney, C. Santato, F. Cicoira, J. Mater. Chem. C **2015**, 3, 6549.

[261] T. Nguyen-Dang, K. Harrison, A. Lill, A. Dixon, E. Lewis, J. Vollbrecht, T. Hachisu, S. Biswas, Y. Visell, T.-Q. Nguyen, Adv. Electron. Mater. **2021**, 7, 2100519.

[262] R. Giridharagopal, L. Q. Flagg, J. S. Harrison, M. E. Ziffer, J. Onorato, C. K. Luscombe, D. S. Ginger, Nat. Mater. **2017**, 16, 737.

[263] F. Cicoira, M. Sessolo, O. Yaghmazadeh, J. A. DeFranco, S. Y. Yang, G. G. Malliaras, Adv. Mater. **2010**, 22, 1012.

[264] G. Tarabella, C. Santato, S. Y. Yang, S. Iannotta, G. G. Malliaras, F. Cicoira, Appl. Phys. Lett. **2010**, 97, 123304.

[265] P. J. Brewer, R. J. Leese, R. J. C. Brown, Electrochimica Acta **2012**, 71, 252.

[266] G.-H. Lee, H. Moon, H. Kim, G. H. Lee, W. Kwon, S. Yoo, D. Myung, S. H. Yun, Z. Bao, S. K. Hahn, Nat. Rev. Mater. **2020**, 5, 149.

[267] L. Xiang, L. Liu, F. Zhang, C. Di, D. Zhu, Adv. Funct. Mater. **2021**, 31, 2102149.

[268] Y. Chang, L. Wang, R. Li, Z. Zhang, Q. Wang, J. Yang, C. F. Guo, T. Pan, Adv. Mater. **2021**, 33, 2003464.

[269] T. Paltrinieri, L. Bondi, V. Đerek, B. Fraboni, E. D. Głowacki, T. Cramer, Adv. Funct. Mater. **2021**, 31, 2010116.

[270] M. Jakešová, M. Silverå Ejneby, V. Đerek, T. Schmidt, M. Gryszel, J. Brask, R. Schindl, D. T. Simon, M. Berggren, F. Elinder, E. D. Głowacki, Sci. Adv. **2019**, 5, eaav5265.

[271] Z. Chen, S. N. Obaid, L. Lu, Opt. Mater. Express **2019**, 9, 3843.

[272] Y. Fang, L. Meng, A. Prominski, E. N. Schaumann, M. Seebald, B. Tian, Chem. Soc. Rev. **2020**, 49, 7978.

[273] P. Bhatnagar, M. Patel, T. T. Nguyen, S. Kim, J. Kim, J. Phys. Chem. Lett. **2021**, 12, 12426.

[274] O. Parlak, A. P. F. Turner, Biosens. Bioelectron. **2016**, 76, 251.

[275] Meenakshi, S. K. Shukla, J. Narang, V. Kumar, P. P. Govender, A. Niv, C. M. Hussain, R. Wang, B. Mangla, R. S. Babu, Chemosensors **2020**, 8, 45.

[276] I. Willner, Acc. Chem. Res. **1997**, 30, 347.

[277] F. Wang, X. Liu, I. Willner, Adv. Mater. **2013**, 25, 349.

[278] A. Goulet-Hanssens, F. Eisenreich, S. Hecht, Adv. Mater. **2020**, 32, 1905966.

[279] I. Tochitsky, M. A. Kienzler, E. Isacoff, R. H. Kramer, Chem. Rev. **2018**, 118, 10748.

[280] K.-J. Baeg, M. Binda, D. Natali, M. Caironi, Y.-Y. Noh, Adv. Mater. **2013**, 25, 4267.

[281] Q. Dai, S. Xu, Y. Peng, W. Lv, L. Sun, Y. Wei, Chem. Phys. Lett. **2020**, 742, 137133.

[282] L. Hou, T. Leydecker, X. Zhang, W. Rekab, M. Herder, C. Cendra, S. Hecht, I. McCulloch, A. Salleo, E. Orgiu, P. Samorì, J. Am. Chem. Soc. **2020**, 142, 11050.

[283] R. Klajn, Chem. Soc. Rev. **2014**, 43, 148.

[284] M. L. Chabinyc, M. F. Toney, R. J. Kline, I. McCulloch, M. Heeney, J. Am. Chem. Soc. **2007**, 129, 3226.

[285] A. Wang, I. Kymissis, V. Bulović, A. I. Akinwande, Appl. Phys. Lett. **2006**, 89, 112109.

[286] P. Kumar, Z. Yi, S. Zhang, A. Sekar, F. Soavi, F. Cicoira, Appl. Phys. Lett. **2015**, 107, 053303.

[287] A. Radu, R. Byrne, N. Alhashimy, M. Fusaro, S. Scarmagnani, D. Diamond, J. Photochem. Photobiol. Chem. **2009**, 206, 109.

[288] J. Kohl-Landgraf, M. Braun, C. Özçoban, D. P. N. Gonçalves, A. Heckel, J. Wachtveitl, J. Am. Chem. Soc. **2012**, 134, 14070.

[289] P. Boufflet, Y. Han, Z. Fei, N. D. Treat, R. Li, D.-M. Smilgies, N. Stingelin, T. D. Anthopoulos, M. Heeney, Adv. Funct. Mater. **2015**, 25, 7038.

[290] Z. Fei, P. Boufflet, S. Wood, J. Wade, J. Moriarty, E. Gann, E. L. Ratcliff, C. R. McNeill, H. Sirringhaus, J.-S. Kim, M. Heeney, J. Am. Chem. Soc. **2015**, 137, 6866.

[291] A. F. Paterson, L. Tsetseris, R. Li, A. Basu, H. Faber, A.-H. Emwas, J. Panidi, Z. Fei, M. R. Niazi, D. H. Anjum, M. Heeney, T. D. Anthopoulos, Adv. Mater. **2019**, 31, 1900871.

[292] M. Waldrip, O. D. Jurchescu, D. J. Gundlach, E. G. Bittle, Adv. Funct. Mater. **2020**, 30, 1904576.

[293] J. W. Borchert, R. T. Weitz, S. Ludwigs, H. Klauk, Adv. Mater. **2022**, 34, 2104075.

[294] F. Wu, Y. Liu, J. Zhang, S. Duan, D. Ji, H. Yang, Small Methods **2021**, 5, 2100676.

[295] Y. Wang, L. Sun, C. Wang, F. Yang, X. Ren, X. Zhang, H. Dong, W. Hu, Chem. Soc. Rev. **2019**, 48, 1492.

[296] Y. Yan, Y. Zhao, Y. Liu, J. Polym. Sci. **2021**, DOI 10.1002/pol.20210457.

[297] H. Kleemann, K. Krechan, A. Fischer, K. Leo, Adv. Funct. Mater. **2020**, 30, 1907113.

[298] J. C. Scott, J. Vac. Sci. Technol. A **2003**, 21, 521.

[299] V. Coropceanu, H. Li, P. Winget, L. Zhu, J.-L. Brédas, Annu. Rev. Mater. Res. **2013**, 43, 63.

[300] M. Nikolka, I. Nasrallah, B. Rose, M. K. Ravva, K. Broch, A. Sadhanala, D. Harkin, J. Charmet, M. Hurhangee, A. Brown, S. Illig, P. Too, J. Jongman, I. McCulloch, J.-L. Bredas, H. Sirringhaus, Nat. Mater. **2017**, 16, 356.

[301] E. Orgiu, J. George, J. A. Hutchison, E. Devaux, J. F. Dayen, B. Doudin, F. Stellacci, C. Genet, J. Schachenmayer, C. Genes, G. Pupillo, P. Samorì, T. W. Ebbesen, Nat. Mater. **2015**, 14, 1123.

[302] K. Nagarajan, J. George, A. Thomas, E. Devaux, T. Chervy, S. Azzini, K. Joseph, A. Jouaiti, M. W. Hosseini, A. Kumar, C. Genet, N. Bartolo, C. Ciuti, T. W. Ebbesen, ACS Nano **2020**, 14, 10219.

[303] R. Naaman, D. H. Waldeck, J. Phys. Chem. Lett. **2012**, 3, 2178.

[304] P. C. Mondal, N. Kantor-Uriel, S. P. Mathew, F. Tassinari, C. Fontanesi, R. Naaman, Adv. Mater. **2015**, 27, 1924.

[305] J. Liu, Z. Qin, H. Gao, H. Dong, J. Zhu, W. Hu, Adv. Funct. Mater. **2019**, 29, 1808453.

[306] M. Höppner, B. Kheradmand-Boroujeni, J. Vahland, M. F. Sawatzki, D. Kneppe, F. Ellinger, H. Kleemann, Adv. Sci. **n.d.**, n/a, 2201660.

[307] H. Kleemann, A. A. Günther, K. Leo, B. Lüssem, Small **2013**, 9, 3670.

[308] Q. Wang, E. J. Juarez-Perez, S. Jiang, M. Xiao, J. Qian, E.-S. Shin, Y.-Y. Noh, Y. Qi, Y. Shi, Y. Li, Phys. Rev. Mater. **2020**, 4, 044604.

[309] C. P. Yu, N. Kojima, S. Kumagai, T. Kurosawa, H. Ishii, G. Watanabe, J. Takeya, T. Okamoto, Commun. Chem. **2021**, 4, 1.

[310] X. Zeng, D. Zhang, Y. Zhu, M. Chen, H. Chen, S. Kasai, H. Meng, O. Goto, J. Mater. Chem. C **2019**, 7, 14275.

[311] F. M. Sawatzki, D. H. Doan, H. Kleemann, M. Liero, A. Glitzky, T. Koprucki, K. Leo, Phys. Rev. Appl. **2018**, 10, 034069.

[312] B. Lüssem, C.-M. Keum, D. Kasemann, B. Naab, Z. Bao, K. Leo, Chem. Rev. **2016**, 116, 13714.

[313] A. D. Scaccabarozzi, A. Basu, F. Aniés, J. Liu, O. Zapata-Arteaga, R. Warren, Y. Firdaus, M. I. Nugraha, Y. Lin, M. Campoy-Quiles, N. Koch, C. Müller, L. Tsetseris, M. Heeney, T. D. Anthopoulos, Chem. Rev. **2022**, 122, 4420.

[314] M. F. Sawatzki, H. Kleemann, B. K. Boroujeni, S.-J. Wang, J. Vahland, F. Ellinger, K. Leo, Adv. Sci. **2021**, 8, 2003519.

[315] J. Y. Lee, S. Roth, Y. W. Park, Appl. Phys. Lett. **2006**, 88, 252106.

[316] C. Reese, Z. Bao, Adv. Mater. **2007**, 19, 4535.

[317] D. Kneppe, F. Talnack, B. K. Boroujeni, C. Teixeira da Rocha, M. Höppner, A. Tahn, S. C. B. Mannsfeld, F. Ellinger, K. Leo, H. Kleemann, Mater. Today Energy **2021**, 21, 100697.

[318] G. Hlawacek, F. S. Khokhar, R. van Gastel, B. Poelsema, C. Teichert, Nano Lett. **2011**, 11, 333.

[319] S. Izawa, K. Nakano, K. Suzuki, Y. Chen, T. Kikitsu, D. Hashizume, T. Koganezawa, T.-Q. Nguyen, K. Tajima, Sci. Rep. **2018**, 8, 481.

[320] J. Lenz, F. del Giudice, F. R. Geisenhof, F. Winterer, R. T. Weitz, Nat. Nanotechnol. **2019**, 14, 579.

[321] E. Guo, Z. Wu, G. Darbandy, S. Xing, S.-J. Wang, A. Tahn, M. Göbel, A. Kloes, K. Leo, H. Kleemann, Nat. Commun. **2020**, 11, 4725.

[322] E. Guo, F. Dollinger, B. Amaya, A. Fischer, H. Kleemann, Adv. Opt. Mater. **2021**, 9, 2002058.

[323] H. Kleemann, G. Schwartz, S. Zott, M. Baumann, M. Furno, Flex. Print. Electron. **2020**, 5, 014009.

[324] B. Kheradmand-Boroujeni, M. P. Klinger, A. Fischer, H. Kleemann, K. Leo, F. Ellinger, Sci. Rep. **2018**, 8, 7643.

[325] U. Zschieschang, U. Waizmann, J. Weis, J. W. Borchert, H. Klauk, Sci. Adv. **2022**, 8, eabm9845.

[326] M. Geiger, R. Lingstädt, T. Wollandt, J. Deuschle, U. Zschieschang, F. Letzkus, J. N. Burghartz, P. A. van Aken, R. T. Weitz, H. Klauk, Adv. Electron. Mater. **2022**, 8, 2101215.

[327] M. J. Loiacono, E. L. Granstrom, C. D. Frisbie, J. Phys. Chem. B **1998**, 102, 1679.

[328] T. W. Kelley, C. D. Frisbie, J. Vac. Sci. Technol. B Microelectron. Nanometer Struct. Process. Meas. Phenom. **2000**, 18, 632.

[329] K. Seshadri, C. D. Frisbie, Appl. Phys. Lett. **2001**, 78, 993.

[330] H. Yang, T. J. Shin, M.-M. Ling, K. Cho, C. Y. Ryu, Z. Bao, J. Am. Chem. Soc. **2005**, 127, 11542.

[331] C. Ionescu-Zanetti, A. Mechler, S. A. Carter, R. Lal, Adv. Mater. **2004**, 16, 385.

[332] H. Yang, E. Glynos, B. Huang, P. F. Green, J. Phys. Chem. C **2013**, 117, 9590.

[333] D. Wood, I. Hancox, T. S. Jones, N. R. Wilson, J. Phys. Chem. C **2015**, 119, 11459.

[334] V. Palermo, A. Liscio, M. Palma, M. Surin, R. Lazzaroni, P. Samorì, Chem. Commun. **2007**, 3326.

[335] J. M. Mativetsky, M. Palma, P. Samorì, in STM AFM Stud. Biomol. Syst. Unravelling Nanoworld (Ed.: P. Samorì), Springer Berlin Heidelberg, Berlin, Heidelberg, **2008**, pp. 157–202.

[336] J. M. Mativetsky, E. Orgiu, I. Lieberwirth, W. Pisula, P. Samorì, Adv. Mater. **2014**, 26, 430.

[337] S. Hunter, T. D. Anthopoulos, Adv. Mater. **2013**, 25, 4320.

[338] G. G. Malliaras, J. R. Salem, P. J. Brock, C. Scott, Phys. Rev. B **1998**, 58, R13411.

[339] Y. Kondo, M. Osaka, H. Benten, H. Ohkita, S. Ito, ACS Macro Lett. **2015**, 4, 879.

[340] J. M. Mativetsky, H. Wang, S. S. Lee, L. Whittaker-Brooks, Y.-L. Loo, Chem. Commun. **2014**, 50, 5319.

[341] S. W. Button, J. M. Mativetsky, Appl. Phys. Lett. **2017**, 111, 083302.

[342] M. Zubair, Y. S. Ang, L. K. Ang, IEEE Trans. Electron Devices **2018**, 65, 3421.

[343] M. A. Rampi, G. M. Whitesides, Chem. Phys. **2002**, 281, 373.

[344] Y. Hu, D. X. Cao, A. T. Lill, L. Jiang, C.-A. Di, X. Gao, H. Sirringhaus, T.-Q. Nguyen, Adv. Electron. Mater. **2018**, 4, 1800175.

[345] X. Bai, K. Zong, J. Ly, J. S. Mehta, M. Hand, K. Molnar, S. Lee, B. Kahr, J. M. Mativetsky, A. Briseno, S. S. Lee, Chem. Mater. **2017**, 29, 7571.

[346] J. S. Mehta, J. M. Mativetsky, ACS Appl. Energy Mater. **2018**, 1, 5656.

[347] J. M. Mativetsky, A. Liscio, E. Treossi, E. Orgiu, A. Zanelli, P. Samorì, V. Palermo, J. Am. Chem. Soc. **2011**, 133, 14320.

[348] U. Celano, T. Hantschel, G. Giammaria, R. C. Chintala, T. Conard, H. Bender, W. Vandervorst, J. Appl. Phys. **2015**, 117, 214305.

[349] D.-Z. Guo, S.-M. Hou, G.-M. Zhang, Z.-Q. Xue, Appl. Surf. Sci. **2006**, 252, 5149.

[350] A. Rose, Phys. Rev. **1955**, 97, 1538.

[351] Z. Chiguvare, V. Dyakonov, Phys. Rev. B **2004**, 70, 235207.

[352] C. Tanase, E. J. Meijer, P. W. M. Blom, D. M. de Leeuw, Phys. Rev. Lett. **2003**, 91, 216601.

[353] P. W. M. Blom, M. J. M. de Jong, M. G. van Munster, Phys. Rev. B **1997**, 55, R656.

[354] J. Huang, G. Li, Y. Yang, Appl. Phys. Lett. **2005**, 87, 112105.

[355] G. Juška, K. Arlauskas, M. Viliūnas, K. Genevičius, R. Österbacka, H. Stubb, Phys. Rev. B **2000**, 62, R16235.

[356] A. Kumar, H.-H. Liao, Y. Yang, Org. Electron. **2009**, 10, 1615.

[357] H. Klauk, Adv. Electron. Mater. **2018**, 4, 1700474.

[358] M. Marinkovic, D. Belaineh, V. Wagner, D. Knipp, Adv. Mater. **2012**, 24, 4005.

[359] F. Ante, D. Kälblein, T. Zaki, U. Zschieschang, K. Takimiya, M. Ikeda, T. Sekitani, T. Someya, J. N. Burghartz, K. Kern, H. Klauk, Small **2012**, 8, 73.

[360] T. J. Richards, H. Sirringhaus, J. Appl. Phys. **2007**, 102, 094510.

[361] A. F. Paterson, S. Singh, K. J. Fallon, T. Hodsden, Y. Han, B. C. Schroeder, H. Bronstein, M. Heeney, I. McCulloch, T. D. Anthopoulos, Adv. Mater. **2018**, 30, 1801079.

[362] S. Donnhäuser, A. Pacheco-Sanchez, K. Haase, S. C. B. Mannsfeld, M. Claus, S. Blawid, Org. Electron. **2021**, 99, 106343.

[363] Z. A. Lamport, K. J. Barth, H. Lee, E. Gann, S. Engmann, H. Chen, M. Guthold, I. McCulloch, J. E. Anthony, L. J. Richter, D. M. DeLongchamp, O. D. Jurchescu, Nat. Commun. **2018**, 9, 5130.

[364] E. Bestelink, U. Zschieschang, I. Bandara R M, H. Klauk, R. A. Sporea, Adv. Electron. Mater. **2022**, 8, 2101101.

[365] H. Chen, W. Zhang, M. Li, G. He, X. Guo, Chem. Rev. **2020**, 120, 2879.

[366] Y. Xu, H. Sun, A. Liu, H.-H. Zhu, W. Li, Y.-F. Lin, Y.-Y. Noh, Adv. Mater. **2018**, 30, 1801830.

[367] T. Matsumoto, W. Ou-Yang, K. Miyake, T. Uemura, J. Takeya, Org. Electron. **2013**, 14, 2590.

[368] A. A. Günther, M. Sawatzki, P. Formánek, D. Kasemann, K. Leo, Adv. Funct. Mater. **2016**, 26, 768.

[369] D. Dahal, P. R. Paudel, V. Kaphle, R. K. Radha Krishnan, B. Lüssem, ACS Appl. Mater. Interfaces **2022**, 14, 7063.

[370] K. Qiao, S. Arakaki, M. Suzuki, K. Nakayama, ACS Omega **2022**, DOI 10.1021/acsomega.2c02085.

[371] A. Anand, J. P. Madalaimuthu, M. Schaal, F. Otto, M. Gruenewald, S. Alam, T. Fritz, U. S. Schubert, H. Hoppe, ACS Appl. Electron. Mater. **2021**, 3, 929.

[372] S. Pang, Y. Hernandez, X. Feng, K. Müllen, Adv. Mater. **2011**, 23, 2779.

[373] I. Valitova, M. Amato, F. Mahvash, G. Cantele, A. Maffucci, C. Santato, R. Martel, F. Cicoira, Nanoscale **2013**, 5, 4638.

[374] J. Meyer, S. Hamwi, M. Kröger, W. Kowalsky, T. Riedl, A. Kahn, Adv. Mater. **2012**, 24, 5408.

[375] A. I. Hofmann, E. Cloutet, G. Hadziioannou, Adv. Electron. Mater. **2018**, 4, 1700412.

[376] Y. Zhou, C. Fuentes-Hernandez, J. Shim, J. Meyer, A. J. Giordano, H. Li, P. Winget, T. Papadopoulos, H. Cheun, J. Kim, M. Fenoll, A. Dindar, W. Haske, E. Najafabadi, T. M. Khan, H. Sojoudi, S. Barlow, S. Graham, J.-L. Brédas, S. R. Marder, A. Kahn, B. Kippelen, Science **2012**, 336, 327.

[377] M. L. Sushko, A. L. Shluger, Adv. Mater. **2009**, 21, 1111.

[378] H. C. Potter, J. M. Blakely, J. Vac. Sci. Technol. **1975**, 12, 635.

[379] R. F. Carvalhal, R. Sanches Freire, L. T. Kubota, Electroanalysis **2005**, 17, 1251.

[380] Y. Golan, L. Margulis, I. Rubinstein, Surf. Sci. **1992**, 264, 312.

[381] M. J. Rost, D. A. Quist, J. W. M. Frenken, Phys. Rev. Lett. **2003**, 91, 026101.

[382] C. E. D. Chidsey, D. N. Loiacono, T. Sleator, S. Nakahara, Surf. Sci. **1988**, 200, 45.

[383] L. Chai, J. Klein, Langmuir **2007**, 23, 7777.

[384] Y. Golan, L. Margulis, S. Matlis, I. Rubinstein, J. Electrochem. Soc. **1995**, 142, 1629.

[385] S. E. Donnelly, V. Vishnyakov, D. Taylor, R. Valizadeh, I. M. Ballard, D. T. Goddard, Appl. Surf. Sci. **1994**, 74, 81.

[386] M. H. Dishner, M. M. Ivey, S. Gorer, J. C. Hemminger, F. J. Feher, J. Vac. Sci. Technol. A **1998**, 16, 3295.

[387] D. Berman, J. Krim, Thin Solid Films **2012**, 520, 6201.

[388] K. Raiber, A. Terfort, C. Benndorf, N. Krings, H.-H. Strehblow, Surf. Sci. **2005**, 595, 56.

[389] T. Smith, J. Colloid Interface Sci. **1980**, 75, 51.

[390] M. S. Inkpen, Z.-F. Liu, H. Li, L. M. Campos, J. B. Neaton, L. Venkataraman, Nat. Chem. **2019**, 11, 351.

[391] D. A. Lamprou, J. R. Smith, T. G. Nevell, E. Barbu, C. Stone, C. R. Willis, R. J. Ewen, J. Tsibouklis, Surf. Sci. **2010**, 604, 541.

[392] M.-T. Lee, C.-C. Hsueh, M. S. Freund, G. S. Ferguson, Langmuir **1998**, 14, 6419.

[393] H. Piao, N. S. McIntyre, Surf. Interface Anal. **2002**, 33, 591.

[394] M. A. Baker, Thin Solid Films **1980**, 69, 359.

[395] R. W. Strayer, W. Mackie, L. W. Swanson, Surf. Sci. **1973**, 34, 225.

[396] J. Lecoeur, J. P. Bellier, C. Koehler, Electrochimica Acta **1990**, 35, 1383.

[397] M. Chelvayohan, C. H. B. Mee, J. Phys. C Solid State Phys. **1982**, 15, 2305.

[398] B. Friedel, T. J. K. Brenner, C. R. McNeill, U. Steiner, N. C. Greenham, Org. Electron. **2011**, 12, 1736.

[399] T. Kagiyama, Y. Saito, K. Otobe, S. Nakajima, Appl. Surf. Sci. **2003**, 216, 542.

[400] J. C. Love, L. A. Estroff, J. K. Kriebel, R. G. Nuzzo, G. M. Whitesides, Chem. Rev. **2005**, 105, 1103.

[401] C. A. Smith, M. R. Narouz, P. A. Lummis, I. Singh, A. Nazemi, C.-H. Li, C. M. Crudden, Chem. Rev. **2019**, 119, 4986.

[402] V. B. Engelkes, J. M. Beebe, C. D. Frisbie, J. Am. Chem. Soc. **2004**, 126, 14287.

[403] S. Ho Choi, B. Kim, C. D. Frisbie, Science **2008**, 320, 1482.

[404] J. M. Mativetsky, G. Pace, M. Elbing, M. A. Rampi, M. Mayor, P. Samorì, J. Am. Chem. Soc. **2008**, 130, 9192.

[405] C. D. Bain, E. B. Troughton, Y. T. Tao, J. Evall, G. M. Whitesides, R. G. Nuzzo, J. Am. Chem. Soc. **1989**, 111, 321.

[406] A. Liscio, E. Orgiu, J. M. Mativetsky, V. Palermo, P. Samorì, Adv. Mater. **2010**, 22, 5018.

[407] O. Fenwick, C. V. Dyck, K. Murugavel, D. Cornil, F. Reinders, S. Haar, M. Mayor, J. Cornil, P. Samorì, J. Mater. Chem. C **2015**, 3, 3007.

[408] P. E. Laibinis, M. Anne. Fox, J. P. Folkers, G. M. Whitesides, Langmuir **1991**, 7, 3167.

[409] S. Tatara, Y. Kuzumoto, M. Kitamura, J. Nanosci. Nanotechnol. **2016**, 16, 3295.

[410] Y. Kuzumoto, M. Kitamura, Appl. Phys. Express **2014**, 7, 035701.

[411] A. B. Chwang, C. D. Frisbie, J. Appl. Phys. **2001**, 90, 1342.

[412] M. J. Kang, I. Doi, H. Mori, E. Miyazaki, K. Takimiya, M. Ikeda, H. Kuwabara, Adv. Mater. **2011**, 23, 1222.

[413] P. Xie, T. Liu, J. Sun, J. Yang, Adv. Funct. Mater. **2022**, 32, 2200843.

[414] S. Yun, C. Yun, D. Ho, W. Chae, T. Earmme, C. Kim, S. Seo, Synth. Met. **2022**, 285, 117022.

[415] S. Chen, Z. Li, Y. Qiao, Y. Song, J. Mater. Chem. C **2021**, 9, 1126.

[416] Y. Gao, Mater. Sci. Eng. R Rep. **2010**, 68, 39.

[417] Z. Wu, Y. Yan, Y. Zhao, Y. Liu, Small Methods **n.d.**, n/a, 2200752.

[418] T. Breuer, A. Karthäuser, H. Klemm, F. Genuzio, G. Peschel, A. Fuhrich, T. Schmidt, G. Witte, ACS Appl. Mater. Interfaces **2017**, 9, 8384.

[419] A. O. F. Jones, B. Chattopadhyay, Y. H. Geerts, R. Resel, Adv. Funct. Mater. **2016**, 26, 2233.

[420] M.-C. Jung, M. R. Leyden, G. O. Nikiforov, M. V. Lee, H.-K. Lee, T. J. Shin, K. Takimiya, Y. Qi, ACS Appl. Mater. Interfaces **2015**, 7, 1833.

[421] D. Käfer, L. Ruppel, G. Witte, Phys. Rev. B **2007**, 75, 085309.

[422] S. Wang, D. Niu, L. Lyu, Y. Huang, X. Wei, C. Wang, H. Xie, Y. Gao, Appl. Surf. Sci. **2017**, 416, 696.

[423] D. Natali, M. Caironi, Adv. Mater. **2012**, 24, 1357.

[424] F. Yu, S. Wu, X. Wang, G. Zhang, H. Lu, L. Qiu, RSC Adv. **2017**, 7, 11572.

[425] J.-I. Park, J. W. Chung, J.-Y. Kim, J. Lee, J. Y. Jung, B. Koo, B.-L. Lee, S. W. Lee, Y. W. Jin, S. Y. Lee, J. Am. Chem. Soc. **2015**, 137, 12175.

[426] E.-K. Lee, M. Y. Lee, A. Choi, J.-Y. Kim, O. Y. Kweon, J.-H. Kim, J. Y. Jung, T.-J. Shin, J. H. Oh, J.-I. Park, S. Y. Lee, Adv. Electron. Mater. **2017**, 3, 1700142.

[427] H. Qiu, X. Dong, J. H. Shim, J. Cho, J. M. Mativetsky, Appl. Phys. Lett. **2018**, 112, 263102.

[428] J.-C. Bolsée, W. D. Oosterbaan, L. Lutsen, D. Vanderzande, J. Manca, Org. Electron. **2011**, 12, 2084.

[429] W. Hourani, K. Rahimi, I. Botiz, F. P. V. Koch, G. Reiter, P. Lienerth, T. Heiser, J.-L. Bubendorff, L. Simon, Nanoscale **2014**, 6, 4774.

[430] D. Moerman, N. Sebaihi, S. E. Kaviyil, P. Leclère, R. Lazzaroni, O. Douhéret, Nanoscale **2014**, 6, 10596.

[431] C. Musumeci, I. Salzmann, S. Bonacchi, C. Röthel, S. Duhm, N. Koch, P. Samorì, Adv. Funct. Mater. **2015**, 25, 2501.

[432] S. Uttiya, L. Miozzo, E. M. Fumagalli, S. Bergantin, R. Ruffo, M. Parravicini, A. Papagni, M. Moret, A. Sassella, J. Mater. Chem. C **2014**, 2, 4147.

[433] P. S. Fernando, J. S. Mehta, D.-M. Smilgies, J. M. Mativetsky, Adv. Electron. Mater. **n.d.**, n/a, 2200156.

[434] U. Zschieschang, F. Ante, T. Yamamoto, K. Takimiya, H. Kuwabara, M. Ikeda, T. Sekitani, T. Someya, K. Kern, H. Klauk, Adv. Mater. **2010**, 22, 982.

[435] J. K. Wenderott, B. Xuan Dong, P. F. Green, Phys. Chem. Chem. Phys. **2021**, 23, 27076.

[436] B. Peng, Z. He, M. Chen, P. K. L. Chan, Adv. Funct. Mater. **2022**, n/a, 2202632.

[437] N. A. Kukhta, A. Marks, C. K. Luscombe, Chem. Rev. **2022**, 122, 4325.

Nicholas TURETTA

Auto-assemblage et caractérisation multi-échelle des structures et des interfaces

Résumé

La compréhension du transport de charge est une condition indispensable du développement de dispositifs optoélectroniques fonctionnels basés sur des semi-conducteurs organiques (petites molécules ou polymères). La thèse commence par une brève introduction sur les semi-conducteurs organiques et les aspects structurels essentiels pour comprendre le transport de charge en électronique organique. Liée à ce premier chapitre, une introduction pratique concernant les différentes techniques expérimentales qui ont été utilisées dans la thèse est présentée de manière comparative. Les trois chapitres suivants se réfèrent chacun à un dispositif fonctionnel particulier : 1 - Capteurs d'humidité basés sur une petite molécule organique hydrophile, 2 - Transistors électrochimiques organiques optiquement commutables basés sur un mélange de polymères avec une molécule photochromique, 3 - Etude du transport de charge hors plan dans des transistors organiques basés sur de petites molécules organiques.

Mots clés :

semi-conducteurs organiques, capteur d'humidité, transistors organiques, molécule photochromique, transport de charge,

Résumé en anglais

Understanding charge transport is the base for the development of functional optoelectronic devices based on organic semiconductors, namely small molecules or polymers. The thesis begins with a brief introduction on organic semiconductors focusing on the structural aspects that are key to understanding charge transport in organic electronics. Tied to this first chapter, a practical introduction concerning the different experimental techniques that have been employed throughout my work as a PhD student is presented in a comparative way. The three following chapters each refer to a particular functional device: 1 - Humidity sensors based on a hydrophilic small organic molecule, 2 - Optically switchable organic electrochemical transistors based on a polymer blend with a photochromic molecule, 3 - Study of the out-of-plane charge transport in organic field effect transistors based on small organic molecules.

Keywords:

organic semiconductors, humidity sensor, organic transistors, photochromic molecule, charge transport.